Applications of terrestrial LiDAR, infrared thermography, and photogrammetry for mapping volcanic rocks in southern BC

by

Megan Dewit

B.Sc. (Hons.), Simon Fraser University, 2015

Thesis Submitted in Partial Fulfillment of the
Requirements for the Degree of
Master of Science

in the
Department of Earth Sciences
Faculty of Science

SIMON FRASER UNIVERSITY
Summer 2020

Declaration of Committee

Name:	**Megan Dewit**
Degree:	**Master of Science**
Thesis title:	**Applications of terrestrial LiDAR, infrared thermography, and photogrammetry for mapping volcanic rocks in southern BC**
Committee:	**Chair:** **Brendan Dyck** Assistant Professor, Earth Sciences
	Doug Stead Co-supervisor Professor Emeritus, Earth Sciences
	Glyn Williams-Jones Co-supervisor Professor, Earth Sciences
	Marc-André Brideau Committee Member Adjunct Faculty, Earth Sciences
	Kelly Russell Examiner Professor, Earth, Ocean and Atmospheric Sciences University of British Columbia

Abstract

Remote sensing methods are widely used in geological applications today, as many outcrops are difficult to access. Terrestrial LiDAR, infrared thermography, and photogrammetry are used at two field sites in BC: the Cheakamus Valley Basalts (CVB) and Chilcotin Group basalts (CG). The physical properties of the rock at each field site such as composition, texture and structure were studied through remote sensing, and compared to analyses completed in the laboratory as well as traditional contact mapping. The CVB site consists of two outcrops of isolated lava flows approximately 10 km southwest of Whistler, BC, and the CG basalts are observed at the Chasm, a 7 km-long canyon approximately 20 km northeast of Clinton, BC. A virtual field site of the Chasm site was constructed from the remote sensing data, and in conjunction with these analyses, this research clearly shows that it is possible to remotely map otherwise inaccessible volcanic rock masses.

Keywords: terrestrial LiDAR; infrared thermography; photogrammetry; remote sensing; basalt; geovisualisation

For my Opa and Auntie Jodi

I wish you were here.

Table of Contents

List of Tables

List of Figures

List of Acronyms

CG	Chilcotin Group Basalts
CVB	Cheakamus Valley Basalts
FOV	Field of View
GUI	Graphic User Interface
GVB	Garibaldi Volcanic Belt
IRT	Infrared Thermography
JS	Joint Set
LiDAR	Light Detection And Ranging
MR	Mixed Reality
POI	Point of Interest
RADAR	Radio Detection and Ranging
RGB	Red, Green, Blue (colour values)
ROI	Region of Interest
SfM	Structures-from-Motion
TLS	Terrestrial Laser Scanner
VR	Virtual Reality

Chapter 1. Introduction

Geologic mapping techniques have traditionally required the geologist to characterize the field area and map the rocks through direct observation, but recent advances in remote sensing technologies have given rise to a new approach for the characterization of outcrops. Traditional contact mapping can be time-consuming and expensive, however can provide highly accurate and reliable results. New technologies have not only expanded the possibilities for mapping large areas in a fraction of the time, but also expanded the accessible area through the development of efficient methods of transportation for equipment and scientists, such as helicopters and all-terrain vehicles (ATV). Some outcrops, however, remain inaccessible for direct observation of geological characteristics, and therefore must be mapped through other means, which is where remote sensing can augment the information collected by traditional contact mapping.

Remote sensing encompasses an enormous variety of methods for obtaining data on objects from a distance, including satellite imagery (e.g. SkySat, Ikonos, SPOT), photography, Light Detection and Ranging (LiDAR), infrared and hyperspectral imagery, and Radio Detection and Ranging (RADAR). Data obtained through remote sensing may come in 3D format, such as point clouds, and show the three-dimensional geometry of an object or surface, or 2D, such as images, which can be captured in colours as seen by the human eye (conventional photography), or the spectral and thermal properties of the material (hyperspectral and thermal imagery). Studies by Franceschi et al. (2009), Burton et al. (2011), and Teza et al. (2015), have shown remote sensing can be useful in the mapping of structural features as well as possibly the identification of different rock types in outcrops, which makes remote sensing a valuable tool for mapping inaccessible outcrops.

Globally, basalt is the most prevalent volcanic rock (National Geographic, 2016), and can be found in many different forms within southern British Columbia. It therefore provides a convenient and efficient means of conducting a preliminary study on the mapping of volcanic rocks using remote sensing, as well as a relevant topic of study for many applications. Further, basalts are ideal in an initial study such as this because of the large variety of characteristics they present, including mineralogy, grain size,

volcanic features, textures, structural features and alteration styles, providing a wide range of rocks for analysis. This study will focus on using three remote sensing methods, terrestrial LiDAR (TLS), both conventional and Structures-from-Motion (SfM) photogrammetry, and infrared thermography (IRT), to map two sites in southern British Columbia, Canada. Previous research using these methods has focused mainly on evaluating sedimentary sequences (Burton et al., 2011; Franceschi et al., 2009; Teza et al., 2015), though some studies have applications on volcanic rocks (Mazzarini et al., 2007; Pesci et al., 2008; Pesci et al., 2011; Shevchenko et al., 2015; Mineo and Pappalardo, 2016). This research will expand upon these previous studies and evaluate the results of these techniques on volcanic successions. The study sites involve lava flows composed primarily of basalt where the emplacement mechanisms and environment differ for each field area, thereby offering a variety of rocks for mapping using remote sensing methods.

1.1. Research Objectives

The primary objectives of this research are to:

- develop techniques for accurately mapping volcanic rocks which would otherwise be inaccessible
- evaluate the advantages and limitations of the remote sensing methods LiDAR, IRT and photogrammetry for areas where traditional contact mapping methods are not possible
- map the geology, alteration, and structural features of two field sites using remote sensing, petrography, and traditional field methods

These objectives will be addressed through the application of the aforementioned remote sensing techniques, field mapping, and petrography of samples at two field sites in southern British Columbia.

1.2. Thesis Structure

This research involves several techniques employed at two field sites, as well as complimentary laboratory studies. Outlined below is the content of each chapter contained in this work.

Chapter 1 is an introductory chapter, and contains an overview of the research project, research objectives, and thesis structure, as well as background information on the field sites visited, remote sensing methods employed, and previous research in relevant subject areas.

Chapter 2 provides a comprehensive description of the methods and materials used in the completion of this research. It includes all methodology adopted for all the applied techniques and field sites.

Results are disseminated into two chapters, Chapters 3 and 4. Some repetition will occur between these two chapters and the remainder of the thesis for ease of presentation and explanation. Chapter 3 describes the results of LiDAR, IRT and photogrammetry mapping at the Chasm Provincial Park field site and Cheakamus Valley Basalts outcrops. Both field and laboratory IRT results for the Chasm are explained in this chapter.

Chapter 4 is presented in journal manuscript format. In this chapter, the development of a geovisualization interface is described, which contains laboratory and field data obtained at the Chasm field site. As this interface includes data from all three remote sensing methods, it serves as a vehicle for synthesizing and presenting the results of this research project.

Chapter 5 discusses the overall results of the research project, and the general implications of this study for the applications of remote sensing techniques to characterize volcanic successions.

Chapter 6 contains the conclusions from this research, provides context for the results, and includes recommendations for further work.

1.3. Study Background

This study includes two field sites, at which three remote sensing methods were employed. Located in British Columbia (Figure 1-1), the field sites are the Cheakamus Valley Basalts (CVB), near Whistler in southwestern BC, and the Chilcotin Group Basalts (CG) at the Chasm, near Clinton in south-central BC. These sites are composed primarily of basaltic lavas, and were chosen for their accessibility, proximity, and variety of lava morphologies, structures, and textures. These sites represent ideal locations for the development of new remote sensing mapping techniques. The CVB are small, isolated lava flows which were erupted during the Fraser Glaciation presumably beneath ice (Green et al., 1988; Mathews, 1958). The Chasm is a 7 km long canyon eroded into multiple layers of plateau basalts of the CG, exhibiting near-vertical cliffs approximately 130 m in height (Farrell et al., 2007; Andrews and Russell, 2007). Three methods of remote sensing are described: LiDAR, infrared thermography, and digital photogrammetry, chosen primarily for their relevance in the remote sensing field, their increasing relevance in mapping rock sequences, and their ability to merge and combine with other remote sensing techniques. These methods are available in satellite, airborne, and terrestrial forms; this project will only involve the use of terrestrial instruments, thus there is an emphasis on the land survey principles for each of the techniques. This section presents a literature review on the field sites and remote sensing methods used in this research.

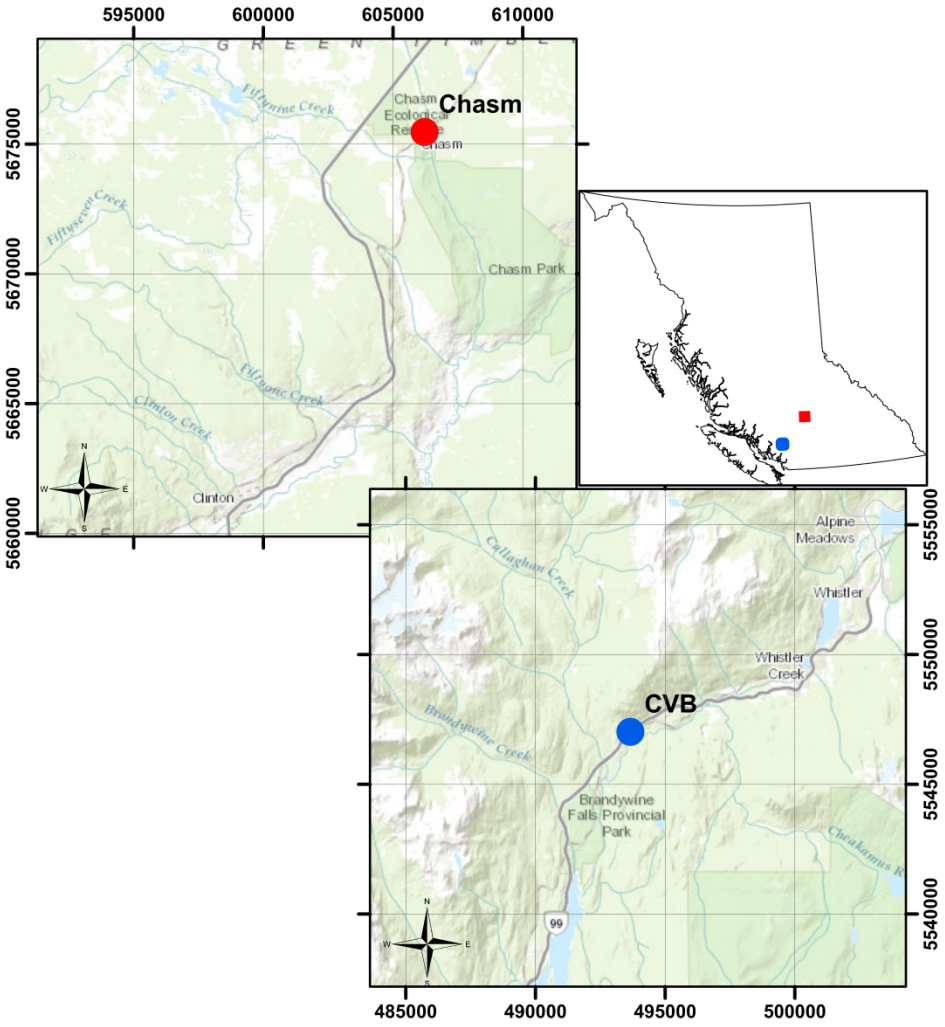

Figure 1-1. Maps showing the general locations of the two field sites in British Columbia (red = Chasm, blue = CVB), and the field sites in their respective local areas. Map units are meters in UTM Zone 10 North (ESRI, 2015).

1.3.1. CVB

The CVB are part of the larger Garibaldi Group volcanics, formed by volcanic features in the Garibaldi Volcanic Belt (GVB) (Woodell, 2012; Green et al., 1988). The GVB is composed of six volcanic fields and extends 240 km approximately parallel to the coastline in southwestern British Columbia (Green et al., 1988). Volcanoes in the GVB vary greatly in size, ranging from large stratovolcanoes to multiple domes or cones, and even single, isolated lava flows and subglacial forms, such as those seen in the CVB (Green et al., 1988). Rocks of the GVB have a range of compositions from basalt to rhyodacite; the basalts, including the CVB, are mainly found in the western portion of the

belt, occurring as valley-filling lavas or as isolated flows (Green et al., 1988). This is the case for the CVB, which, through radiocarbon dating of wood within lacustrine sediments of the same age, have been dated at 34,200±800 yrs B.P. (Green et al., 1988). The CVB complex began with an early episode of volcanism at approximately 0.05 Ma (dated by K-Ar whole-rock analysis), and subsequently eroded by the advance and retreat of a continental ice sheet during the Salmon Springs Glaciation (Green et al., 1988). The later flows, including the field site for this study, are plagiophyric basalts occurring as isolated ridges above the surface of the older flows, which have been eroded by glaciers (Green et al., 1988). Mathews (1958) hypothesized that due to the lack of glacial erosional features on these newer flows, they were likely erupted during the latter part of the Fraser Glaciation into trenches within the ice sheet, which had been originally formed by heated meltwater.

The two outcrops, CVB1 and CVB2, investigated for this study lie along the Sea-to-Sky Highway (Highway 99) in southwestern British Columbia, approximately 4 km north of Brandywine Falls Provincial Park and 10 km southwest of Whistler (Figure 1-2). There are several outcrops of CVB located in this particular area along Highway 99, which may at one point have been a single flow, but erosion has created several isolated 'islands' (Woodell, 2012). These outcrops were selected because of their accessibility, lack of obstructions such as vegetation, and lack of extensive alteration, weathering, and erosion.

Previous studies of the overall geochemistry of the assemblage state the CVB contain varying amounts of olivine (7-16%), plagioclase (10-16%), and clinopyroxene (1-11%) with 64-72% groundmass, and are classified as olivine basalts (Green, 1981). They are mildly alkaline, containing between 48.57 and 51.09% SiO_2, and through calculations involving co-existing Fe-Ti oxides, a temperature of 1027°C±30°C was obtained for the basalts (Green, 1981). Woodell (2012) analyzed thin sections of the CVB at the same outcrops as investigated in this study and found olivine and plagioclase phenocrysts in a groundmass made mostly of glass, with minor magnetite, pyroxene, and plagioclase. The geochemical characteristics of the CVB vary between and within individual outcrops, offering a variety of compositions and textures for mapping in this project using remote sensing technologies.

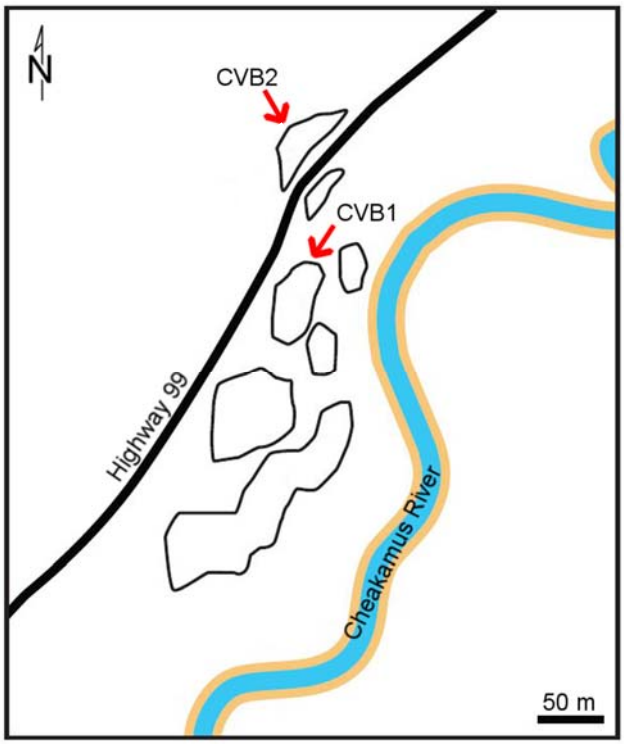

Figure 1-2. Zoomed-in map of outcrops in the CVB field area; outcrops used in this study are indicated with red arrows (modified from Woodell, 2012).

1.3.2. Chasm

Previous studies of the CG have included reconnaissance and regional scale mapping, geochemistry, magnetic susceptibility, porosity, density, and conductivity (Bevier, 1982; Bevier, 1983a; Bevier, 1983b; Mathews 1989; Tipper 1971; Dostal et al., 1996; Anderson et al., 2001; Farrell et al., 2007; Farrell et al., 2008, Andrews and Russell, 2007; Dohaney, 2009). The CG are a series of transitional alkaline to subalkaline basalts which cover an area of approximately 17,000 km^2 in south-central British Columbia, and range in age from 28 to 1 Ma (Dohaney, 2009; Farrell et al., 2008; Andrews and Russell, 2007). They are described by Bevier (1983b) as plains basalts, and likened by Andrews and Russell (2007) to the Columbia River Flood Basalts because of their sub-horizontal orientation, columnar jointing or lack of structure within each flow, and due to their similar composition. The CG basalts, however, exhibit smaller thicknesses and less continuity than their Oregon-Washington counterparts, and so are thought to have been extruded at a lower rate (Mathews, 1989). The Chasm in the Chasm Provincial Park field site (hereafter referred to as the Chasm), is located

approximately 20 km northeast of the town of Clinton in British Columbia, and is a canyon which exposes a nearly continuous outcrop of CG basalts in the canyon walls for several kilometers on either side (Figure 1-3) (Farrell et al., 2007; Andrews and Russell, 2007). The characteristics of the flood basalts comprising the Chasm allow for a field site with easily recognizable units, unit divisions, structure, and other features, which in turn provide a framework for analysis with minimal complications.

There are 10 continuous flows of the CG exposed in the Chasm, exhibiting a slight tilt from horizontal (Figure 1-3), dated by Farrell (2010) to be between 8.72 ± 0.37 Ma and 10.00 ± 0.48 Ma, with the estimated duration of volcanism in the Chasm area as 1.28 ± 0.61 Ma. Underlying the lava flows is a sequence of more than 15 m of hyaloclastite breccia, indicating subaqueous deposition of the lavas before the lava height exceeded that of the water body; subsequent deposits were subaerial (Andrews and Russell, 2007; Farrell et al., 2008). The sources of the lavas in the Chasm are not known, and spatter deposits and volcanic bombs which normally indicate proximity of deposits to the lava source are not encountered (Farrell et al., 2007). Gabbroic stocks, located approximately 30 km north of the Chasm, have been identified as possible feeders for the CG basalts, having been eroded over time (Farquharson and Stipp, 1969).

Figure 1-3. Chasm cliff face showing ten lava flows with either massive, sheet-like morphology (top and base of section), or lobate, lensoidal morphology (middle of the section). Lava flows are separated by red paleosols. Photograph taken looking east.

The CG basalts are divided by Andrews and Russell (2007) into three lithofacies: Chasm-style, Bull Canyon-style, and Dog Creek-style, which exhibit diverse lava morphologies and types. The type section for Chasm-style lithofacies (Figure 1-4; Figure 1-5) of the CG is located approximately midway down the Chasm canyon on the east wall, and is described by Andrews and Russell (2007) and Farrell et al. (2007) as having thick (≤15 m) massive basalt lava flows, which near the base and top of the section appear continuous for several kilometers, and in the middle of the section exhibit lensoidal morphologies less than 50 m across. Within each lava flow is a basal vesicular zone (≤1 m), a columnar-jointed, non-vesicular central zone (≤10 m), and an upper vesicular, amygdaloidal zone. Between successive lava flows is typically a red-brown paleosol and erosion surface with monolithic regolith basalt breccia, interpreted by Andrews and Russell (2007) to indicate many thousands of years passed between successive flows, allowing for erosion and development of soil horizons. The variety of features found in the Chasm basalts offer an interesting opportunity for comparison of remote sensing methods and results, and provide an opportunity to develop a technique for mapping a diverse range of lithologies.

A petrographic study of coherent rock samples and paleosols of CG lava flows at the Chasm by Farrell (2010) revealed alkali olivine porphyritic basalt, with modal percentages of 5-30% olivine. Olivine phenocrysts are commonly partially iddingsitized and skeletal, and vesicles average 3% abundance with sizes between 0.28-0.95 mm. The groundmass is comprised of plagioclase feldspar laths, with clinopyroxene, augite, bladed oxides, and interstitial glass, and accessory minerals of potassium feldspar and nepheline. Dikytaxitic textures of the plagioclase laths are common; ophitic and poikilitic textures also occur. The mineralogy of the various lavas exposed in the Chasm does not vary significantly, however grain sizes and textures differ between separate flow fields (Farrell, 2010). The paleosols are composed primarily of two parent materials, mafic basalt and felsic tephra. These materials are typically in horizons grading from weathered basalt at the bottom (exhibited by montmorillonite/smectite clays), upwards to floating basalt fragments in a finer-grained matrix, which then grades upwards to pipe vesicles. The graded horizons are then finally overlain by a new lava layer (Farrell, 2010). To expand upon the research of Farrell (2010), a petrographic study of each of the lava layers and several paleosols is undertaken in order to gain an overview of the

mineralogy of the main cliff face used in this study and provide a means of reference for remote sensing mapping.

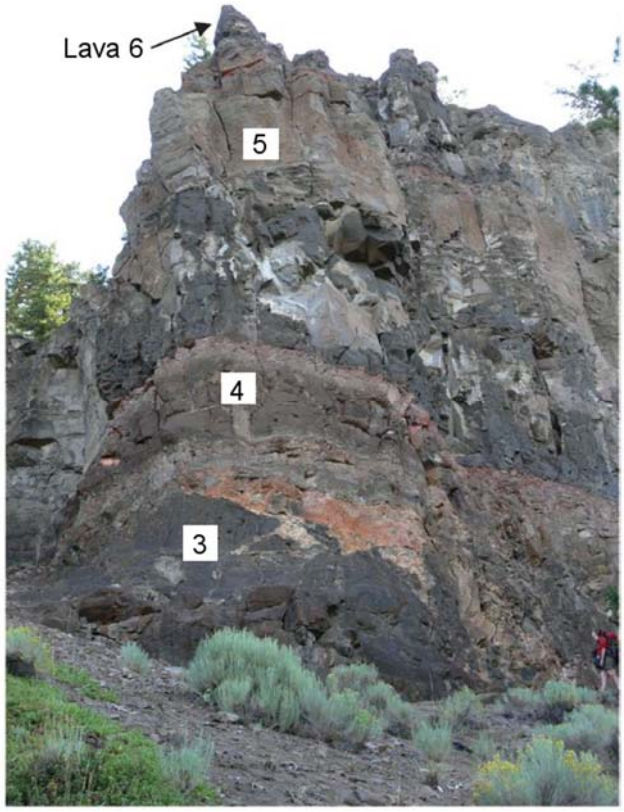

Figure 1-4. Chasm-type lithofacies type section, showing four lava flows described by Farrell et al. (2007). Lava 3 is massive lava, lava 4 is particularly vesicular, lava 5 is lobate with columnar jointed centers, and lava 6 is amygdaloidal and lobate. Image from Farrell et al. (2007).

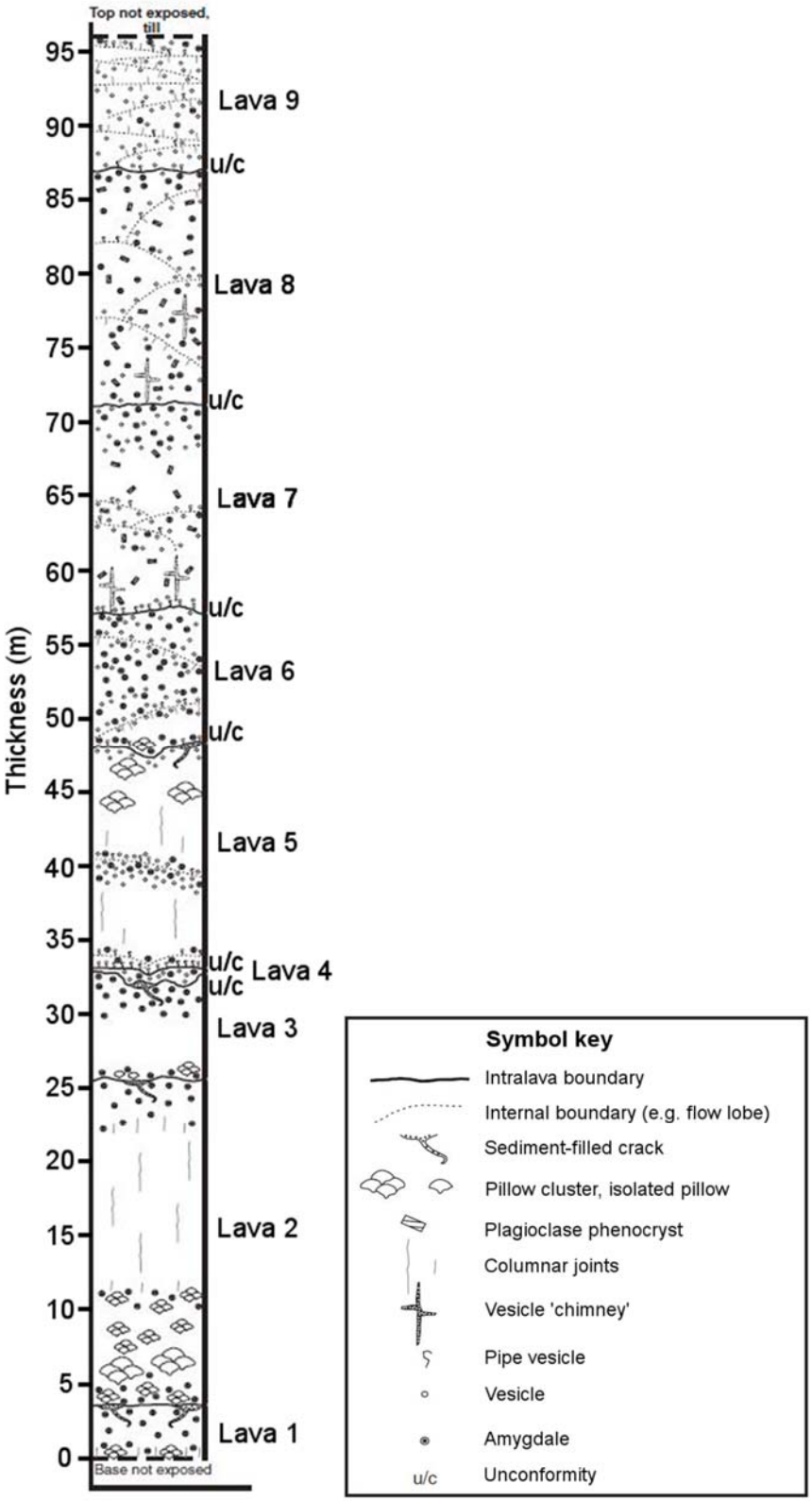

Figure 1-5. Type section of Chasm-type lithofacies of the CG (Farrell et al., 2007).

1.3.3. Columnar Jointing

Columnar joints form in intrusive or extrusive igneous melts, such as sills, dykes, or lava flows, and were observed and described by Woodell (2012) with specific reference to the CVB. Columnar joints are contractional joints, generated by a decrease in volume of the melt during cooling, causing a brittle release of tensile stress (Woodell, 2012). Columnar joints generally have an elongate geometry, forming a hexagonal shape in plan view (Figure 1-6)(Woodell, 2012). They do not occur in all cooled igneous bodies, however they have been observed in a range of igneous lithologies from mafic to felsic, in coherent and fragmental rocks (Woodell, 2012).

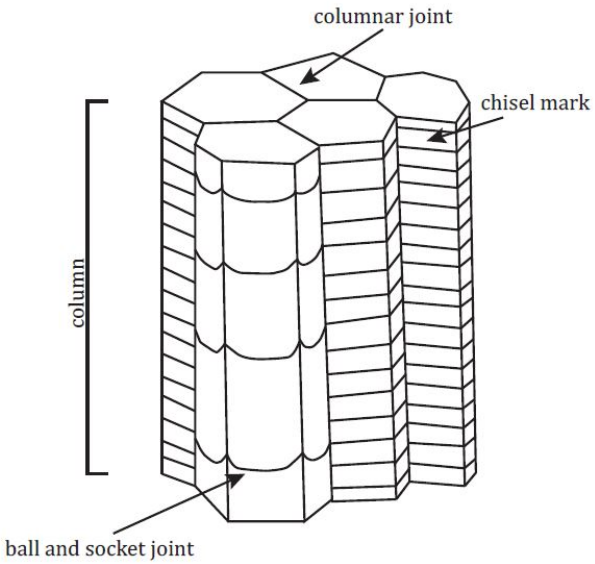

Figure 1-6. Features of columnar jointing.

Other features sometimes occur with columnar jointing, such as chisel marks and ball-and-socket joints (Figure 1-6). Chisel marks only occur on the surface of the columnar joints, and like plumose structures, they delineate propagational stages of the joint as it formed (Woodell, 2012). Ball-and-socket joints are planar to curved, and cut the columns into sections, penetrating fully through the columns (Woodell, 2012).

Columnar joints form parallel to the heat flow (meaning their elongation direction is parallel to the heat flow) and perpendicular to cooling surfaces (Woodell, 2012). Lava flows with columns contain distinctive zones, called the colonnade and entabulature (Woodell, 2012). The colonnade can be subdivided into the upper and lower colonnade, both of which contain equally spaced, linear, usually hexagonal columns of

approximately the same size (Woodell, 2012). The entabulature lies between the upper and lower colonnades, and generally is comprised of smaller, curved and irregular columns which have various plan-view shapes and numbers of sides (Woodell, 2012). In thicker flows, particularly, this entabulature zone is chaotic.

1.3.4. LiDAR

The rapid acquisition of precise point data using LiDAR, which carries other physical properties of the reflective material, has allowed for the creation of extremely high accuracy three-dimensional models of geological outcrops, for which interpretation of geological structures and subsequent analysis have been made easier than ever before (Buckley et al., 2008). Though remotely sensed data cannot, through modern methods, be a direct substitute for data obtained via hands-on field geological survey, methodologies are rapidly evolving to vastly improve the quality of remotely sensed data, as well as allow even for quantitative analyses (Buckley et al., 2008). Field surveys in geology are essential for the capture and subsequent analysis of data at scales ranging from a single bed in an outcrop, to regional geological frameworks. Remote sensing is an efficient way to visualize geological outcrops and can complement the field data collected with the purpose of enhancing observations by providing a framework for quantitative analysis (Buckley et al., 2008).

LiDAR uses light in the form of lasers to create accurate three-dimensional surfaces of topography, buildings, tree canopies, geological outcrops, and everything else with which the laser comes into contact (Jensen, 2006a, Campbell, 2007). Using light in the near infrared wavelengths (0.72-1.3 μm), LiDAR instruments, or laser scanners, emit a laser pulse to a target, and through measuring the time required for the emitted laser pulse to return to the instrument (time of flight), a distance to target is calculated using the equation:

$$R = \frac{1}{2}tc \quad (1)$$

where R is the range, or distance, to the target, t is the time of flight, and c is the speed of light (3×10^8 m s^{-1}) (Jensen, 2006a, Campbell, 2007). The scanner repeats the distance ranging process over a grid, which then combines to create a point cloud, or three-dimensional model, of the target (Campbell, 2007).

Lasers, because they are a form of light, travel as waves through the air and therefore have properties such as frequency and amplitude; LiDAR returns have several other properties including reflectance and intensity which can be used in studying the material of the three-dimensional object being imaged (Jensen, 2006a; Burton et al., 2011). LiDAR returns are modified by the material off which they are reflected, and can aid in the assessment, categorization, and analysis of materials through observing the changes in the attributes of the returned waveforms (Burton et al., 2011; Campbell, 2007; Chang et al., 2015). LiDAR reflectance is a property of the material from which the laser pulse has been reflected, and essentially describes the brightness of the target, whereby a higher reflectance, such as that exhibited by white marble or limestone, can be attributed to a bright target (Riegl, 2015). A low reflectance means the target is dark or does not reflect laser light very well, such as wet ice or black tar paper (Riegl, 2015). LiDAR intensity describes the ratio between the power returned and the power emitted, which may seem like a similar property to reflectance, however intensity is affected by the amount of scattering inflicted upon the laser pulse by target range and reflectivity, scan angle, and surface roughness (Burton et al., 2011). Once distance-normalized, LiDAR intensity can be viewed as a similar property to reflectance, or even amplitude, of the waveform (Figure 1-7) (Jensen, 2006a). As these properties are dependent upon the reflective material, LiDAR can be a very useful tool for studying the underlying properties of the surfaces being scanned (Jensen, 2006a, Burton et al., 2011). LiDAR instruments collect thousands of points per second at distances up to 6 km, and so have become a valuable method for both three-dimensional visualization of surfaces, as well as more recently, a tool for researching the composition of the surfaces themselves (Burton et al., 2011; Campbell, 2007).

LiDAR models are very high in accuracy, and have applications on a range of scales from large regional studies to small outcrops. Bellian et al. (2005) integrated LiDAR data collected from several different outcrops over a large geographical area to create Digital Outcrop Models (DOMs), which were used to map geological contacts and faults, follow particular beds, and correlate stratigraphy from multiple areas. The general concept of DOMs using LiDAR data is useful in a study at the Chasm, as lava units will correlate across the canyon, and can be mapped as such using LiDAR models.

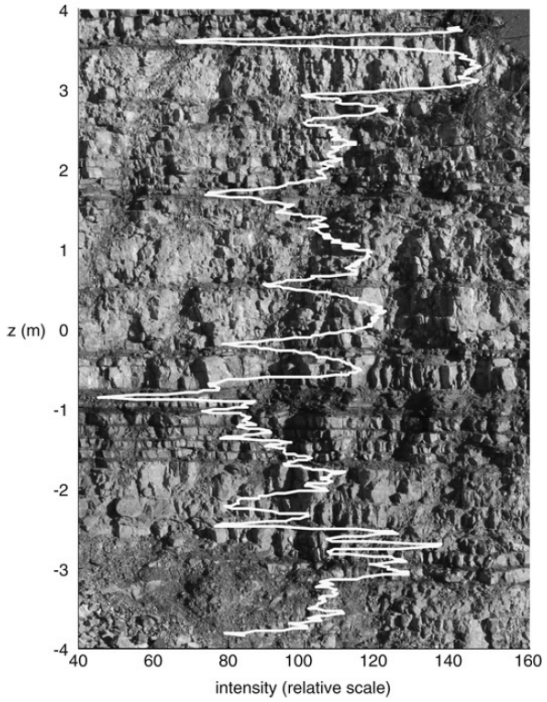

Figure 1-7. Intensity profile of an outcrop from terrestrial LiDAR data overlain on a photograph of the same stratigraphic profile (Franceschi et al., 2009).

The study and monitoring of landslides in hazardous regions pose a continuous problem of safety for field surveyors, but the use of LiDAR has greatly reduced these risks (Kromer et al., 2017; Jones, 2006). Obtaining the geometries of slopes using LiDAR can not only be helpful for simple visualization of topography, but time-series LiDAR can be used for detecting landslide displacement fields, landslide hazard identification and monitoring, as well as detecting geology and structures. Volcanoes, due to their inherent instability and active processes, are particularly dangerous; terrestrial LiDAR provides several important benefits such as rapid acquisition of data, lack of close or direct interaction with active processes thereby vastly reducing the risks involved with monitoring the activity at volcanoes, and three-dimensional models can be produced without the need for targets placed on the slope, such as is the case in photogrammetric surveys (Jones, 2006). Pesci et al. (2011) found that because scans could be completed with reliable accuracy and precision, monitoring of Mount Vesuvius volcano (Italy) could be undertaken as a relatively simple and low-cost venture using LiDAR, and recognized several landslide events within the crater of Vesuvius using multi-temporal terrestrial laser scans carried out over a four-year span. Pesci et al. (2008) used the LiDAR data obtained in the crater of Mount Vesuvius, as undertaken at

the Chasm in this study, to delineate zones of volcanic deposits from various eruptive episodes and other stratigraphic features, using reflectance of the materials and the complementary RGB data obtained with a calibrated digital camera. LiDAR can improve the safety of workers in hazardous landslide-prone areas through reducing the time of survey in dangerous terrain, and acquiring accurate topographical data of slopes from a distance, as well as aiding in the mapping of stratigraphy using LiDAR reflectance and intensity.

The geometry of slopes provided by LiDAR data is very useful for many types of studies, however the properties of the LiDAR data itself, such as intensity, are also extremely important for carrying out research in geology. Mazzarini et al. (2007) found that because of a balance between surface roughness and texture of lava flow surfaces at Mount Etna (Italy), which become weathered over time, there was a correlation between LiDAR intensity and lava flow age, which they used to chronologically map the lava flows at the volcano. Intensity values can also be distance-normalized, at which point they are proportional to reflectivity (Burton et al., 2011). Franceschi et al. (2009) mapped the limestone and marl lithology distributions within outcrops using the intensity of LiDAR returns, through finding an inverse relationship of reflectance to weight percent of clay in the rock. Burton et al. (2011) also found a positive correlation between reflectivity and weight percent quartz, plagioclase, and potassium feldspar, with a similar inverse correlation to weight percent clay in sand and shale outcrops. Both studies found that alteration, weathering, and the presence of vegetation reduced the contrast observed in reflectance between lithologies, so cleaner outcrops, such as those at the Chasm and CVB, are recommended for these types of studies (Burton et al., 2011; Franceschi et al., 2009). Both LiDAR intensity and reflectivity are valuable tools for the detection of geological features, and can be used in conjunction with the three-dimensional geometry for mapping of outcrops.

1.3.5. Infrared Thermography

Short-wavelength energy (e.g. ultraviolet) emitted from the Sun is absorbed by objects on the Earth's surface, and subsequently emitted from these objects as long-wavelength radiation in the form of visible light and infrared (Jensen, 2006b). Infrared radiation wavelengths range from 0.72-14 μm in length, however thermal infrared occurs

only between 3-14 μm, which is the basis for remote sensing using infrared thermography (Jensen, 2006b).

Volcanoes are features which can sometimes exhibit large temperature variations over small areas due to degassing, hot springs, lava flows and lakes, and other geothermal activity, so infrared thermography (IRT) has proven useful in the understanding of volcanic hazards, deposits, and phenomena (Spampinato et al., 2011). Infrared thermography (IRT) is the study of varying temperatures of a material using the thermal infrared wavelength of light. Normally this is done in an instant in time, whereby the information gained is limited to the temperature of the material for that given point in time, however recent studies have experimented with using IRT over a certain time interval. The work by Mineo and Pappalardo (2016), for example, concluded that it is possible to estimate the porosity of lava samples obtained from the flows of Mount Etna through artificially heating the samples and observing their rate of cooling. Through examining the cooling rate of the samples over specific time intervals, Mineo and Pappalardo (2016) could differentiate between samples with various porosities. Teza et al. (2012) completed work based on a similar concept in the field on rock slopes in Italy, where they obtained thermal images of the slope at regular intervals over an entire cooling cycle of the rock after sunset. Through analysis of the thermal imagery time-series, Teza et al. (2012) characterized the damage and fracture networks within the rock slope, and thus monitor the condition of the slope. Radiation from the Sun causes rocks to heat during the day and cool during the night, when the Sun is no longer above the horizon. This interplay between heating and cooling cycles provides a medium for studying the temperature variations of rocks over time, which proved to be a useful technique for observing the features of the cooled lava flows at the Chasm.

1.3.6. Photogrammetry

Due to the current ubiquity of digital cameras of all forms, photogrammetry and SfM have become extremely widespread and common methods of gaining three-dimensional information on objects through the simple principle of stereoscopic viewing (Linder, 2009; Micheletti et al., 2015). To precisely locate objects and create an accurate, geographically located model, traditional photogrammetric methods require the use of GPS systems and ‘targets’, or points of known location within the images (Linder, 2009). If the location of several targets is well constrained and the targets are well-

spaced throughout the area of interest, the resulting three-dimensional model can be oriented and referenced to a specific geographic location (Linder, 2009). Precision is very important in photogrammetry, as points, lines and areas are digitized from inspection and analysis of the model, which can eventually be purposed for calculations such as slope angle, distances, and volumes (Linder, 2009). Three-dimensional models, created to scale, via photogrammetric methods are extremely versatile in their possible applications.

SfM photogrammetry is a very quick and inexpensive method for generating 3D models of objects, and has been found to create high-quality results (Westoby et al., 2012), which makes it extremely useful for studies in remote areas like the Chasm. SfM operates in a similar manner to traditional photogrammetry with matching of photographs, however a fundamental difference between the two is that SfM does not require targets of known locations within the scene, and camera location specifications are found through the bundle adjustment completed by the SfM software (Westoby et al.,2012). The SfM technique normally includes a moving sensor, capturing images of a three-dimensional object from many positions and perspectives (Figure 1-8) (Westoby et al., 2012).

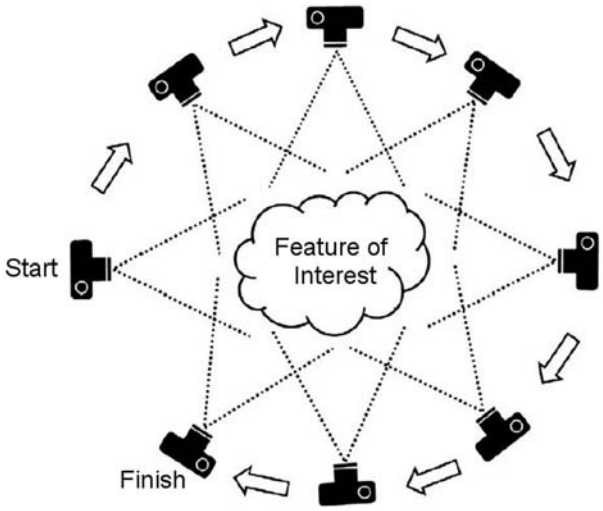

Figure 1-8. The SfM photogrammetry technique, whereby images are captured of the target feature from multiple perspectives, with overlapping images (Westoby et al., 2012).

Photogrammetry is widely used in slope stability assessments and the characterization of rock slopes. Sturzenegger and Stead (2009), for example, used

close-range terrestrial photogrammetry to map discontinuities within a rock mass, and found that the models allowed for accurate measurement of joint and fracture networks, hence mapping of structural features from photogrammetry at the Chasm and CVB was undertaken.

Volcanoes are also extensively studied using photogrammetry, and the mapping of volcanic deposits, such as the work done for this research, will serve to improve our understanding of volcanic phenomena. Shevchenko et al. (2015) processed a series of aerial photographs taken over several years in photogrammetry software, and used the resultant models to measure the volume of a growing dome at Molodoy Shiveluch Volcano in Kamchatka. Through the monitoring of the volcano over time with photogrammetry, Shevchenko et al. (2015) could estimate the volumes of failures of the dome, propagation of morphological features, and identify areas where there was deposition of failure deposits. Pesci et al. (2007) completed an aerial digital photogrammetry survey over Mount Vesuvius volcano, generating very accurate models of the terrain within and around the crater. Through the analysis of 3D models of volcanoes, their surrounding terrain, and 3D mapping of volcanic stratigraphy, the eruptive histories can be learned and potential hazards found, which has the possibility of reducing the risk volcanoes pose to surrounding communities.

1.3.7. Merging Remote Sensing Techniques

Recent studies have shown that integrating remote sensing techniques has the potential to yield results which would have been unattainable with a single method alone. Teza et al. (2015) used LiDAR imagery in conjunction with thermography to locate joints and damage within the slope of the Passo della Morte landslide in Italy, and found that LiDAR and thermography data correlated well with on-site data gathered using extensometers and inclinometers, and so can be used as a relatively low-cost, efficient method for studying landslides in more difficult to access or hazardous regions. When 2D imagery, such as thermal imagery, is properly georeferenced onto a three-dimensional model such as that provided by LiDAR imagery, the combined model becomes a powerful tool for geological interpretation and detailed mapping (Buckley et al., 2010). Pesci et al. (2008) found that using photography in conjunction with LiDAR reflectance data, such as done at the Chasm for this research, was extremely successful in differentiating between rock types, depositional properties such as bedding, as well as

the identification of failure deposits. They analyzed rock composition of the Mount Vesuvius crater walls, and found that there is a link between the visible (photographs) and infrared (LiDAR laser) spectral signals, and the LiDAR reflectance data added valuable information to the study (Pesci et al., 2008). In many cases, one method of remote sensing may serve only to enhance another technique, however it has been shown that merging remote sensing technologies can open a new realm of possibilities for research.

Chapter 2. Research Methods

In order to address the research objectives outlined in Section 1.1, the methods employed for this study include a collection of data at a wide range of scales, using varied instrumentation and software. The importance of making observations at multiple scales cannot be overstated, as information obtained from a thin section with micrometer-sized features is different than that from an outcrop, which can in turn be one piece of a regional-scale puzzle. Data has therefore been collected in a variety of surveys including at thin section, hand sample and outcrop scales in both the field and laboratory. Analysis was completed for datasets both individually, and as an integrated amalgamation from multiple surveys. The focus of this study is mapping at the outcrop scale, as this is usually the scale used in traditional contact mapping methods.

Detailed mapping of the Chasm-type lithofacies by Farrell et al. (2007) and Farrell et al. (2008) provides a geological type section with which to base a comparison between data obtained through traditional contact methods, and remotely sensed data. Hand sample data obtained through laboratory methods described in Section 2.2 provided further base-level data for comparison with remote sensing methods, and were used to evaluate the difference between techniques for data collection. The data collected via the TLS, IRT and photogrammetry surveys were used to create remote sensing windows, which are a characterization of the lava sequences solely through data obtained from a distance. These windows were directly evaluated for contrasts with the geological type section and hand sample data, allowing for an assessment of the accuracy of terrestrial LiDAR, infrared thermography and photogrammetry for the prediction of geological parameters, and value of the remote sensing methods for mapping geology from a distance.

2.1. Field Surveys

2.1.1. Stations

Field surveys using terrestrial LiDAR, infrared thermography, and digital photogrammetry (conventional and SfM) were carried out during the period of spring and summer, 2015 and 2016. Each survey location was selected for its visibility, access,

and specific survey requirements such as number of stations necessary, lighting, and viewing angle relative to the slope. Stations were located in geographical space, with position coordinates obtained using a Garmin eTrex 10 handheld GPS unit, a Topcon Total Station, and a Leica GPS-500 differential GPS system with a base and rover station setup (Figure 2-1). The height of the tripod and facing azimuths of the instruments were recorded to ensure accurate elevation values and correct orientation, and the coordinates of recognizable features at both sites noted for use as control points. Survey locations for the CVB field site (Table 2-1)(Figure 2-2) were obtained using the Garmin handheld GPS unit at CVB1, the Garmin handheld and Total Station at CVB2, and all GPS methods were used at the Chasm field site (Table 2-2)(Figure 2-3).

Figure 2-1. Base (left) and rover (right) Leica GPS-500 station set-up. Rover system is mounted on a 2 m tall pole, the base of which was positioned over the points from which LiDAR, IRT and photogrammetry surveys were performed.

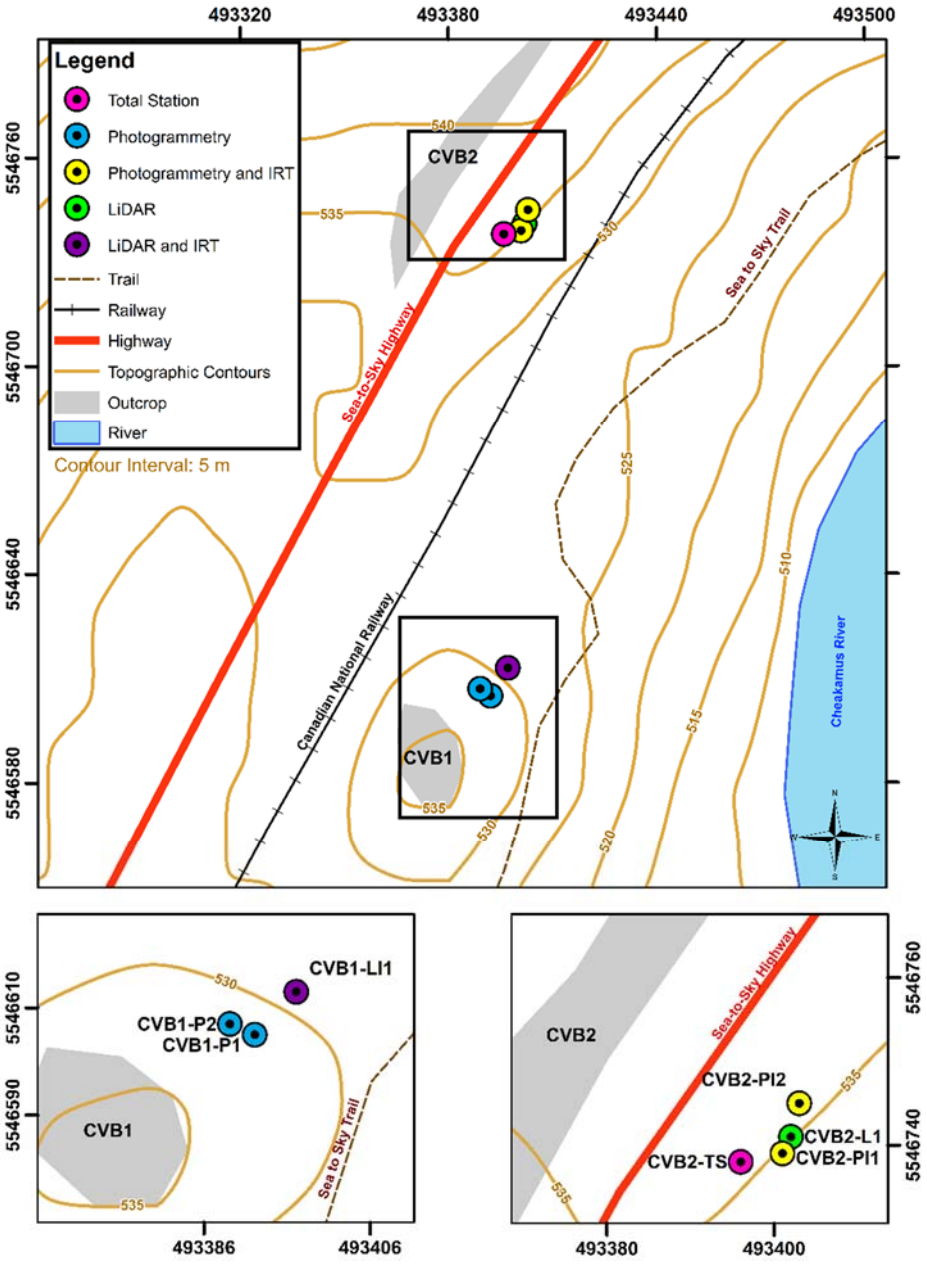

Figure 2-2. Regional map of Cheakamus Valley Basalt field site, with detailed station survey locations on inset maps (black outline). Coordinates are in WGS 84 UTM Zone 10N.

Table 2-1. Coordinates of photogrammetry, LiDAR, and IRT stations at each CVB outcrop in UTM Zone 10N. P=photogrammetry, L=LiDAR, I=IRT, TS=Total Station.

Survey Station	UTM Easting (m)	UTM Northing (m)	Height (m)	Error Margin (m)
CVB1-P1	0493392	5546605	535	± 3
CVB1-P2	0493389	5546607	532	± 3
CVB1-LI1	0493397	5546613	533	± 3
CVB2-TS	0493396	5546738	543	± 3
CVB2-PI1	0493401	5546739	538	± 3
CVB2-L1	0493402	5546741	540	± 3
CVB2-PI2	0493403	5546745	544	± 3

Table 2-2. Coordinates of photogrammetry, LiDAR, and IRT stations at the Chasm field site from differential GPS in UTM Zone 10N. P=photogrammetry, L=LiDAR, I=IRT, TS=Total Station.

Survey Station	UTM Easting (m)	UTM Northing (m)	Height (m)
LIP1	606507.62	5674839.66	1058.4
LIP2	606084.55	5675404.71	1063.4
LI1	608863.12	5671307.32	943.3
L1	606096.51	5675235.20	1062.4
L2	606087.73	5675220.22	1062.6
L3	606087.72	5674926.97	1057.8
L4	606097.79	5674909.72	1056.7
L5	606165.78	5674763.72	1043.7
L6	606112.83	5675506.87	1061.4
L7	606318.90	5675605.47	1064.2
L8	606439.93	5675337.65	1060.1
L9	606476.06	5675158.85	1053.7
L10	606533.72	5674386.65	1036.1
P1	606085.57	5675429.77	1062.9
P2	606080.02	5675346.55	1062.5
P3	606090.37	5675298.71	1062.2
P4	606436.22	5675354.93	1056.9
P5	606453.60	5675274.63	1057.4
P6	606464.99	5675237.49	1058.7
P7	606509.02	5675068.64	1055.5
P8	606529.08	5674920.21	1057.4
P9	606543.96	5674711.26	1058.4
P10	606537.09	5674638.47	1043.7
TS	606084.41	5675408.27	1063.5

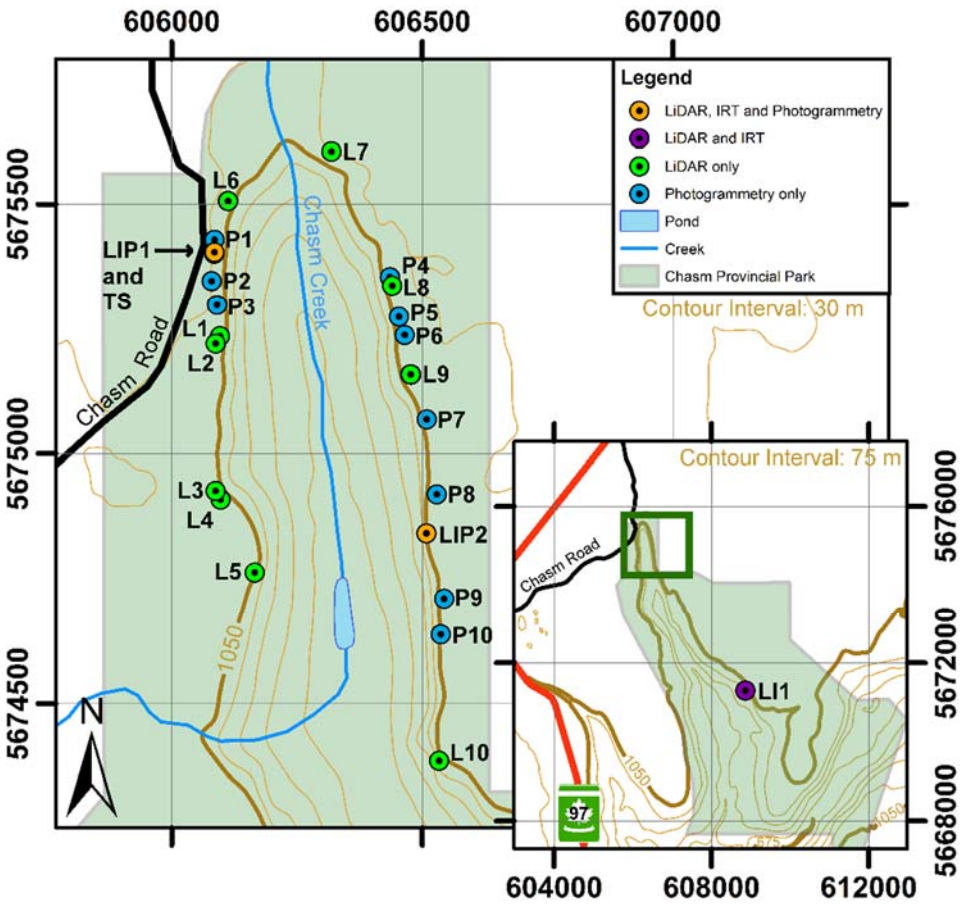

Figure 2-3. Map of Chasm area and field survey stations. Extent of station map in regional map shown in green. Coordinates are in WGS84 UTM Zone 10 North. Base map imagery adapted from Esri (2016).

2.1.2. Slope Targets

A Total Station was used to gather the coordinates of several targets on the outcrops at CVB2 (Figure 2-4), as well as the photogrammetry stations. The Total Station gives coordinates of other objects or points in XYZ format as relative positions, whereby 0,0,0 is the position of the Total Station. Using the handheld GPS coordinates obtained for the position of the Total Station at CVB2, the relative positions of the targets and stations were converted to UTM Easting, Northing, and elevation, respectively (Table 2-3).

Figure 2-4. CVB2 target locations. Numbers are shown above actual targets.

Table 2-3. Total station coordinates (X, Y, and Z) and converted UTM (Zone 10N) coordinates (Easting, Northing, and Elevation) for CVB2 photogrammetry stations and targets. All units are in meters.

Object	X	Y	Z	UTM Easting	UTM Northing	Elevation
CVB2-PI1	1.327	2.414	-1.424	493397	5546740	541
CVB2-PI2	2.233	7.433	-1.189	493398	5546745	541
Target 3	-26.926	6.391	9.092	493369	5546744	552
Target 4	-25.404	12.049	9.633	493370	5546750	552
Target 5	-23.707	5.990	1.438	493372	5546743	544
Target 6	-21.843	10.592	1.292	493374	5546748	544
Target 7	-21.007	14.555	3.571	493374	5546752	546
Target 8	-19.783	14.614	0.488	493376	5546752	543

2.1.3. Terrestrial LiDAR

Terrestrial LiDAR surveys were accomplished with the use of the Riegl VZ-4000 long-range terrestrial laser scanner (TLS) (Figure 2-5) (Riegl Laser Measurement Systems, 2015), which has various parameters which can be optimized for each survey. This TLS system has a specified maximum range of up to 4000 m, can scan a full 360°, uses the infrared wavelength of the electromagnetic spectrum for the laser beam (and therefore is deemed eye-safe), and has the capability of characterizing the full-waveform of the LiDAR returns (Riegl Laser Measurement Systems, 2015). Resolution for each scan is set within the TLS software as an angular value, and therefore is chosen as a different value for each survey based on the distance to the slope, the purpose of the

scan in subsequent analysis (for example, a high-resolution centimeter-scale analysis or a model of an entire canyon), and the memory storage requirements for the scan. The actual resolution (i.e. distance between points) on the slope or target of the scan is then calculated using simple trigonometry based on the angular resolution and distance to the slope. The Riegl TLS offers four different options for the laser pulse frequency (30, 50, 150 and 300 kHz) which correspond to various distance ranges, as higher frequencies (and therefore shorter wavelengths) cannot travel as far as lower frequencies (longer wavelengths) (Riegl Laser Measurement Systems, 2015).

Figure 2-5. Station set-up of Riegl VZ-4000 TLS. The point from which survey was taken was projected beneath the scanner using the 'plummet laser' option on the Riegl scanner internal software.

The environmental characteristics differ between the CVB and Chasm field sites, and therefore each required a different setting of survey parameters. The two CVB outcrops were too small in scale to warrant multiple scans; one scan was taken at both outcrops (Figure 2-2, Table 2-4). Due to the large height and length and complicated geometry of the exposed Chasm lava outcrops, multiple scans were taken along the outcrop edge on either side of the canyon in order to maximize the area captured and minimize the amount of occlusion due to survey perspective and vegetation cover (Figure 2-3, Table 2-4).

There are several different parameters which will change for every scan or survey, including the line and frame start and stop angles, as well as their resolution.

The line angle for this laser scanner is the angle along the vertical axis of the scan, whereby 0° is straight up increasing downwards to 90°, which is the facing direction of the scanner at horizontal (Riegl Laser Measurement Systems, 2015). The frame angle is the angle along the horizontal axis of the scan and changes the facing direction of the scanner, such that 0° is defined when the scanner faces its power port, and increases in a clockwise direction to 180° when the scanner faces in the opposite direction of its power port (Riegl Laser Measurement Systems, 2015). The TLS was set up in each survey in the direction such that the facing direction azimuth would be the same direction as when the scanner faces forward (i.e. the frame angle is 180°), which provides a means to easily calculate the azimuths of each scan. The settings utilized in the surveys completed for the CVB and Chasm field sites are outlined in Table 2-4.

Table 2-4. LiDAR survey settings at the CVB and Chasm field sites. Distances to slope at the Chasm stations are along a W-E line and are approximate.

Station	Frequency (kHz)	Line Start (°)	Line Stop (°)	Line Resolution (°)	Frame Start (°)	Frame Stop (°)	Frame Resolution (°)	Facing Direction Azimuth (°)	Distance to Slope (m)
CVB1	300	72.034	98.303	0.003	140.511	196.851	0.010	240	25
CVB2	300	69.412	94.207	0.003	134.819	212.929	0.010	310	23
LIP1	150	85.246	102.685	0.002	170.000	206.053	0.002	083	330
LIP2	150	85.970	111.983	0.003	169.829	204.200	0.003	270	340
LI1	150	60.000	68.000	0.002	193.000	207.001	0.002	-	100**
L1	150	83.978	120.000	0.006	185.223	285.531	0.006	105	350
L2	150	86.824	120.000	0.006	86.553	187.659	0.006	070	360
L3	150	85.614	120.000	0.006	140.000	238.700	0.006	108	420
L4	150	87.407	113.406	0.004	170.000	190.000	0.004	052	410
L5	150	84.211	119.997	0.006	141.702	225.00	0.006	089	360
L6	150	85.000	119.999	0.006	89.106	283.470	0.006	137	240
L7	150	80.704	120.000	0.006	133.617	209.997	0.006	244	160*
L8	150	84.908	120.002	0.006	109.318	207.646	0.006	263	330
L9	150	85.153	120.000	0.006	137.452	231.634	0.006	270	370
L10	150	85.401	120.000	0.006	101.277	179.631	0.006	266	440

* Distance is minimum distance to slope. ** Distance measured is to nearest section of slope.

2.1.4. Infrared Thermography

To identify fractures, joints, and other characteristics of the rock mass based on time-series IRT imagery, a FLIR SC-7650 infrared camera with a *f = 100 mm* lens was employed for infrared thermography surveys (Figure 2-6). The detectable temperature range of this camera is -20 °C to 300 °C, and its detector is indium-antimonide, which is stated to be ideal for mid-wave infrared wavelengths (FLIR Systems, Inc., 2015).

Figure 2-6. IRT station set-up. System includes FLIR camera, gasoline generator, and laptop with ResearchIR software.

Sequences of images were captured at multiple time intervals to create a time-series dataset of thermal imagery for the Chasm sites, as well as on samples of Chasm rocks. Time-series surveys were completed over the cooling cycles of the rock face, which correspond to the sunset to sunrise time period. Two outcrop sections at the Chasm, LIP1 and LI1, were captured in infrared imagery (Figure 2-3). Each survey involved time-series thermal imaging of the outcrops at 60 minute intervals over the specific time periods. As the rock slopes in these studies are too large to be contained in one frame of a 100 mm focal length lens, multiple images were taken at each time interval, with approximately 40-50% overlap, in order to capture the entire slope. A 'snaking' pattern was employed, whereby the camera was moved left to right, then down, and right to left. The survey details, number of images, and the distance range to the slope can be found in Table 2-5.

Table 2-5. Field survey details for time-series infrared thermography.

Field Site	Approx. Distance to Target (m)	Survey Start Time	Survey End Time	Number of images	Average Images per Time Stamp
LIP1	300	20:05, August 2 2015	05:05, August 3 2015	2730	124
LI1	50	20:45, August 25 2015	05:45, August 26 2015	261	14

2.1.5. Digital Photogrammetry and SfM

A Canon EOS 50D digital camera was used in the image capture for photogrammetric and SfM surveys at the Chasm and CVB (Figure 2-7). Lenses with a range of focal lengths from *f = 20 mm* to *f = 400 mm* were used to allow the desired research objectives to be achieved. The focal length chosen for each survey was determined by the distance to the target outcrop (a further distance required a larger focal length lens), and the desired resolution of the model, whereby a higher resolution model corresponds to a series of images with a larger focal length. The distance between successive stations in a survey was decided predominantly by the requirement for a station/distance to outcrop ratio of 1:5 to 1:8, but also considering the accessibility and visibility of the outcrop, and interference due to vegetation. As SfM involves less rigorous but similar survey techniques to conventional photogrammetry, images used in the generation of the SfM models were taken from the series of images captured in the initial photogrammetric surveys. The survey details and parameters are provided in Table 2-6 and Table 2-7, with station locations in Figure 2-2 and Figure 2-3.

Figure 2-7. Photogrammetry station set-up using the Canon EOS 50D, *f* = 400 mm lens.

Images were taken at two photogrammetry stations at each outcrop of the CVB, and spaced according to the recommendation that the distance between photogrammetry stations (base line distance) must be no greater than 20% of the distance to the outcrop (Sturzenegger, 2010).

Table 2-6. Photogrammetric images obtained and overlap of images for both CVB1 and CVB2 outcrops.

Station	Distance to Outcrop (m)	Distance Between Stations (m)	Lens Focal Length (mm)	Number of Images Collected
CVB1-P1	14	3	20	24
CVB1-P2	14	3	20	34
CVB2-PI1	25	5	20	16
CVB2-PI2	25	5	20	32

As the Chasm field site is much larger and contains continuous outcrops for approximately 7 km on either side of the canyon, photogrammetry and SfM surveys were completed using numerous stations on both sides of the Chasm. The distance between stations is irregular due to the presence of trees or lack of viewpoint along the slope edge, however the recommended ratio of between 1:5 and 1:8 for distances between

stations and distances from stations to outcrop was upheld; actual distances between stations and the outcrop are described in Table 2-7.

Table 2-7. Photogrammetric and SfM field survey details and parameters for the Chasm field site.

Station	Distance to Slope (m)	Distance to Adjacent Station (North) (m)	Distance to Adjacent Station (South) (m)	Lens Focal Length (mm)	Number of Images Collected
LIP1	330	28	55	50, 100, 200, 400	171
LIP2	340	83	133	400	183
P1	310	-	28	50, 100, 200, 400	226
P2	340	55	49	50, 100, 200, 400	195
P3	350	49	-	50, 100, 200, 400	182
P4	330	-	82	50, 100, 200, 400	256
P5	340	82	39	100, 200	32
P6	360	39	174	50, 100, 200, 400	261
P7	420	174	150	50, 100, 200, 400	180
P8	420	150	83	400	138
P9	400	133	73	400	169
P10	410	73	-	400	146

2.2. Laboratory Testing Program

Laboratory surveys included IRT imagery, SfM, and petrographic analyses. Laboratory IRT tests were carried out on hand samples collected from the Chasm LIP1 outcrop to constrain the remote sensing analyses with data collected in a controlled environment with known parameters. SfM was completed on several of the same hand samples used in the IRT imagery for input into the virtual field site described in Section 2.4 and Chapter 4. All hand samples from the LIP1 slope, except one which was not competent enough, were cut into petrographic sections to study the mineralogy and textures of the units for correlation to field survey results.

2.2.1. Hand Samples

Samples were obtained from twenty-two locations at outcrops accessible on foot (Figure 2-8, Table 2-8) to gain a more complete description of the lithology, as well as to perform laboratory experiments. All of the samples show changes in lithology, textures, and structures throughout the slope; detailed descriptions are provided in Chapter 3.

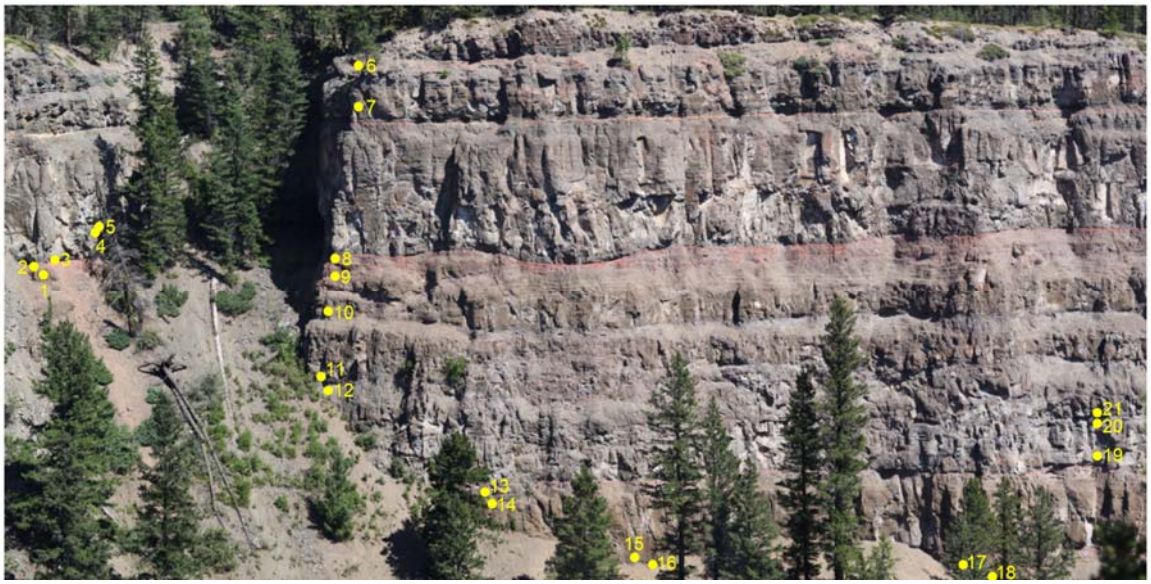

Figure 2-8. Locations on the LIP1 Chasm slope from which samples were taken at the outcrop.

Table 2-8. Samples taken from the extraction locations on the Chasm LIP1 slope.

Location (Figure 2-8)	Sample ID	Geological Unit
1	MD-CH06-01	7
2	MD-CH06-02	6
3	MD-CH-P67-01	6
4	MD-CH07-01	5
5	MD-CH07-02	5
6	MD-CH08-02	3
7	MD-CH08-01	3
8	MD-CH-P67-02	6
9	MD-CH06-03	7
10	MD-CH06-04	9
11	MD-CH05-01	11
12	MD-CH04-01	12
13	MD-CH-P23-01	14
14	MD-CH02-01	15
15	MD-CH02-02	15
16	MD-CH-P12-01	16
17	MD-CH01-01	17
18	MD-CH01-02	17
19	MD-CH03-01	13
20	MD-CH03-02	13
21	MD-CH03-03	13

2.2.2. IRT

The laboratory IRT surveys were completed to compare cooling trends between and within units in the LIP1 sample set, as well as correlate with cooling trends in the same units in the field survey. A focal length, $f = 50\ mm$ lens was used with the infrared camera kept stationary, and samples were heated in an oven at 93 °C (200 °F) for approximately 48 hours. The samples were then placed into a white paper-lined box, which provided a high contrast background. The box was placed approximately 3 m from the camera lens, and temperature values were recorded through the capturing of images every ten minutes for seven hours or until the samples' surface temperature reached room temperature.

2.2.3. SfM

SfM surveys were performed in the laboratory to create 3D models of hand samples for use in the virtual field site described in Section 2.4 and Chapter 4. They were done using a Canon EOS 50D digital camera with an *f = 35 mm* lens, and samples placed upon a stool. A stool was used to allow maximum access to all angles around the sample, and a white sheet of paper was placed on top for a greater colour contrast between the sample and the stool and easy removal from the resultant model. Images were captured in a circle around the stool at approximately 20 ° intervals, with the camera located at a distance between 30-50 cm from the sample. The number of images taken to complete the model for each sample depended on the size, overall complexity in shape, and detail required in the sample model. The samples surveyed and number of images for each sample are shown in Table 2-9.

Table 2-9. SfM laboratory survey details.

Sample ID	Number of Images Collected
MD-CH-P67-02	55
MD-CH08-01	55
MD-CH06-03a	32
MD-CH06-03b	39
MD-CH-P23-01	42
MD-CH-P67-01a	57
MD-CH-P67-01b	44
MD-CH03-02a	35
MD-CH03-02b	48

2.2.4. Petrography

Petrographic thin sections were made from the samples where possible, and compositional and textural data were acquired using a petrographic microscope. The features observed in the petrographic thin sections provided a basis upon which to compare the observed physical rock properties in hand sample with the remotely sensed data.

2.3. Data Analysis

2.3.1. Terrestrial LiDAR

LiDAR Point Cloud Processing

The initial raw scan data is recorded in the TLS as *.rxp format, which is a format proprietary to Riegl scanner systems, and therefore initial analysis of the scans must be undertaken using Riegl's TLS software, RiSCAN PRO v.2.0 (Riegl Laser Measurement Systems, 2018). This software was used to perform an initial conversion of the scan format, and colour the points of the point cloud based on RGB data obtained from photographs using the on-board scanner camera.

As the scans were originally referenced into a coordinate system specific to each scan position, it was necessary to convert the point clouds into UTM coordinates in order to perform further analysis in other programs. This was done within RiSCAN PRO, whereby a reference system file was created using UTM Zone 10 North. The VZ-4000 scanner contains an on-board GPS which records the scanner position coordinates for each scan; all coordinates for points in a scan are XYZ values in relation to the scanner position, and therefore a conversion of point cloud coordinates was performed using the UTM reference system file and the scanner position coordinates.

At the sites where multiple scans were taken, the scans were manually stitched together in RiSCAN PRO using 'tie points', or common points present in two or more scans, in order to create a single, unified three-dimensional model of the outcrops.

Reflectivity Profiles

Post-processing, the laser scans were used to create reflectivity profiles, where reflectivity is a scalar value describing the brightness of a target on a -25 (low, e.g. black tar paper) to 25 dB (high, e.g. limestone) range (Riegl Laser Measurement Systems, 2015). The reflectivity of the point cloud data was analyzed and used to delineate boundaries between layers based on the values of reflectivity along the profile. This process does not exist as a built-in function of RiSCAN PRO, therefore a novel approach was devised, whereby a column of point data was extracted from the point cloud and exported from the RiSCAN program as a text file (Figure 2-9). The text file contains information on the XYZ coordinates of each point, along with its reflectivity value. The

column of points extracted is three-dimensional, and contains several vertical profiles of points (i.e. there are multiple points and therefore multiple reflectivity values for each elevation value). In order to create a single profile of the data, a script was created in MATLAB (The MathWorks, Inc., 2019) called *Reflectivity.m* (Appendix A) to import the text file into MATLAB and average all the reflectivity values for each specific elevation, providing a resulting text file in which there is only one reflectivity value for each elevation value. The reflectivity and elevations can then be graphed to provide a reflectivity profile for a specific column of the outcrop.

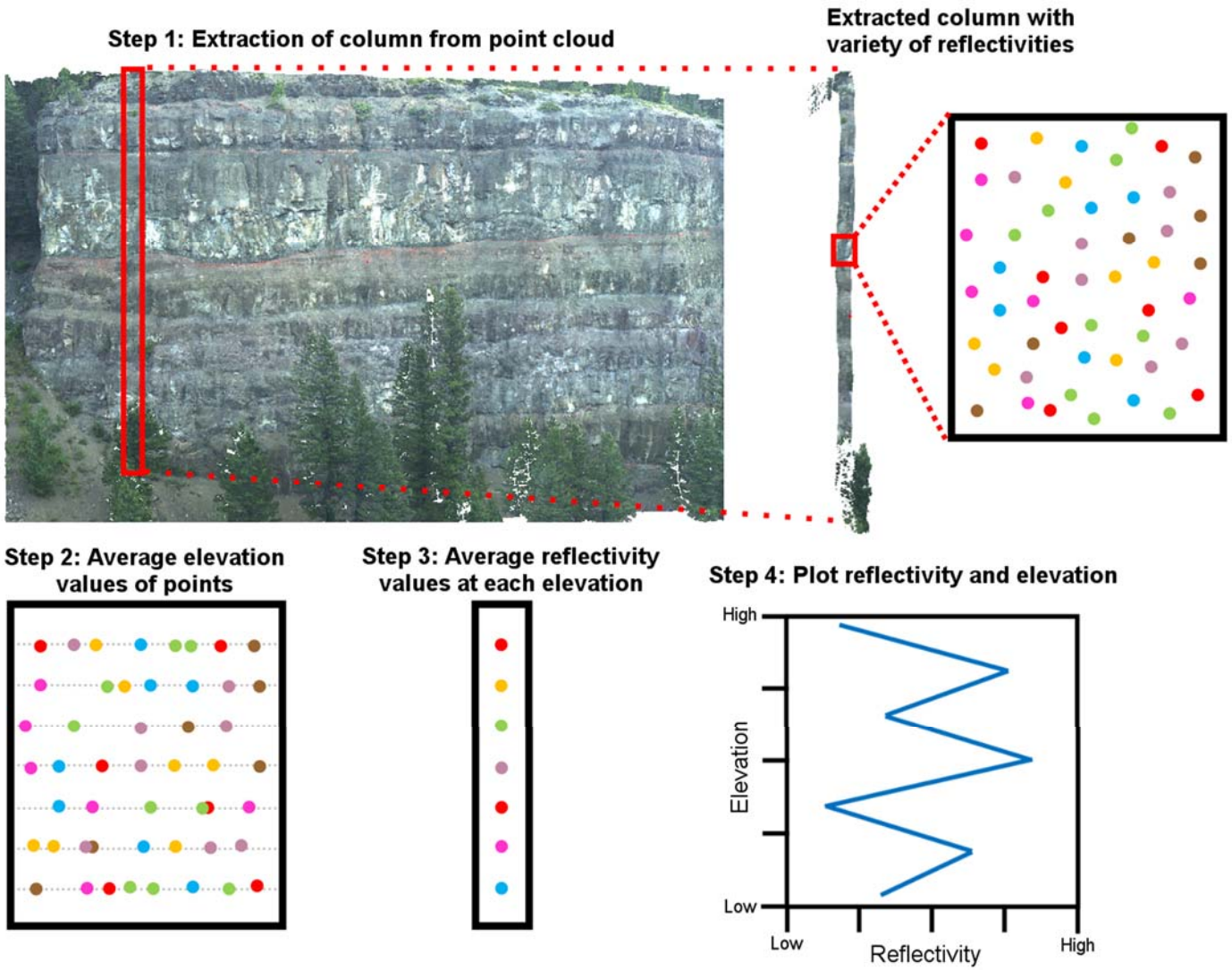

Figure 2-9. Schematic of workflow for creation of reflectivity profiles from a LiDAR point cloud.

Erosion Profiles

The processed laser scans were also used in the generation of erosional profiles along the slope of LIP1, in a similar process as creating reflectivity profiles. Columns of point cloud data were extracted from the full point cloud in RiSCAN PRO, which were subsequently imported into MATLAB using an original script, *ErosionProfile.m* (Appendix A), which was written to complete the creation of erosional profiles. First, the elevation values of all points in the new column point cloud are rounded to the nearest tenth of a meter. Consequently, there are multiple points at each elevation value, so the average location of these points at a certain elevation needs to be determined. This is done through averaging the Northing and Easting values at each unique elevation, and as the Chasm slope is not parallel with the UTM grid (N-S or W-E), trigonometry ($a^2 + b^2 = c^2$) was used to find the oblique distance from the UTM grid reference point. This minimum oblique distance is subtracted from all values, resulting in the normalized distance of each point at each elevation. The distance and elevation values are then plotted.

Mapping Joints and Calculating P_{21}

Following the creation of the project in the RiSCAN PRO software (post-field survey), planes were generated on the CVB scans to represent joint and fracture surfaces. The visible joint surfaces on the outer surface of the outcrop allowed for the use of the function which creates a plane from a selected area, but this method would not be viable for use on joints which appeared as lines in the outcrop (such as the horizontal joints along the chisel marks). Therefore, the method used to create the horizontal joint planes is the function which used three points to create a plane. Ideally, these three points will be the vertices of the joint plane in a three-dimensional view of the plane, but for some joints this was not possible; therefore the joints which could not be viewed in three dimensions are not represented in the plane data for each outcrop, as a reliable orientation could not be found. It is possible in the software to adjust the length, width, and position of the planes once they are created; these parameters were adjusted in all of the planes drawn in the scan of CVB1 in order to obtain the persistence of the joints and joint sets.

Spacing of the joint sets was measured from the point cloud of the laser scan by using the measure distance function in the software. The distance between each joint was, in the ideal case, measured perpendicular to two joints (where possible), otherwise the closest estimation to a perpendicular distance was obtained.

A P_{21} value, which is a measure of the intensity of jointing; was calculated for each joint set using the equation:

$$P_{21} = \frac{length\ of\ fracture\ traces}{area\ of\ exposure}$$ (Mauldon and Dershowitz, 2000)

This was done in RiSCAN for the CVB data by generating a closed polyline, and clipping the joint data to within that window. One window was made on the CVB1 model, measuring 2.5 m high by 4.4 m wide (Figure 2-10), as the scale of the region of interest at this outcrop is quite small. The four windows at the Chasm were completed using a slightly different methodology for P_{21} calculations. As the joint orientation data was being mapped using photogrammetry, only the joints lengths were acquired from the LiDAR scan instead of making representative planes for all the joints with length, width, and orientation. Polylines (lines of any shape which are created using multiple points) were used to trace joints on the point cloud within the windows, and the lengths of these polylines provided the basis for P_{21} and persistence calculations at the Chasm.

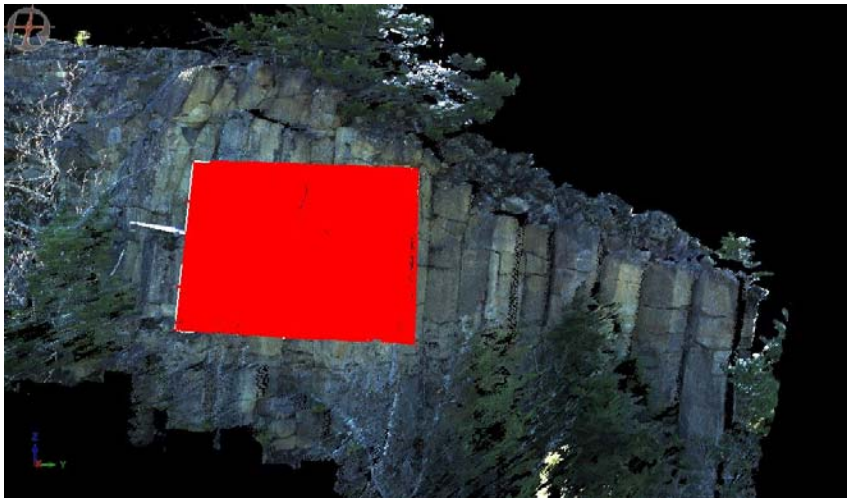

Figure 2-10. Red box indicates area of window on CVB1 laser point cloud model used in calculation of P_{21} values for each joint set. For scale, there is a meter stick in the image, aligned perpendicular to the columnar jointing.

2.3.2. Infrared Thermography

General Image Processing

IRT images were captured using the FLIR software, ResearchIR MAX v.4.20.2.74 as *.ptw format, which is internal to FLIR systems (FLIR Systems, Inc., 2018). Therefore, the initial analyses were completed within ResearchIR, and images were subsequently exported as greyscale *.jpg or *.tif files. The images of the CVB and the Chasm were exported and stitched into panoramas using an open source software called Hugin, which uses feature recognition to match the images together (d'Angelo et al., 2019).

The processing of time-series infrared thermography was completed on several 'windows', or particular regions of interest, from the full dataset of each field site. The full imagery for each site was not processed because of heavy time demands for manual alignment of the image series from each time stamp, and the unknown errors inherent to manual stitching of panoramas. It was decided to capture detailed and in-depth observations of the features on the slopes for which it was better to use smaller scale windows.

Several windows were therefore studied, including four windows on the Chasm LIP1 slope, as well as one on the Chasm-lithofacies type section (LI1 outcrop). All images within each of the windows are further referred to as 'window series'. The area of the slopes surveyed exceeded the Field of View (FOV) of the FLIR camera lens, therefore multiple images were taken for each time slot; these series of images are referred to as the 'slot series'. Each image within the slot series shows a different area of the slope, and consequently has a unique maximum and minimum temperature. To facilitate alignment and further processing of the slot series images, maximum and minimum temperatures for each entire slot series were determined through analysis using the ResearchIR MAX software, and used as the temperature scale at which all images within the slot series were exported. Images within each slot series were exported as *.jpg files, to be used in subsequent GIMP (The Gimp Team, 2018) and MATLAB processing.

Windows were selected from slot series to create window series. Images within each window series were imported as layers into GIMP, an image processing software,

with each window series saved into a separate project; the following is a description of the work done within each project for the separate windows. Images were aligned using the 'Move Tool' and 'Rotate Tool' in a sequential manner, starting with the first slot series image for the window, and aligning each successive image to the image from the previous slot series (i.e. the 21:05 slot series image in Window 1 was aligned to the 20:05 slot series image from Window 1, and 22:05 was aligned to 21:05, 23:05 was aligned to 22:05, and so on). Image alignment was completed in this way because alignment between successive images is extremely important during subsequent MATLAB processing, where if alignment is erroneous, the results of the processing are rendered completely invalid. Perfect alignment between images, however, is generally not possible, due to the difference in focus of the lens for each image, the different view of features in each image due to changing temperatures, and the inherent human error which occurs from manual alignment. Once images were aligned properly, the window was cut to the largest possible area, determined by the extent to which all images of the window series overlap. The cropped images were saved separately, and subsequently used in MATLAB for further processing.

The chronology of thermal contrasts was examined between and within lava flow units at the Chasm, to compare the thermal behaviour of the units. As with the terrestrial LiDAR, profiles were made of the thermal contrast, and analyzed for thermal boundaries with the objective of correlating the thermal properties to geological features.

Creating Contrast Imagery and Thermal Profiles

A MATLAB script, *IRT_IMPROC2.m* (Appendix A), was written to execute the processing of thermal imagery, and performs the tasks of creating thermal contrast imagery and temperature profiles. To do this, the script first reads in all images for a window series into MATLAB, and converts them from greyscale images to matrices of temperature values. When the images are in this format, each image in the window series is subtracted from the previous time slot's image, resulting in a matrix of values reflecting the temperature change between each time slot. This temperature change matrix, the thermal contrast, is exported from MATLAB as an image. As ten slot series were gathered at LIP1 in the Chasm, nine contrast images are created. The maximum and minimum temperature values for each temperature contrast image are also saved into a text file for accurate image colour scaling.

Ten row and ten column temperature profiles were extracted from each slot series image in each window series. *IRT_IMPROC2* calculates what pixel locations these profiles will occur in each image, as each window series image is a different size. The temperatures for each row and column profile are taken from the matrices of temperatures (created in the process of thermal contrast imagery), and plotted on MATLAB figures with temperatures vs. elevation, with all row profiles for different time slots from one window series shown on the same figure, and all column profiles for different time slots from one window series shown on a separate figure. This results in ten row profile figures, and ten column profile figures for each window series. Lastly, the profiles are plotted on the original greyscale images and exported, so the pixel locations as well as the visual locations of the profiles on the slope can be determined. As an example, Column 224 from Window 1 and the row and column profiles on the Window 1 greyscale image at 20:05 are shown in Figure 2-11.

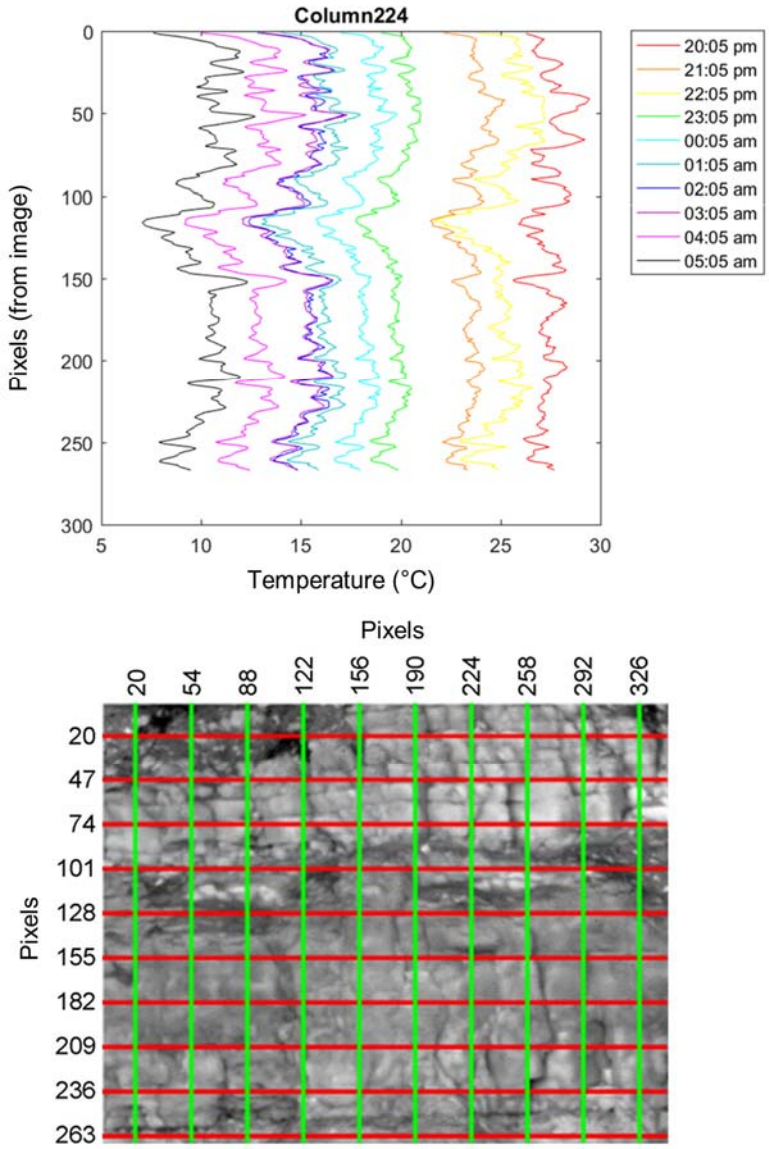

Figure 2-11. Column temperature profiles for Column 224 in Window 1 (top), and row (red) and column (green) profile locations overlain on 20:05 image of Window 1 (bottom).

Laboratory Thermography

The images were processed in ResearchIR MAX, whereby Points of Interest (POIs) were marked, and statistics on the temperature of each POI within the image were generated. As the camera was kept stationary, the POI has the same location in every image, and the change in temperature of a point over time can be found through the ROI statistics from each individual image. The temperature statistics for every image were exported individually from ResearchIR MAX as text files, and subsequently imported into MATLAB, where using the *LabIRT_timeseries.m* script (Figure

2-12)(Appendix A), the statistics were extracted for each individual POI, and then copied and graphed as temperature decay curves. The curve data was also brought into Excel, and with the trendline function, polynomial equations were fit to the curve of each POI to quantify the differences between the thermal responses of the samples.

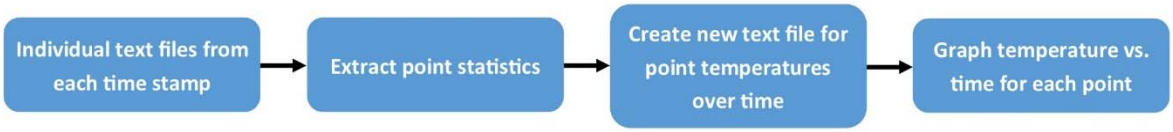

Figure 2-12. *LabIRT_timeseries.m* script functionality. The script imports individual text files from each time stamp, extracts the point statistics from the text files and creates a new text file for each point with its corresponding temperatures over time and then graphs the temperatures vs. time for each point.

Window POI Temperature Curves

Similar to the laboratory thermal data, POIs were chosen in each window on the Chasm slope to observe the temperature patterns over time for certain features. To calibrate these data and compare the slope POI temperature curves to the air temperature at the Chasm, temperature data from three weather stations was gathered. A script was created in MATLAB, *Tdecay_pointseries.m* (Appendix A), which extracts the POI temperature data from the greyscale thermal images (similar to *IRT_IMPROC2.m*), creates text files with the data, and graphs the POI temperature curves for each window on the same graph.

2.3.3. Photogrammetry

Photogrammetric models of the field sites were created using the 3DM CalibCam and 3DM Analyst software programs developed by Adam Technology (2014), as well as using SfM in Metashape version 1.6.3 (Agisoft LLC, 2020). These models were used to map outcrop features, such as structures (individual discontinuities and joint sets), volcanological features (vesicularity, vesicle chimneys), alteration, lithological units, and vegetation cover. A characterisation of the joints and joint sets was undertaken using the photogrammetric models at the CVB and Chasm, and the high-resolution photographs (f = 400 mm) were used for detailed mapping in combination with the LiDAR and IRT datasets.

AdamTech Models

The images obtained in the CVB photogrammetry surveys were subsequently imported into the 3DM CalibCam software, and a photogrammetry model was generated following the workflow outlined in Sturzenegger (2010). This was done using three overlapping images for CVB2-PI1 and four for CVB2-PI2 to create the CVB2 model, and two overlapping images at each of CVB1-P1 and CVB1-P2 to create the CVB1 model. The models were then viewed in 3DM Analyst, and planes were created to represent joints and joint surfaces in the outcrops. The joints in each outcrop were then divided into several different joint sets for each outcrop, based on their dip and dip directions, and contours in the discontinuity analysis stereonet in the software. The planes are drawn on the model as circles, and therefore the diameter of the circles was used as a length property for the joints to estimate persistence.

Metashape Models

The images from the Chasm field and laboratory surveys were imported into Metashape and organized into the stations from which each was captured, to assist the program with determining the camera perspectives. The software automatically aligned the images to create three-dimensional point clouds. After removing all background points (e.g., vegetation and talus slope from field data, points from the white paper underneath the sample for laboratory data) from the clouds, meshes were made from the remaining points in the form of *.obj files, and textured with colours from the images. The textures include one or more *.tif files, which are the actual colours for the mesh, and a *.mat file, which acts as a map for the *.tif file(s), indicating to the program which sections of the *.tif file(s) correspond to which sections of the *.obj file. The laboratory *.obj files were not processed further, and imported into the geovisualization interface described in Section 2.4 and Chapter 4.

Discontinuities were mapped on the Metashape models in the Chasm slope Windows 1-4 through first georeferencing the models with several point coordinates obtained from the LiDAR scan of the slope (Table 2-10, Figure 2-13). Once oriented in geographic space, the models were imported into CloudCompare version 2.11.0 (CloudCompare, 2020). A joint surface was mapped by selecting a polygon of points on the point cloud through CloudCompare's segment tool (in the Compass plugin), then fitting a plane to that segment, thereby finding the dip and dip direction of the joint.

Table 2-10. Coordinates of points used for georeferencing Chasm Metashape models for Windows 1-4. All values are in UTM Zone 10N.

Window	Point	Easting (m)	Northing (m)	Elevation (m)
1	1	606335.32	5675581.07	1052.72
	2	606336.88	5675582.53	1059.50
	3	606341.83	5675573.72	1060.05
	4	606337.92	5675572.94	1052.24
	5	606337.01	5675575.44	1055.92
2	1	606334.62	5675574.49	1041.35
	2	606334.95	5675572.38	1047.37
	3	606340.58	5675566.93	1045.93
	4	606339.34	5675567.77	1038.84
	5	606337.21	5675570.10	1042.84
3	1	606323.64	5675598.12	1025.94
	2	606329.11	5675597.01	1040.46
	3	606332.89	5675578.83	1041.63
	4	606331.75	5675575.75	1029.16
	5	606330.27	5675583.82	1034.06
4	1	606363.76	5675519.36	1004.17
	2	606362.76	5675521.90	1014.07
	3	606365.60	5675515.51	1014.50
	4	606365.08	5675514.28	1002.27
	5	606363.82	5675515.62	1007.27

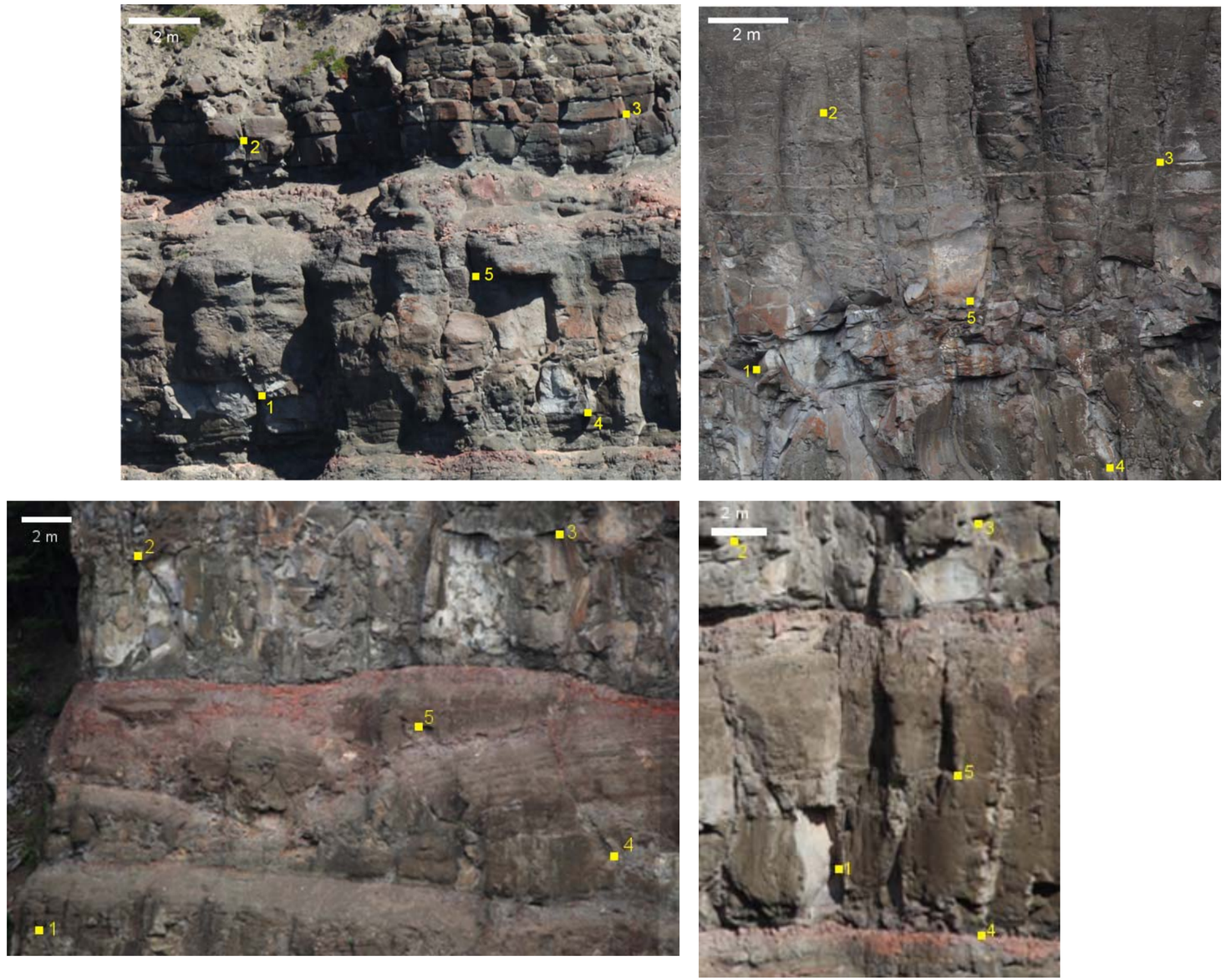

Figure 2-13. Control points used for georeferencing Metashape models of Chasm Windows 1-4, numbers correspond to those in Table 2-10.

Stereonets and Kinematic Analysis

All joint dip and dip direction data were imported as tables into the software DIPS version 6.0 (Roscience, Inc., 2020), which uses the orientations of the joints to create stereonets. Joint sets were manually delineated based on dominant joint orientations (dense contours on the stereonets) with a threshold of variation of approximately 30°. Kinematic analysis was only performed on the CVB data, and is done automatically in the DIPS software based on joint orientations; the input friction angle was assumed as 34° for this analysis (a detailed description of input parameters is in Section 3.3.2).

2.3.4. Alteration Mapping

The mapping of altered areas on the Chasm slope was completed using the LiDAR point clouds of the windows, as well as high-resolution photographs. Two methods were explored to distinguish white alteration and iron staining from fresh surfaces, reflectivity and RGB values.

To map alteration using reflectivity, the point cloud was viewed in RiSCAN, and a representative area for each iron staining and white alteration were chosen. The software contains a function which allows the user to select points in the point cloud according to certain parameters, so once a representative area was delineated, all points in the cloud which matched the reflectivity values of this area were selected. Images of the selected areas were taken, and subsequently analyzed visually against photographs of the windows for verification of the validity of the results.

Similarly, alteration was mapped using RGB values in the LiDAR with the selection tool, using the auto-georeferenced photographs taken by the laser scanner during the scan of the outcrop. RGB values in photographs, however, were picked in the GIMP software using the colour picking tool. This tool requires the user to choose a pixel with the desired colour, and selects all other pixels of the image with the same RGB values plus a threshold value. The threshold chosen for the colour picking during alteration mapping in GIMP was ±15 (based on a 0-255 RGB colour value scale).

2.4. Geovisualization Interface

Remote sensing provides information on outcrops which would otherwise be inaccessible, however visualizing this data is necessary to fully study the slope. To visualize the data gathered and analyzed in this study, a geovisualization interface called 'Up Close with Virtual Outcrops' was created using the virtual reality game engine software, Unity 3D version 5.3.4f1 (Unity Technologies, 2016), to provide unrestricted access to a virtual field site at the Chasm. 'Up Close with Virtual Outcrops' was set up to be a virtual environment, within which the user can visualize several types of the data in this study. An empty 3D space, infinite in size, was used as the medium for starting the environment; this 3D space is a 'scene'. All data visualizations and corresponding objects were put into the scene, including cameras for viewing, Graphic User Interface (GUI) objects for interaction and movement through the space and data, and the data models and images.

2.4.1. Data Visualizations

'Up Close with Virtual Outcrops' contains both two-dimensional and three-dimensional datasets. Two-dimensional datasets in the geovisualization include temperature decay curves created from laboratory IRT experiments on hand samples (Section 2.2.2), LiDAR reflectivity profiles (Section 2.3.1), stitched panorama infrared imagery from multiple time stamps at station LIP1 (Section 2.3.2), and thin section images (Section 2.2.4). The reflectivity profiles and panorama IRT images were coarsely georeferenced in the geovisualization interface through lines placed in front of the slope, and positioning the image in front of the slope, respectively. Three-dimensional data within 'Up Close with Virtual Outcrops' are SfM models of two detailed windows of the LIP1 slope (Section 2.3.3), and SfM models of five hand samples (Section 2.2.3) taken from the slope. The locations of samples and windows are indicated on the slope model within the geovisualization. A complete review of the workflows for the various datasets described is presented in Figure 2-14, including data formats for interoperability between software packages, and scripts created for data analysis.

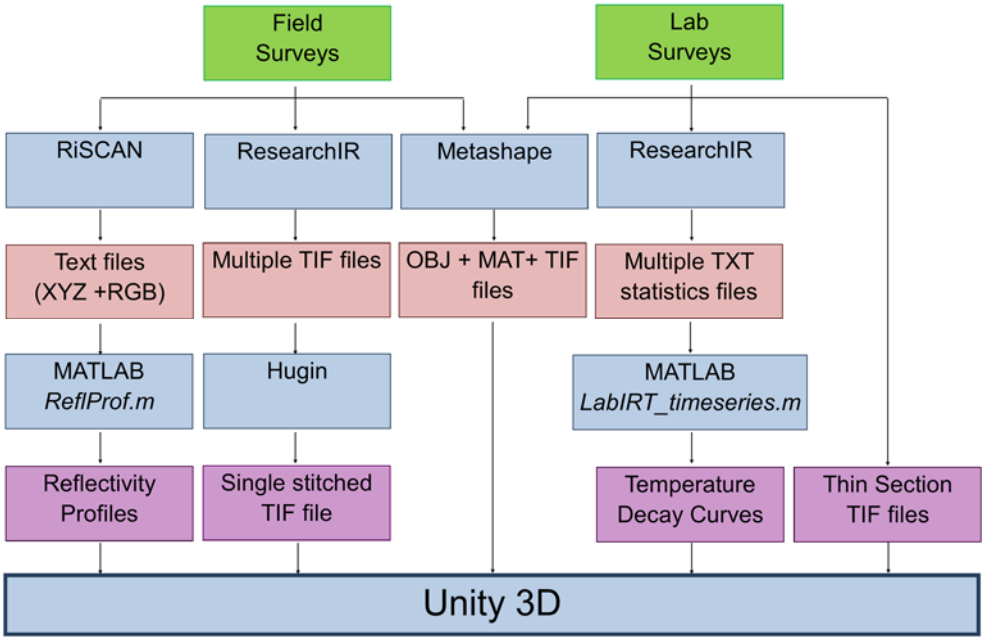

Figure 2-14. Geovisualization design and workflows. Green boxes indicate surveys for data collection, blue boxes represent software packages used for processing, pink boxes show file formats for interoperability, and purple boxes show processed data products which were input into Unity 3D. Italicized text indicates the scripts written for data processing.

2.4.2. User Interface

The user interface for "Up Close with Virtual Outcrops" has been designed as a self-guided experience, where the user can be involved in a virtual field site which simulates organic methods of field surveying. This is especially important at a site like the Chasm, as the near-vertical slopes severely impede traditional investigation of the slope. In contrast, a virtual Chasm model can be viewed from any angle, distance, or scale.

'Up Close with Virtual Outcrops' was created in Unity 3D, a game engine software within which the user can create a three-dimensional interactive virtual environment. The virtual space, or scene, is built using 3D and 2D objects, as well as Graphical User Interface (GUI) elements; scripts created with C# or Javascript codes are used to carry out actions and functions within the environment. A separate scene was used for each 3D model, to facilitate faster loading capabilities and prevent lagging of the virtual environment with large datasets. Two-dimensional (planar) objects in the Unity software are termed 'sprites' (Unity Technologies, 2016), and are normally used in

game engines as boundaries (e.g., walls) or background imagery. In the developed interface, however, sprites display datasets which have only two dimensions, such as graphs and images.

Virtual camera objects are included in the environment to control the user's viewpoints and perspectives; the user can only view where the camera object is pointing. Movement of the user through the scene, therefore, is allowed through the use of a C# script attached to the main camera object, *ExtendedFlyCam.cs* (Lochhead, 2016), which gives the user the ability to move through the environment with the computer mouse and keyboard keys (arrow keys and WASD).

GUI elements are those with which the user interacts, such as a button, and change the conditions of the virtual environment. This is possible through attaching one or more scripts to the GUI object, and through an action by the user on the object such as a click, functions within the attached script(s) are carried out. Two basic GUI elements were utilized to facilitate user interaction in the 'Up Close with Virtual Outcrops' scenes, buttons and toggles. Toggles, which are essentially logical (true/false) indicators, were used to display datasets. When the toggle box is checked, the function is called in which the 'active' attribute of the element is turned on, and a data visualization appears on the screen. Buttons were used in this interface to both switch scenes through the *ButtonNextLevel.cs* script (Appendix A), and facilitate tours in which certain characteristics of the three-dimensional models are pointed out. For all toggles and buttons which switch between datasets, the *CameraPos.cs* script (Appendix A) is also attached to the main camera, and adjusts the position and lighting to optimal settings for viewing the different types of data. The complete design and flow of the geovisualization interface is shown in Figure 2-15.

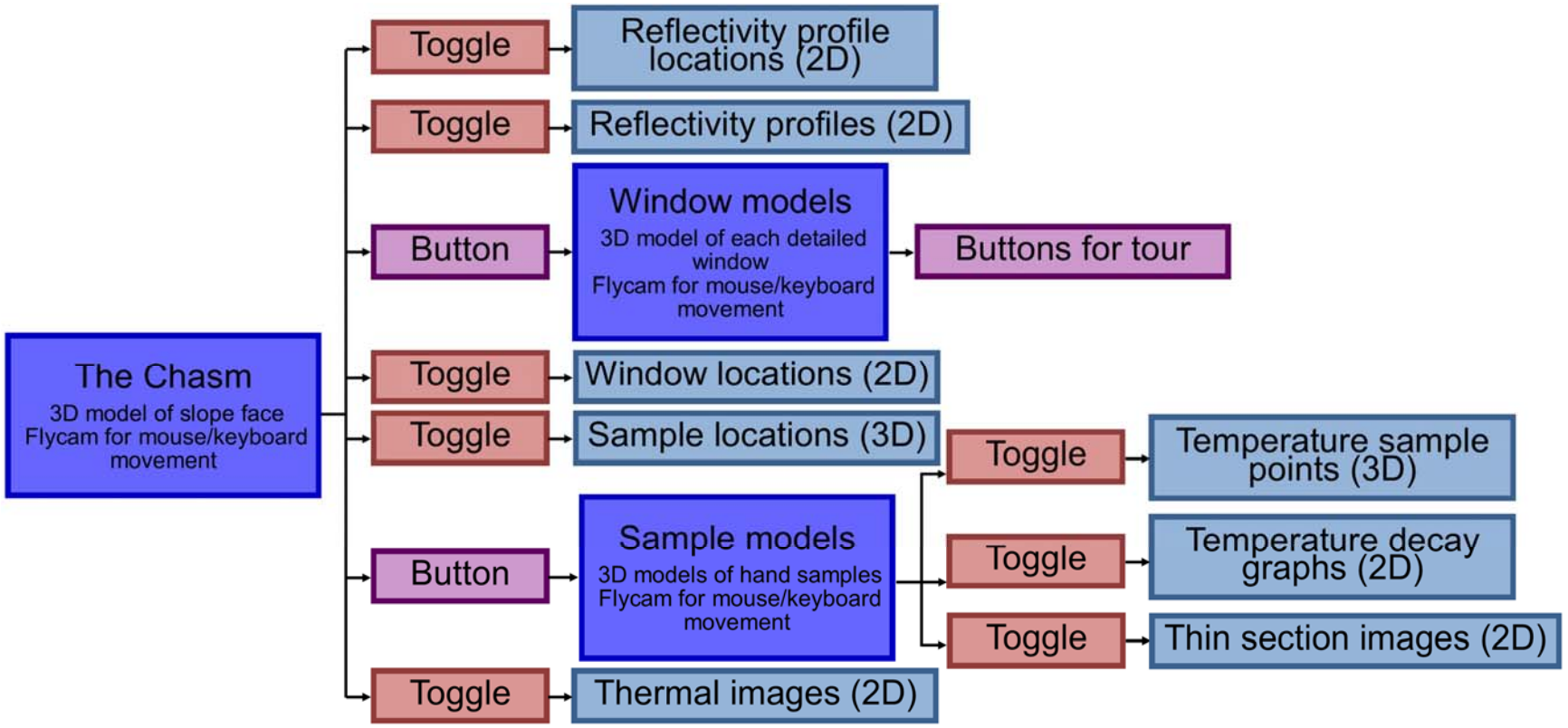

Figure 2-15. Geovisualization interface design. Dark blue boxes indicate scenes, pink boxes denote toggles, purple boxes buttons; light blue boxes show data visualizations with dimensionality indicated.

Chapter 3. Multi-scale Remote Sensing

3.1. Introduction

The results of the different types of field (IRT, terrestrial LiDAR, and photogrammetry) and laboratory (IRT, SfM) surveys conducted are presented in this chapter. Findings are reported at four scales of observations: full outcrops, detailed windows cut from full outcrops, hand samples, and thin sections.

Infrared thermography is employed in this research as a tool for the field and laboratory analysis of lava flows. At the first field site investigated, the Chasm, thermal imagery was captured in a time-series format, whereby multiple images of the same outcrop were collected at time intervals 60 minutes apart over eight to nine hours. As the outcrops were too large to include in one image, multiple images were taken at each time interval, then stitched into thermal panorama images. To analyze the results, observations were made on greyscale thermal images from each hour mark, for several different 'windows' or 'regions of interest' (ROI). These hourly images were used to create temperature contrast images, by subtracting one image from the previous one and obtaining an hourly pixel-based change in temperature. Rock samples were collected from the eastern outcrop visible from station LIP1, heated in the laboratory for approximately 48 hours in a 93 °C oven, and left to cool with images taken every ten minutes over the cooling process.

Terrestrial LiDAR had three main uses in this study: erosional and reflectivity profiles, and alteration mapping. Profiles of the slope were created using the LiDAR data to analyze the erosion of the lava sequences. Reflectivity profiles were created using LiDAR reflectivity values down the slope, and the resultant graphs were analyzed for changes related to lithological characteristics. Reflectivity and RGB values were used to map different types of alteration in the four windows on the slope.

Discontinuity characterization was completed at the four Chasm windows and both CVB outcrops using SfM and LiDAR models. Kinematic analysis with LiDAR joint orientations was carried out at CVB1 and CVB2.

3.2. Chasm

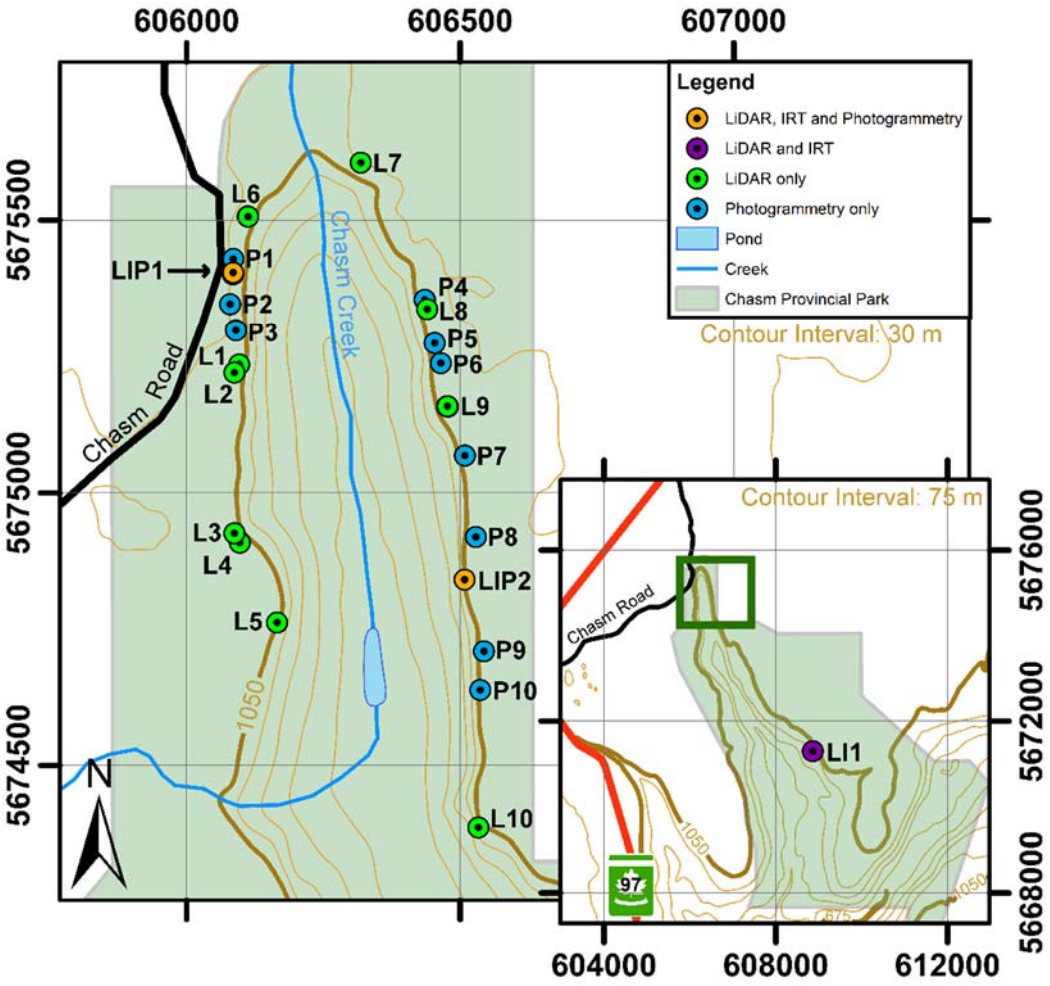

Figure 3-1. Map of Chasm area and field survey stations. Coordinates are in WGS84 UTM Zone 10 North. Green outline on map in forefront indicates extent of detailed station map in background.

The slopes on both sides of the Chasm were included in field surveys (Figure 3-1), which were selected slopes for IRT surveys, and the greatest spatial coverage possible for LiDAR and photogrammetry surveys. Two stations were used to analyze outcrops through the use of IRT at the Chasm, one on the east side of the valley (LI1) and one on the west (LIP1) (Figure 3-1). Station LIP1 faces east, and covers the outcrop visible on the east side of the Chasm. Station LI1 faces east, and an outcrop on the east side of the Chasm was surveyed; surveys at this station were conducted on the Chasm lithofacies type section from Farrell et al. (2007). Both investigated outcrops surveyed from LI1 and LIP1 had thermal images taken over a cooling cycle of the rock,

between sunset at approximately 8:50 pm and sunrise at approximately 5:30 am the next morning. The slope visible from LIP1 is the main outcrop studied and is approximately 100 meters from the apex of the canyon.

3.2.1. LIP1 Outcrop/Station

LIP1 is composed of ten lava flows, separated by red, unconsolidated, oxidized units (Figure 3-2). These unconsolidated oxidized layers were mapped by Farrell (2010) to be brunisolic paleosols; for the purposes of this research, these units will be referred to as paleosols. The lava flows vary in thickness, structure, age and morphology, but are similar in composition (Farrell, 2010; Farrell et al., 2007). Four areas, or 'windows', were analyzed in detail using all three remote sensing techniques, to facilitate the study of the data at multiple scales (Figure 3-2). The smallest scale studied at the LIP1 outcrop were thin sections, which were created from hand samples collected from the slope at locations exhibited in Figure 3-2. Descriptions of the thin sections and hand samples are shown in Table 3-1, and thorough rock descriptions are presented in the following Rock Descriptions section.

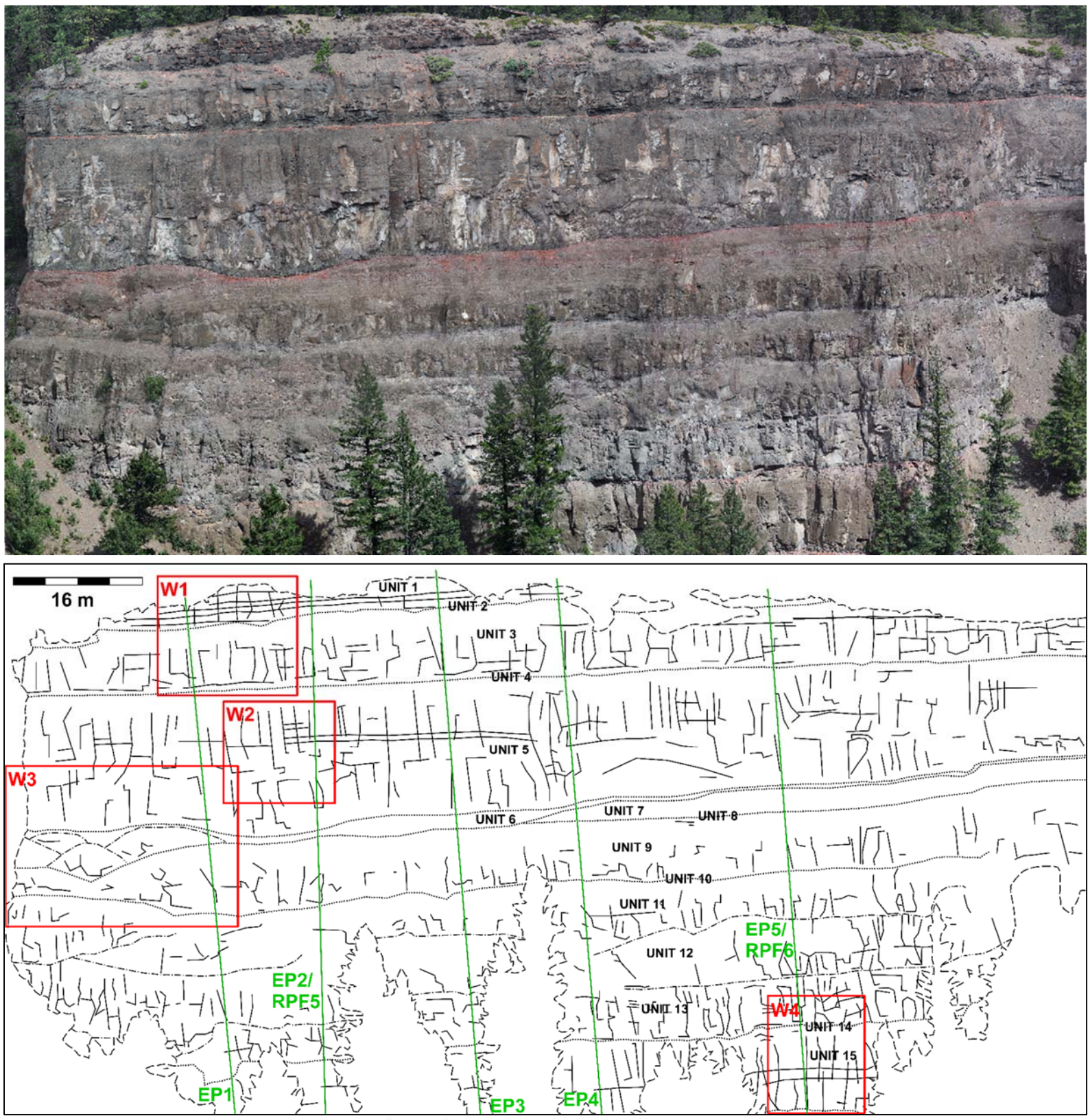

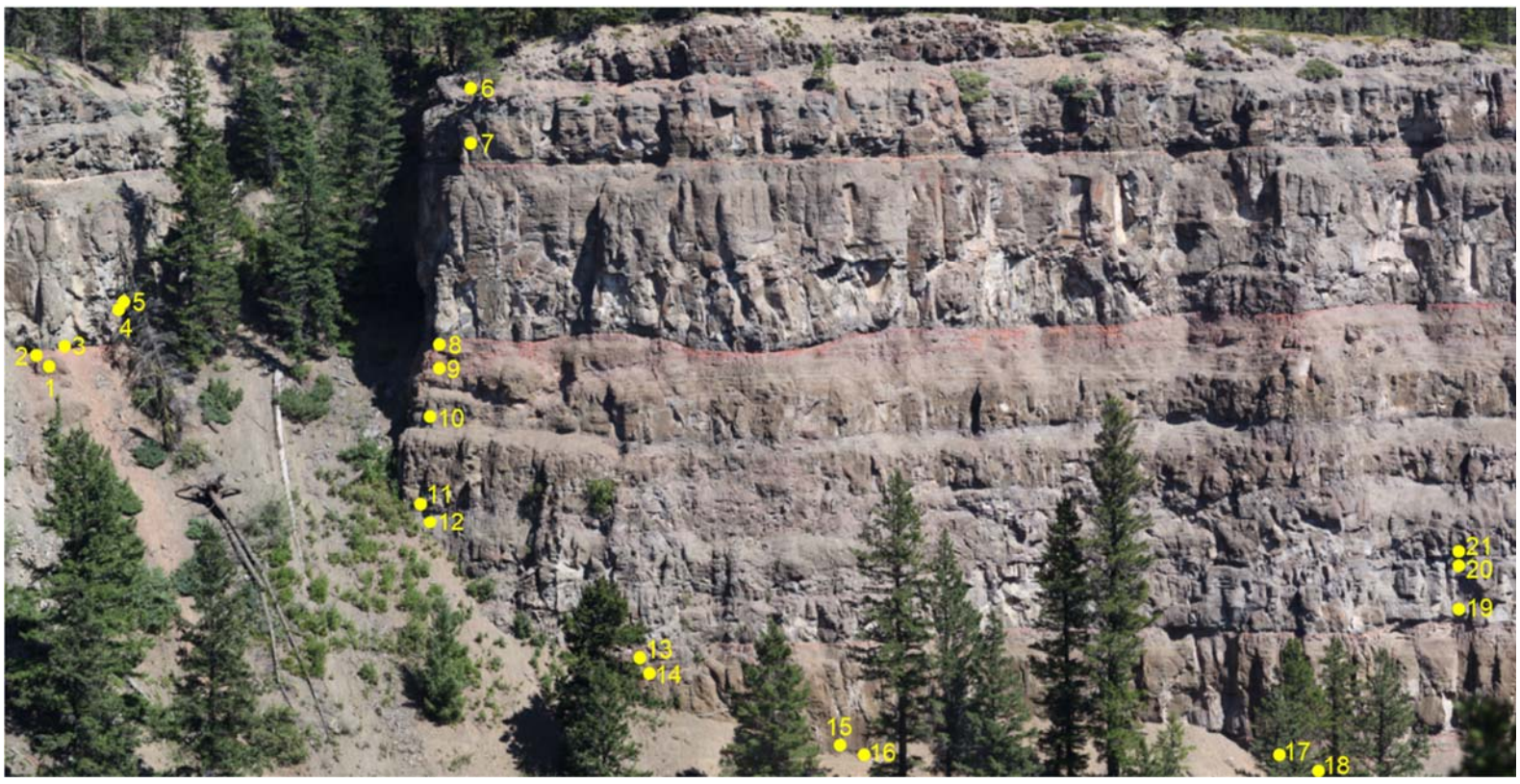

Figure 3-2. RGB image of the LIP1 slope on the east side of the Chasm (top), and corresponding line drawing of LIP1 (middle), indicating locations of detailed windows (W1, W2, W3 and W4) as well as erosional (EP) and reflectivity (RPF) profiles. Bottom image shows sample locations on the LIP1 and adjacent slopes, with sample numbers corresponding to those in Table 3-1.

Table 3-1. Descriptions of hand samples obtained from each location on the LIP1 outcrop. Degree of weathering is assessed using ISRM (1978) classification.

Location (Figure 3-2)	Sample	Geological Unit	Grain Size	Texture/Fabric	Weathered Colour	Fresh Colour	Weathering/Alteration	Vesicles	Thin Section Description
1	MD-CH06-01	7	Fine grained Sub-mm	Equigranular Homogeneous	Reddish brown	Reddish brown	Slightly weathered, minor occurrences of lichen, minor alteration to white mineral (clays?)	<1% vesicularity Sub-mm to 1 mm size Subrounded shape Partially to fully infilled with zeolites/quartz	Anhedral pyroxenes exhibit ophitic to subophitic textures, euhedral to subhedral plagioclase laths are dominant in modal abundance and partially seritized. Anhedral to subhedral olivines with iddingsite along fractures and rims, some crystals completely iddingsitized. Minor iron oxides.
2	MD-CH06-02	6	Fine grained Sub-mm	Equigranular Homogeneous	Dark brown	Brown	Highly weathered and fractured, rubbly and crumbles easily, minor alteration to white mineral (clays?)	<1% vesicularity Sub-mm to 4 mm size Irregular shape Partially to fully infilled with zeolites/quartz	Euhedral to subhedral plagioclase laths are dominant in abundance, and partially altered to sericite. Subhedral to anhedral pyroxenes, subhedral olivines almost completely iddingsitized. Minor iron oxides.
3	MD-CH-P67-01	6	Aphanitic	Homogeneous	Reddish brown	Red	Moderately weathered, fractured	~30% vesicularity 1-41 mm size Irregular to subrounded shape Some vesicles partially to fully infilled with zeolites/quartz and (calcite/chalcedony?)	Subhedral to euhedral plagioclase laths and blades, partially to fully altered to sericite. Subhedral to euhedral olivines replaced by iddingsite around rims. Groundmass is abundant and is comprised of aphanitic red-brown to black material.
4	MD-CH07-01	5	Fine to medium grained Sub-mm to 1 mm	Equigranular Homogeneous	Orangey light grey	Light grey	Slightly weathered	~1% vesicularity 1 to >30 mm size Irregular shape Partially to fully infilled with zeolites/quartz	Euhedral to subhedral plagioclase laths are dominant in abundance, and completely seritized. Subhedral to anhedral pyroxenes, subhedral to anhedral olivines partially iddingsitized around rims. Minor iron oxides.
5	MD-CH07-02	5	Fine grained Sub-mm	Equigranular Homogeneous	Brownish grey	Brownish grey	Slightly weathered, minor occurrences of lichen and iron staining, fractured	~2% vesicularity 1-46 mm size Irregular shape Some vesicles partially to fully infilled with zeolites/quartz and (calcite/chalcedony?)	Subhedral to anhedral plagioclase laths are dominant in abundance, and partially altered to sericite. Subhedral to anhedral pyroxenes and olivines, minor iddingsite around rims and along fractures of olivines. Minor iron oxides. Amygdales filled with nepheline/zeolites(?)
6	MD-CH08-02	3	Fine to medium grained Sub-mm to 1 mm	Equigranular Bedded/Stratified	Brownish grey	Light grey	Slightly weathered	~1% vesicularity 1-38 mm size Irregular shape Partially to fully infilled with zeolites/quartz	Anhedral pyroxenes exhibit ophitic to subophitic textures, anhedral to subhedral plagioclase laths are dominant in modal abundance and partially seritized. Anhedral to subhedral olivines partially iddingsitized along rims and fractures. Minor iron oxides.
7	MD-CH08-01	3	Fine grained Sub-mm	Porphyritic	Brownish grey	Light grey	Slightly weathered	No visible vesicles	Anhedral pyroxenes exhibit ophitic to subophitic textures, euhedral to subhedral plagioclase laths are dominant in modal abundance and completely seritized. Anhedral to subhedral olivines almost completely iddingsitized. Minor iron oxides.

Table 3-1 (continued).

Location (Figure 3-2)	Sample	Geological Unit	Grain Size	Texture/Fabric	Weathered Colour	Fresh Colour	Weathering/Alteration	Vesicles	Thin Section Description
8	MD-CH-P67-02	6	Aphanitic	Bedded/Stratified	Reddish brown	Red	Slightly weathered, minor occurrences of lichen, several fractures	~20% vesicularity Sub-mm to 17 mm size Irregular to subrounded shape Some vesicles partially to fully infilled with zeolites/quartz Some vesicles partially to fully infilled with (calcite/chalcedony?) Samples becomes more vesicular to one edge	Subhedral to euhedral plagioclase laths and blades, partially to fully altered to sericite. Subhedral to euhedral olivines completely to partially replaced by iddingsite. Groundmass is abundant and is comprised of aphanitic red-brown to black material. Amygdales infilled with zeolites(?).
9	MD-CH06-03	7	Aphanitic	Homogeneous	Reddish brown	Brownish red	Moderately weathered, some quartz mineralization in possible former vein or fracture infill, several fractures	~25% vesicularity 1-14 mm size Irregular to rounded shape Partially to fully infilled with zeolites/quartz and (calcite/chalcedony?)	Material too unstable – thin section could not be obtained.
10	MD-CH06-04	9	Aphanitic	Bedded/Stratified	Reddish grey	Dark brownish grey	Slightly weathered, some alteration to white mineral (clays?)	~25% vesicularity Sub-mm to 21 mm size Irregular to rounded shape Some vesicles partially to fully infilled with zeolites/quartz Changes in vesicularity and mineralogy occur over stratification Some layers have completely infilled vesicles, some have no vesicles, some have vesicles with no infill	Euhedral to subhedral plagioclase laths are dominant in abundance, and almost completely seritized. Subhedral to anhedral pyroxenes, subhedral to anhedral olivines almost completely iddingsitized. Minor iron oxides.
11	MD-CH05-01	11	Fine grained Sub-mm	Equigranular Homogeneous	Brownish grey	Grey	Slightly weathered, minor occurrences of lichen and alteration to white mineral (clays?), quartz mineralization along former vein, several fractures	<1% vesicularity Sub-mm to 1 mm size Subrounded to rounded shape Partially infilled with zeolites/quartz	Anhedral pyroxenes exhibit ophitic to subophitic textures, euhedral to subhedral plagioclase laths are dominant in modal abundance and partially seritized. Euhedral to subhedral olivines with iddingsite along fractures and rims. Minor iron oxides.
12	MD-CH04-01	12	Aphanitic	Homogeneous	Orangey brown	Brownish grey	Moderately weathered, some alteration to white mineral (clays?), very fractured	~50% vesicularity Sub-mm to 27 mm size Irregular shape Partially infilled with zeolites/quartz	Anhedral pyroxenes exhibit ophitic to subophitic textures, euhedral to subhedral plagioclase laths are dominant in modal abundance and are almost completely seritized. Euhedral to subhedral olivines with iddingsite along fractures and rims. Minor iron oxides.
13	MD-CH-P23-01	14	Aphanitic	Homogeneous	Reddish brown	Brownish red	Moderately weathered, several fractures, some orange to white alteration	~25% vesicularity 1-20 mm size Irregular to rounded shape Partially to fully infilled with zeolites/quartz and (calcite/chalcedony?)	Subhedral to euhedral plagioclase laths and blades, partially to fully altered to sericite. Subhedral to euhedral olivines replaced by iddingsite around rims. Groundmass is abundant and is comprised of aphanitic red-brown to black material.

Table 3-1 (continued).

Location (Figure 3-2)	Sample	Geological Unit	Grain Size	Texture/Fabric	Weathered Colour	Fresh Colour	Weathering/Alteration	Vesicles	Thin Section Description
14	MD-CH02-01	15	Aphanitic	Homogeneous	Brownish grey	Dark grey	Moderately weathered, minor occurrences of quartz mineralization, several fractures	~35% vesicularity Sub-mm to 8 mm size Irregular to rounded shape Partially to fully infilled with zeolites/quartz	Anhedral pyroxenes exhibit ophitic to subophitic textures, euhedral to subhedral plagioclase laths are dominant in modal abundance. All olivines completely iddingsitized. Minor iron oxides.
15	MD-CH02-02	15	Fine grained Sub-mm	Equigranular Homogeneous	Brown	Brownish grey	Moderately weathered, minor occurrences of alteration to white mineral (clays?), several fractures	~1% vesicularity Sub-mm to 8 mm size Irregular to subrounded shape Some vesicles partially infilled with zeolites/quartz	Highly altered abundant groundmass (glass?), almost complete seritization of plagioclase. Minor iron oxides.
16	MD-CH-P12-01	16	Aphanitic	Homogeneous	Reddish brown	Red	Moderately weathered, several fractures	~35% vesicularity Sub-mm to 13 mm size Irregular to subrounded shape Some vesicles partially infilled with zeolites/quartz Infilled vesicles occur along possible former vein	Subhedral to euhedral plagioclase laths partially to fully altered to sericite; in some places laths exhibit variolitic texture. Subhedral to euhedral olivines completely replaced by iddingsite. Amygdales filled with nepheline(?). Groundmass is aphanitic red-brown material and dominates in abundance.
17	MD-CH01-01	17	Aphanitic	Homogeneous	Brown	Grey	Moderately weathered, minor occurrences of alteration to white mineral (clays?), some fractures	~30% vesicularity Sub-mm to 30 mm size Irregular to subrounded shape Some vesicles partially infilled with zeolites Some vesicles partially infilled with (calcite/chalcedony?) Elongate in single orientation (direction not determined)	Anhedral pyroxenes exhibit ophitic to subophitic textures, euhedral to subhedral plagioclase laths are dominant in modal abundance. Seritization is common on plagioclase. Minor iron oxides.
18	MD-CH01-02	17	Fine grained Sub-mm	Equigranular Homogeneous	Orangey grey	Grey	Slightly weathered, iron stained	~2% vesicularity 1-9 mm size Subrounded to rounded shape Some vesicles partially infilled with zeolites/quartz	Anhedral pyroxenes exhibit ophitic to subophitic textures, euhedral to subhedral plagioclase laths are dominant in modal abundance. All olivines completely iddingsitized. Seritization is minor on plagioclase. Minor iron oxides.
19	MD-CH03-01	13	Fine to medium grained Sub-mm to 1 mm	Equigranular Homogeneous	Grey	Grey	Slightly weathered	<1% vesicularity 1-32 mm size Irregular shape Partially to fully infilled with zeolites/quartz ~90% of vesicles in sample occur along one band, with preferred elongation direction parallel to length of band	Euhedral to subhedral plagioclase laths dominant in abundance and almost completely altered to sericite. Anhedral to subhedral pyroxene and olivine. Olivines are iddingsitized along fractures and rims. Minor iron oxides.
20	MD-CH03-02	13	Aphanitic	Homogeneous	Greyish brown	Grey	Moderately weathered, minor occurrences of alteration to white mineral (clays?), several fractures	~35% vesicularity Sub-mm to 16 mm size Irregular to subrounded shape Some vesicles partially infilled with zeolites/quartz	Euhedral to subhedral plagioclase laths dominant in abundance and almost completely altered to sericite. Anhedral to subhedral pyroxene and olivine. Olivines are iddingsitized along fractures and rims. Minor iron oxides. Amygdales abundant with infill of nepheline/zeolites (?)
21	MD-CH03-03	13	Fine grained Sub-mm	Equigranular homogeneous	Grey	grey	Slightly weathered, some quartz mineralization along possible former vein	<1% vesicularity (all in single band) Sub-mm to 5 mm size Irregular shape	Anhedral pyroxenes exhibit ophitic to subophitic textures, euhedral to subhedral plagioclase laths are dominant in modal abundance and have minor alteration to sericite. Euhedral to subhedral olivines with iddingsite along fractures and rims.

Rock Descriptions

Four windows on the LIP1 slope were selected for detailed remote sensing analysis (Figure 3-2). They were chosen to highlight differences between geological units, explore variation within units, study certain structural and volcanological characteristics, and to compare remote sensing techniques with hand samples that could be collected. Detailed descriptions of the units in each window are presented in the following sections.

Window 1

This window comprises a section of the two uppermost lava flows visible at the Chasm (W1 in Figure 3-2). It was selected to highlight possible contrasts in thermal response between lava flows and because it exhibits a variety of structures. Persistent sub-horizontal joints are visible in the upper lava flow in addition to vertical joints characteristic of columnar jointing associated with lava cooling. Reddish sediment occurs continuously between the two lava flows, indicating a paleosol layer is present. The ROI for Window 1 is shown in Figure 3-3.

Unit 1 is a dark grey basalt (Figure 3-3). It is of variable thickness, approximately 2 to 5 m. There are two types of alteration in Unit 1, iron staining and white alteration. Both alteration types occur on joint surfaces and exposed sections. The white alteration is likely where the basalt has altered to clay minerals. Unit 1 overlies Unit 2 with a sharp and undulating boundary.

Unit 2 is an orange-grey paleosol composed of loose and lithified soil, as well as various sizes of blocks of Unit 3 (Figure 3-3). The blocks range in size from several centimeters to 1 m in diameter, and are highly altered to an orange colour, likely hematite due to iron alteration. This unit varies greatly in thickness, ranging from 0.8 m to 2 m. Unit 2 overlies Unit 3 along an erosional and highly irregular boundary.

Unit 3 is a brownish-grey basalt (Figure 3-3). It varies in thickness from 6 to 6.5 m. The two types of alteration observed in Unit 1 also occur in Unit 3, similarly on joint surfaces and exposed sections. Unit 3 and Unit 4 are separated by a sharp and relatively linear boundary.

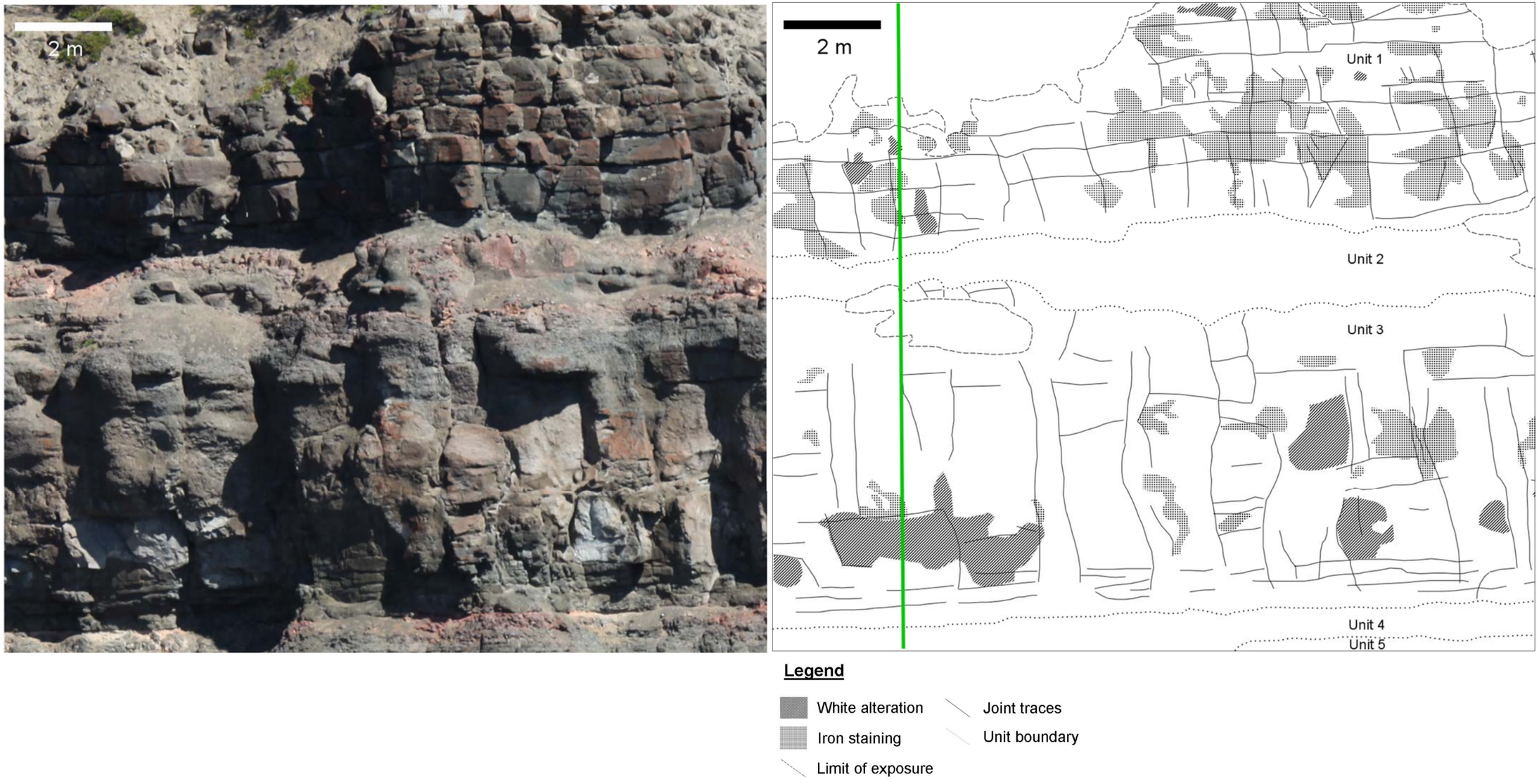

Figure 3-3. Photograph of Window 1 in RGB colour (left). The features visible in the window are shown in the line drawing (right), including joints, alteration types, and unit. Reflectivity Profile 1 (RP1) is shown on the line drawing as a vertical green line.

Unit 4 is similar to Unit 2 in that it is an orange-grey paleosol composed of loose and lithified soil with blocks, however the blocks present in Unit 4 are much smaller than those in Unit 2 (Figure 3-3). The blocks range in size in the order of several centimeters in diameter, and are highly altered to orange-coloured minerals, likely hematite and other iron-bearing minerals. Unit 4 is thin and does not vary greatly in thickness, from 0.4 to 1 m. Unit 4 overlies Unit 5, and the boundary is erosional and irregular. In this window Unit 5 can be observed to be similar in composition to Unit 3.

Unit 1 has a high percentage of its surface area altered, with the majority of alteration being the iron staining. The type of alteration which dominates in Unit 3 is white alteration, however the percentage of the total surface area altered in this unit is less than that of Unit 1. This is likely due to the greater amount of closely spaced joints in Unit 1, which allows for greater circulation of fluids through the rock.

The colour of the paleosols, Units 2 and 4, are indicative of iron mineral alteration as well, however the colour is dissimilar to the rusty brown of typical iron staining. The bright orange colour is likely due to the erosion of the underlying lava flow into a soil, in which each particle has a greater surface area on which alteration can occur due to their smaller size. The lavas are basalt, and therefore contain large amounts of iron-bearing minerals, including olivine, augite and iron oxides (Farrell, 2010). The heat of the subsequent overlying lava flow likely baked the existing soil, resulting in thermal oxidation of the eroded basalt soils.

Window 2

Only one unit, Unit 5, is present in this window (W2 in Figure 3-2; Figure 3-4). The selection of this window was made with the aim of examining the thermal response of a relatively uniform area, as compared to other windows which contain multiple units. Columnar jointing (0.2-2 m persistence) in the top half of Window 2 is generally well developed and is considered the colonnade portion of the flow. In the bottom half of the window, however, joints are shorter (0.2-2 m), curved, or non-existent, and are characteristic of the entabulature zone of the flow. A sub-horizontal joint set is persistent across the window, with many joints in the upper half of the section extending across the entire window. The ROI for Window 2 is shown in Figure 3-4.

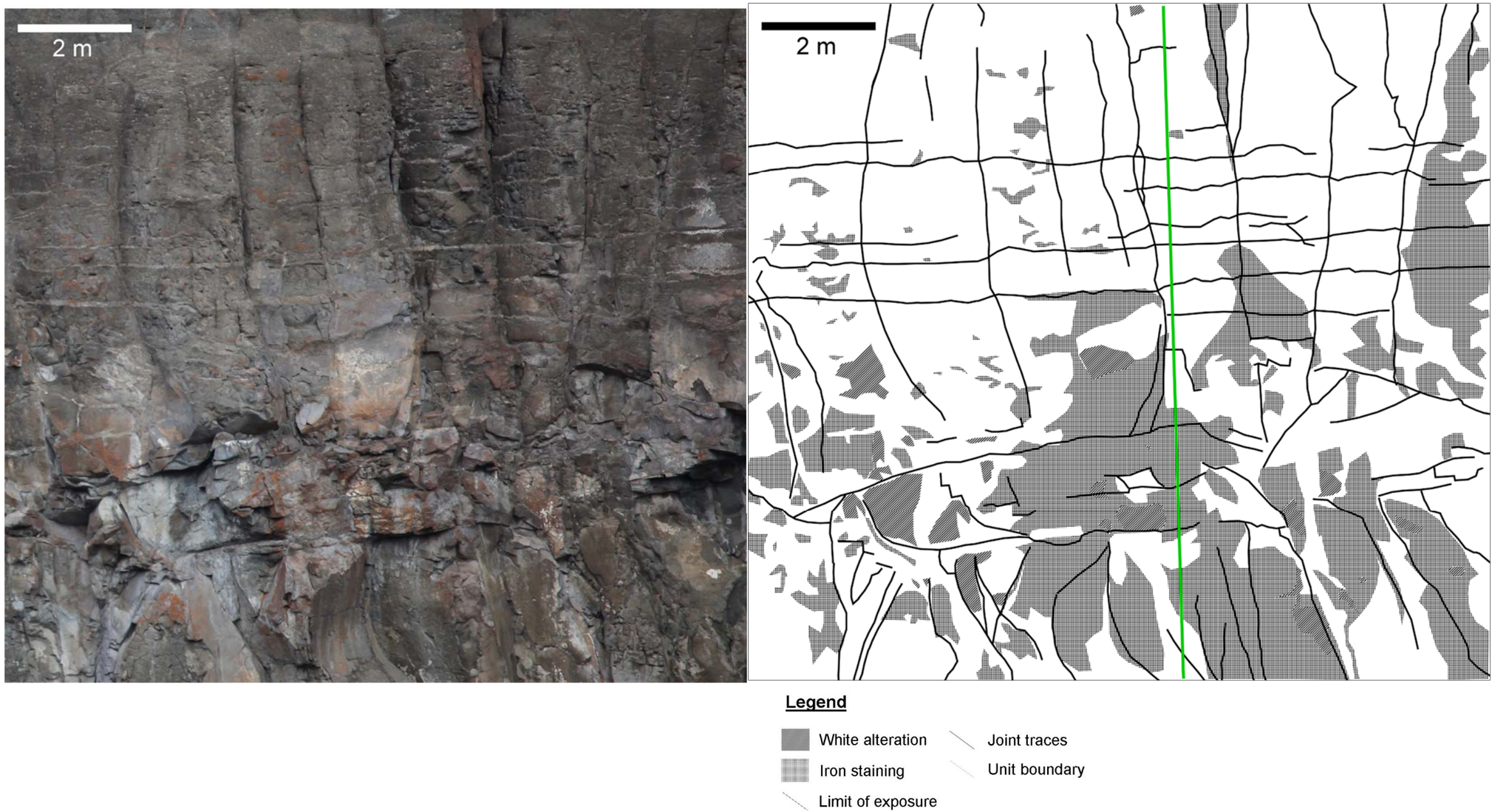

Figure 3-4. Photograph of Window 2 in RGB colour (left). The features visible in the window are shown in the line drawing (right), including joints, alteration types, and units. RP2 is shown on the line drawing as a vertical green line.

As stated above, Unit 5 is observed to be similar in composition to Unit 3. It is a brownish-grey basalt (Figure 3-4), and varies in thickness from 13 to 17 m. The two main types of surface alteration described for Window 1 are also present in Window 2 on exposed surfaces of joints. Alteration is more prevalent in the lower half of the window, probably due to the presence of more exposed surfaces. The middle to lower half of the section consists of more chaotic jointing (the entabulature zone), and joint surfaces are less continuous and create smaller blocks. Exposed surfaces are therefore more numerous, allowing for more surfaces on which weathering and alteration can occur.

Four joint sets are observed in this unit; one joint set is sub-horizontal, and three are the result of columnar jointing and are sub-vertical. The sub-horizontal joint set has high persistence, as do the sub-vertical columnar joints, however the lower half of the window shows fewer joints and lower persistence in general.

Window 3

Window 3 (W3 in Figure 3-2; Figure 3-5) is comprised of several units, including three paleosols and four lavas. It was selected to observe the differences in thermal response between thicker and thinner lava units and paleosols, as well as the variability of units with respect to the development of columnar jointing. Reddish-orange sediment and rock indicate units of paleosols. The ROI for Window 3 is shown in Figure 3-5.

The top of the window exhibits Unit 5, which is described in previous sections. Underlying Unit 5 is Unit 6, a reddish-orange paleosol layer composed of lithified and unconsolidated iron-rich soil with block inclusions of Unit 7. The blocks are between 0.3 and 13 m in diameter and are altered in some places to the same reddish-orange colour of the paleosol. Unit 6 varies in thickness from 0.4 to 2 m and overlies Unit 7 on an erosional and irregular boundary.

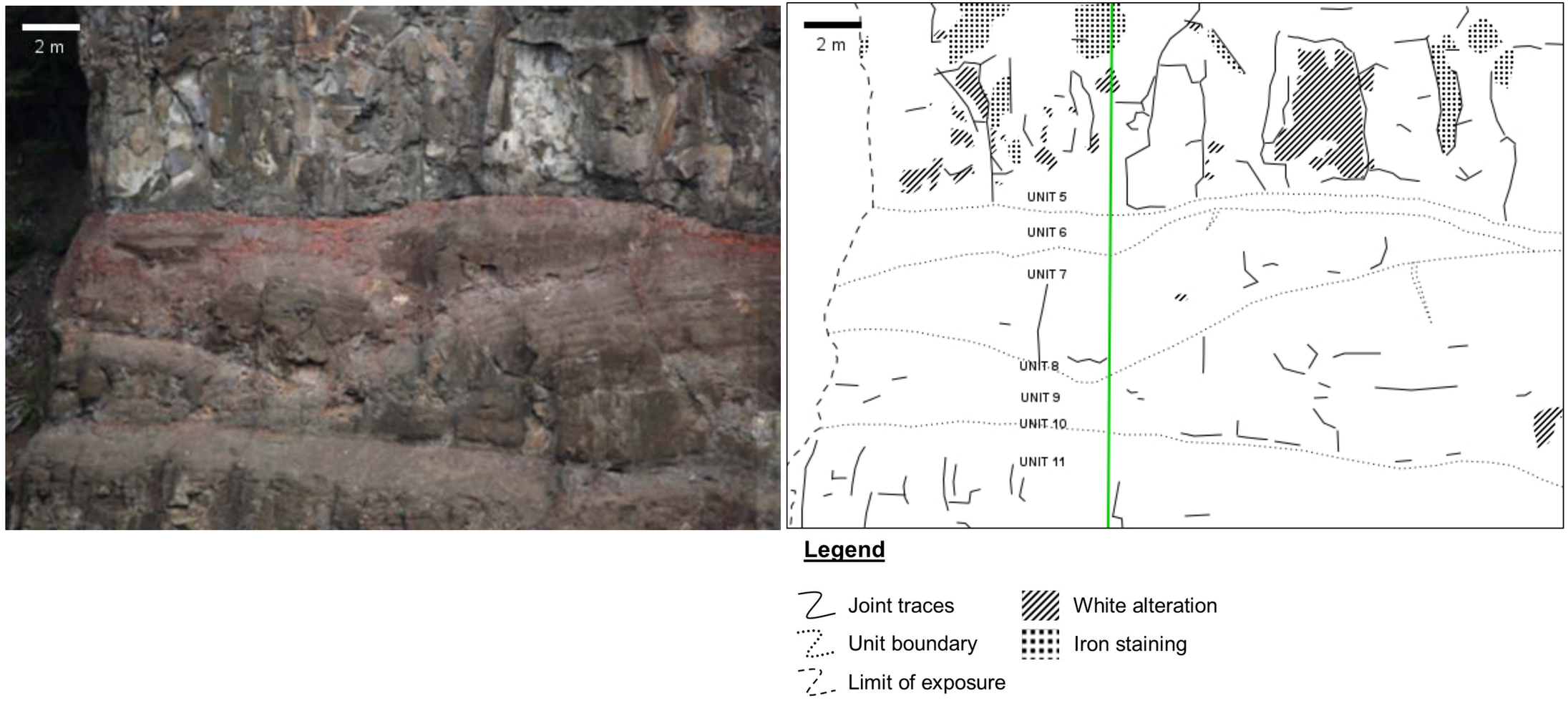

Figure 3-5. Photograph of Window 3 in RGB colour (left). The features visible in the window are shown in the line drawing (right), including joints, alteration types, and units.

Unit 7 is similar to Units 3 and 5, and is a brownish-grey basalt with thicknesses between 0.7-5 m where it exists, but also pinches out in the right side of Window 3 and after approximately 12 m, is observed again as a continuous layer. As it is not a thick flow, well-developed columnar jointing did not form in this unit, though minor non-uniform sub-vertical jointing is observed. It contains minor local white alteration and iron staining, and numerous eroded cracks along joints in the top of the flow are infilled with the paleosol of Unit 6. The boundary between Unit 7 and Unit 8 is undulatory and irregular.

Unit 8 is similar to Unit 6, and is a red-brown paleosol unit with smaller thicknesses between 0.1-0.5 m. The boundary between Unit 8 and Unit 9 is erosional, gradational and irregular.

Unit 9 is another lava flow, with similarly underdeveloped columnar jointing to Unit 7, but is slightly thicker (2-8 m). It is brownish-grey, comprised of many areas along joints and on joint surfaces with white alteration and iron staining. The top half of the flow exhibits banding parallel to the top of the flow which is continuous for the visible length of the slope, and is likely chatter marks resulting from the cooling process after emplacement. A sharp, undulatory boundary separates Unit 9 and Unit 10.

Unit 10 is a discontinuous paleosol, with thicknesses up to 0.4 m. It is observed as a red-brown unconsolidated layer on the more northern part of the LIP1 slope, and continues south as an orangish-grey unconsolidated soil. As Unit 10 is discontinuous, Unit 11 shares a boundary with both Unit 9 and Unit 10; this contact is erosional and irregular.

Unit 11 is a brownish-grey basalt lava flow between 2-8 m thick. The vast difference in thickness is due to the paleo-topography created by Unit 12, the underlying lava flow, in which there were large “valleys” to be filled by Unit 11 in between lobes of Unit 12. In most of the length of the Unit 11 flow, the thickness of the flow was such that a colonnade zone could be formed. The columnar joints are not completely uniform, but well-developed, in that they are regularly spaced and persistent through most of the thickness of the flow. Similar to previous flows, Unit 11 exhibits both iron staining and white alteration, again on joint surfaces and exposed sections where blocks have fallen. This alteration, however, is mostly restricted to the bottom two thirds of the flow

thickness in this unit. The contact between Unit 11 and Unit 12 is undulatory and irregular, but sharp in most places. In some areas, however, the boundary between Units 11 and 12 is obscured by jointing and vegetation. In rare areas, a very thin (<0.1 m) paleosol is observed at this contact.

Unit 12 is not observed in any of the four windows, so will be described in this section. It has thicknesses between 3 and 7 m, and is a brownish-grey basalt lava. Similar to all lavas in this sequence, Unit 12 contains areas with iron staining and white alteration, all upon joint surfaces and fracture faces. Jointing is observed in this unit, however it is chaotic and irregular (entabulature zone), indicating the flow was either not thick enough to develop a full colonnade, or it cooled quicker than other flows. The boundary between Unit 12 and 13 is sharp and undulatory.

Window 4

The five units of Window 4 (W4 in Figure 3-2) include two paleosols and three lava units. The ROI for Window 4 is shown in Figure 3-6. The first lava unit is Unit 13, a grey basalt 4-6 m thick. It is comprised of mostly fresh surfaces, with minor iron staining and white alteration along joint faces. It exhibits well developed, if irregular, columnar and sub-horizontal jointing, and its bottom contact with Unit 14 is sharp, irregular and undulatory.

Unit 14 is a red-brown paleosol unit similar to those above, and contains blocks of the underlying Unit 15. It varies in thickness from 0.1-0.7 m, and carries blocks between several centimeters to 0.1 m large. It is continuous over the length of the slope, and shares an erosional and irregular contact with Unit 15.

Unit 15 can be described similarly to the previous brownish-grey lava units, and is comprised of regular well developed columnar jointing in the colonnade. It is 8-10 m thick, and is in contact with Unit 16, a red-brown paleosol like Unit 14, at a sharp and undulatory boundary. Unit 16 varies in thickness between 0.2-0.7 m, and overlies Unit 17, a brownish-grey lava, at an erosional and irregular contact. The maximum thickness observed in Unit 17, as the remainder is covered in the scree slope, is 6 m.

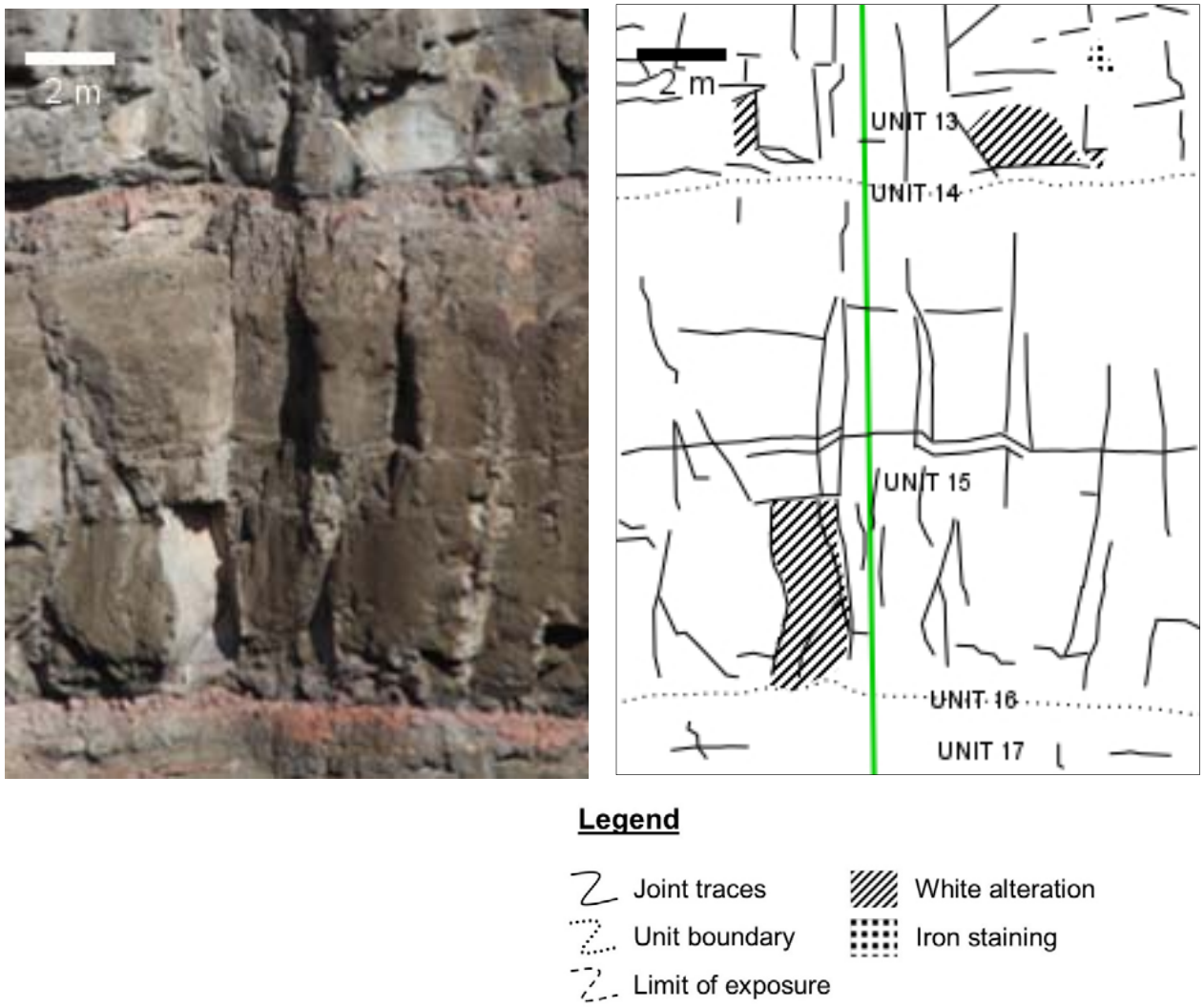

Figure 3-6. Photograph of Window 4 in RGB colour (left). The features visible in the window are shown in the line drawing (right), including joints, alteration types, and units. RP4 is shown on the line drawing as a vertical green line.

Erosional Profiles Using LiDAR

Topographic profiles were extracted from LiDAR scan data to observe the differential erosion patterns on the LIP1 slope (Figure 3-7). The northern profiles (EP1, EP2, EP3) show that paleosol layers are eroded more readily than the lava flow units. The paleosols are finer grained and have a higher portion of vesicles (as seen in hand sample), factors which contribute to a greater surface area for weathering to occur. Weathering weakens the rock, making it more susceptible to erosion. These weak layers are eroded more quickly, and undercut the overlying more competent layers, contributing to overall slope erosion once the overlying layers are undercut enough to release blocks.

The paleosols are thicker and more continuous in the more recent (upper) lava flows on the north side of the LIP1 slope, as well as in the older (lower) lava flows on the south side of the outcrop. This is evident in both RGB photographs of the slope, where thicker bands of red-orange are seen, as well as the pronounced difference in slope angle at the paleosols in the erosional profiles, in which the profiles exhibit undercutting of competent lavas above thicker layers of paleosols. These differences in the upper slope paleosols and lower slope paleosol erosional patterns on the north side may indicate larger hiatuses between successive lava flows further up in the sequence, allowing for more fully developed paleosols, though only the uppermost lava visible at the Chasm has been K-Ar dated, so no geochronological data exists to corroborate this (Mathews, 1989; Andrews and Russell, 2007).

The paleosols in the lower section of the sequence on the south side of the LIP1 slope (EP4 and EP5), however, are also thick and continuous, so it is more likely that the variation in erosional profiles of the paleosols are due to slight changes in lava emplacement styles. In the cases where paleosols are thicker and thereby observed more easily in both photographs and erosional profiles, the lava styles tend to be more sheet-like, rather than lobe-like in morphology. This is possibly due to the lobes of lava exhibiting a less continuous footprint overlying the paleosols, which could have affected the preservation of the paleosols.

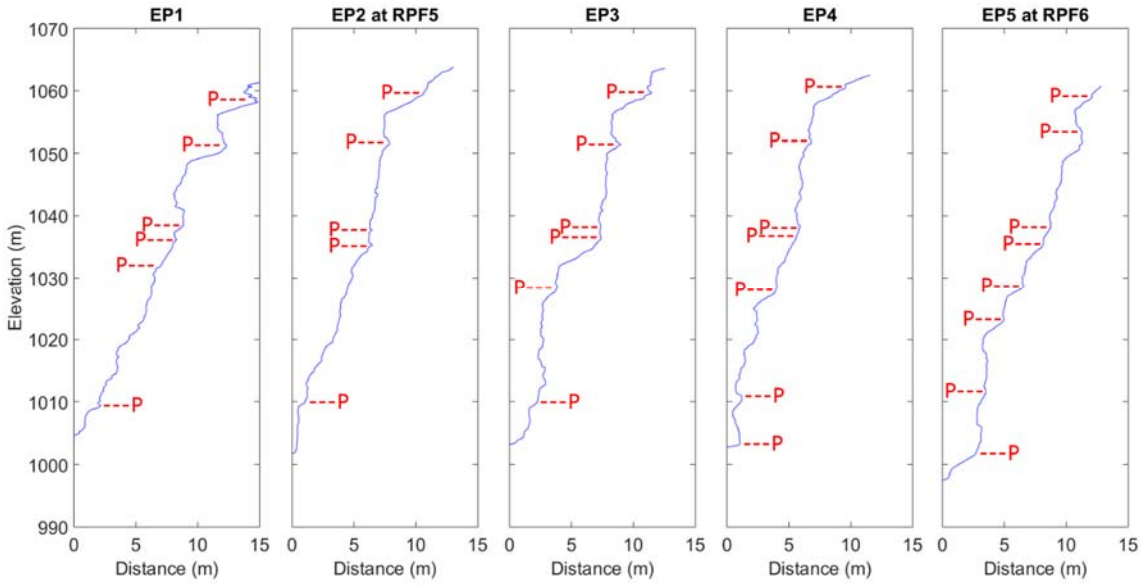

Figure 3-7. Profiles along LIP1 slope. "P" indicates a paleosol layer; the locations of the profiles on the slope are denoted in Figure 3-2.

Alteration Mapping Using LiDAR and Photographs

The two main types of alteration observed at the Chasm, white alteration and iron staining, were mapped out manually (see the interpretive line drawings for Window 1 in Figure 3-3, Window 2 in Figure 3-4, Window 3 in Figure 3-5, and Window 4 in Figure 3-6) as well as with RGB and reflectivity values from the LiDAR data collected. All three methods were employed in each of the windows, with results discussed in this section.

In general, reflectivity values in the chosen representative areas of alteration within the windows were comprised of a wide range of values. For example, the representative areas in Window 1 with white alteration exhibited reflectivity between -8.65 and -4.29 dB, which when considering the majority of the LIP1 slope is comprised of reflectivity values of -9 to -3 dB, is quite an extensive range. This leads to the obscuring of important mappable properties, because they are not highlighted by a narrow range of reflectivity. In Figure 3-8, for example, the -8.65 to -4.29 dB range is used to display reflectivities which would be representative of white alteration on the slope. It is obvious, however, that the majority of the slope is represented by this range, and therefore is not effective for mapping white alteration. Similar problems are observed with the mapping of iron staining and white alteration in all windows using LiDAR reflectivity.

Figure 3-8. LiDAR point cloud of Window 1 with reflectivity values matching that of representative areas of white alteration highlighted in red.

A similar process was used to obtain parameters for red, green and blue values (RGB) to map iron staining and white alteration in the LiDAR point clouds, as well as on photographs in GIMP. As seen in Figure 3-9, the RGB value ranges for the representative iron stained areas in Window 1 (Table 3-2) are too broad in the LiDAR method, similar to the response with reflectivity. The areas mapped as “iron stains” are not all iron staining, and in fact cover most of the rock face. In the photograph method, however, a narrow range of RGB values was used (Table 3-2), and a more representative map was created for iron staining in Window 1. Oxidation in the paleosol layer has also been mapped as iron staining, which is not surprising as both processes result from the presence of iron in the slope and exhibit similar hues.

RGB values for representative white alteration in Window 1, also provide a narrower range for mapping (Table 3-2) near one side of the RGB colour spectrum (white) for both the LiDAR and photograph methods (Figure 3-9). As a result, many areas of alteration mapped with this method are consistent with what was mapped manually on photographs, with the exception of soil-covered areas also being captured as alteration. There are still many areas which are mapped as white alteration, which upon further inspection do not appear to have white alteration, so this method does require a manual review of the results.

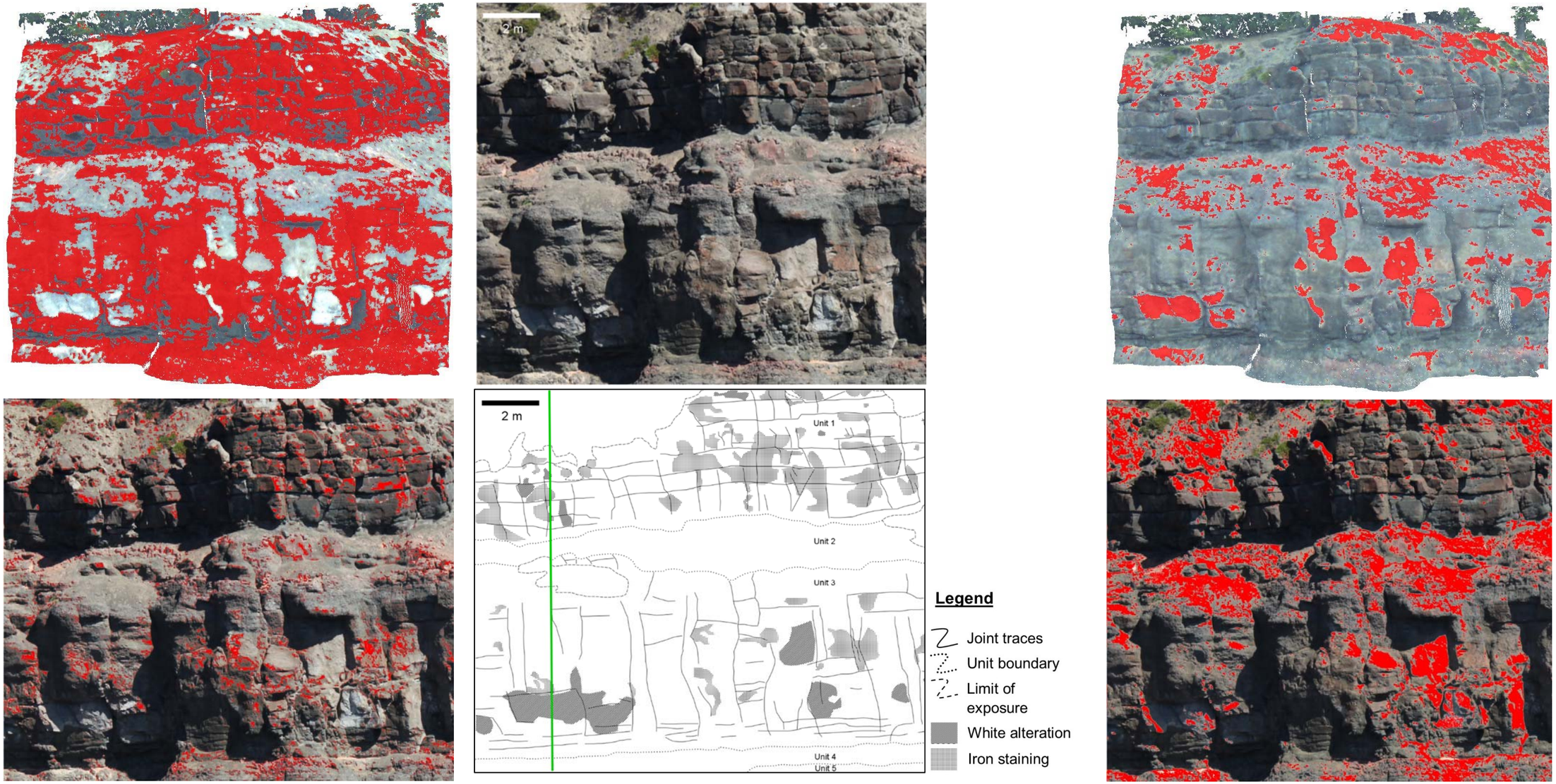

Figure 3-9. Maps of iron staining using RGB on LiDAR (top left) and photograph (bottom left); maps of white alteration using RGB on LiDAR (top right) and photograph (bottom right) for Window 2, with mapped features shown in red. The photograph (top middle) and the interpretive line drawing (bottom middle) for Window 2 are also shown.

Table 3-2. Iron staining and white alteration RGB values for RGB mapping in LiDAR point clouds and photographs. In the GIMP photograph method, the colours of each pixel used to select similar colours in the image are shown; the threshold of colour picking was ±15 (on the 0-255 RGB value scale).

Alteration	Window	Method	R Min	R Max	G Min	G Max	B Min	B Max
Iron Staining	1	LiDAR Point Cloud	100	184	109	195	115	178
		Photograph	137		109		97	
	2	LiDAR Point Cloud	136	168	126	169	119	164
		Photograph	83 109 150		59 69 104		49 57 81	
	3	LiDAR Point Cloud	137	185	135	191	125	180
		Photograph	127 160		81 133		65 114	
	4	LiDAR Point Cloud	116	159	128	168	123	166
		Photograph	112		94		76	
White Alteration	1	LiDAR Point Cloud	146	255	174	255	194	255
		Photograph	176 206 221		172 192 222		169 183 208	
	2	LiDAR Point Cloud	173	255	206	255	213	255
		Photograph	143 165 198 218		146 169 197 217		153 168 195 215	
	3	LiDAR Point Cloud	210	255	234	255	227	255
		Photograph	171 181 204 215		164 189 192 211		156 191 178 200	
	4	LiDAR Point Cloud	152	255	177	255	170	255
		Photograph	182 197		184 200		182 196	

In Window 2, the RGB alteration mapping method was successful for both iron staining and white alteration using LiDAR point clouds, as well as with the photographs in GIMP (Figure 3-10). Iron stain maps exhibit varying degrees of coverage for detected iron stained areas within the window, with the GIMP-generated image having a greater area delineated than the LiDAR. Both methods, however, display similar patterns of alteration on the slope. When compared to the original interpretive line drawing localities for iron staining, both LiDAR and photograph maps have less continuous areas, resulting in a spotty pattern of alteration. This is likely because manual mapping implies a degree of generalization, and in this case, areas which were dominantly the iron staining alteration were mapped as contiguous. It is also notable that though RGB values for the LiDAR point cloud imagery and photogrammetry imagery are different (they were taken at different times of day with different instruments), similar patterns of alteration can be mapped due to the use of representative RGB values of the alteration within each dataset.

Similar observations can be made of the white alteration maps in Figure 3-10, whereby both LiDAR and photogrammetry methods yield comparable alteration coverage for Window 2. The areas of white alteration delineated in the interpretive line drawing are all represented in both datasets, with the addition of some areas that were too small or discontinuous to map manually. As with the iron staining in the previous figure, the photogrammetry-generated alteration map has more coverage than the LiDAR-generated map. This is possibly from the picking of representative RGB values, in that the photogrammetry range is broader than that of the LiDAR.

Alteration maps for Window 3 also show consistency in areas designated for iron staining and white alteration between methods (Figure 3-11). Oxidation of paleosols, however, has both in LiDAR and photograph RGB values been mapped as iron staining. This oxidation does have a similar hue as the iron staining, but implies different processes of iron alteration, so takes away from the effectiveness of using RGB values for mapping iron staining on a slope. Beyond the paleosols, however, the delineation of iron staining in Unit 5 was consistent with the major areas exhibited in the line drawing. The mapping of white alteration using RGB was more effective in Window 3, and all major areas mapped manually were represented in both the LiDAR and photograph RGB maps.

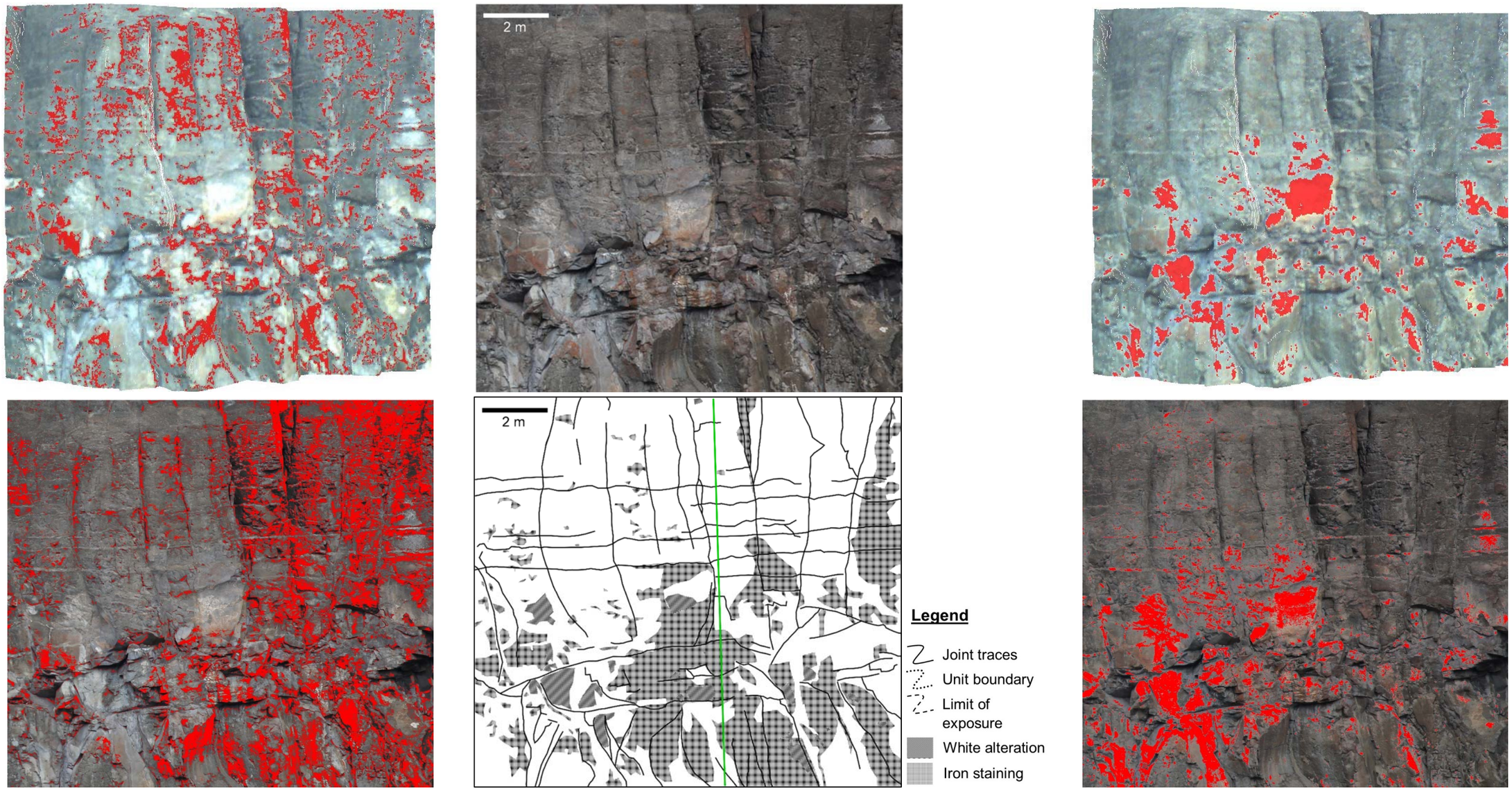

Figure 3-10. Maps of iron staining using RGB on LiDAR (top left) and photograph (bottom left); maps of white alteration using RGB on LiDAR (top right) and photograph (bottom right) for Window 2, with mapped features shown in red. The photograph (top middle) and the interpretive line drawing (bottom middle) for Window 2 are also shown.

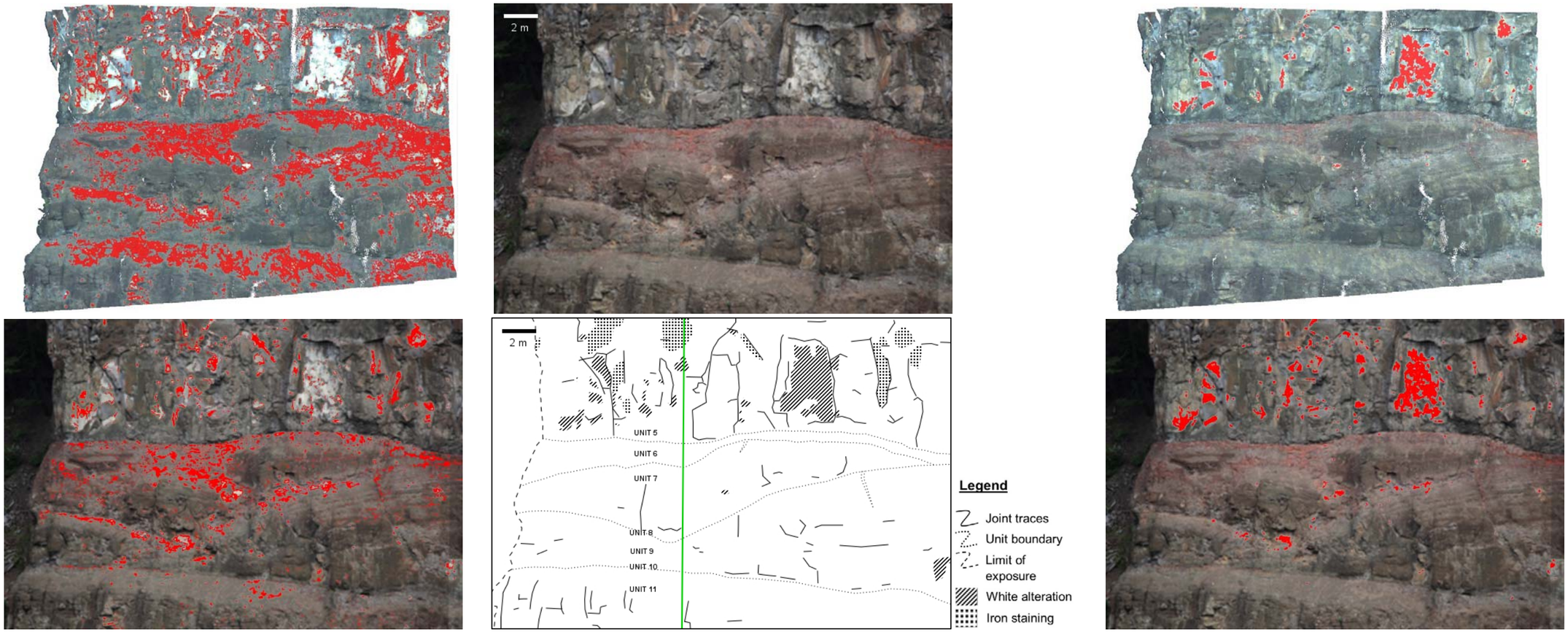

Figure 3-11. Maps of iron staining using RGB on LiDAR (top left) and photograph (bottom left); maps of white alteration using RGB on LiDAR (top right) and photograph (bottom right) for Window 3, with mapped features shown in red. The photograph (top middle) and the interpretive line drawing (bottom middle) for Window 3 are also shown.

As seen with Windows 1 and 3, oxidized paleosol layers were mapped with iron staining in Window 4 in the LiDAR point cloud method, but they are not recognized as having the same RGB signature as iron stained areas in the GIMP method (Figure 3-12). Many areas without iron staining are distinguished as such in the LiDAR, indicating the RGB values used as representative (Table 3-2) were too broad or non-unique. The GIMP-generated image also exhibits problems with the RGB range chosen (Table 3-2), since it maps much of Unit 15 as iron stained, when it is weathered to a brown colour. The RGB ranges for iron staining in Window 4 were therefore neither ideal, though there is very little iron staining in the window at all, so there were not enough representative areas from which to take RGB values. The LiDAR point cloud and GIMP-generated white alteration maps show very similar results, and both are consistent with the manual mapping done for the interpretive line drawing of Window 4 (Figure 3-12).

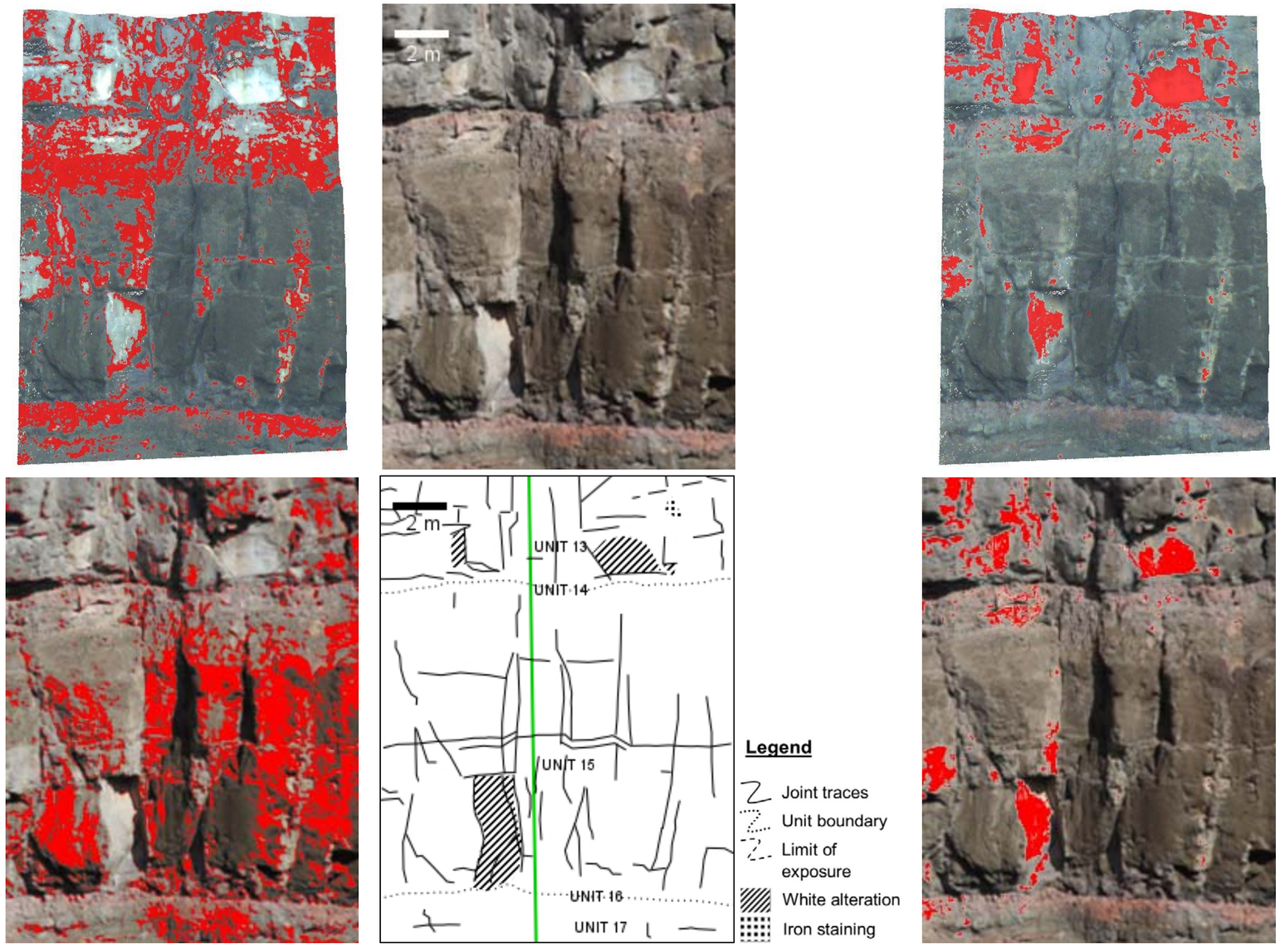

Figure 3-12. Maps of iron staining using RGB on LiDAR (top left) and photograph (bottom left); maps of white alteration using RGB on LiDAR (top right) and photograph (bottom right) for Window 4, with mapped features shown in red. The photograph (top middle) and the interpretive line drawing (bottom middle) for Window 4 are also shown.

Discontinuity Characteristics from Photogrammetry

The slope discontinuities were mapped in each window, with the purpose of characterizing the joint and joint set properties. Data for discontinuity characterization were obtained through photogrammetry models created with Metashape; resultant models were mapped using CloudCompare. Each window exhibits four joint sets: three sub-vertical sets representing columnar jointing, and one sub-horizontal set which approximately follows chatter marks on columns. In lava flows such as these, columnar jointing is the dominant pattern of jointing and is generally comprised of sub-vertical and sub-horizontal joint sets, if cooling surfaces for the fresh lava (such as existing topography and the outside air) are sub-horizontal. Joint set ellipses were therefore chosen based on the density of contours (clusters of joint orientations), and clusters of joint orientations within certain dip angle parameters (i.e. Sub-vertical joints would normally be within 30° of vertical). The number of joints in each joint set was also recorded, to indicate the relative frequency and consider directional bias. Bias is evident due to the orientation of the joint sets, in that some joints are easier to observe in the face of the slope than others. General observations and measurements were taken from the terrestrial LiDAR model of the LIP1 slope for units which were thick and continuous enough to observe jointing.

General Observations

In Unit 1, the sub-horizontal joint set throughout the unit has a higher persistence than the sub-vertical jointing, with some joints continuous over 40 m in length. Spacing between the sub-horizontal joints is between 0.4 and 0.8 m, and sub-vertical joint sets create columns approximately 2 m in diameter.

Contrary to that of Unit 1, the horizontal joint set in Unit 3 has a lower persistence than the columnar jointing, with joints reaching approximately 0.8 m in length. Spacing between horizontal joints is highly variable and ranges between 0.2 and 3 m, whereas vertical joint spacing has a smaller range between 0.3 and 0.8 m.

The sub-horizontal joint set in Unit 5 has a higher persistence than the sub-vertical sets, and some joints reach a length of over 40 m. The sub-horizontal joints have between 0.4-0.9 m spacing, and columns created by sub-vertical joint sets are on average approximately 2 m in diameter.

Units 9, 11, 12 and 13 are not as thick as Unit 5 and have less well-developed columnar jointing, though jointing is still well observed. In Unit 9, columns approximately 1 m wide are observed, and columnar joints are between approximately 0.7-5 m long. Sub-horizontal jointing is sporadically encountered in this unit, so spacing could not accurately be determined, though persistence ranges between 0.3-0.9 m. Unit 11 is comprised of columnar jointing approximately 0.6-4 m in length, and columns about 0.9-3 m wide. Persistence of sub-horizontal jointing is between 0.4-10 m, and similar to Unit 9, spacing of the sub-horizontal joint set was not observed due to the small number of joints in this set. Columns are marginally more defined in Unit 12 than in Units 9 and 11, exhibit widths between 0.7-2 m, and have lengths of columnar joints approximately 1-5 m. Sub-horizontal joints are not common in Unit 12, and most are within the range of 0.3-1 m, though one joint reaches over 16 m. In Unit 13, sub-horizontal joints are more numerous than in the previous several units, they have lengths between 0.4-10 m and are spaced approximately 0.4-2 m apart. Columns are between 0.4-2 m wide, and sub-vertical columnar jointing measures between 0.7-3 m in length.

Unit 15 is comprised of columnar joints between 1-9 m long, creating columns approximately 0.8-3 m wide. Sub-horizontal jointing exhibits about 0.8-1 m spacing, and the joints are between 1-15 m in length. Some joints may extend beyond 15 m, but are obscured behind trees on the slope.

Window 1

One hundred and three joints were identified in Window 1. Of these, 55 joints were mapped in Unit 1, and 48 in Unit 3 (Table 3-3) (Figure 3-13). Joint sets 1, 2 and 3 (JS1, JS2 and JS3, respectively) in Unit 1 are sub-vertical, average dip values are within several degrees of each other, and the dominant dip directions are offset by approximately 55° and 80°. These offsets indicate the columns in Unit 1 created by columnar jointing are irregular hexagons, where the angles between faces of the columns are not all similar. The average persistence of the three sub-vertical joint sets within Window 1, as stated in the general observations, is lower than that of the sub-horizontal joint set. Joint set 4 (JS4) consists of low-angle joints having a wide range of dip directions and no clear dominant direction.

JS1, JS2 and JS3 in Unit 3 are also sub-vertical, and average dip values are similar. Average dip directions of these joint sets are within 41° and 86° of each other,

and therefore similar to Unit 1 in that the columns created by these joints are irregularly shaped. JS4 in Unit 3 has a higher dip angle than that of Unit 1, however the dip directions also have no clear dominant value.

Units 1 and 3 within Window 1 show similar orientations for each of the joint sets, though dominant dip directions vary slightly. The boundaries between joint sets are clearer in Unit 1, as there is a large range of orientations for JS1 and JS2 in Unit 3. The joint intensity value, P_{21}, for Unit 1 is higher than that of Unit 3, and overall the P_{21} value is low.

Table 3-3. Joint set properties within Window 1.

Unit	Joint Set	Average Dip	Average Dip Direction	Description	Number of joints in set	Average Persistence (m)	P_{21} Value (m/m^2)	
1	1	82°	246°	Sub-vertical columnar joint, some are curved	18	2	2	1.3
	2	80°	101°		8			
	3	77°	166°		16			
	4	12°	-	Sub-horizontal joint, some are curved; ball-and-socket joints	7	13		
3	1	82°	237°	Sub-vertical columnar joint, some are curved	20	2	1.3	
	2	83°	278°		12			
	3	81°	151°		6			
	4	20°	-	Sub-horizontal joint, some are curved; ball-and-socket joints	8	2		

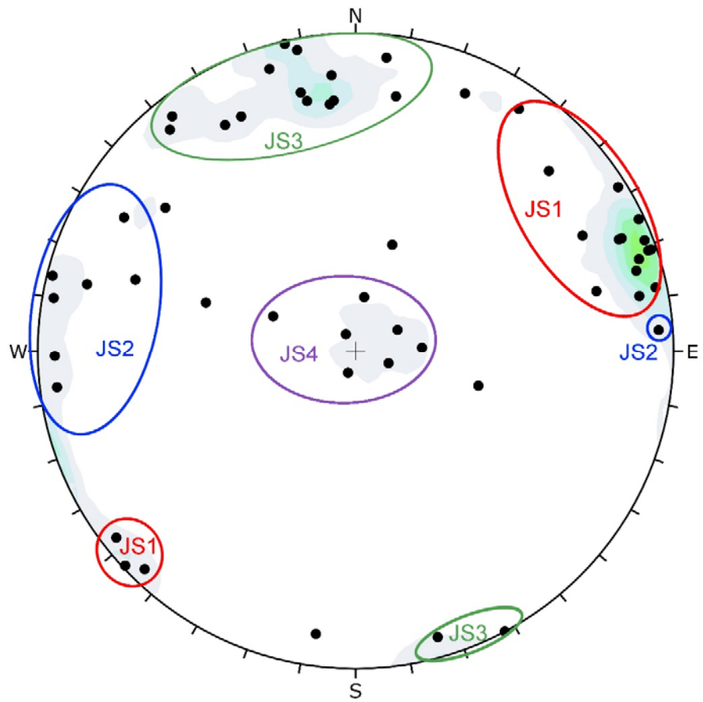

A

Color	Density Concentrations
	0.00 - 2.50
	2.50 - 5.00
	5.00 - 7.50
	7.50 - 10.00
	10.00 - 12.50
	12.50 - 15.00
	15.00 - 17.50
	17.50 - 20.00
	20.00 - 22.50
	22.50 <

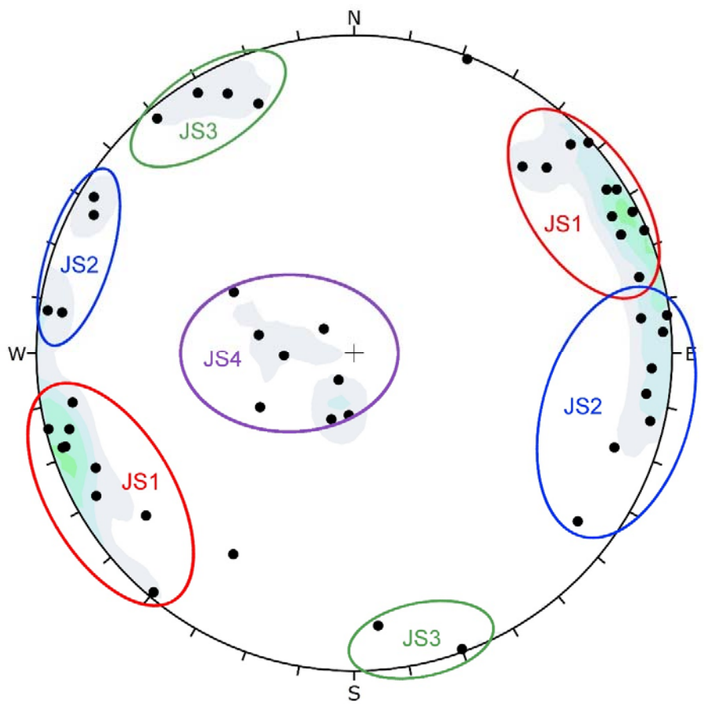

B

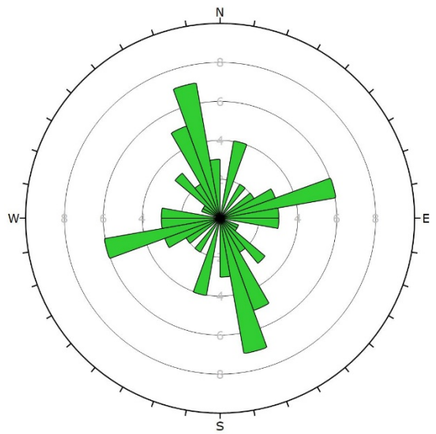

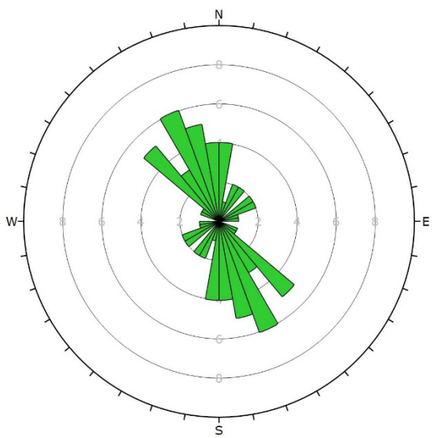

Figure 3-13. Lower hemisphere equal-area stereonet (top) and corresponding rosette diagram (bottom) for joints in Window 1 (Table 3-3). The stereonet and rosette diagram in A are for joints in Unit 1 (n=45), and Unit 3 joints (n=40) are in B.

Window 2

There were 65 joints identified in Window 2 (Table 3-4, Figure 3-14). JS1, JS2 and JS3 average dip values are close to those in Window 1, however average dip directions in Window 2 are slightly rotated with respect to those in Window 1. This slight rotation results in the difference of dip directions between sets as 53° and 50°. The similarity between these angles indicates more regularly shaped columns in this unit. JS4 has a similar average dip to Unit 3 in Window 1, and also exhibits variable dip directions. The P_{21} value of this unit, Unit 5, is higher than that of Window 1 as a whole, but closer to that of Unit 1.

Table 3-4. Joint set properties in Window 2.

Unit	Joint Set	Average Dip	Average Dip Direction	Description	Number of joints in set	Average Persistence (m)	P_{21} Value (m/m^2)
5	1	84°	249°	Sub-vertical columnar joint, some are curved	25	2	2
	2	81°	146°		6		
	3	80°	199°		17		
	4	19°	-	Sub-horizontal joint, some are curved; ball-and-socket joints	5	2	

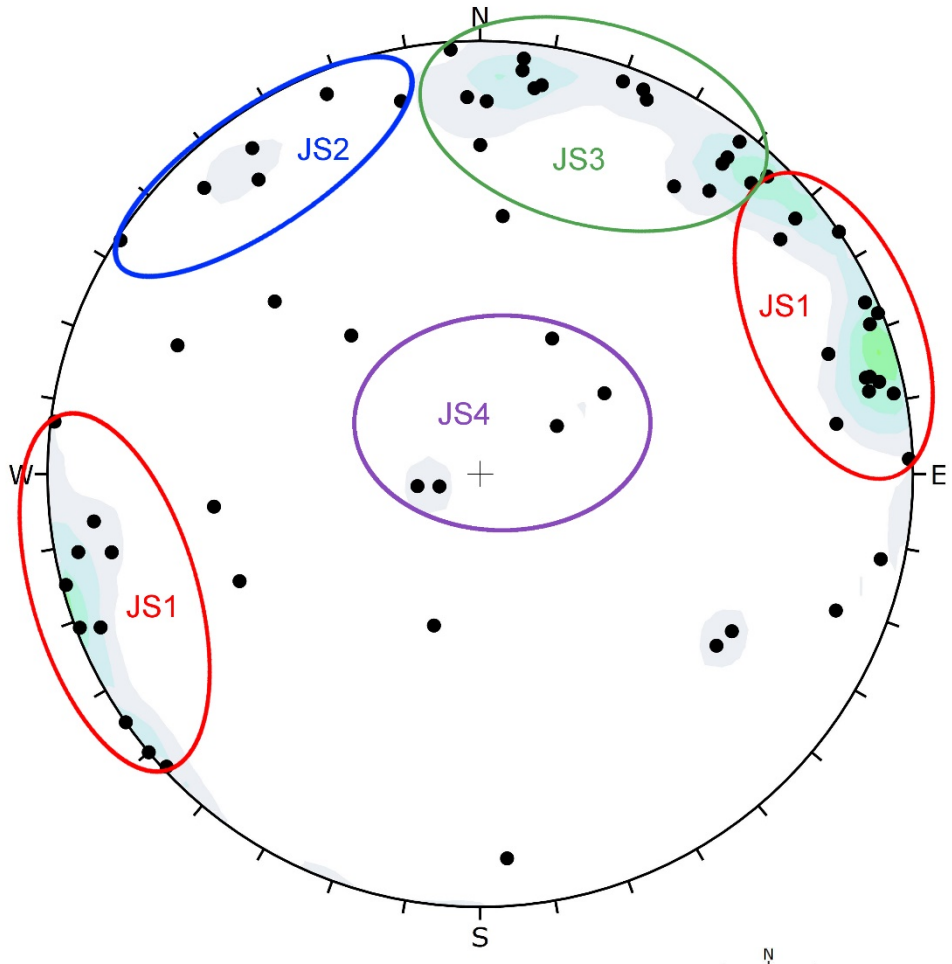

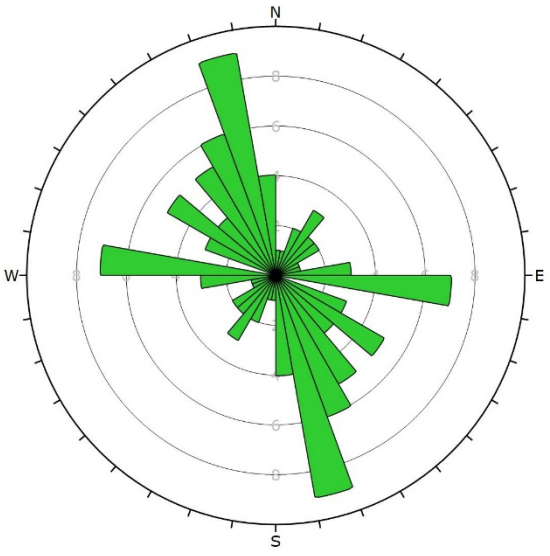

Color	Density Concentrations
	0.00 - 2.50
	2.50 - 5.00
	5.00 - 7.50
	7.50 - 10.00
	10.00 - 12.50
	12.50 - 15.00
	15.00 - 17.50
	17.50 - 20.00
	20.00 - 22.50
	22.50 <

Figure 3-14. Lower hemisphere equal-area stereonet (top) and corresponding rosette diagram (bottom right, n=58) for joints in Window 2 (Table 3-4).

Window 3

All the joints in Window 3 are analyzed together, as Units 6 through 11 did not contain enough joints on their own to define joint sets. Window 3 exhibited a total of 115 joints in four sets, with JS1 as the set with the highest number of joints observed (Table 3-5; Figure 3-15). Similar to previous windows, the average dip directions of the columnar joint sets are slightly rotated in reference to Windows 1 and 2, however average dip for all joint sets are almost identical to previous windows. Within Window 3, the dip directions of the columnar joint sets differ by 56° and 43°, indicating the columns in this window are more irregular in shape rather than perfect hexagons. Though most of the observed joints are within Unit 5, the full-window analysis of the joints in this window will likely influence the observed joint directions for columns in a specific unit. The overall P_{21} value of Window 3 is the lowest of all windows at 1 m/m^2, and both columnar and sub-horizontal joint sets have an average persistence on the low end at 1 m.

Table 3-5. Joint set properties in Window 3.

Unit	Joint Set	Average Dip	Average Dip Direction	Description	Number of joints in set	Average Persistence (m)	P_{21} Value (m/m^2)
5, 6, 7, 8, 9, 10, 11	1	83°	254°	Sub-vertical columnar joint, some are curved	49	1	1
	2	82°	310°		19		
	3	79°	029°		17		
	4	19°	-	Sub-horizontal joint, some are curved; ball-and-socket joints	9	1	

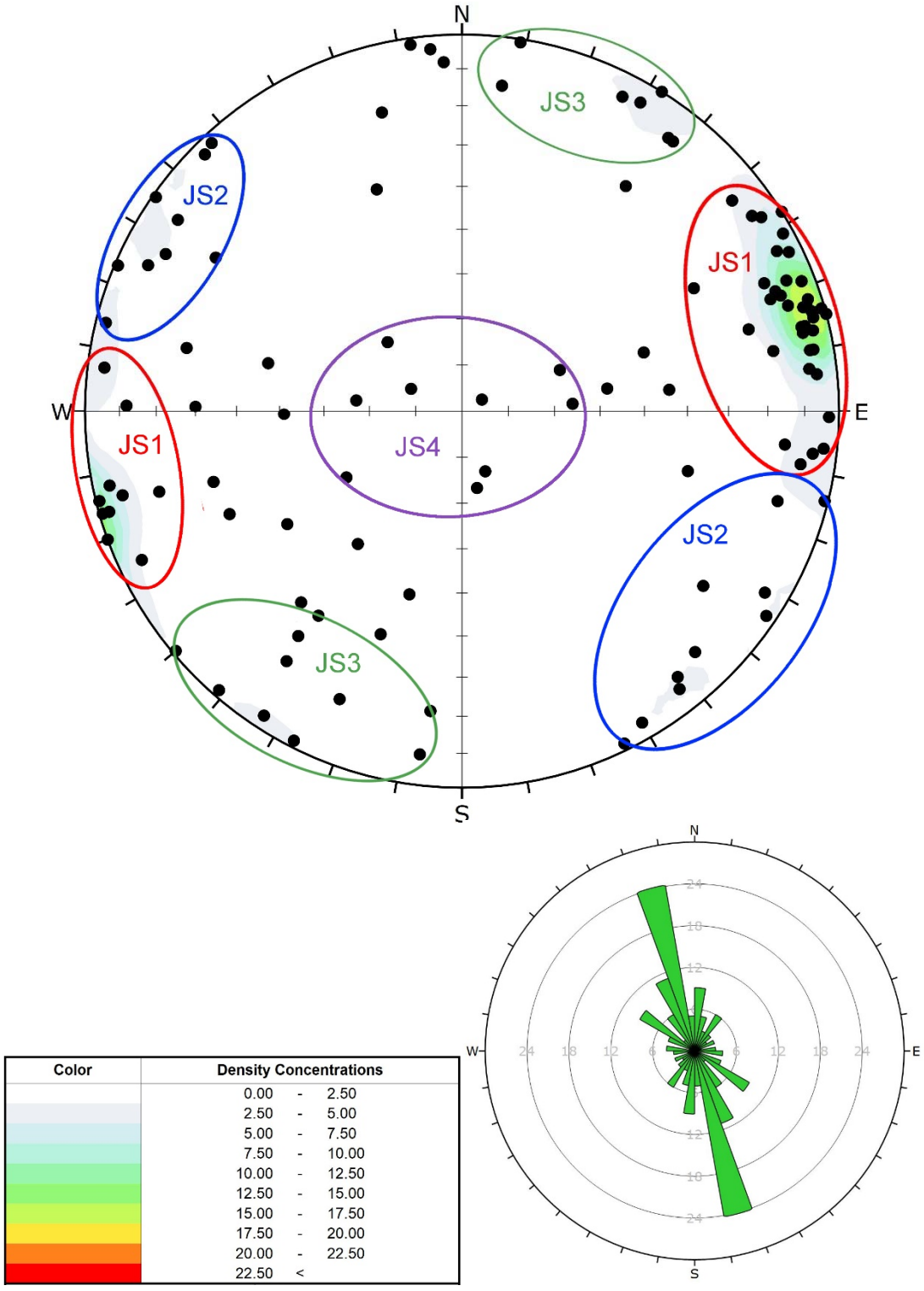

Figure 3-15. Lower hemisphere equal-area stereonet (top) and corresponding rosette diagram (bottom right, n=100) for joints in Window 3 (Table 3-5).

Window 4

A total of 63 joints in Window 4 were observed between Unit 13 (32 joints) and Unit 15 (31 joints) (Table 3-6) (Figure 3-16). As with previous windows, JS1, JS2 and JS3 are sub-vertical columnar jointing in both units. Average dip angle for each of these joint sets in Unit 13 are slightly closer to vertical than in other units, but for the sub-horizontal joint set, JS4, the average dip angle is much higher than in any other unit. JS1, JS2 and JS3 dip directions differ by 48° and 41°, meaning the columns are more of a regular hexagon in shape than Windows 1 and 3. The average persistence of sub-vertical joint sets in Unit 13 is higher than that of the sub-horizontal joint set, which is consistent with all other units with the exception of Unit 1. The P_{21} value of 2 for Unit 13 is the highest observed in all windows and units in the LIP1 slope, indicating this unit and Unit 5 (at least in the window ROI) contain the most visible joints.

The average dip angle for JS1, JS2 and JS3 in Unit 15 are all the same, and similar to Unit 13, exhibit a higher dip than most other units. The difference between dip directions is 76° and 46°, thereby creating irregular hexagonal columns. The average persistence of sub-vertical and sub-horizontal joint sets is high, and like previous units, JS1, JS2 and JS3 have a higher average persistence than JS4. JS4 in Unit 15 is quite variable, with a high average dip of 40°. The P_{21} value of Unit 15 is lower than that of Unit 13, leading to an overall P_{21} value of under 2 m/m^2.

The average dip directions for JS1 and JS3 in Units 13 and 15 are quite similar, but JS2 in Unit 15 is slightly rotated with respect to Unit 13. JS1 in both units contains the highest number of observed joints, indicating this orientation is most optimal for viewing on the LIP1 slope.

Table 3-6. Joint set properties in Window 4.

Unit	Joint Set	Average Dip	Average Dip Direction	Description	Number of joints in set	Average Persistence (m)	P_{21} Value (m/m^2)	
13	1	84°	243°	Sub-vertical columnar joint, some are curved	14	1	2	2
	2	86°	291°		3			
	3	83°	192°		7			
	4	31°	050°	Sub-horizontal joint, some are curved; ball-and-socket joints	8	0.7		
15	1	85°	245°	Sub-vertical columnar joint, some are curved	17	3	2	
	2	85°	123°		7			
	3	85°	199°		3			
	4	40°	018°	Sub-horizontal joint, some are curved; ball-and-socket joints	4	2		

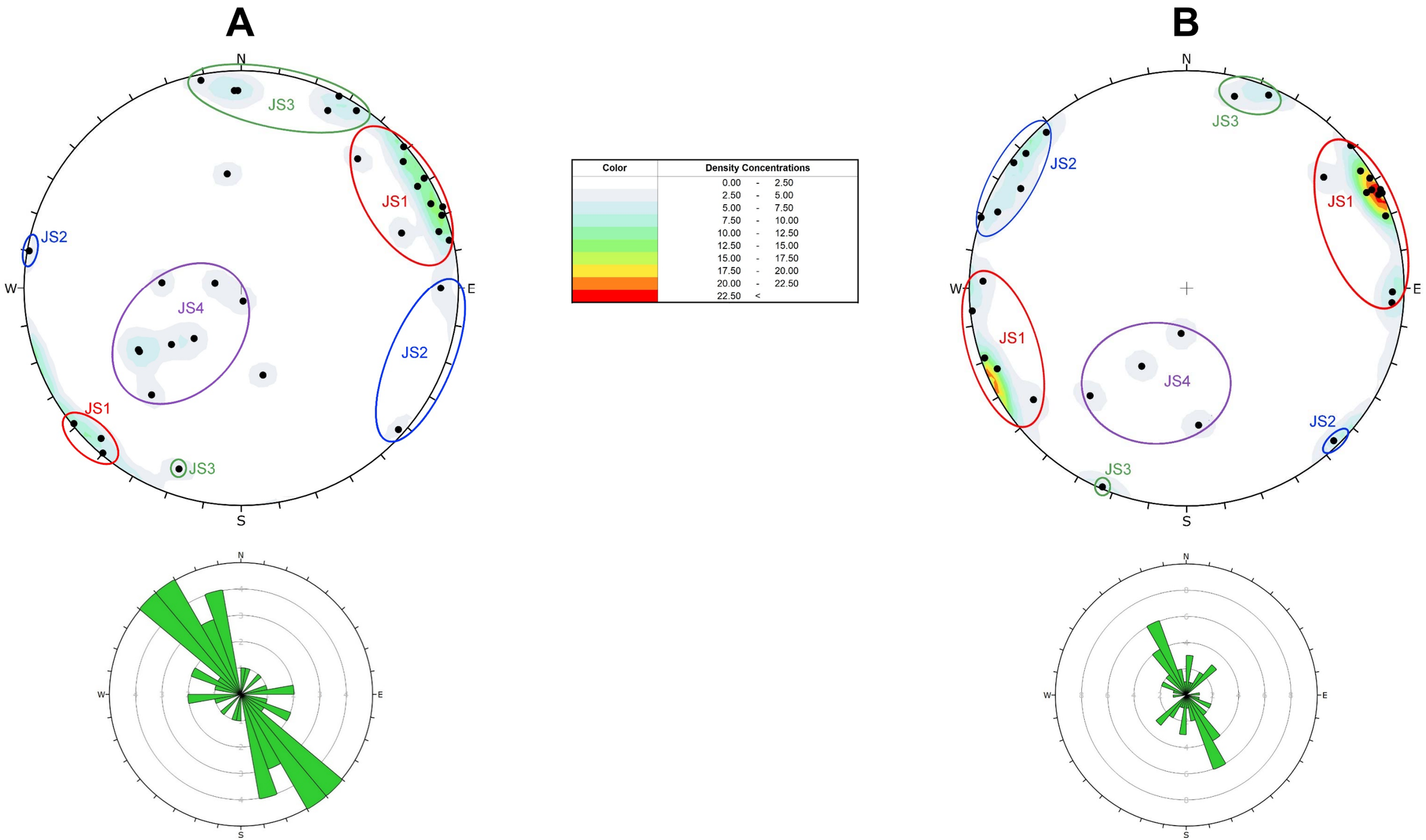

Figure 3-16. Lower hemisphere equal-area stereonet (top) and corresponding rosette diagram (bottom) for joints in Window 4 (Table 3-6). The stereonet and rosette diagram in A are for joints in Unit 13 (n=27), and Unit 15 joints (n=29) are in B.

Infrared Thermography

Several analyses were used to interpret a series of thermal images captured hourly at the LIP1 outcrop between 20:05 August 2, 2015 and 05:05 August 3, 2015. The hourly images were analyzed for the features visible at each time interval, and POI were used in each window to further characterize the temperatures throughout the survey. Contrast images were created from the hourly panoramas to determine what further characteristics are visible through the changes in temperature every hour. Finally, thermal profiles were taken through window thermal imagery to extract patterns from the thermal conductivity of the slope. Temperature scales are optimized for each image and graph to facilitate observations of outcrop features.

Hourly Imagery and Thermal Decay

An IRT survey of the cooling cycle (sunset to sunrise) of the LIP1 slope was carried out, and the results are presented in this section. Images taken of the slope at each hour were stitched together for panoramic thermal images of the entire slope at each survey interval. For example, the stitched thermal image at 20:05 on August 2, 2015 (Figure 3-17) shows the LIP1 slope at a single point in time, and highlights the difference in temperature of the vegetation (~24.0-25.2 °C) versus the rock (~25.0-30.5 °C), as well as the columnar jointing (~1-5 °C cooler than surrounding rock), division of units (paleosols between lava units are generally 1-2 °C cooler), and the effects of weathering (in some cases 1-2 °C warmer).

To further study the thermal response of the slope in a cooling cycle, representative POI were chosen within each of the four windows and their temperatures over the survey were graphed. Each POI was chosen to represent one of four distinguishing features on the LIP1 slope: the fresh surface of a different unit, an area of iron staining, an area with white alteration, or a joint. The POI chosen are listed in Table 3-7.

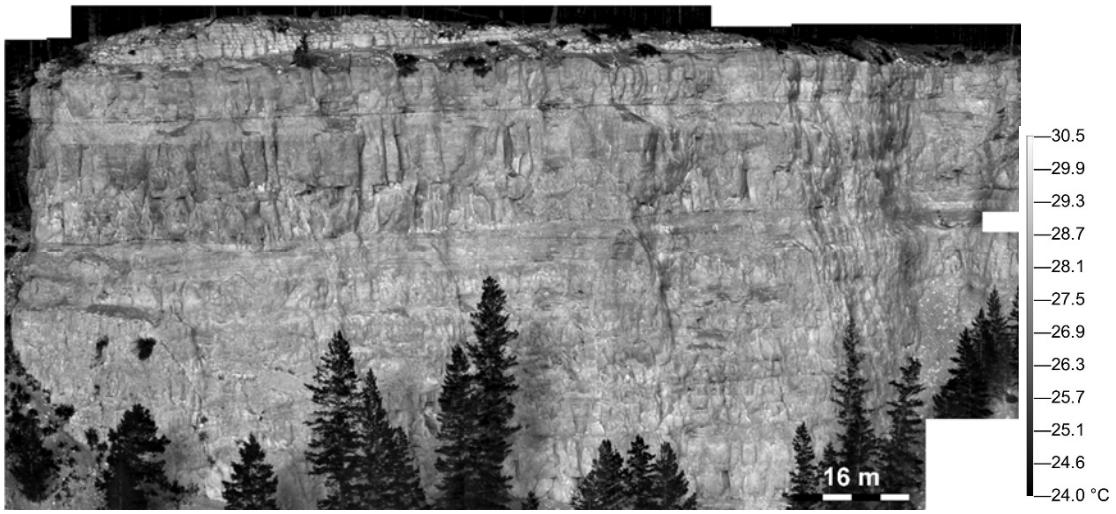

Figure 3-17. Thermal image of the outcrop on the eastern side of the canyon, taken from LIP1 at 20:05 on August 2, 2015, at the beginning of the survey, at approximately 300 m distance.

Table 3-7. POI chosen for the study of temperature decay in each window. The row and column values are the location of the POI on the thermal image of the window in pixels.

Window	POI	Row	Column	Unit	Purpose
1	1	100	217	1	Baseline, fresh area
	2	84	188	1	Iron staining
	3	128	232	2	Oxidized paleosol
	4	262	253	3	White alteration
	5	169	249	3	Baseline, fresh area
2	1	60	114	5	Baseline, fresh area
	2	175	54	5	White alteration
	3	43	174	5	Columnar joint
3	1	166	249	6	Oxidized paleosol
	2	27	376	5	Columnar joint
	3	288	71	7	Baseline, fresh area
4	1	52	166	13	White alteration
	2	157	176	15	Baseline, fresh area
	3	194	78	15	Corner of two joints

Several general observations can be made on the patterns of temperatures in the infrared image of Window 1 at 20:05 on August 2, 2015 (Figure 3-18), attributable to the variations in surface area for cooling, as well as colour. The uppermost lava flow in the

image is hotter than the lower flow (by 1-2 °C), possibly due to the darker colour of the upper flow (which absorbs more radiation during the day), or that it was the last to receive sunlight before dusk (it received solar radiation more recently). The rock units are hotter than the sediment (by 1-4 °C), as the sediment is composed of smaller particles and therefore cools much faster after sunset than the surrounding rock. Similarly, vegetation stands out in the image as cooler, by temperatures more than 1.5 °C lower than the soil. Structures in the lavas are easily observed due to their relative cooler thermal signatures with respect to those of rock blocks (1.2-1.5 °C cooler); both the horizontal and vertical structures seen in daylight are visible in the thermal images. This is because the joints are surfaces exposed to the air, and therefore cool to equilibrate with the air temperature. Also, joints and the blocks they create provide areas for shade, which leads to less solar radiation hitting the rock, thereby equating to a lower temperature.

The POI temperature curves for Window 1 (Figure 3-18) exhibit similar patterns of thermal decay, in that peaks and troughs for each curve are generally at the same times, however the curves do differ. POIs 3 and 5 have the most similar curves, with temperatures that do not vary more than 0.8 °C from each other, with an average difference of 0.2 °C. This is unexpected, as POI 3 is the oxidized surface of the Unit 2 paleosol, whereas POI 5 is the fresh surface of Unit 3, a lava flow. Paleosol and lava units, however, can be distinguished in the thermal imagery at most times during the survey, and are observed as different temperatures. POIs 1 and 2 are also consistently alike in temperature, with an average difference of 0.4 °C throughout the survey. They are both located within Unit 1, but POI 1 is a fresh surface, and POI 2 is comprised of an iron stained surface. POI 4 begins the survey at similar temperatures as POIs 3 and 5, but when the survey is terminated, POI 4 lies within a similar temperature range to POIs 1 and 2. POI 4 is a joint surface with white alteration, and the observed temperature curve indicates this point has a lower average slope than the others (-1.65 °C/hour as opposed to -1.70 to -1.85 °C/hour).

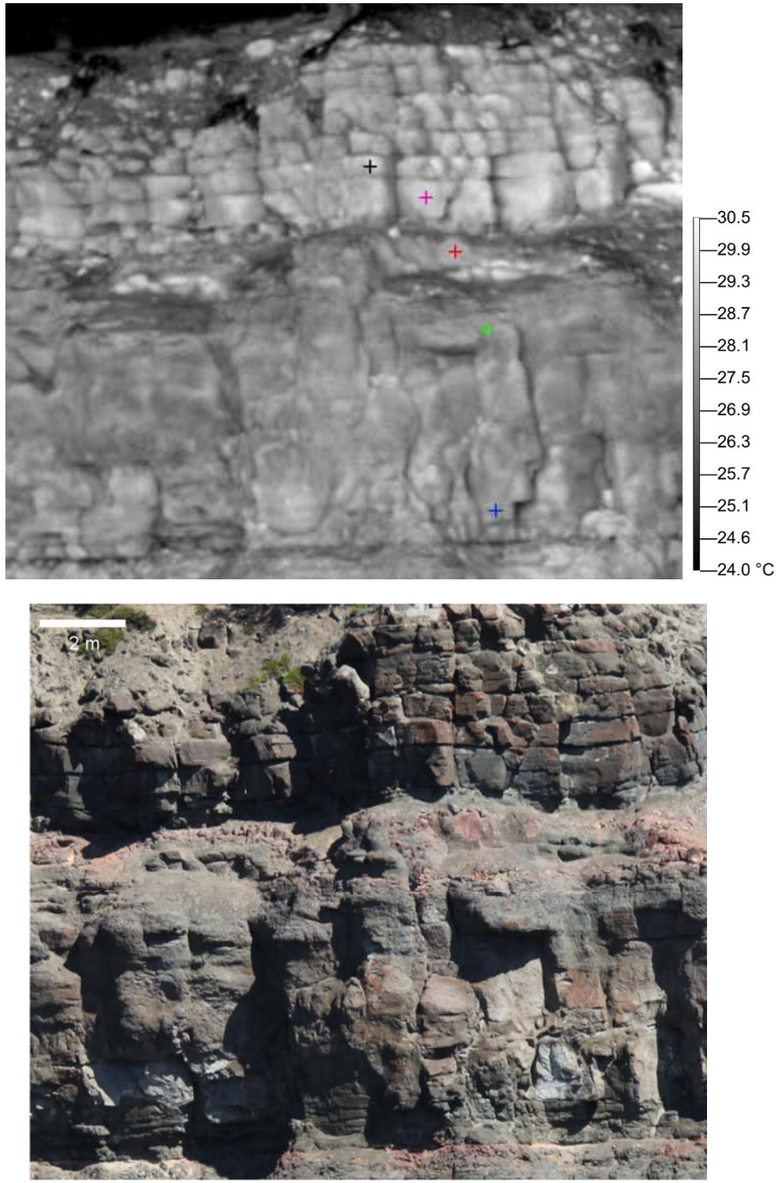

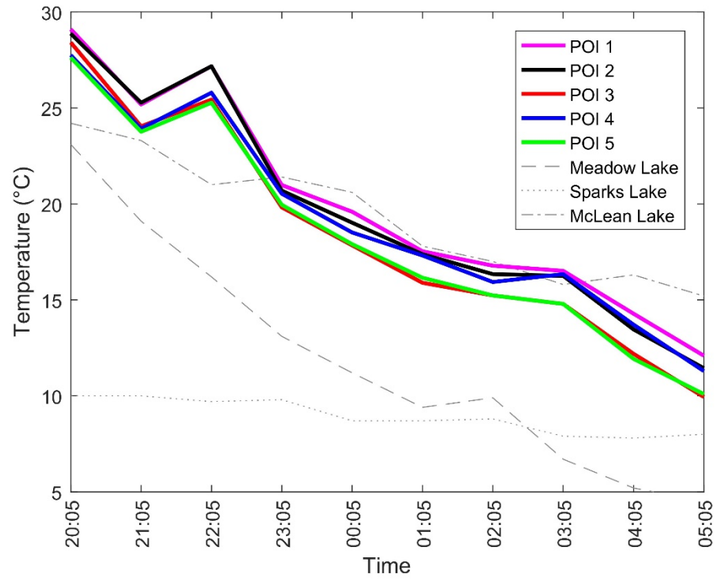

Figure 3-18. Infrared image of Window 1 at 20:05, August 2, 2015 (top left). POI are shown in similar colours as the temperature decay graph for POI on the slope (top right). A photograph of Window 1 (bottom left) and the interpretive line drawing (bottom right) are also shown for reference.

Temperatures at three weather stations were taken every hour on the hour, and are within the general area of the Chasm (Meadow Lake ~24 km NNE, McLean Lake ~49 km SSE, and Sparks Lake ~54 km ESE), so the temperature data is graphed against POI data to find a rough correlation to the air temperatures at the Chasm during the survey (Figure 3-18). The slopes of the datasets for Meadow, Sparks and McLean Lake are -1.86 °C/hour, -0.2 °C/hour, and -0.9 °C/hour, respectively. Meadow Lake is closest to the Chasm and exhibits a slope similar to those of the POIs, therefore this is the dataset which is thought to be most representative of the air temperatures at the Chasm. The only significant peak (02:05) in the Meadow Lake data does not correlate with a significant peak or trough in the POI curves. As the slopes between the two datasets are comparable, however, it is evident that air temperatures decreasing play a role in the thermal response of the slope, but transient changes in the overall air temperature trend do not affect the slope temperatures significantly.

The entirety of Window 2 at 20:05 on August 2, 2015 is relatively uniform in temperature (between ~26.8-28.8 °C), with the notable exceptions of the joints (~0.5-0.8 °C cooler)(Figure 3-19, top left image). This is due to the window consisting of a single unit, with no occurrences of soil or vegetation in the section, other than a small area at the top of the window (dark grey, ~0.2-0.8 °C cooler than rock). The more obvious (darker or more contrasting) joints are cooler (by up to 1.5 °C), due to a larger opening between joint walls, allowing for more exposure to air and faster cooling than the surrounding areas. These joints may also have been in the shade for the latter part of the day, which would reduce the amount of solar heating they received, thereby producing a cooler thermal signature in the imagery.

The infrared image of Window 2 at 23:05 on August 2, 2015 (Figure 3-19, top middle image), however, shows different characteristics. As much of the slope has further equilibrated with air temperature several hours after sunset, the joints are less apparent, though still visible (~0.2-0.5 °C cooler). Warmer spots on the slope (white, ~0.2-1 °c warmer), however, roughly correlate with areas which exhibit higher amounts of surface alteration, i.e. iron staining and white alteration. This may be that these areas have a favourable aspect with respect to the afternoon/evening sunlight, or that alteration is a factor for thermal conduction on the slope.

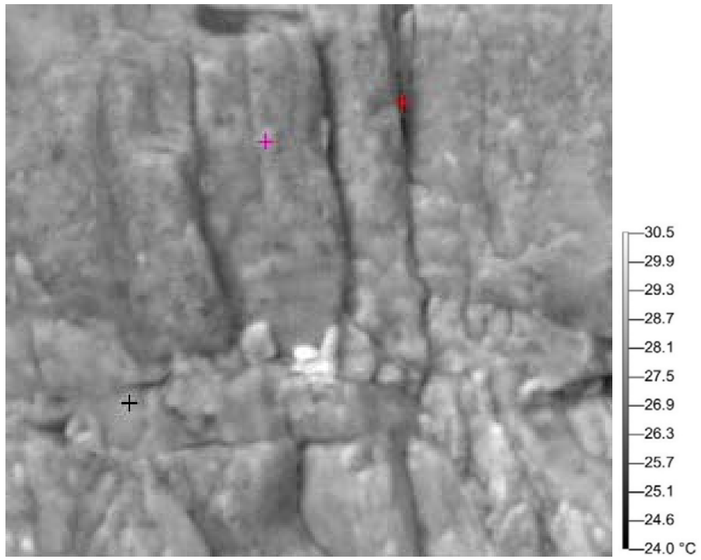

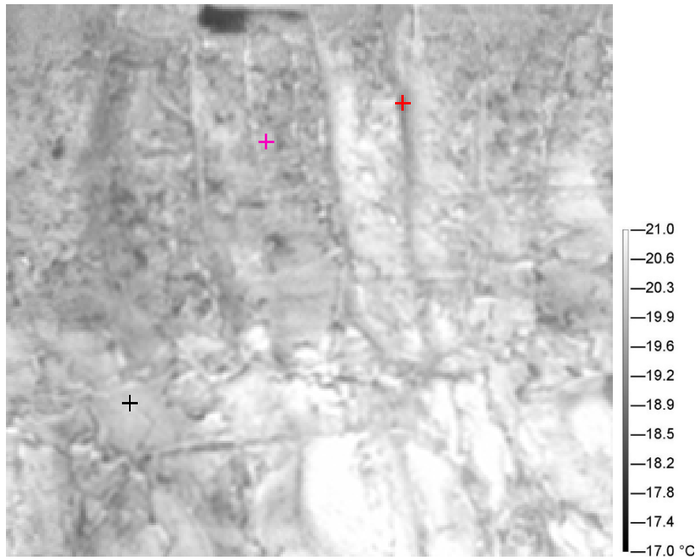

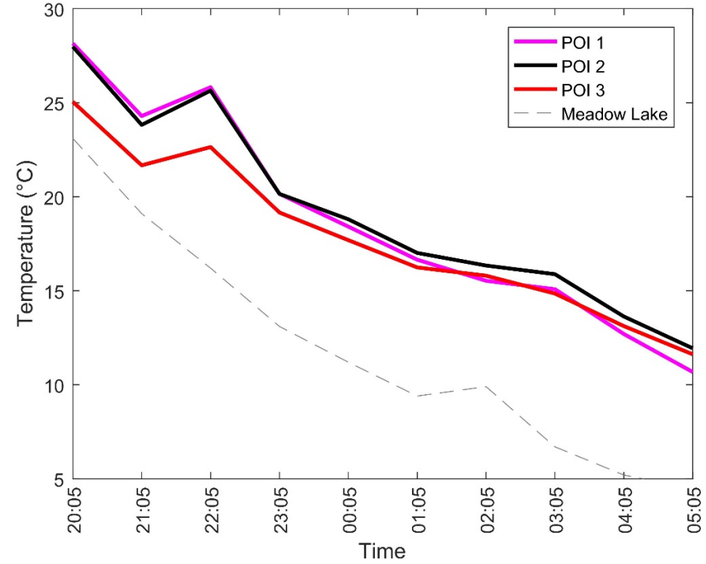

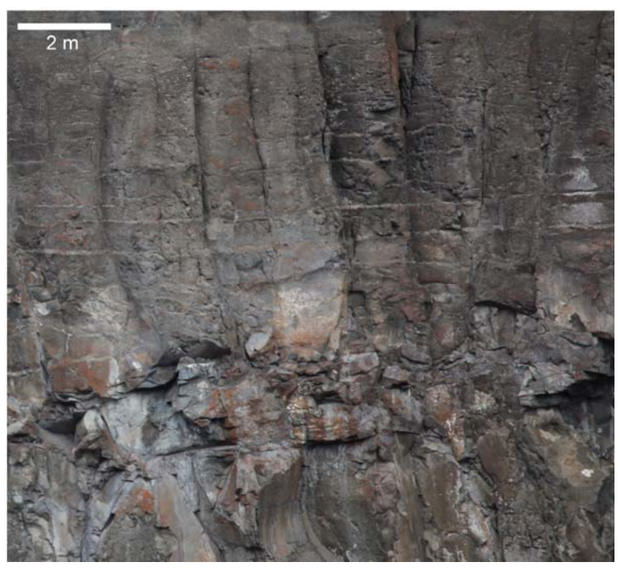

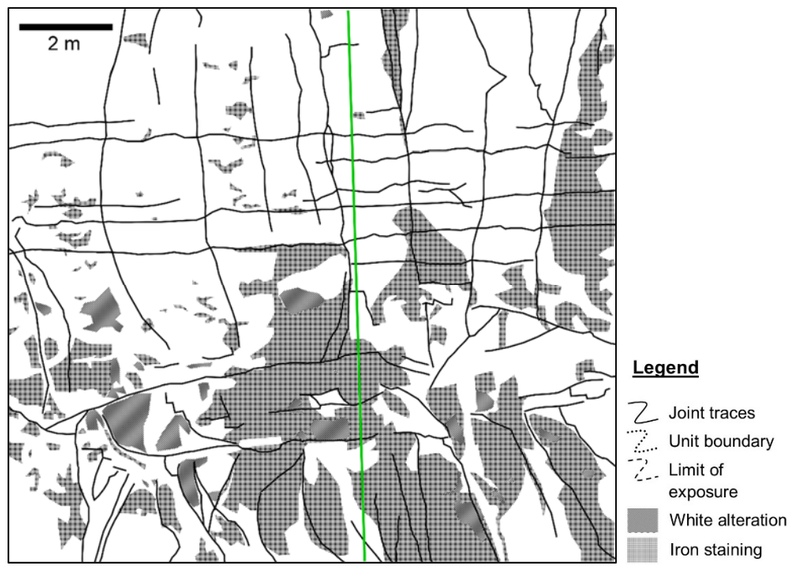

Figure 3-19. Infrared image of Window 2 at 20:05 (top left) and 23:05 (top middle), August 2, 2015. POI are shown in similar colours as the temperature decay graph for POI on the slope (top right). A photograph of Window 2 (bottom left) and the interpretive line drawing (bottom right) are also shown for reference.

The POI temperature decay curves for the three points in Window 2 show several characteristics (Figure 3-19, top right image). All POI are located in Unit 5, but POI 1 is a fresh surface of the lava, POI 2 lies on a joint surface exhibiting white alteration, and POI 3 is in a columnar joint. POI 1 and 2 curves are comparable at the beginning of the survey, but start to diverge at 23:05 with POI 1 decreasing in temperature faster than POI 2. At the end of the survey, POI 1 and 2 differ by 1.2 °C. The fresh lava therefore cools more quickly than the area with white alteration, with slopes of -1.74 °C/hour and -1.61 °C/hour, respectively. The slope of POI 3, however is 1.35 °C/hour, indicating the point inside the columnar joint cooled slowest. POI 3 began the survey approximately 3 °C below POIs 1 and 2, and at dawn was comparable to POI 2. As the columnar joint was already a lower temperature at dusk, it would follow that it would be slower to equilibrate with air temperature because the difference between the two was not as large.

At 20:05 on August 2, 2015 (Figure 3-20, top left), Window 3 exhibits minor variation between units (0-4 °C) and within units (0-5 °C), and most contrasting temperatures can be attributed to vegetated or soil-covered regions of the slope (1-6 °C cooler). The boundary between Units 5 and 6 is visible in this image (0.5-3.5 °C cooler than surrounding rock), though the unit boundary between Units 6 and 7 is less clear (0-0.2 °C difference). In the thermal image at 03:05 on August 3, 2015 (Figure 3-20, top middle), however, the unit divisions are more obvious, due to the presence of cooler areas (~0.5-1.5 °C cooler) along the undulating boundaries. These areas with lower temperature correlate to the paleosols present between lava flows, which are highly oxidized, vesicular, and in most cases, unconsolidated sediments. In this image, however, joints are less visible due to negligible differences in temperature (0-0.2 °C), as the rock face has reached more of an equilibrium over time.

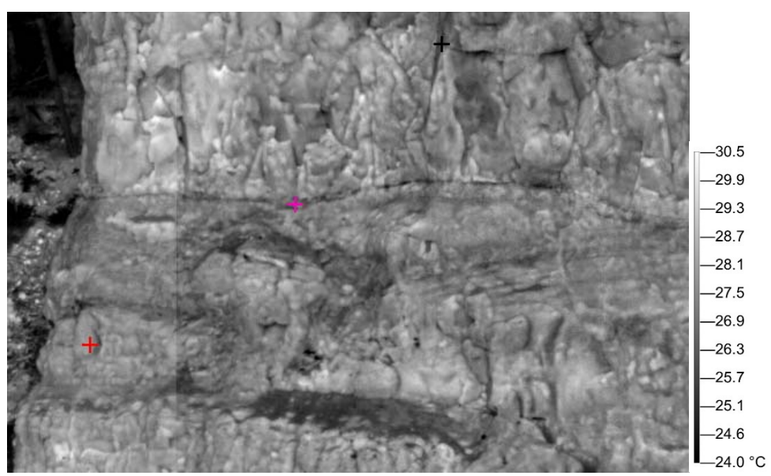

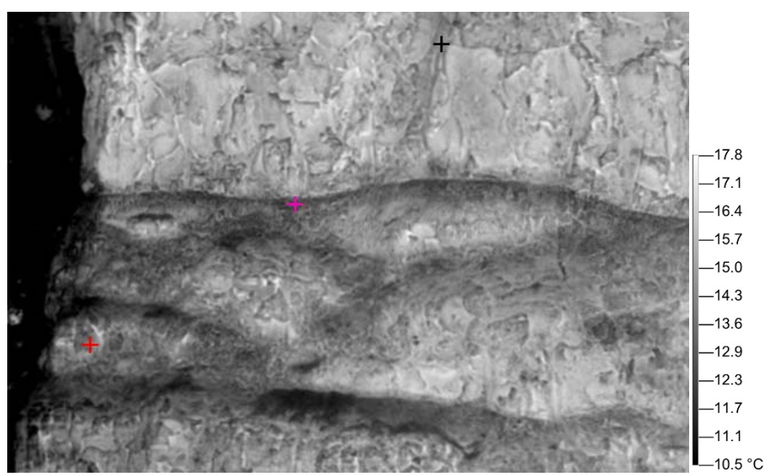

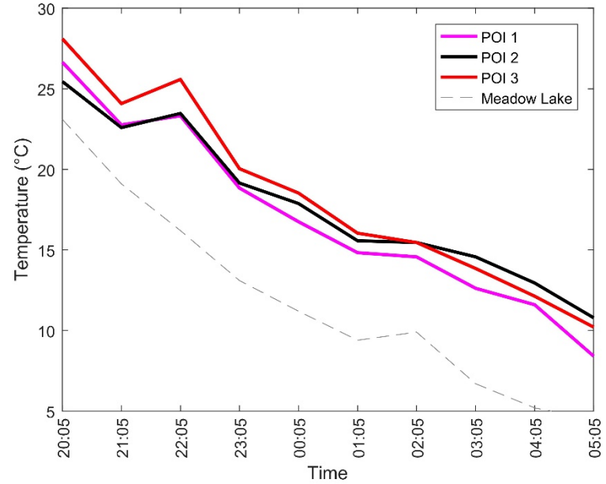

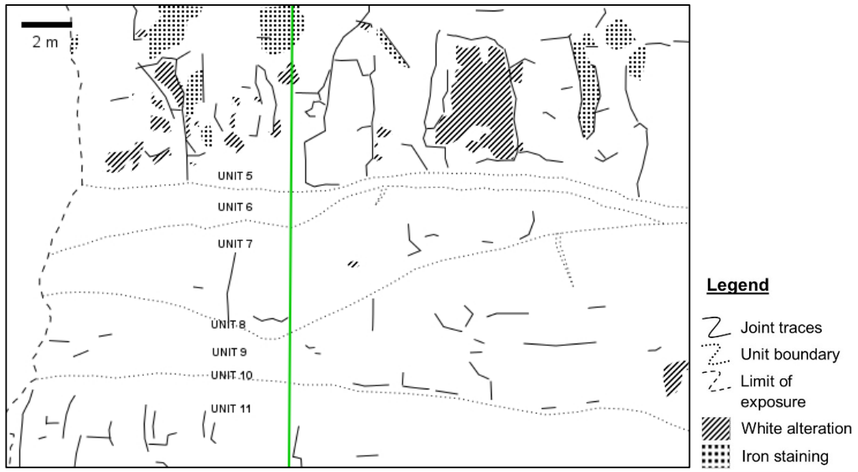

Figure 3-20. Infrared image of Window 3 at 20:05 (top left) and 03:05 (top middle) on August 2 and August 3, 2015, respectively. POI are shown in similar colours as the temperature decay graph for POI on the slope (top right). A photograph of Window 3 (bottom left) and the interpretive line drawing (bottom right) are also shown for reference. The line visible in the top image is a consequence of the stitching of the panorama, and does not depict a major feature in the rock face.

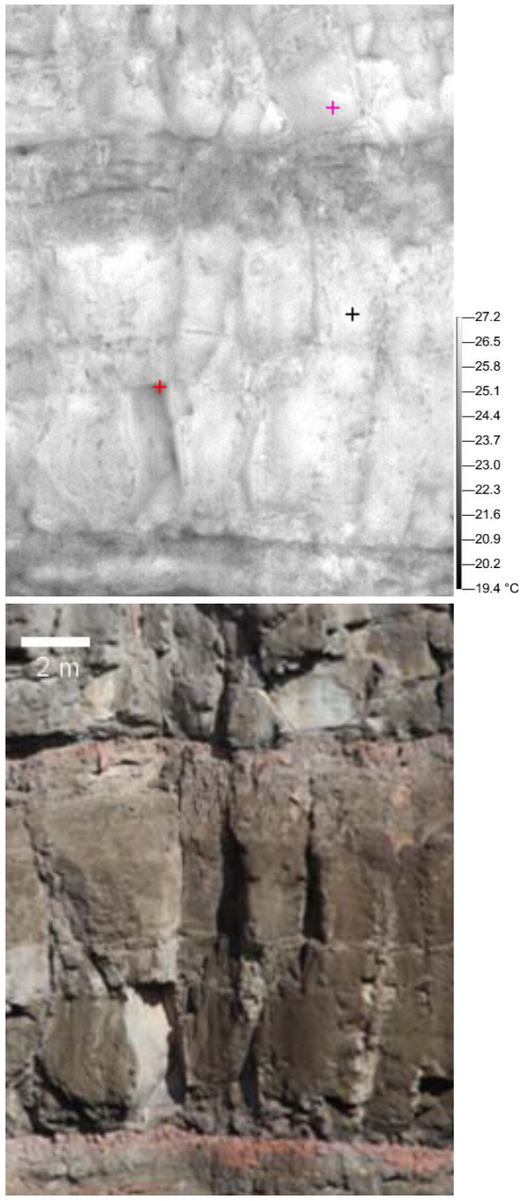

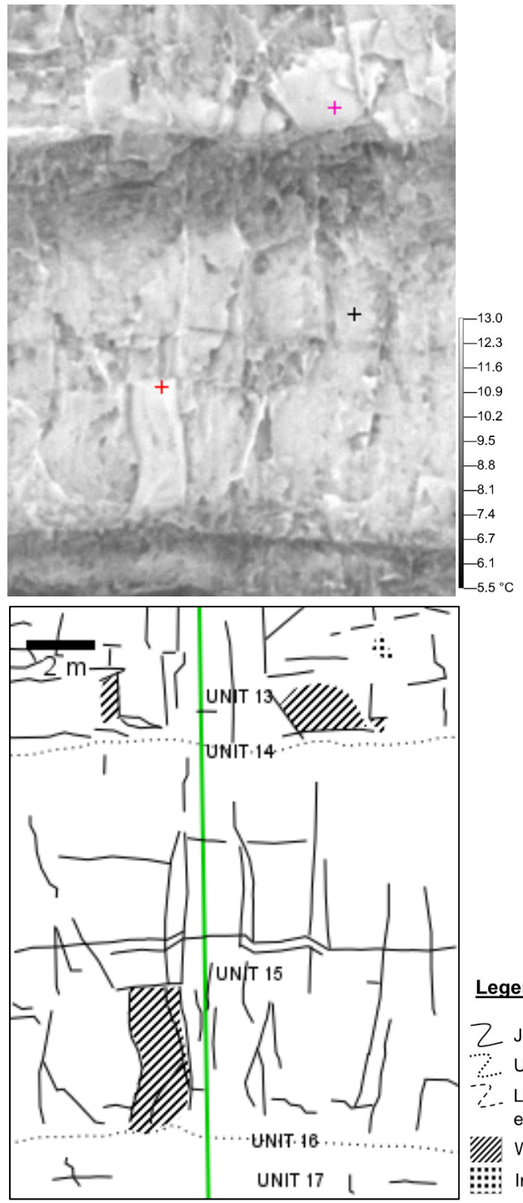

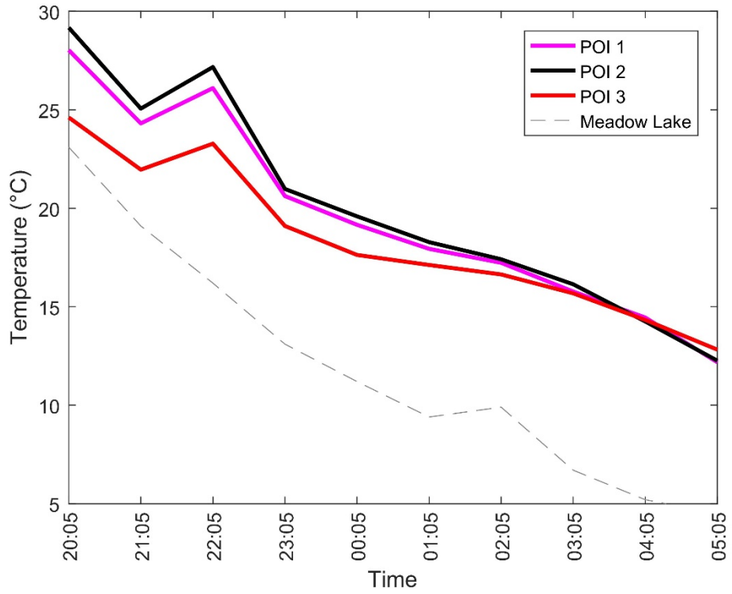

Figure 3-21. Infrared images of Window 4 at 22:05 (top left) and 05:05 (top middle), August 2 and August 3, 2015, respectively. POI are shown in similar colours as the temperature decay graph for POI on the slope (top right). A photograph of Window 4 (bottom left) and the interpretive line drawing (bottom right) are also shown for reference.

POIs in Window 3 exhibit temperature curves which are non-parallel, and the points represent a variety of features (Figure 3-20, top right image). POI 1, a point within the oxidized paleosol of Unit 6, has consistently lower temperatures than the other two points following 23:05 (between 0.3 °C and 2.2 °C), but before that is most like POI 2, with an average difference in temperature of 0.5 °C. POI 2 is inside a columnar joint, and similar to the columnar joint in Window 2, is characterized by the lowest slope (-1.46 °C/hour). POI 3, the baseline point for a fresh surface of the lava of Unit 7, has the highest temperatures throughout most of the survey, however the slope for POI 1 and 3 are similar (-1.82 °C/hour and -1.79 °C/hour, respectively).

In the thermal image of Window 4 at 22:05 on August 2, 2015 (Figure 3-21, top left), joints are visible, though not obvious (0.4-1.8 °C cooler), divisions between units are observed with cooler areas (0.6-4.9 °C cooler), and there is little variation of temperature within the units themselves (<2.1 °C). In contrast, within the same window at 05:05 on August 3, 2015 (Figure 3-21, top middle) the joints are difficult to discern (0-2 °C cooler), and in many places higher temperatures (12.5-13.0 °C) roughly correlate to altered areas on the slope. This indicates alteration may influence the temperatures of the slope at certain times.

The POI curves for Window 4 began the survey with temperatures several degrees different from each other (POI 1, 28.0 °C, POI 2, 29.2 °C, and POI 3, 24.6 °C)(Figure 3-21, top right image). As the survey progressed the difference between POI temperatures decreased, and the curves converged at 03:05, continuing at approximately the same temperature for the remainder of the survey (average difference in temperature was 0.4 °C). POI 1, an area with white alteration, and POI 2, a baseline point for a fresh surface of the Unit 15 lava, are most similar in temperature throughout the survey, with differences in temperatures between 0.1 °C (04:05 and 05:05) and 1.1 °C (22:05). POI 3, a corner between a columnar a sub-horizontal joint, begins the survey with the lowest temperature (by 3.4 °C), as it was likely shaded for much of the latter part of the day. The slope of POI 1 is -1.58 °C/hour, similar to that of areas of white alteration in previous windows, and POI 2 and POI 3 are also quite similar to the slope range of previous lavas and columnar jointing, with a slope of -1.69 °C/hour and -1.18 °C/hour, respectively.

If POIs from all the windows are plotted on the same graph (Figure 3-22), the same patterns are observed in most of the curves. A dip in the trend is found at 21:05, with a subsequent jump in temperature (between 0.5-2.1 °C) at all points, by an average of 1.5 °C. This increase in temperature is likely due to the air temperature cooling rapidly between 20:05 and 22:05 after the sun has set. As the rock cools to equilibrate, the surface of the rock cools first (hence an initial drop in temperature), and subsequently starts cooling beneath the surface by radiating heat (hence an apparent increase in temperature). Once the initial 'shock' of the air temperature drop has occurred, and the rock has already started to radiate its latent heat, the curves flatten to reflect a more consistent rate of cooling.

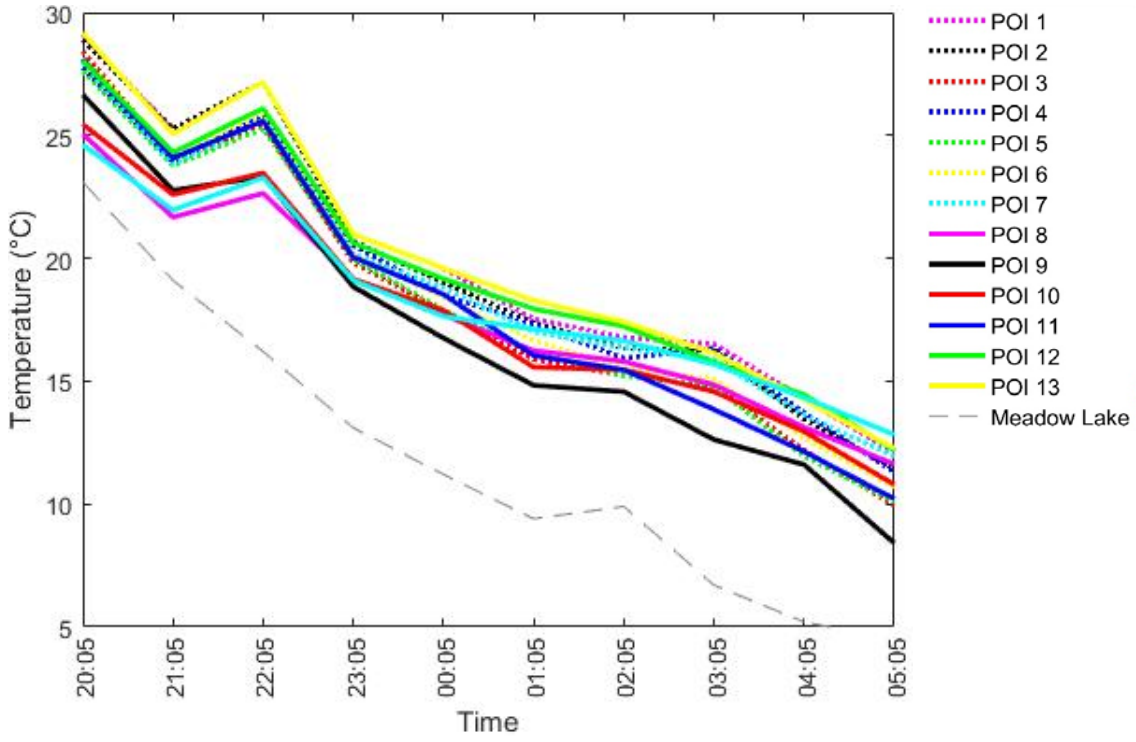

Figure 3-22. POI temperature curves for POIs from all four windows.

Within each of the four windows, it is apparent that certain characteristics are more likely to be visible in the infrared imagery within particular time frames, though the optimal time frame for observing all features of the slope differs between windows. The full list of window observations for each hourly image is found in Table 3-8, with check marks indicating when the features are visible in the image, a blank indicating the features are indistinguishable, and a dash where the features do not occur in the

window. A check mark was only assigned when the feature was clearly visible, had a different colour than its immediate surroundings (and therefore different temperature), and could be correlated to the features mapped in the interpretive line drawing of the windows.

In all windows, the optimal time for differentiating joints well enough to map was between 20:05 and 21:05, with Windows 3 and 4 having visible joints in the 22:05 images as well. The likely cause of this time constraint is that solar radiation and aspect have the most effect during the day and just after sunset. So, as the cooling cycle continues throughout the night, the cooled shadows and heated faces have come closer to equilibrating with their surroundings. The boundaries between units in Windows 1, 3, and 4 were generally more noticeable between 22:05 and 05:05, which is possibly due to the same reason as the joints having more definition in the earlier hours after sunset. As the rock face equilibrates more with its surroundings, the temperatures are likely more influenced by the properties of the rock itself and therefore differences in vesicularity, mineralogy, and textures become the dominant forces behind temperature variance in the thermal imagery. As each of the three windows with multiple units exhibits paleosols between each lava flow, the differences between unit characteristics are significant enough to be recorded in the infrared. The soil (Windows 1, 2 and 3) and vegetation (Windows 1 and 3) components in each window were generally distinguishable throughout the entire survey, indicating there is a consistent, perceptible difference in temperature between soil, vegetation and rock. There are only two images where alteration roughly correlates with higher temperatures: 22:05 in Window 2 and 05:05 in Window 4. As a result, alteration is not thought to play a major role in the temperature changes of the slope over time.

Table 3-8. Characteristics visible in the hourly thermal imagery from 20:05 August 2, 2015 to 05:05 August 3, 2015 for each window. A check mark denotes the features are easily distinguished from surroundings, a blank space indicates the features are not easily seen, and a dash is used when those features do not occur in the window at all.

Window	Time	Columnar Joints	Horizontal Joints	Units	Soil	Vegetation	Alteration
1	20:05	✓	✓	✓	✓	✓	
	21:05	✓	✓	✓	✓	✓	
	22:05			✓	✓	✓	
	23:05		✓	✓	✓	✓	
	00:05	✓	✓	✓	✓	✓	
	01:05		✓	✓	✓		
	02:05		✓	✓	✓		
	03:05		✓	✓	✓	✓	
	04:05		✓	✓	✓		
	05:05		✓	✓	✓	✓	
2	20:05	✓		-	✓	-	
	21:05	✓		-	✓	-	
	22:05	✓		-	✓	-	✓
	23:05	✓		-	✓	-	
	00:05	✓		-	✓	-	
	01:05	✓		-	✓	-	
	02:05	✓		-	✓	-	
	03:05	✓		-	✓	-	
	04:05	✓		-	✓	-	
	05:05	✓		-	✓	-	
3	20:05	✓	✓		✓	✓	
	21:05	✓	✓		✓	✓	
	22:05	✓	✓	✓	✓	✓	
	23:05			✓	✓	✓	
	00:05			✓	✓	✓	
	01:05			✓	✓	✓	
	02:05			✓	✓	✓	
	03:05			✓	✓	✓	
	04:05			✓	✓	✓	
	05:05			✓	✓	✓	
4	20:05	✓	✓		-	-	
	21:05	✓	✓		-	-	
	22:05	✓	✓	✓	-	-	
	23:05			✓	-	-	
	00:05			✓	-	-	
	01:05			✓	-	-	
	02:05			✓	-	-	
	03:05			✓	-	-	
	04:05			✓	-	-	
	05:05			✓	-	-	✓

Temperature Contrast Imagery

To better understand how the temperatures of the rock change during the cooling cycle, temperature contrast images were constructed to analyze the changing patterns of thermal radiation. Each contrast image is the result of subtracting an image from the previous image. For example, a contrast image A was created by subtracting the temperatures in the image at time 2 from the temperatures in the image at time 1. The temperature scale for contrast image A is therefore the difference in temperatures between time 1 and time 2. Similarly, a contrast image B was created by subtracting the thermal image at time 3 from the thermal image at time 2, and so on. Contrast image sets were generated for all windows on the LIP1 slope.

The temperature change between 20:05 and 21:05 in Window 1 (Figure 3-23, top left) shows the greatest temperature difference in the soils and vegetation (-4 to -6.2 °C), and the least temperature change in the joints (-1.5 to -3.2 °C), as might be expected. The temperature decreased the most in the loose soils because of the smaller particles, which cool faster than large bodies of rock due to the greater surface area to size ratio. The temperature decreased the least in the joints likely because they received little solar radiation during the day if they were shaded, therefore the sun setting made only a small difference. Sub-horizontal and vertical joints are discernable, but both units are relatively similar in contrast (-3 to -5 °C) and the boundary between them is not easily detectable.

The second temperature contrast image in Figure 3-23 (top right) results from the temperature contrast between 21:05 and 22:05 in Window 1, wherein the loose soil and vegetation in the window continue to show the greatest decrease in temperature (+0.5 to -1.5 °C), and the rock shows a slight increase in temperature (+1-3.5 °). Most of the temperatures, in fact, have risen between these time images. In this hour, the sun had set, and the air temperatures likely fell quickly. The slope, however, takes longer to cool and equilibrate, therefore as it equilibrates, its surfaces are ‘warmed’ by the temperatures of the inner rock, giving an appearance of warming. This is corroborated by the temperature patterns observed in Figure 3-22. The difference in warming magnitude between Unit 1 (+1.5-3.5 °C) and Unit 3 (+0.5-3 °C) allows for observation of the unit boundaries in this image, and like the 20:05-21:05 image, the temperature difference between soils (+0.5 to -1.5 °C), vegetation (-1.5 °C), and columnar and sub-

horizontal jointing (~0.5 °C difference in contrast between joints and rock) are detectable.

The top left image in Figure 3-24 is the temperature change between 21:05 and 22:05 in Window 2, and displays the slight increase in temperatures in this hour (0-2.5 °C), similar to that of Window 1. The greatest warming (1.5-2.5 °C) appears to occur in areas where there are larger amounts of surface alteration. The alteration may, due to its lighter colour, absorb less solar radiation than unaltered lava. It could also have an effect on the conduction of the thermal radiation, such as making the surface of the rock more porous, and therefore allowing heat to escape more easily than in unaltered areas, causing the appearance of warming.

Temperature changes between 22:05 and 23:05 in Window 2 are shown in Figure 3-24 (top right). The largest amount of cooling in this time frame, which was in some areas greater than a 9 °C decrease in temperature, occurred in the joints as well as areas with alteration. Again, the joints would be expected to cool faster due to the greater surface area exposed to lower air temperatures. This is why a greater temperature decrease (by ~2-3 °C) is observed in the lower portions of the window, the entabulature zone of the flow. The entabulature zone is more heavily jointed and is comprised of smaller blocks than the colonnade, thereby allowing faster cooling. The areas with alteration, however, also cooled more quickly than surrounding rock (by ~1-3 °C). This observation is likely caused by the higher temperature observed during the last hour (top left image, Figure 3-24), causing an apparent larger change in temperature over this hour as the slope cooled.

The image depicting the change in temperature between 22:05 and 23:05 for Window 3 (Figure 3-25, top left) consists of three lava flow units, easily distinguished by the significant difference in temperature contrast compared to the two paleosol units. The lava units are characterized by the largest drops in temperature over the hour with some areas (mostly within joints) marking a 10 °C change, whereas paleosol temperatures only decrease by between 1-5 °C. The lavas are likely still cooling rapidly from the previous day's absorbed solar radiation, whereas the paleosols are primarily loose material, and have already cooled to a closer temperature to the surrounding air.

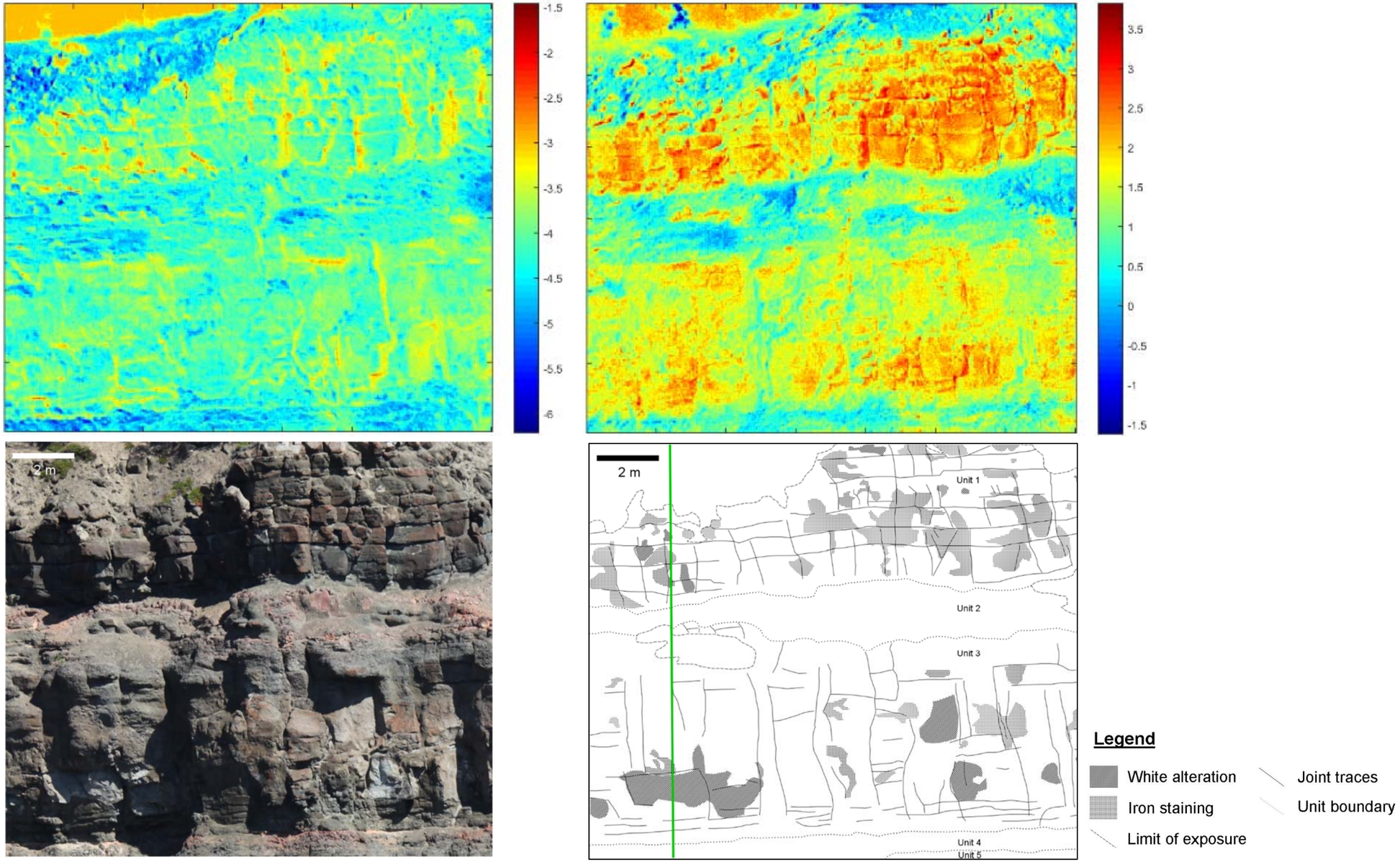

Figure 3-23. Thermal contrast images of Window 1 for 20:05-21:05 (top left) and 21:05-22:05 (top right); temperature scales are in degrees Celsius. The bottom left image is an RGB photograph of Window 1, and the interpretive line drawing is shown on the bottom right.

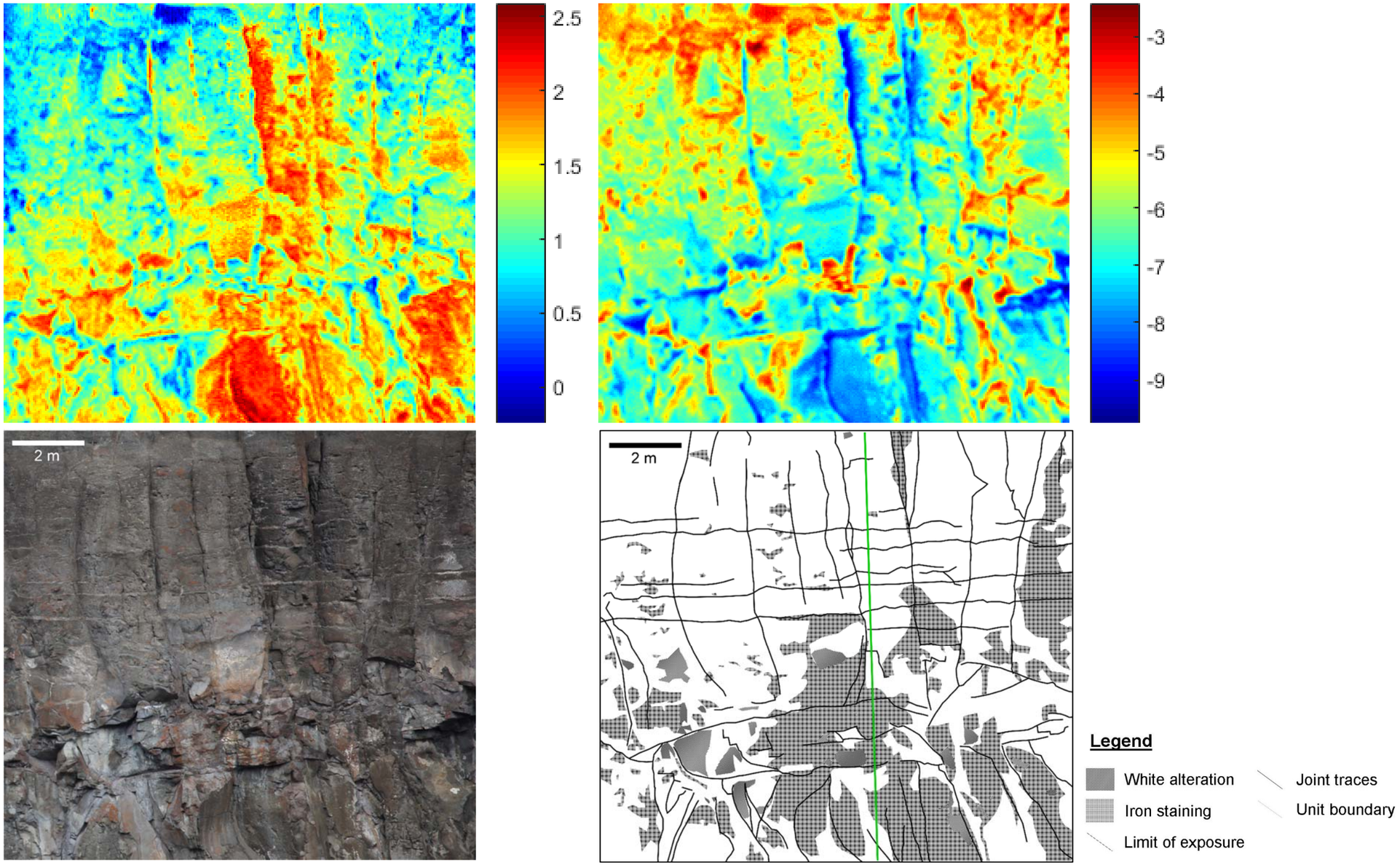

Figure 3-24. Thermal contrast images of Window 2 for 21:05-22:05 (top left) and 22:05-23:05 (top right); temperature scales are in degrees Celsius. The bottom left image is an RGB photograph of Window 2, and the interpretive line drawing is shown on the bottom right.

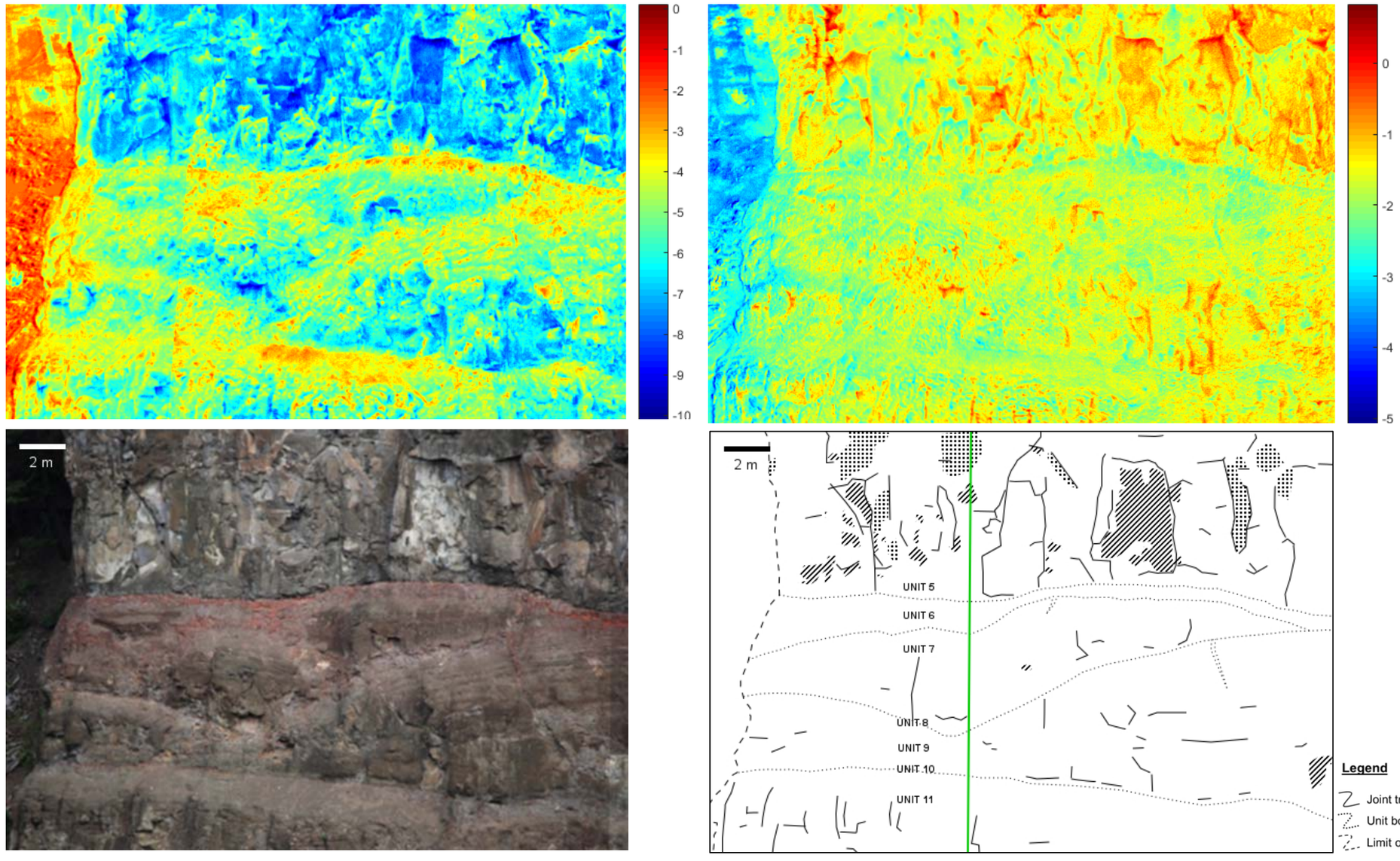

Figure 3-25. Thermal contrast images of Window 3 for 22:05-23:05 (top left) and 01:05-02:05 (top right); temperature scales are in degrees Celsius. The bottom left image is an RGB photograph of Window 3, and the interpretive line drawing is shown on the bottom right.

The change in temperature from 01:05-02:05 in Window 3 (Figure 3-25, top right) over the slope is relatively uniform between and within units, with an average temperature drop between 1-3 °C. The units of the slope, therefore, have likely reached equilibrium with regards to their relative temperatures; further images in the survey record similar observations. The areas on the slope with little temperature change at all (red areas with a 0 °C temperature change) roughly coincide with altered portions of the units, which possibly indicates alteration plays a role in the cooling cycle of a rock face. These areas, however, are also where blocks have fallen from the slope leaving large overhangs, which may be a contributing factor to the temperature patterns as well.

From 21:05 to 22:05 in Window 4 (Figure 3-26, top left), the majority of the lava units have gotten 0.5-2.5 °C warmer, as was seen in previous windows in this time period just after sunset. Jointing (~0.5 °C difference) and unit boundaries (~1-2 °C difference) are easily differentiated from their surroundings, as the paleosols are the main areas where the only decrease in temperature over the hour was observed (+0.5 to -0.5 °C).

The image from 01:05-02:05 of Window 4 (Figure 3-26, top right) shows the greatest temperature drop continues to occur in the paleosol units (~-1 to -2 °C). The lava units, however, are observed to have temperature changes closer to the paleosols than in the 21:05-22:05 image, with only a difference in temperature contrast of approximately 1 °C. The areas in the image which show no change to a slight increase in temperature are, similar to Window 3, areas with relatively higher amounts of alteration, and areas with significant overhangs (0-1 °C difference).

As all features were not always discernible in the hourly thermal imagery, it would follow that the same would be observed in the thermal contrast imagery since the contrast images are a product of the hourly imagery. Using the same criteria for check mark and blank designations as the hourly thermal imagery, the results are shown in Table 3-9.

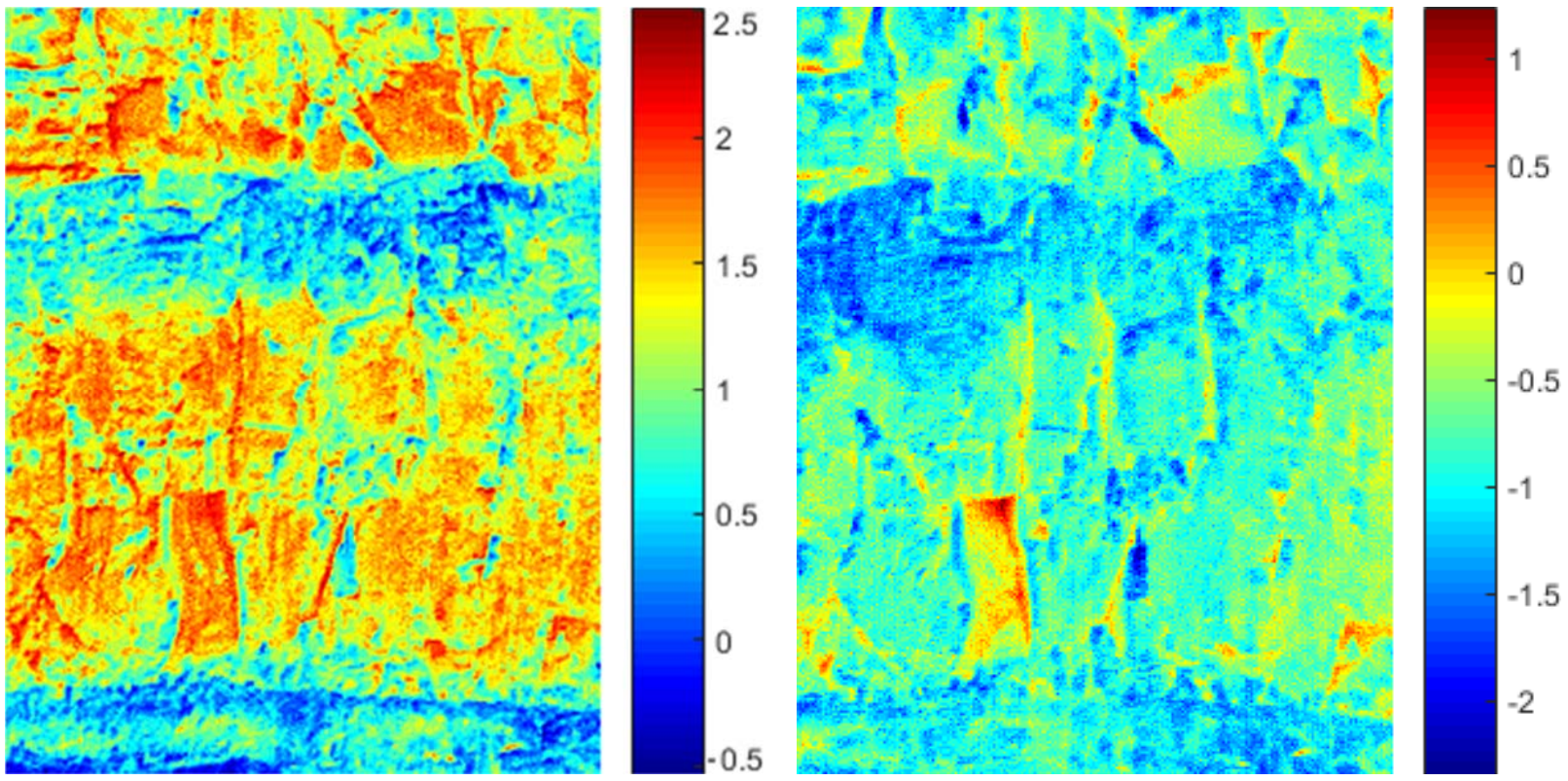

Figure 3-26. Thermal contrast images of Window 4 for 21:05-22:05 (top left) and 01:05-02:05 (top right); temperature scales are in degrees Celsius. The bottom left image is an RGB photograph of Window 4, and the interpretive line drawing is shown on the bottom right.

It was determined that for all windows, fewer rock face characteristics were observed in the contrast images in the latter portion of the cooling cycle, and in some cases there were no discernable features at all (Windows 1, 3, and 4). In Windows 1, 3, and 4, it was found that in general, when columnar jointing could be detected, horizontal jointing was visible as well. In Window 2, however, columnar jointing was perceivable throughout the majority of the survey, but sub-horizontal jointing was only found detectable in the beginning (20:05-21:05) and middle (01:05-02:05) of the survey. The sub-horizontal jointing in Window 2 is less persistent than the columnar jointing, which may explain the relative ease of identifying columnar over sub-horizontal jointing. Unit boundaries were generally observed more easily in the beginning to middle of the survey for all applicable windows (Windows 1, 3, and 4), though for Windows 1 and 3 the differentiation of units was only intermittently possible. As the cooling cycle progressed, all units in the slope became closer in temperature to reaching an equilibrium with each other, thereby obscuring unit boundaries. Soil and vegetation, with the exception of the latter portion of the survey, were generally observed throughout the range of images. In Window 2 the soil was rarely differentiated from surrounding rock, but there is only a very small area with soil in the region of interest, so a determination of the actual difference between soil and rock observability in this window is difficult.

A major difference between the hourly imagery and temperature contrast sets, however, is that areas with alteration on the slope are more easily differentiated from the surrounding rock using thermal contrast. In Windows 2, 3, and 4, temperature patterns (in some cases the areas in the image with the greatest rise in temperature, and in others the areas in the image with the greatest decrease in temperature) are roughly correlated to areas of alteration in several images, though there is no clear pattern of times at which it is optimal to view alteration in the survey. This likely indicates that the correlation between patterns in the temperature contrast and areas with alteration is different for every window because of the variations in aspect, composition, and structure within and between each of the windows.

Table 3-9. Characteristics visible in the contrast thermal imagery from 20:05 August 2, 2015 to 05:05 August 3, 2015 for each window. A check mark denotes the features are easily distinguished from surroundings, a blank space indicates the features are not easily seen, and a dash is used when those features do not occur in the window at all.

Window	Time	Columnar Joints	Horizontal Joints	Units	Soil	Vegetation	Alteration
1	20:05-21:05	✓	✓		✓	✓	
	21:05-22:05	✓	✓	✓	✓	✓	
	22:05-23:05	✓	✓	✓	✓	✓	
	23:05-00:05		✓				
	00:05-01:05		✓	✓	✓	✓	
	01:05-02:05	✓	✓				
	02:05-03:05	✓	✓			✓	
	03:05-04:05					✓	
	04:05-05:05						
2	20:05-21:05	✓	✓	-		-	✓
	21:05-22:05	✓		-	✓	-	✓
	22:05-23:05	✓		-		-	
	23:05-00:05	✓		-	✓	-	
	00:05-01:05	✓		-		-	
	01:05-02:05	✓	✓	-		-	
	02:05-03:05	✓		-		-	✓
	03:05-04:05			-		-	✓
	04:05-05:05	✓		-		-	
3	20:05-21:05			✓	✓	✓	
	21:05-22:05				✓	✓	
	22:05-23:05	✓	✓	✓	✓	✓	
	23:05-00:05			✓	✓	✓	
	00:05-01:05					✓	✓
	01:05-02:05	✓	✓			✓	
	02:05-03:05			✓	✓		
	03:05-04:05					✓	
	04:05-05:05						
4	20:05-21:05	✓	✓	✓	-	-	
	21:05-22:05	✓	✓	✓	-	-	
	22:05-23:05	✓	✓	✓	-	-	✓
	23:05-00:05	✓	✓	✓	-	-	
	00:05-01:05			✓	-	-	
	01:05-02:05	✓	✓	✓	-	-	✓
	02:05-03:05	✓			-	-	
	03:05-04:05				-	-	
	04:05-05:05	✓			-	-	

Laboratory Imagery

Three laboratory infrared thermography surveys were completed, in which all samples were heated in a 200 °F (93 °C) oven for over 24 hours. They were then taken out of the oven and placed into a white paper-lined box, which provided a uniform background for detailed analysis of the survey results. Images were captured every ten minutes for six hours, and multiple POI on each sample were analyzed in a temperature-time graph. At least two POI were chosen for each unit sample: one to get a baseline on the bulk sample composition, where there appeared to be little variation and alteration, and one to find variability in the sample, such as an amygdale, phenocryst, or area with significant alteration.

Lab Survey 1: Samples MD-CH03-01, MD-CH03-02 and MD-CH08-01

MD-CH03-01 and MD-CH03-02 (Figure 3-27) are from Unit 13. The unit is a greyish-brown aphanitic and vesicular lava, with minor infilling of some vesicles. The samples are highly vesicular (30-40% vesicles), with large vesicles ranging from sub-mm to 32 mm in size. MD-CH08-01 (Figure 3-27) is a sample from Unit 3, a brownish-grey porphyritic lava. Both units are coherent, and samples do not break apart easily.

The initial survey image (t=0 min) shows all surfaces of the samples have temperatures above 64.9 °C (Figure 3-28), which in the thermal camera software ResearchIR Max, is the threshold in this image for temperatures being categorized as ‘saturated’. This means they exceed the calibration limits of the instrument itself (FLIR Systems, Inc., 2015). The instrument is therefore unable to definitively determine the temperatures of the samples in the first few images of the survey, as they are too hot. It is not until the image taken 40 minutes into the survey (t=40 min) that we do not observe saturated temperatures (Table 3-10). We will thereby be analyzing the first 20-30 minutes (depending on when there is no saturation in the survey images) of all laboratory surveys qualitatively, rather than quantitatively.

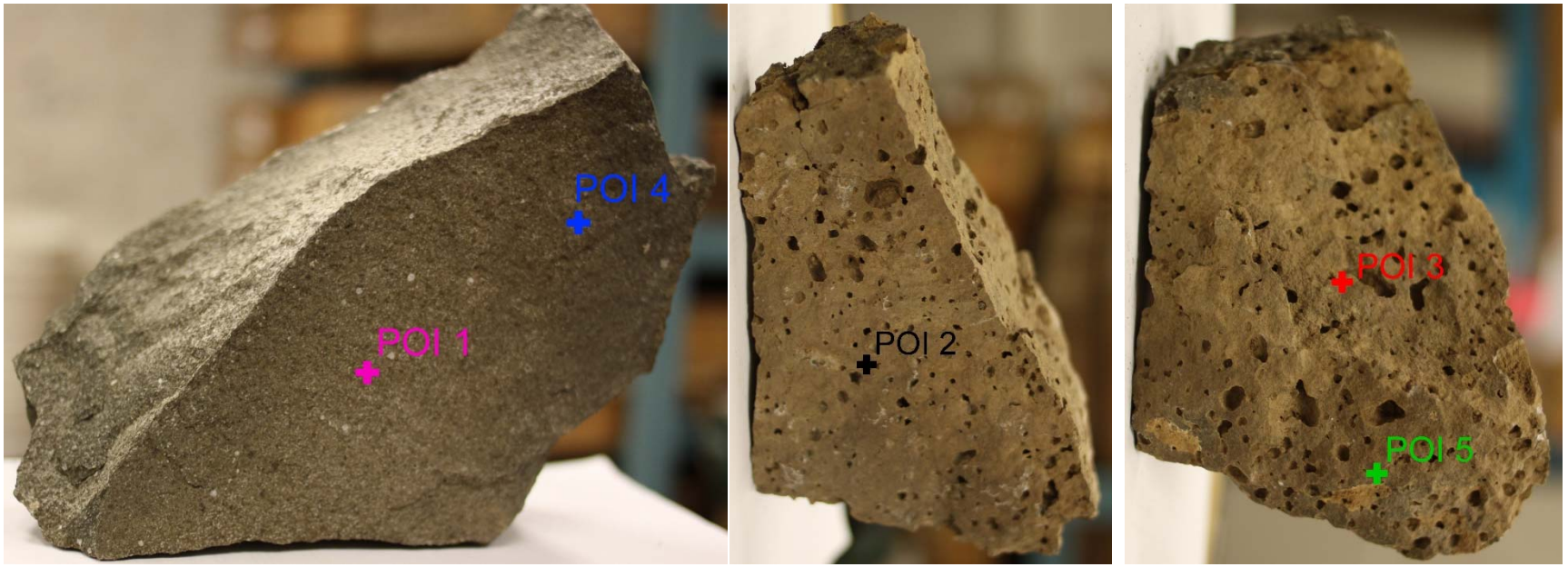

Figure 3-27. RGB images of samples MD-CH08-01 (left), MD-CH03-01 (middle) and MD-CH03-02 (right) in similar orientations as in the thermal survey, with POI locations shown in same colours as shown in Figure 3-29.

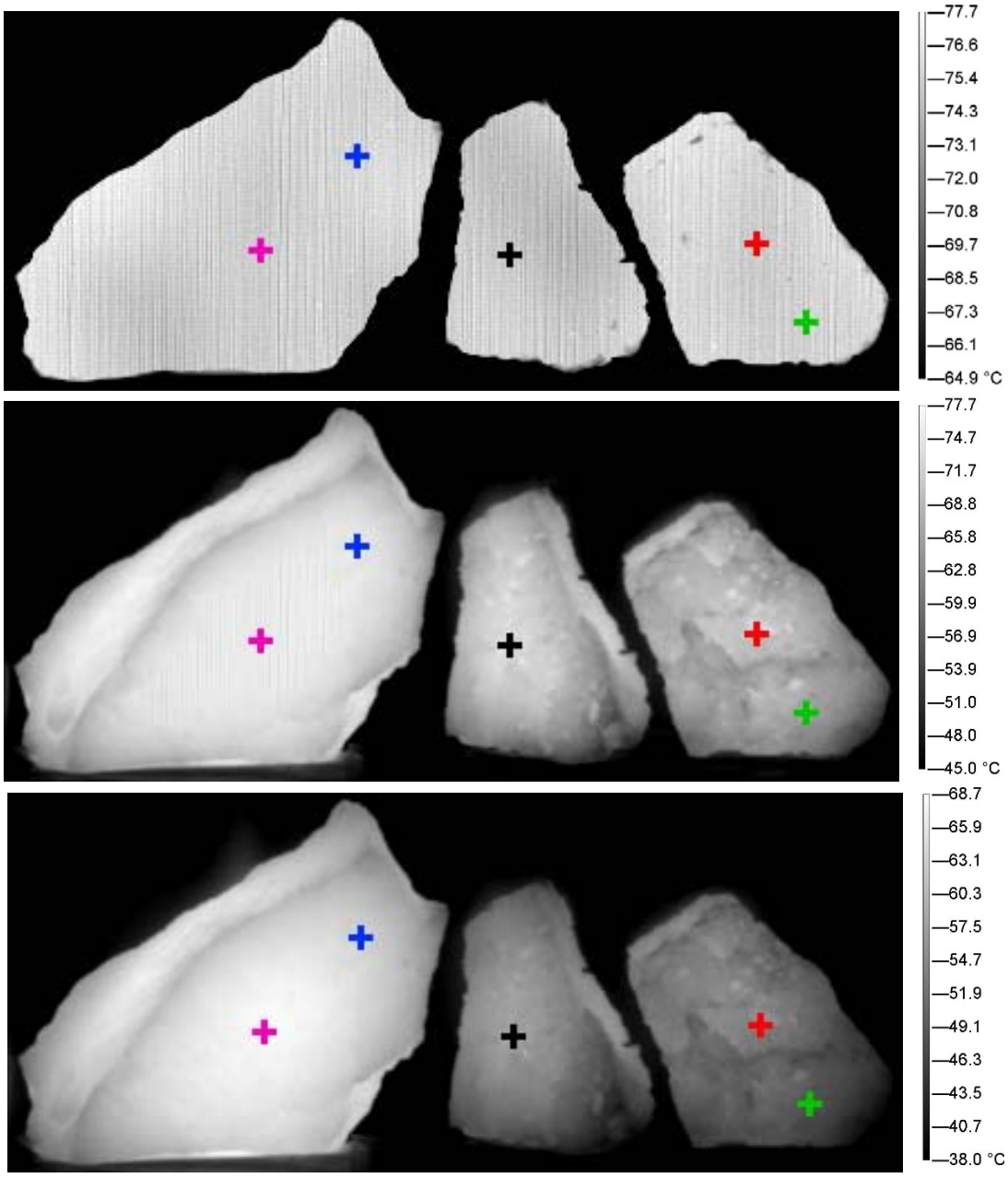

Figure 3-28. The t = 0 min (top), t = 10 min (middle) and t = 30 min (bottom) thermal images of the survey of MD-CH08-01 (left sample) and MD-CH-03-01 (middle sample) and MD-CH03-02 (right sample). All temperatures above 64.9 °C (t = 0 min) and 65.1 °C (t = 10 min, t = 30 min) are saturated; these areas have vertical lines through them. POI locations are shown with the same colour as in Figure 3-27 and Figure 3-29.

Table 3-10. Saturation temperatures for images in the MD-CH03-01, MD-CH03-02 and MD-CH08-01 laboratory thermal survey.

Image	Time into survey (t) (minutes)	Saturation temperature (°C)
01000	0	64.9
01001	10	65.1
01002	20	65.1
01003	30	65.1
01004	40	No temperatures are saturated

Due to the saturation of temperatures, and that effectively no time has passed since the samples were taken out of the oven, the first image (t = 0 min) of the survey shows no detail on cooling patterns (Figure 3-28). In the second image (t = 10 min), however, more detail can be observed even with many temperatures being saturated (Figure 3-28). MD-CH08-01 shows little cooling overall with the exception of the edges of the sample; temperatures range from 58.4-77.1 °C. Both samples of MD-CH03 show cooling along the edges of the samples as well, however details of the samples also begin to appear, such as vesicles appearing as hotter (whiter) dots on the samples. The vesicles may be appear hotter than the surrounding rock because they are semi-circular, which means there is a lot of surface area which is giving off heat to cool, but because these vesicles are not completely exposed to the outer surface of the rock, some of the heat which is radiating off the inner surfaces of the rock inside the vesicle is trapped, making the vesicle appear hotter. The temperatures in MD-CH03-01 range from 49.6-75.4 °C, and 50.4-74.1 °C in MD-CH03-02. Overall, MD-CH03-01 appears to have retained more heat, and show less variability, than MD-CH03-02.

POI temperature decay curves differ between and within samples, as would be expected based on the different composition and method of choosing POI (Figure 3-29). POI 1 and 4 are from MD-CH08-01, and exhibit consistently higher temperatures than POI 2, 3, and 5 from samples MD-CH03-01 and MD-CH03-02. The main compositional difference between MD-CH08-01 and MD-CH03 observed in thin sections was the amount of alteration (MD-CH08-01 exhibited greater amounts of plagioclase alteration to sericite), and the difference in vesicularity, in that MD-CH08-01 did not have vesicles, and the other samples did. As the vesicularity is a major factor for air flow over and through the samples, it is thought that the alteration did not play a significant role in the

differences in temperature decay curves in this case. Similar to Mineo and Pappalardo's (2016) Mount Etna samples, the difference in porosity between and within Chasm samples was observed in this survey.

POI 1 is at a location where there is a phenocryst, and exhibits a higher overall temperature than POI 4, a baseline point for the groundmass of the sample. POI 2, 3, and 5 occur on the MD-CH03 samples, and also show a variety of temperature decay curves. POI 2 is on MD-CH03-01, and is located within a vesicle in the sample. POI 3 and 5, on MD-CH03-02, are both locations for baselines of the sample's overall response, but differ slightly from one another. As seen in the initial images of the survey (Figure 3-28), vesicles retain heat more readily than the overall sample, as heat gets trapped during the cooling process; so it would follow that the temperature of POI 2 remains higher than POI 3 and 5, as observed (Figure 3-29). The difference between the curves of the MD-CH03 baseline points (POI 3 and 5) illustrates quantitatively a pattern seen in the initial images of the survey, whereby the lower portion of the MD-CH03-02 sample cools faster than the upper portion. This is likely indicative that the amount and/or size of vesicles has increased towards the bottom of the sample, allowing for less heat retention. The photograph of the sample (Figure 3-27) supports this theory.

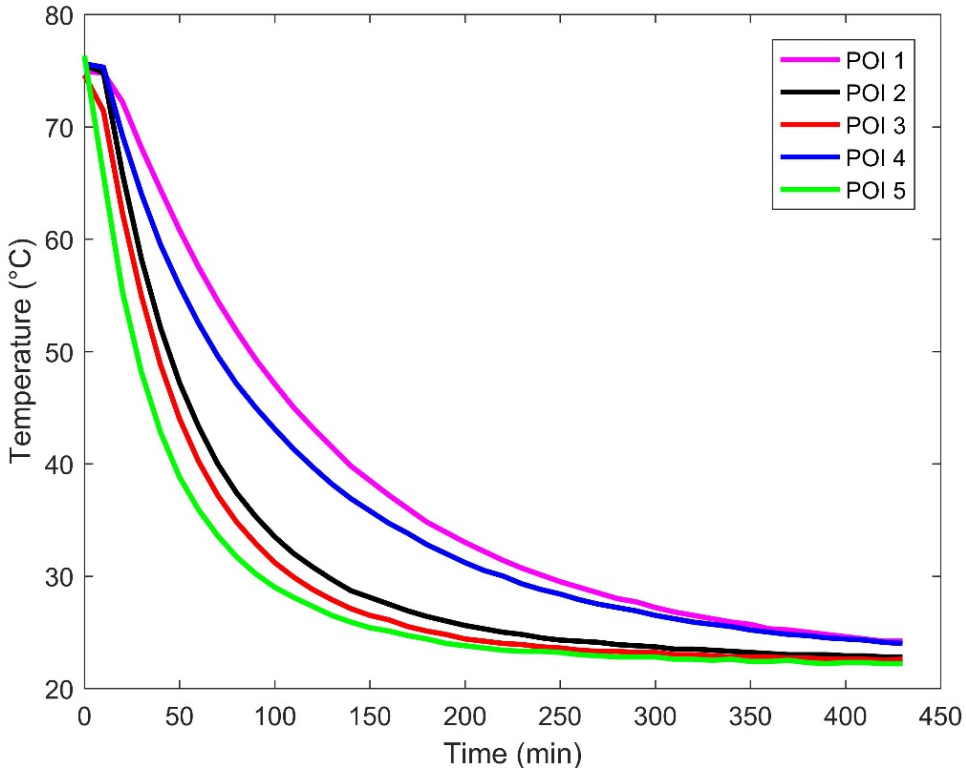

Figure 3-29. Temperature graph of POI 1-5 for samples MD-CH03-01 and MD-CH08-01.

Lab Survey 2: Samples MD-CH06-03 and MD-CH-P23-01

MD-CH06-03 is sampled from Unit 8, and is aphanitic, approximately 25% vesicular with some vesicles partially to fully infilled with zeolites (Figure 3-30). It is moderately weathered and reddish brown. MD-CH-P23-01 is very similar in appearance, and was collected from Unit 14, a paleosol unit.

Similar to samples in the previous section, saturated temperatures are observed for MD-CH06-03 and MD-CH-P23-01, with observations listed in Table 3-11. At t=30 min, there are no observed saturated temperatures in the survey image; this is the first image shown in Figure 3-31. MD-CH-P23-01 has retained more heat than the samples of MD-CH06-03 at t=30 minutes in the survey, exhibiting a maximum temperature of 62.2 °C as opposed to the maximum observed in the other samples of 50.3 °C. All samples show the most cooling around edges of the samples, as seen in Lab Survey 1, however samples are more irregularly shaped in this lab survey. The irregularity in edges has resulted in a less uniform cooling pattern than in Lab Survey 1. It is evident, for example, that at t=110 min (Figure 3-31), sample MD-CH-P23-01 displays

approximately 40.4 °C on surfaces near the middle of the sample, whereas near the bottom left corner of the sample on the same surface temperatures are closer to 25.9 °C. There are more fractures in the bottom portion of the sample, allowing for more air flow, which explains the significant difference in temperature patterns. The third image in Figure 3-31 is for t=250 minutes, and exhibits more uniform temperatures on the samples as the survey has progressed. Individual features on the samples are not distinguishable, and MD-CH-P23-01 and MD-CH06-03 are still on average approximately 2-3 °C above room temperature (22-23 °C), but have evidently reached equilibrium within the samples themselves as the approximate difference between minimum and maximum temperatures on the samples are between 1-2 °C.

Table 3-11. Saturation temperatures for images in the MD-CH06-03 and MD-CH-P23-01 laboratory thermal survey.

Image	Time into survey (t) (minutes)	Saturation temperature (°C)
01081	0	65.3
01082	10	65.1
01083	20	65.1
01084	30	No temperatures are saturated

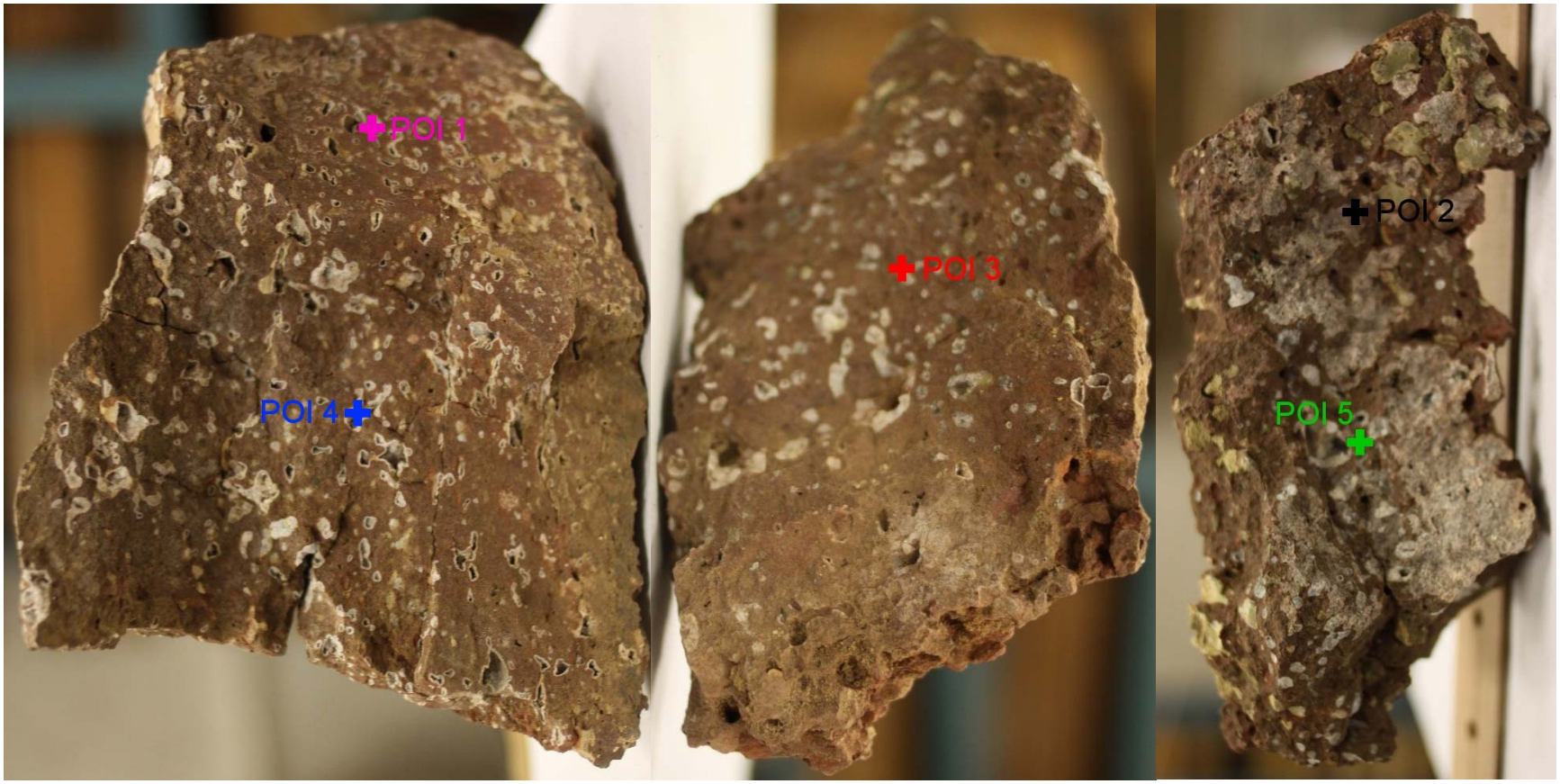

Figure 3-30. RGB images of samples MD-CH-P23-01 (left) and MD-CH06-03 (middle and right) in similar orientations as in the thermal survey, with POI locations shown in same colours as shown in Figure 3-32.

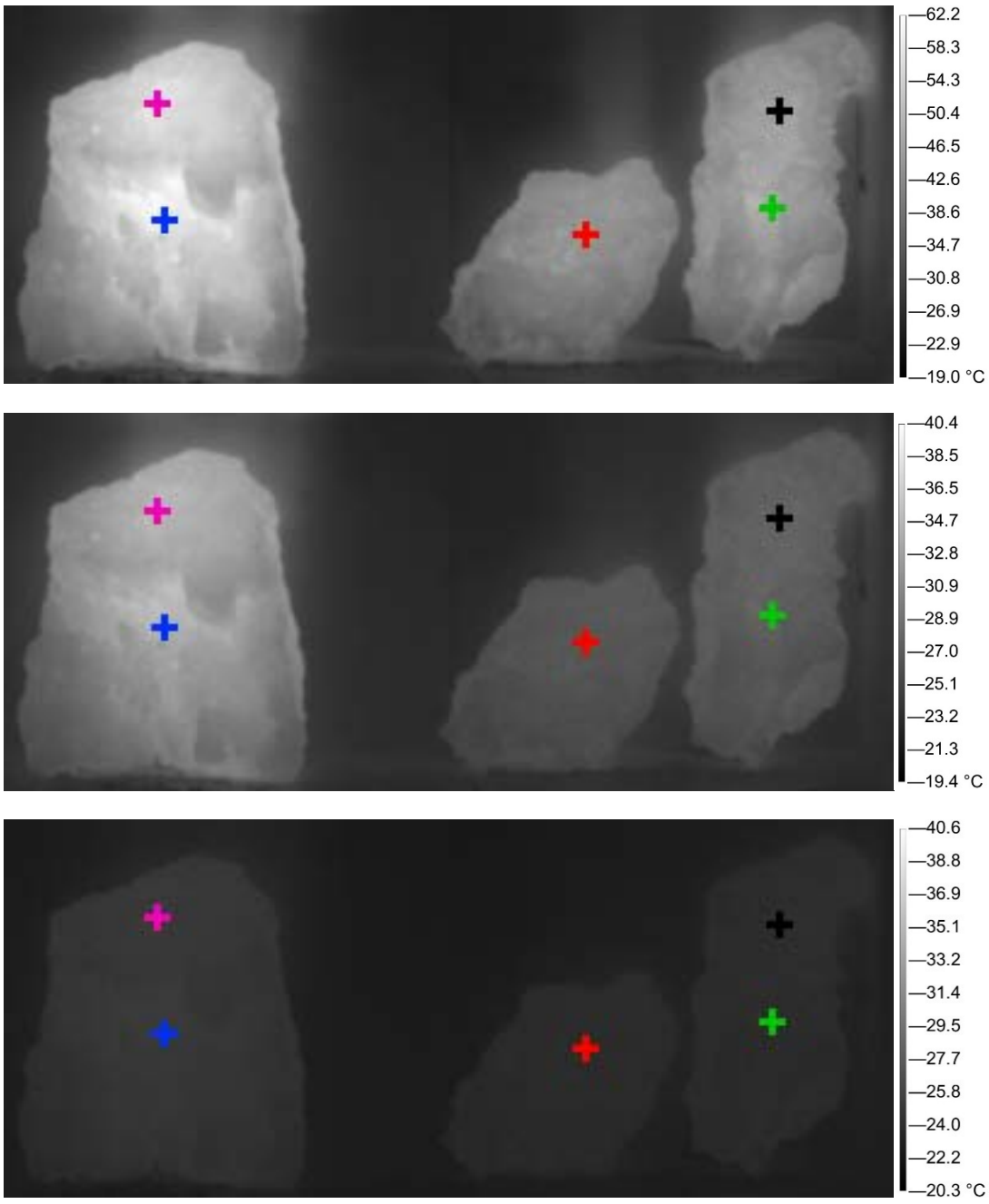

Figure 3-31. The t = 30 min (top), t = 110 min (middle) and t = 250 min (bottom) thermal images of the survey of MD-CH-P23-01 (left sample) and MD-CH06-03 (middle and right samples). POI locations are shown with the same colour as in Figure 3-30 and Figure 3-32.

Similar to Lab Survey 1, POI temperature decay curves are different between samples, however in this survey there are more similarities in the curves within each sample (Figure 3-32). Both POI 1 and 4 occur on MD-CH-P23-01, and show

temperatures over the survey that differ by approximately 1-2 °C until t=70 minutes, beyond which point the temperatures differ for the remainder of the survey by no more than 0.3 °C. POI 1 and 4 are within vesicles in the sample, both of which are rimmed with zeolites and have similar sizes, so it follows they would behave similarly with temperature decay over time. POI on sample MD-CH-P23-01 show consistently higher temperatures than those on MD-CH06-03 samples, with an average difference of approximately 3 °C, and a maximum difference of 10.6 °C. POI 3 exhibits the lowest temperatures throughout the survey, and is the only POI on the first sample of MD-CH06-03, chosen as a baseline for overall behavior of the sample. POI 2 and 5 are both on the second sample of MD-CH06-03, and do not differ by more than 1.3 °C throughout the survey. POI 2 is located on an area which is comprised of white alteration, and POI 5 is the baseline for that sample. Given POI 2 and 5 do not significantly differ in their thermal responses, alteration is not thought to play a major role in thermal response in this sample. The differences between samples, as the samples have similar compositional characteristics, is thought to be the size of the samples themselves. MD-CH-P23-01 is a larger sample, hence it retained heat for longer in the survey.

In this survey, an apparent “step” at t=60 min in the survey interrupts the otherwise continuous temperature decay curves. The step is in all POI curves, and the data indicates that there were no temperature changes in any of the POI between t=50 min and t=60 min. This is highly unlikely and is interpreted to be a systematic error with the t=60 min image, in that it did not record the temperatures properly. The connection between the camera and the laptop running the camera software was likely interrupted, leading to the image in the software failing to update with real-time temperature before the t=60 min image was taken.

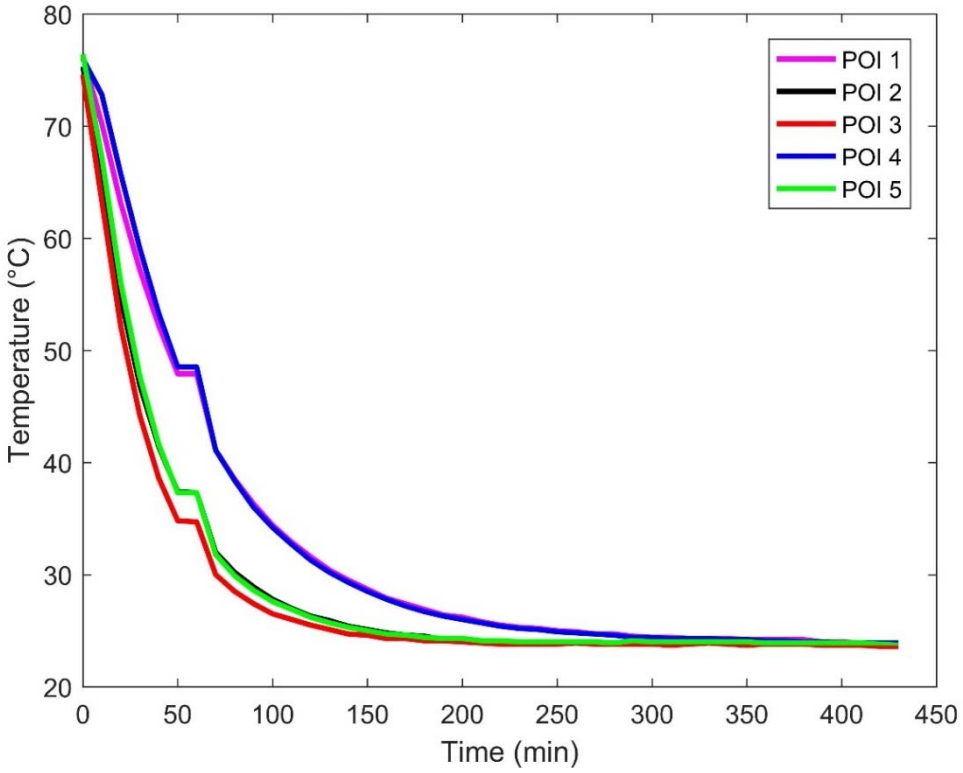

Figure 3-32. Temperature graph of POI 1 to 5 for samples MD-CH-P23-01 and MD-CH06-03.

Lab Survey 3: Samples MD-CH-P67-01 and MD-CH-P67-02

MD-CH-P67-01 and MD-CH-P67-02 are both samples from Unit 6, a reddish brown paleosol with 20-30% vesicles (Figure 3-33). They are aphanitic, and vesicles are partially to fully filled with zeolites. The samples were taken from two different sides of an eroded portion of the slope, but the unit is correlated across. Saturated temperatures are observed in this survey until t=20 minutes, after which time samples exhibit no saturated temperatures (Table 3-12).

Table 3-12. Saturation temperatures for images in the MD-CH-P67-01 and MD-CH-P67-02 laboratory thermal survey.

Image	Time into survey (t) (minutes)	Saturation temperature (°C)
01044	0	65.1
01045	10	65.1
01046	20	65.1
01047	30	No temperatures are saturated

Though some temperatures in the t=20 min thermal image are saturated, some observations can still be made on general cooling patterns in the samples (Figure 3-34). MD-CH-P67-01 appears to cool more slowly than the two samples of MD-CH-P67-02, and exhibits temperatures approximately 10 °C higher, on average. MD-CH-P67-02 samples show significant differences in temperature between vesicles and rock mass, in some places exceeding a difference of 18 °C. This pattern continues in the MD-CH-P67-02 samples in t=80 min and t=230 min, though temperature contrasts are not as pronounced (up to 8 °C and up to 6 °C differences, respectively). The sample MD-CH-P67-01 appears to cool more uniformly, with differences in temperature between maximum and minimum below 10 °C for the entire sample at t=20 min, the beginning of the exponential decay of temperature where contrast should be greatest.

Consistent with both Lab Survey 1 and Lab Survey 2, POI which have locations on the same sample show similar temperature decay curves, and POI on different samples exhibit temperatures which differ between samples (Figure 3-35). POI 1 and 4 are located on MD-CH-P67-01; POI 1 is the baseline for the sample, and POI 4 is in an area of white alteration. As temperatures between the two points differ by 1 °C on average, alteration is not considered to contribute significantly to thermal response in this sample. POI 2 is located on a separate sample of MD-CH-P67-02 than POI 3 and 5, but all three POI have similar temperature decay curves, with differences in temperatures over the survey of no more than 5 °C, and an average of 0.8 °C difference. POI 2 is the baseline point for the sample, POI 3 is on a fracture trace, and POI 5 is in an area of white alteration. As there are not significant differences in temperature between these three POI, alteration is not thought to affect thermal decay in this sample. The only significant differences in temperature patterns in these samples are, as mentioned before, the vesicles versus the rock itself.

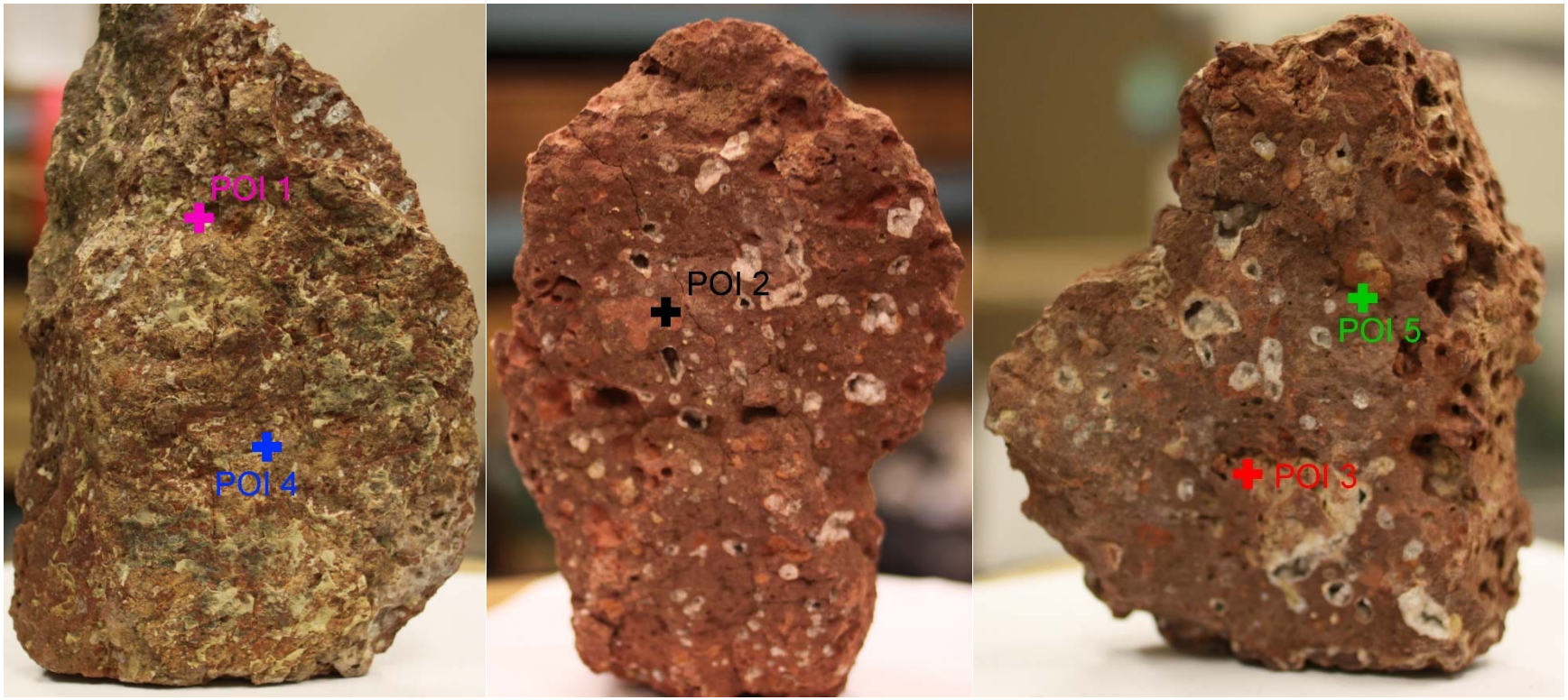

Figure 3-33. RGB images of samples MD-CH-P67-02 (left) and MD-CH-P67-01 (middle and right) in similar orientations as in the thermal survey.

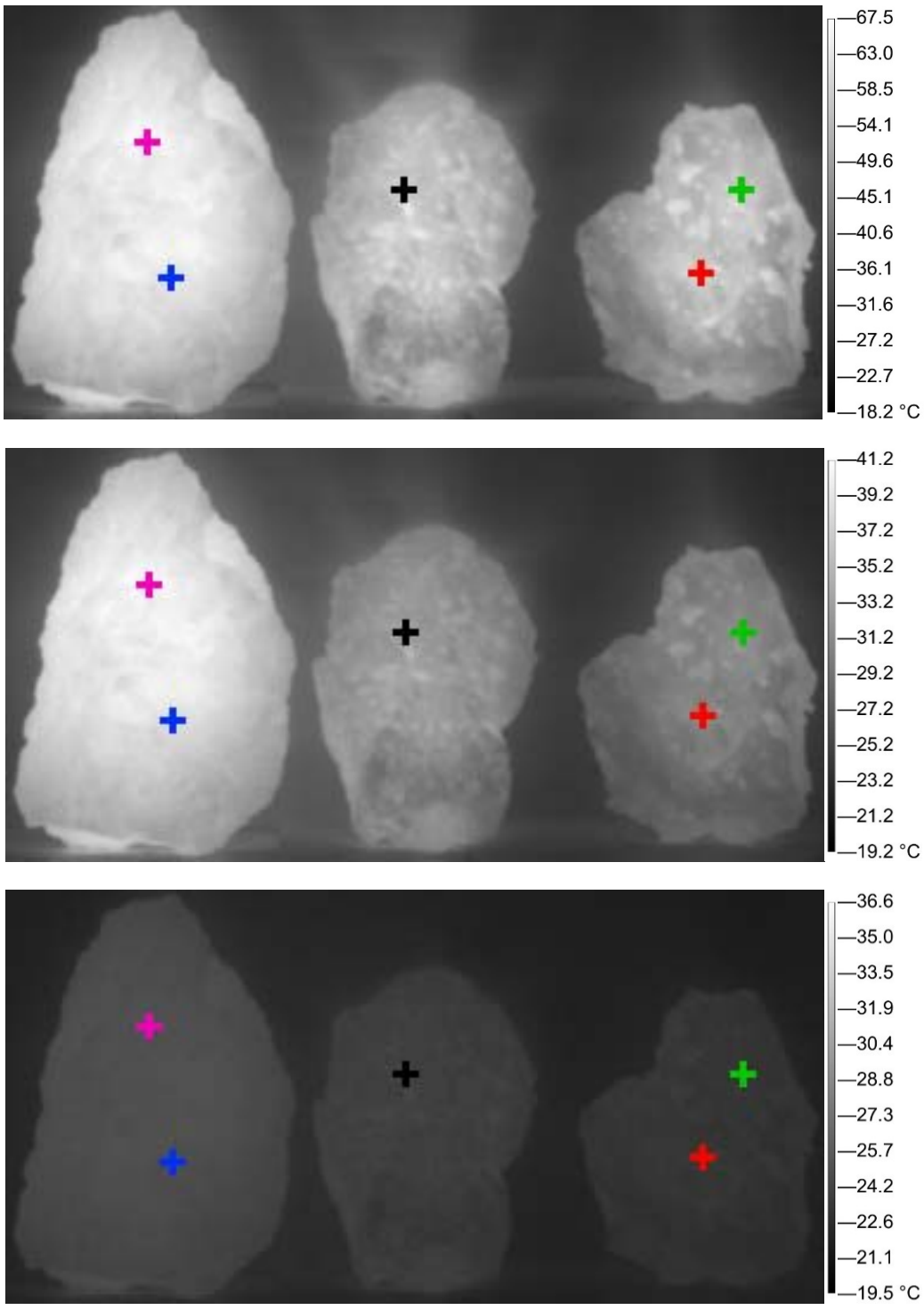

Figure 3-34. The t = 20 min (top), t = 80 min (middle) and t = 230 min (bottom) thermal images of the survey of MD-CH-P67-01 (left sample) and MD-CH-P67-02 (middle and right samples). POI locations are shown with the same colour as in Figure 3-33 and Figure 3-35.

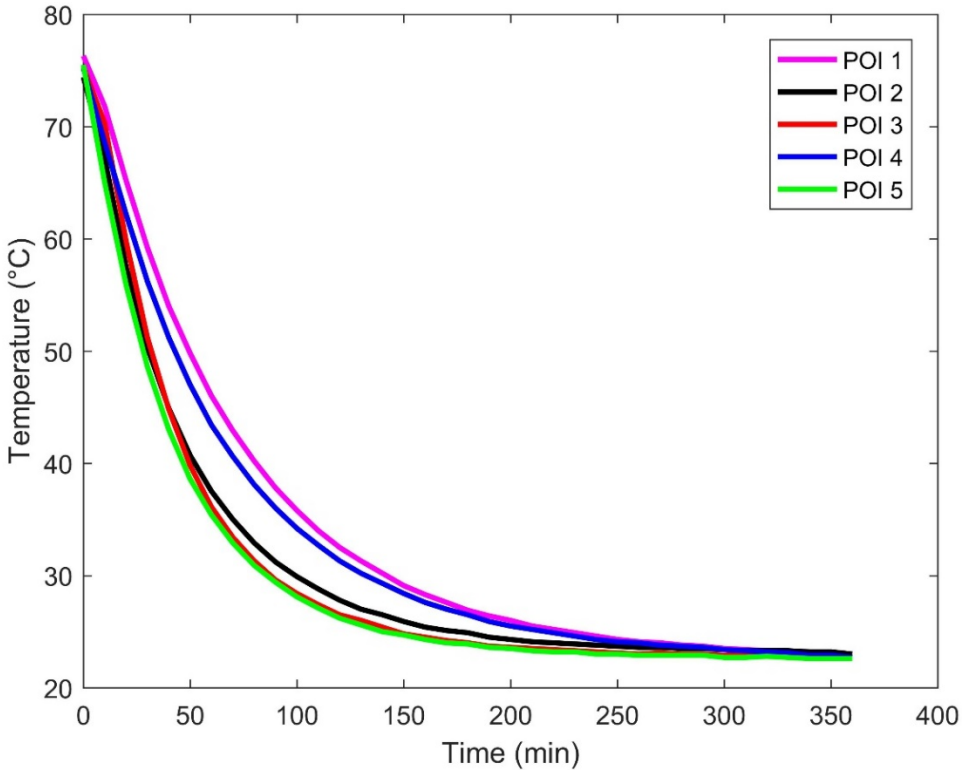

Figure 3-35. Temperature graph of POI 1-5 for samples MD-CH-P67-01 and MD-CH-P67-02.

Overall Results

The overall results of the surveys were summarized by fitting power functions to the temperature decay curves of all POIs from the three lab surveys using Microsoft Excel (Microsoft, 2016)(Table 3-13). The power function was chosen over the logarithmic, exponential or linear curve fitting equations because it generally had the best R^2 value for each curve. R^2, a value between -1 and 1 which describes the degree of correlation the best fit equation has for the data (-1 or 1 being the perfect fit, with -1 having a negative slope and 1 a positive slope), was used to determine how well the calculated equations fit the data curves.

R^2 values averaged 0.9374, meaning the power equations fit well with the data. The average exponent was $x^{-0.358}$, with a standard deviation of 0.036. These numbers seem small, but as the entire slope is composed of variations of basalt, it is evident that these small variations in the exponent and preceding constants in the equations are what will characterize the thermal response of each unit.

Table 3-13. Power functions fit to the POI temperature decay curves, and their associated R^2 values.

Sample	POI	Description	Equation	R^2
MD-CH08-01	1	Phenocryst	$y = 272.03x^{-0.394}$	0.9448
	4	Baseline/fresh	$y = 244.65x^{-0.382}$	0.9694
MD-CH03-01	2	Vesicle	$y = 207.12x^{-0.378}$	0.9599
MD-CH03-02	3	Baseline/fresh	$y = 185.1x^{-0.364}$	0.9480
	5	Baseline/fresh	$y = 153.49x^{-0.336}$	0.9423
MD-CH-P23-01	1	Amygdale	$y = 194.45x^{-0.361}$	0.9552
	4	Amygdale	$y = 202.5x^{-0.369}$	0.9483
MD-CH06-03 (Sample 1)	3	Baseline/fresh	$y = 117.6x^{-0.285}$	0.8542
MD-CH06-03 (Sample 2)	2	White alteration	$y = 131.65x^{-0.302}$	0.8823
	5	Baseline/fresh	$y = 134.03x^{-0.306}$	0.8740
MD-CH-P67-02	1	Baseline/fresh	$y = 240.37x^{-0.407}$	0.9727
	4	White alteration	$y = 216.79x^{-0.391}$	0.9774
MD-CH-P67-01 (Sample 1)	2	Baseline/fresh	$y = 173.68x^{-0.359}$	0.9559
MD-CH-P67-01 (Sample 2)	3	Fracture trace	$y = 180.02x^{-0.371}$	0.9351
	5	White alteration	$y = 166.31x^{-0.358}$	0.9416

Constants and exponents within each sample appear to be close, though as POI were selected in different areas of the sample (alteration, phenocryst, amygdale, vesicle, baseline), it is expected that these will differ slightly within each sample set. The two equations for POI on MD-CH03-02 (POI 3 and 5) differ the most, with a 31.61 difference in the constant and 0.028 difference in the exponent. Both of these POI are meant to be baselines for the sample, but show that there is enough variation in the base composition of the sample to result in a difference in temperature equations. The sample which has the least variation in equations is MD-CH06-03 with POI 2 and 5, which shows only a 2.38 difference in constant and 0.004 change in exponent. POI 2 is an area of white alteration on the sample, and POI 5 is the baseline. The lack of significant difference between these two curves leads to the inference that white alteration does not play a role in changing the thermal response of the sample.

Combining LiDAR and IRT Techniques

Profiles were taken through the LIP1 slope using both LiDAR and IRT at approximately the same areas for each window to allow for the comparison of slope reflectivity and thermal response. They were chosen to highlight differences between units, various features in the slope, and alteration. As there was only one LiDAR scan taken, there is a single reflectivity profile for each window. The IRT survey, however, is comprised of ten thermal images for each window (one for each hour during the survey), and therefore ten thermal profiles are used for comparison against reflectivity. The temperature profiles show the variation in temperature along the profile for each measured time, and were captured through the selection of a single column of pixels in the image. Mapping of these profiles was completed by matching peaks and troughs in each profile to features observed in the rock slope; the results are presented below.

Window 1

The profiles chosen for Window 1 LiDAR and IRT are RP1 and Column 54, respectively (Figure 3-36). By cross-referencing RP1, the Column 54 thermal profiles, and a photograph of the profile area, rock units and features were interpreted and delineated (Figure 3-37). The highest elevations in the profiles are characterized by highly variable LiDAR reflectance values and relatively low temperatures, approximately 0-4 °C colder than that of the underlying section Soil A (Table 3-14, Table 3-15). These are indicative of vegetation, as the branches in trees and shrubbery have huge variability in angle and distance with respect to the scanner. Vegetation also is not as efficient at retaining heat as soil and rock, and therefore is generally observed as lower temperatures in the profiles.

The area marked as Soil A in Figure 3-37 is characterized by peaks and troughs in the range of 2 dB. Soil, as it is composed of smaller particles, tends to scatter LiDAR pulses more than solid rock, hence relative peaks in reflectivity due to the presence of cobbles and boulders in the soil. The temperature profiles for Soil A show a similar pattern of peaks for cobbles and boulders, and troughs for soil, with a temperature range of 2.5-4 °C between peaks and troughs in the profiles. The peaks in the temperature profiles correspond well with the peaks in reflectivity.

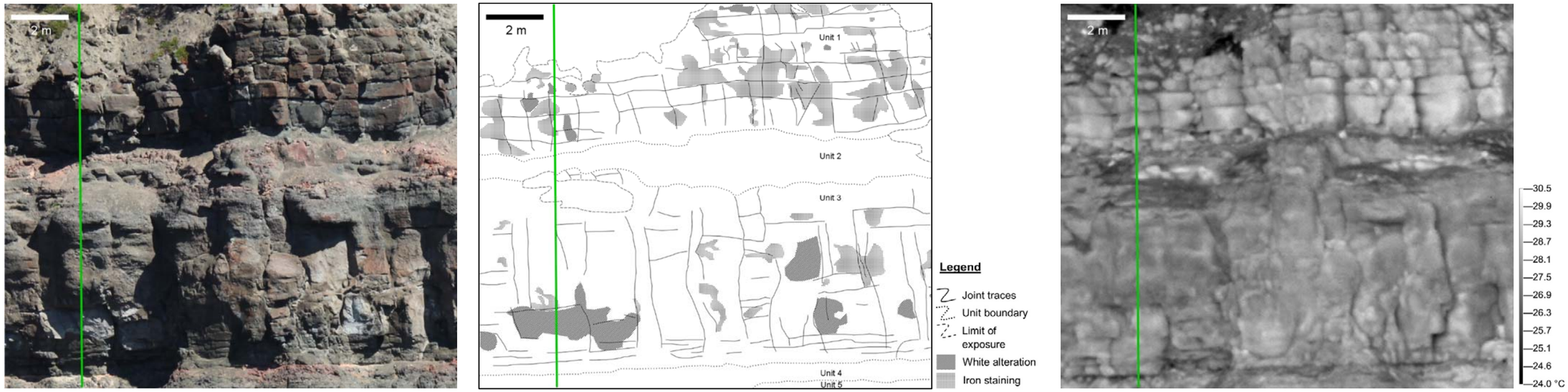

Figure 3-36. Photograph of Window 1 (left), interpretive line drawing of Window 1 with features shown (middle), and thermal image of Window 1 at 20:05, August 2, 2015 (right). Column 54 (thermal profile) and RP1 (reflectivity profile) are shown as a thick green line in all images.

Table 3-14. Minimum and maximum temperatures observed in the thermal profiles for Window 1. Temperatures are expressed in degrees Celsius. The hottest temperatures for each time frame are denoted with red font, the coolest, blue. The highest and lowest temperatures overall (encompassing all windows and units) are in bold font.

	20:05		21:05		22:05		23:05		00:05		01:05		02:05		03:05		04:05		05:05	
Unit	Min	Max	Min	Max	Min	Max	Min	Max	Min	Max	Min	Max	Min	Max	Min	Max	Min	Max	Min	Max
Vegetation	24	26.5	21	21.5	22	23	17.5	18	15.5	16.5	13	13	12	12	11.5	12	9	9	**6**	7
Soil A	26	28	21	24	22	26.5	17.5	20.5	15.5	18.5	13	16	12	15.5	12	15.5	9	12.5	7	11
Unit 1	26	28.5	22.5	24.5	23	26.5	19	20.5	17.5	19	15	17.5	14.5	17	14.5	17	10.5	14	9	12.5
Unit 2	26.5	29	22	24.5	23	25.5	18	20	16.5	17.5	14.5	15.5	13.5	15	13.5	15	10.5	11.5	8.5	10
Soil B	26	28.5	21.5	23	22	24	18	19	16	17	13.5	15	12.5	14	12.5	14	9.5	10.5	7.5	8.5
Unit 3	25.5	28.5	21.5	24.5	21.5	26.5	17.5	20.5	16	18.5	14	16.5	13.5	16	13.5	16	10.5	13.5	8.5	11.5
Unit 4	26.5	27.5	21.5	23	23.5	24	18	18.5	16	17	14.5	14.5	13.5	14	13.5	14	11	11	8.5	8.5

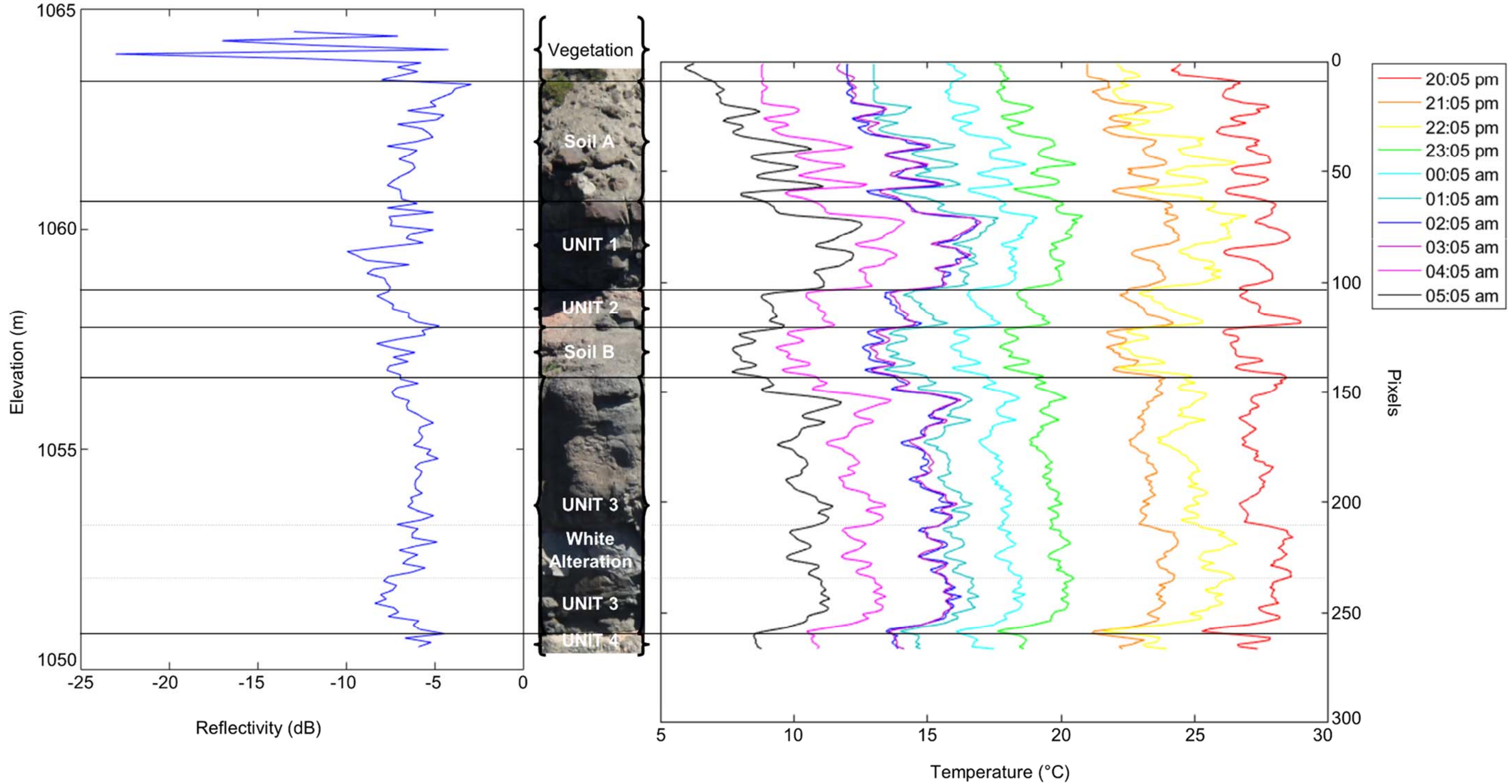

Figure 3-37. RP1 (left) and Column 54 temperature profiles (right). Solid lines indicate breaks between units, dashed lines indicate the area of white alteration within Unit 3.

Table 3-15. Reflectivity of units in the RP1 profile in Window 1. Elevations and reflectivity values are rounded to the nearest half.

Unit	Elevation of Lower Boundary (m)	Elevation of Upper Boundary (m)	Reflectivity Minimum (dB)	Reflectivity Maximum (dB)
Vegetation	1063.5	>1064.5	-23	-4
Soil A	1060.5	1063.5	-8	-3
Unit 1	1058.5	1060.5	-10	-5
Unit 2	1057.5	1058.5	-8	-5
Soil B	1056.5	1057.5	-8	-5
Unit 3	1051	1056.5	-8	-5
Unit 4	<1050.5	1051	-6.5	-4.5

Unit 1 in Figure 3-37 shows a 2 dB lower reflectance value than that of Soil A , with slightly more variation (approximately 5 dB). Temperatures in Unit 1 are higher than those in Soil A, due to the fact Unit 1 is rock and therefore retains heat longer than the smaller particles found in Soil A. Troughs in the temperature profiles of approximately 1-1.5 °C in magnitude delineate the location of joints in the slope; these troughs correlate well with troughs in reflectivity of approximately 2-4 dB in magnitude.

The transition from Unit 1 to the underlying Unit 2 is sharp and easily observed. There is an approximate 1.5-3 °C drop in temperature at this contact, and a difference in pattern of reflectivity whereby the peaks and troughs have decreased significantly, and the range has decreased by 2 dB. Both the reflectivity and thermal profiles show a gradual increase as elevation decreases because the top of Unit 2 is a soil, which grades into rock downslope, indicating a gradational boundary between Unit 2 and the underlying Unit 3.

Unit 3 is less eroded than Unit 2 and has a shallow slope angle at its top, so eroded material from the slope above comes to rest here creating Soil B. This unit exhibits a similar reflectivity range to Unit 2, and is 0.5-1.5 °C cooler than Unit 2 for the entire survey. As it is likely mostly composed of material eroded from Unit 2, is would follow that Soil B has similar reflectivity. The temperature difference, however, is due to the unit being a soil, which does not retain heat as well as soil and rock in combination.

The transition from Soil B to Unit 3 is not apparent in the reflectivity profile, but is significant in temperature profiles, which show an increase in temperature of up to 3.5

°C. As with previous units, troughs in the temperature profiles (~0.5-1.5 °C) indicate locations of joints and correlate well with troughs in reflectivity (~0.5-1 dB). Temperature profiles in Unit 3 remain in a relatively constant range (within 2-3 °C) with the exception of an area of white alteration. The white alteration exhibits similar reflectivity to the remainder of Unit 3, but a slight rise in temperature (0.5-1 °C) in profiles from the beginning of the survey (20:05-22:05).

Unit 4 underlies Unit 3, and reflectivity is within a narrower (by 0.5 dB) and higher range (by 0.5-1.5 dB) than Unit 3. Temperatures of Unit 4 show a more marked change across the Unit 3-Unit 4 contact, and decrease by 1-3 ° C.

Window 2

RP2 and Column 155 were chosen for the reflectivity and thermal profiles of Window 2 (Figure 3-38); profiles are shown in Figure 3-39. Window 2 is within a single unit, so the profiles were chosen to observe variability within the unit. The reflectivity values exhibited all lie within a narrow range of 3.5-4.5 dB (Table 3-16), and temperatures do not vary more than 4 °C over the entire profile (Table 3-17). The largest peaks and troughs in the profiles occur at locations with joints, and the colonnade and entabulature zones exhibit a change in peak magnitudes. In the colonnade portion of the flow, the chatter marks and ball-and-socket joints on the columns display troughs of approximately 0.5 °C and 1 dB in magnitude, whereas joints in the entabulature portion are indicated by temperature troughs in the range of 0.5-1 °C and reflectivity troughs of 1-2 dB. Joints in the entabulature zone are open and overhang more than those in the colonnade, therefore offering increased amounts of shade and variability in the slope, hence the drops in temperature and reflectivity, respectively.

Table 3-16. Reflectivity of units in the RP2 profile in Window 2. Elevations and reflectivity values are rounded to the nearest half.

Unit	Elevation of Lower Boundary (m)	Elevation of Upper Boundary (m)	Reflectivity Minimum (dB)	Reflectivity Maximum (dB)
Colonnade	1043	>1049.5	-8	-4.5
Entabulature	1060.5	1063.5	-9	-4.5

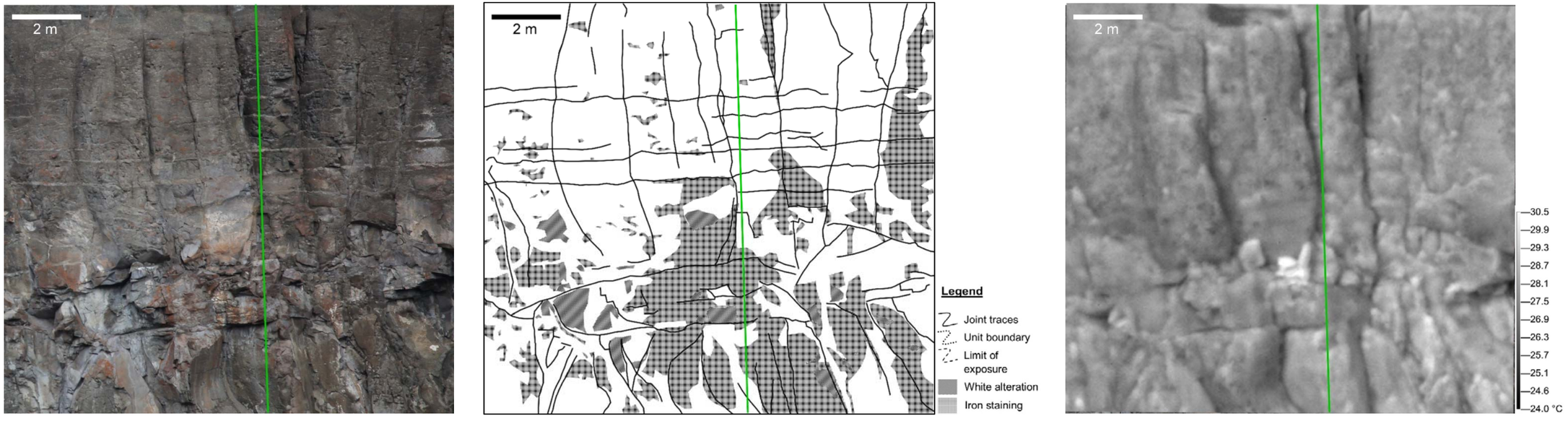

Figure 3-38. Photograph of Window 2 (left), interpretive line drawing of Window 2 with features shown (middle), and thermal image of Window 2 at 20:05, August 2, 2015 (right). Column 155 and RP2 are shown as a thick green line in all images.

Table 3-17. Minimum and maximum temperatures observed in the thermal profiles for Window 2. Temperatures are expressed in degrees Celsius. The hottest temperatures for each time frame are denoted with red font, the coolest, blue. The highest and lowest temperatures overall (encompassing all windows and units) are in bold font.

	20:05		21:05		22:05		23:05		00:05		01:05		02:05		03:05		04:05		05:05	
Unit	Min	Max	Min	Max	Min	Max	Min	Max	Min	Max	Min	Max	Min	Max	Min	Max	Min	Max	Min	Max
Colonnade	26.5	***30.5***	22.5	25.5	23.5	27	18.5	20	16.5	19	16	18	14.5	16.5	14.5	17.5	11.5	15	9	12
Entabulature	26.5	***30.5***	23	25.5	24.5	27.5	19	20	17.5	19.5	17	18.5	15	17.5	16	17.5	13	16	9.5	13

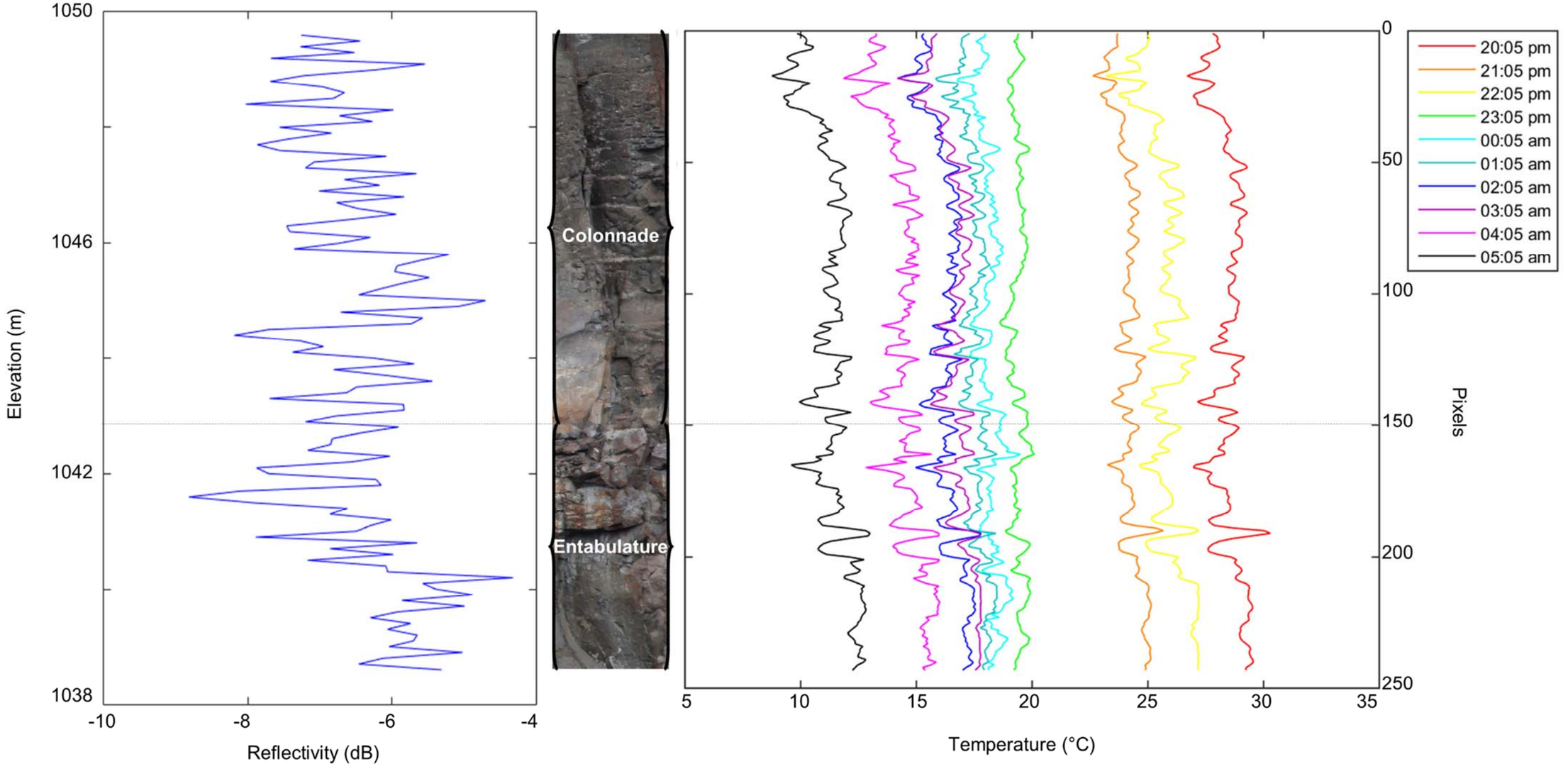

Figure 3-39. RP2 (left) and Column 155 temperature profiles (right). The dashed line indicates the approximate division between the colonnade and entabulature in Unit 5.

Window 3

The profiles of Window 3 for reflectivity and temperature are RP3 and Column 256, respectively, and cut through all visible units in the window as well as several different types of alteration (Figure 3-40, Figure 3-41). The highest elevations belong to Unit 5, which is comprised of similar reflectivity values to the Unit 5 in Window 2 (Table 3-18). Temperatures of this unit are also similar with Window 2 (Table 3-19), and Unit 5 in this window exhibits the maximum temperatures of the profile throughout most of the survey. The troughs in both the reflectivity (1-2 dB) and temperature profiles (0.5-1.5 °C) in Unit 5 are representative of joint locations, and it does not appear that alteration significantly changes either parameter. Alteration in this unit, however, is weak to moderate at the location of the profiles, so a large difference is not expected.

The transition between Unit 5 and the underlying Unit 6 is sharp and detectable in both the reflectivity and temperatures. Reflectivity increases by 0.5-1.5 dB in this interval, with peak reflectivity at a location with highly oxidized paleosol. Peaks and troughs in the temperature profiles become more even in Unit 6, with temperatures approximately 0.5-3 °C cooler than in Unit 5. As seen with previous paleosol units, they are lighter in colour, more vesicular, and in some cases unconsolidated, so it would follow that these units would have a higher reflectivity and lower temperature response.

Table 3-18. Reflectivity of units in the RP3 profile in Window 3. Elevations and reflectivity values are rounded to the nearest half.

Unit	Elevation of Lower Boundary (m)	Elevation of Upper Boundary (m)	Reflectivity Minimum (dB)	Reflectivity Maximum (dB)
Unit 5	1036	>1043	-8	-4.5
Unit 6	1034.5	1036	-7.5	-3
Unit 7	1029	1034.5	-9	-4
Unit 8	1029	1029	-7.5	-7.5
Soil C	1027.5	1029	-8.5	-6.5
Unit 9	<1025.5	1027.5	-8.5	-5.5

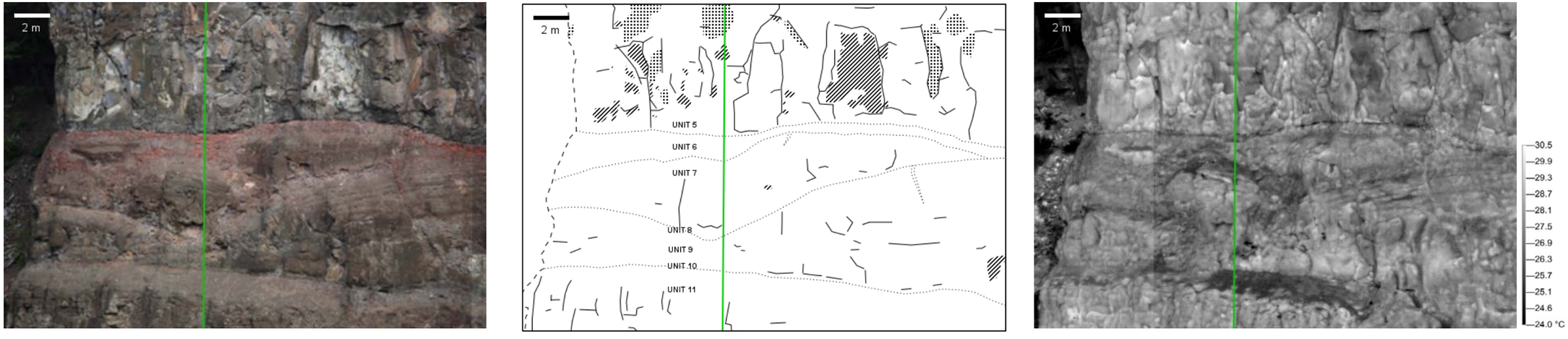

Figure 3-40. Photograph of Window 3 (left), interpretive line drawing of Window 3 with features shown (middle), and thermal image of Window 3 at 20:05, August 2, 2015 (right). Column 256 and RP3 are shown as a thick green line in all images.

Table 3-19. Minimum and maximum temperatures observed in the thermal profiles for Window 3. Temperatures are expressed in degrees Celsius. The hottest temperatures for each time frame are denoted with red font, the coolest, blue.

	20:05		21:05		22:05		23:05		00:05		01:05		02:05		03:05		04:05		05:05	
Unit	Min	Max	Min	Max	Min	Max	Min	Max	Min	Max	Min	Max	Min	Max	Min	Max	Min	Max	Min	Max
Unit 5	26.5	29.5	23.5	25	24.5	27	18.5	20	17	18.5	16.5	18	15	16.5	15.5	17	13.5	15	10	12
Unit 6	26	27	23	24	22	24	18	19.5	16.5	17.5	15.5	16.5	14	15	13.5	15.5	11	13	8.5	10
Unit 7	25	28.5	22.5	24.5	22	26	18	20.5	15.5	19	15.5	18	13	16	13	17	11	14.5	7.5	11.5
Unit 8	26		23		23		19.5		17		16.5		14		14		11.5		9	
Soil C	24.5	25.5	22	22.5	21	22	17.5	18.5	15.5	16	14.5	15.5	12.5	13.5	11.5	12.5	9.5	10.5	6.5	8
Unit 9	25.5	28.5	22.5	25	21	26.5	18	19.5	16	18	15.5	17	13.5	16	12.5	16	10.5	14	8	11

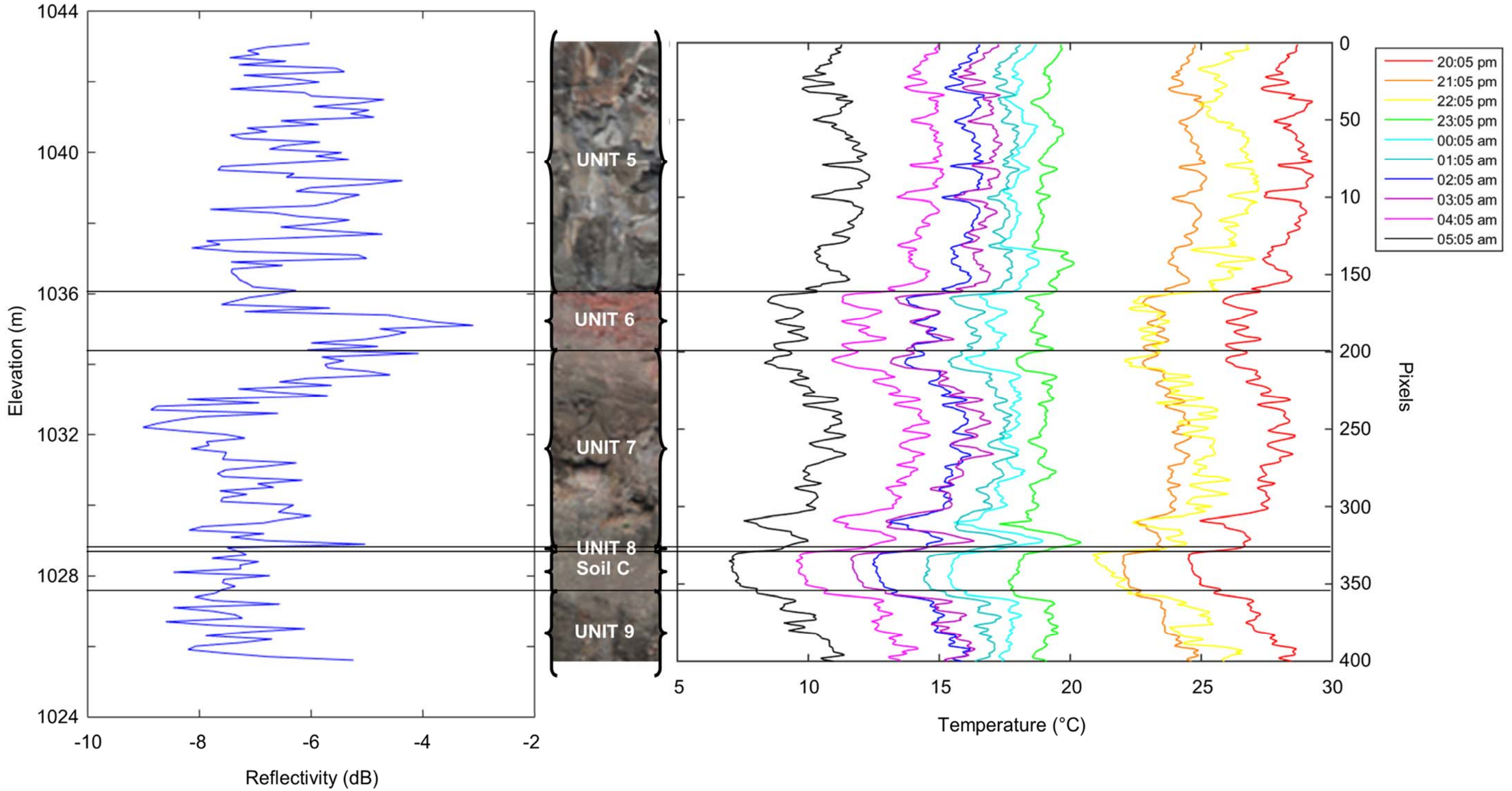

Figure 3-41. RP3 (left) and Column 256 temperature profiles (right). Solid lines indicate breaks between units.

Unit 7 differs from Unit 6 and Unit 5 in thermal response, whereby the top and bottom of Unit 7 are lower in temperature by approximately 1.5-2 °C than the middle of the unit. Reflectivity of Unit 7, in contrast, exhibits higher values of reflectivity at the top and bottom of the unit than the middle, by approximately 1-2 dB. This may be indicative of the top of bottom of the Unit 7 lava flow being more vesicular than the center, as higher reflectivity and lower temperatures have been associated with paleosols and high vesicularity.

Unit 8 is a very thin paleosol unit (0.1-0.5 m) which marks a significant difference in responses in both reflectivity and temperature profiles. Temperatures drop by 1-3 °C compared to Unit 7, and reflectivity of this unit is equal to the approximate average reflectivity of both Unit 7 and the underlying Soil C.

Soil C is similar to Soil B in that it is not a discrete unit on the slope, but rather erosional material which has accumulated on the slope and affects the thermal and LiDAR responses. The temperatures of Soil C are relatively constant within each time frame, with no more than a 1.5 °C difference between the minimum and maximum temperatures observed, indicating a consistent composition. The reflectivity of Soil C is similar to that of the underlying unit, Unit 9, and also is comprised of a small range (2 dB) of values.

Unit 9 shows a similar pattern in temperatures to Unit 7, in that the temperatures increase with decreased elevation on the slope. The full thickness of Unit 9 is not observed in this window, and the trend of increased temperatures continues to the end of the profile. The reflectivity of this unit, however, does not show a clear decrease as observed for Unit 7. The reflectivity range is not high (3 dB), and values are similar to Soil C.

Window 4

The profiles for the reflectivity and temperature values of Window 4 are RP4 and Column 89, taken through the unaltered portions of the slope to observe the differences between units (Figure 3-42). In Unit 13, reflectivity varies around -7 dB, decreasing to -8 dB near the bottom of the unit (Table 3-20, Figure 3-43). The temperatures also show a different pattern at the base of the unit, not differing by more than 1-2 °C until about 0.5 m from the bottom where the temperature rises by about 1 °C, then falls by 2-2.5 °C

(Table 3-21). These changes are small, and may only indicate variability within the unit, or they may indicate a slight change in composition of Unit 13 at the base.

Paleosol Unit 14 is markedly different from the overlying Unit 13, and exhibits a 1-2 dB higher reflectivity and a 0.5-2.5 °C cooler temperature. Both reflectivity and temperatures appear to increase with increased depth on the slope.

The profiles of reflectivity and temperature for Unit 15 behave quite similarly to Unit 7 in the previous Window 3, whereby the reflectivity is higher at the top and bottom of the unit (by ~0.5-1 dB) and temperatures are lower for those same intervals (by ~1-1.5 °C). As with Unit 7, this is interpreted to mean that vesicularity increases in the flow top and flow bottom of the Unit 15 lava flow.

Unit 16, another paleosol unit, exhibits reflectivity similar to the bottom of Unit 15, but temperatures are lower (by up to 2.5 °C). Unit 16 is comparable to Unit 14 in that temperatures also increase with depth in this layer. This is interpreted to mean there is a gradational boundary, from unconsolidated sediment to rock, between Unit 16 and the underlying Unit 17.

In Unit 17, reflectivity decreases compared to Unit 16 by 0.5-2 dB. The temperature trend of increasing with depth continues between Unit 16 to the top of Unit 17, but after less than 0.5 m, a 2.5 °C drop in temperature is observed. As this is the bottom of the window and the end of the profile, it is difficult to discern the reason, but it is possible a large joint occurs at that location.

Table 3-20. Reflectivity of units in the RP4 profile in Window 4. Elevations and reflectivity values are rounded to the nearest half.

Unit	Elevation of Lower Boundary (m)	Elevation of Upper Boundary (m)	Reflectivity Minimum (dB)	Reflectivity Maximum (dB)
Unit 13	1012.5	>1015.5	-8.5	-6.5
Unit 14	1012	1012.5	-6.5	-5.5
Unit 15	1003	1012	-8	-4.5
Unit 16	1002	1003	-7.5	-4.5
Unit 17	<1001	1002	-8	-6.5

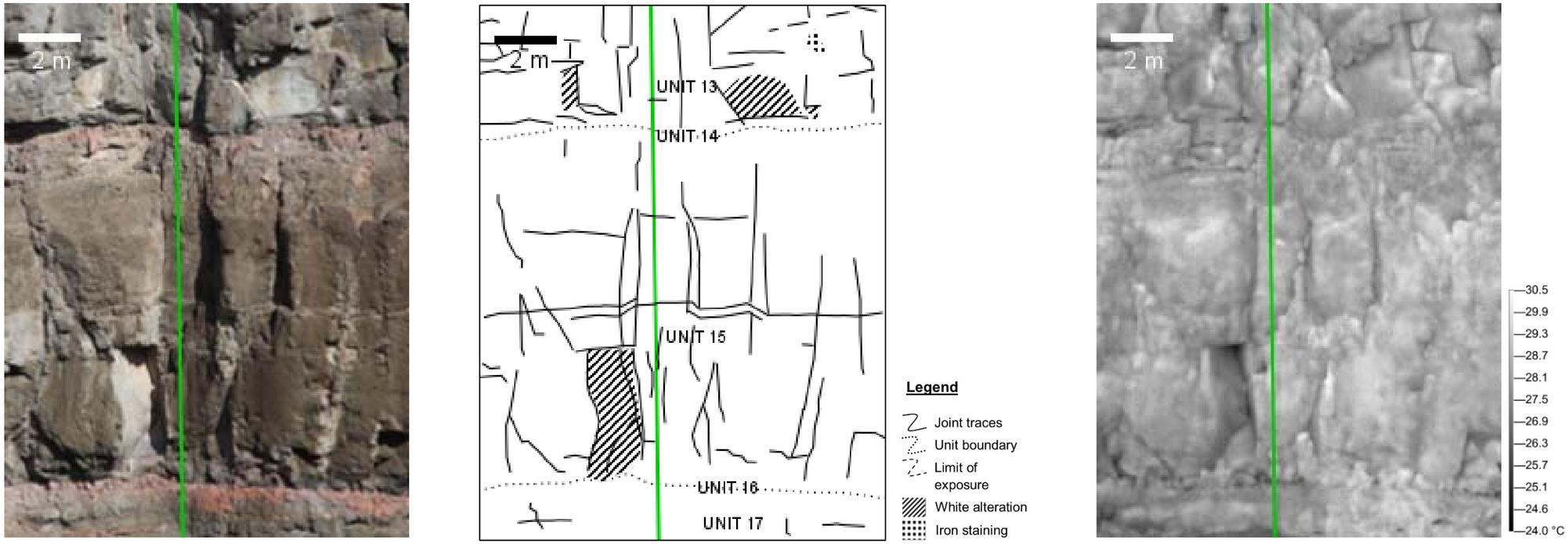

Figure 3-42. Photograph of Window 4 (left), interpretive line drawing of Window 4 with features shown (middle), and thermal image of Window 4 at 20:05, August 2, 2015 (right). Column 89 and RP4 are shown as a thick green line in all images.

Table 3-21. Minimum and maximum temperatures observed in the thermal profiles for Window 4. Temperatures are expressed in degrees Celsius. The hottest temperatures for each time frame are denoted with red font, the coolest, blue.

	20:05		21:05		22:05		23:05		00:05		01:05		02:05		03:05		04:05		05:05	
Unit	Min	Max	Min	Max	Min	Max	Min	Max	Min	Max	Min	Max	Min	Max	Min	Max	Min	Max	Min	Max
Unit 13	26.5	29	23.5	25	24.5	26.5	18	20	16.5	18.5	16	17.5	16	17	14.5	16.5	13	14.5	10.5	12
Unit 14	26	27	23	23.5	23	24	19	19.5	17	17.5	16	16.5	15	15.5	13.5	15	11.5	12.5	9	9.5
Unit 15	26	29.5	22.5	25	23	26.5	18.5	20	17	18.5	16.5	18	15	17.5	14	18	12	15.5	8.5	12.5
Unit 16	26	27.5	23	24	23.5	24.5	18.5	19	17	17.5	16	16.5	15	16	13.5	16	11.5	13.5	9	10.5
Unit 17	25.5	28	22.5	24	22	25	18.5	20	16.5	18	15	17	14	16.5	12.5	16	10.5	13.5	7.5	10.5

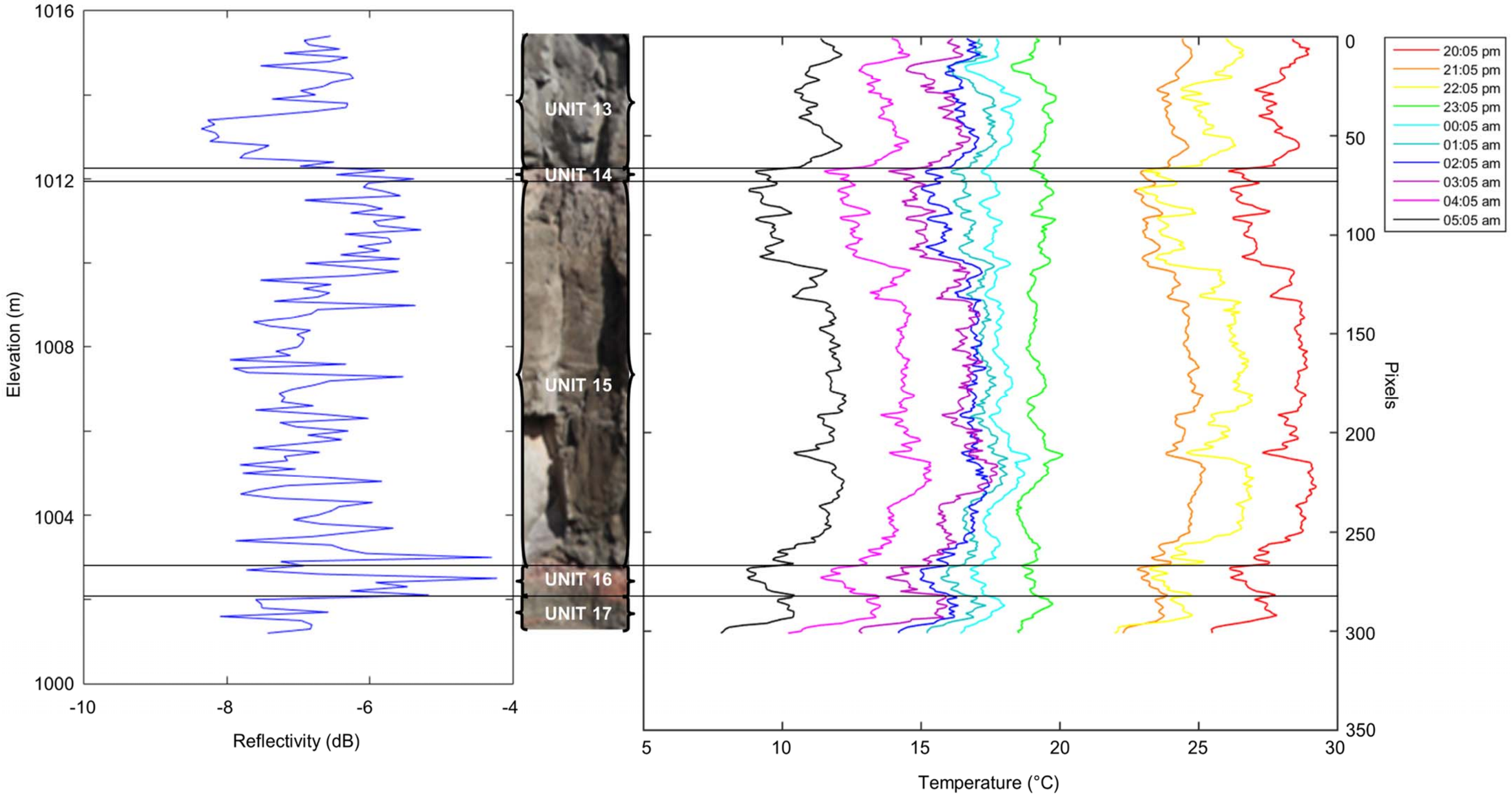

Figure 3-43. RP4 (left) and Column 89 temperature profiles (right). Solid lines indicate breaks between units.

3.2.2. LI1 Outcrop

The LI1 outcrop is on the eastern side of the Chasm, approximately 5.5 km from the Chasm canyon apex (Figure 3-1, Figure 3-44). This outcrop was used by Farrell (2010) and Farrell et al. (2007) as part of the Chasm lithofacies type section, whereby the Chasm was traversed on foot and outcrops were mapped by hand to create a composite geological log for the LI1 and neighbouring outcrops. It is intended in this section to demonstrate the mapping capabilities of the remote sensing surveys carried out in this study, and to facilitate the comparison of elements observed in both distanced and up-close methodologies. Unit designations by Farrell et al. (2007) are used instead of continuing the units from the LIP1 outcrop to allow for easier review of the two methods on one outcrop.

As mentioned in Chapter 2, a LiDAR scan, photographs, and an IRT survey of the cooling cycle of the rock were carried out on the LI1 outcrop from 20:45 on August 25, 2015 to 05:45 on August 26, 2015. The results of these surveys are presented below.

Photography

Photographs of the LI1 outcrop were taken both with a digital camera, as well as with the onboard camera of the LiDAR instrument. Both cameras offer high-resolution imagery, and although the images captured with the separate digital camera were higher resolution than those of the LiDAR onboard camera, the LiDAR images are employed for mapping of the slope. The LiDAR and IRT were both surveyed from approximately the same position, and therefore have similar views of the slope, whereas the photographs were taken up closer to the slope with the digital camera, thereby offering a view from a slightly different angle. It is thus better for comparison to use the LiDAR imagery in mapping, and use the separate photography as supplementary detailed photographs of units and features.

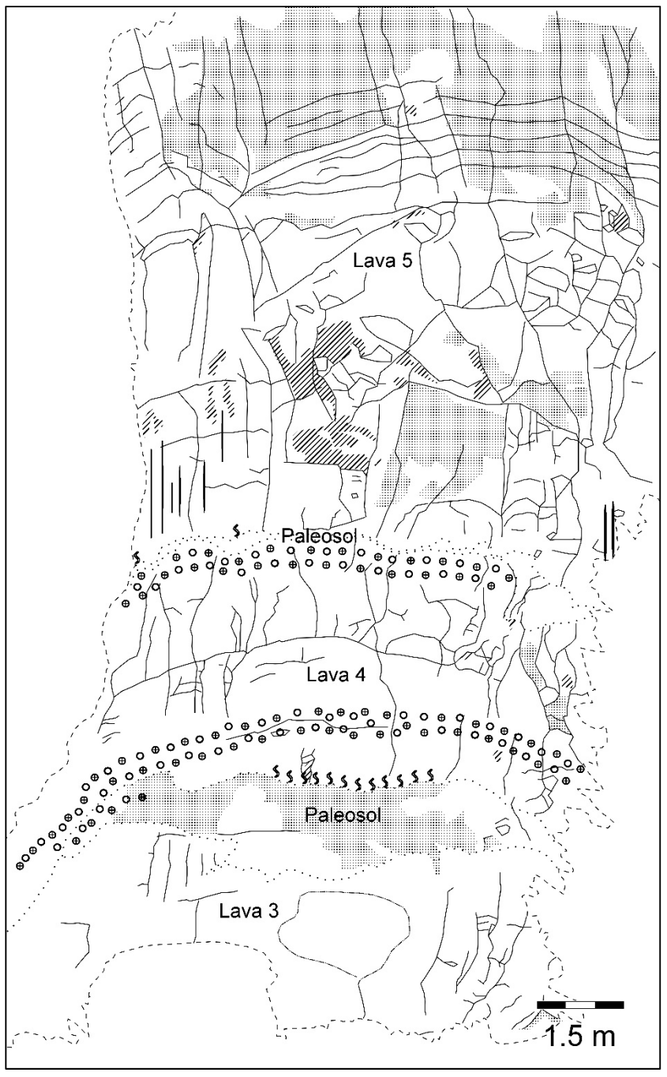

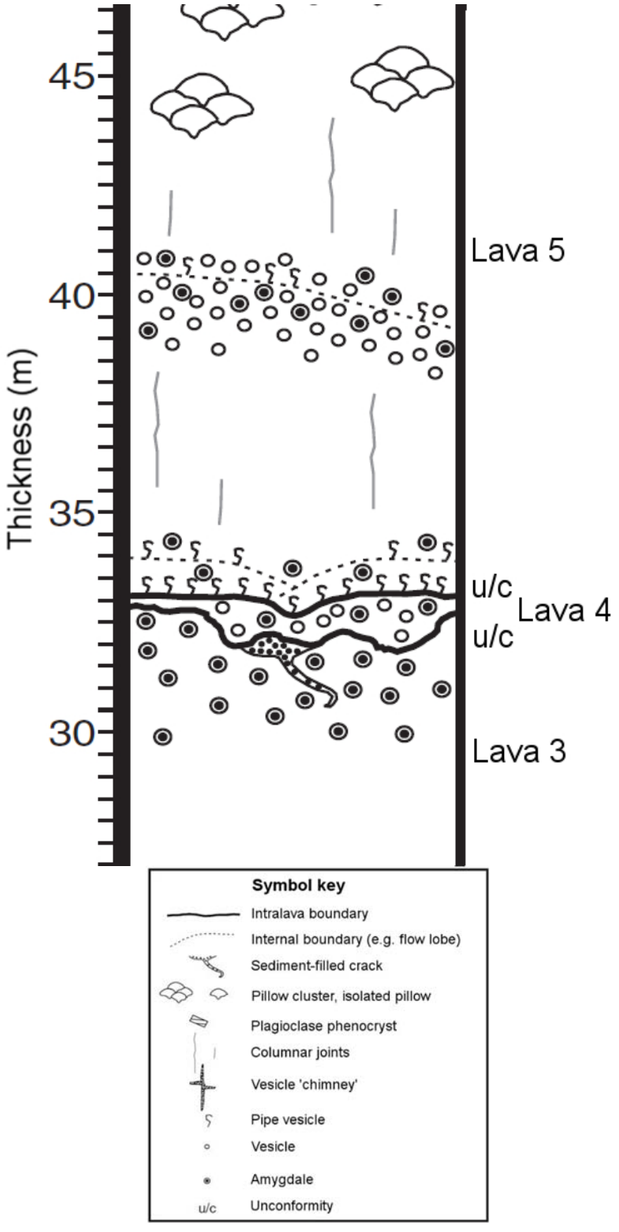

Figure 3-44. Photograph (left) and interpretive line drawing (middle) of the LI1 slope. The right image shows the composite section created by Farrell et al. (2007), clipped to the lavas relevant in LI1.

The LiDAR panorama is shown in Figure 3-44, and exhibits an outcrop with several lava and paleosol units. It is apparent that the imagery does not cover the entire outcrop, as the top of the exposed rock face is cut out of the image. The position at which the surveys could be conducted was on an ATV trail approximately 114 m downslope, resulting in a high view angle for the surveys. The LiDAR instrument can scan up to a maximum angle of 68° from horizontal, and even though the instrument was tilted to allow for greater coverage of the slope in this window, some of the upper portions of the slope were still not successfully scanned. As the LiDAR does not cover the missing portion of the LI1 slope, all analysis will be undertaken on the portions visible in all surveys.

Lava 3 is the stratigraphically lowest unit exposed, and is a non-vesicular unit of black basalt which exhibits very little to no alteration, with a maximum observable thickness of 4.5 m (Figure 3-44). Farrell et al. (2007) have mapped this unit to have an amygdaloidal flow top, though as their log is a composite (using major characteristics mapped from multiple correlated outcrops to create a representative section), the amygdales may not have been observable in the LI1 slope, and were not observed in photographs. In general, Lava 3 is amorphous, though does show what looks to possibly be a lobe of lava in the center of this outcrop. The flow top is irregular and has a sharp erosional boundary with the overlying paleosol. Farrell et al. (2007) also observed sediment-filled cracks in the upper boundary of Lava 3, which as seen in a photograph of the LIP1 slope (Figure 3-45), were observed in this study as well.

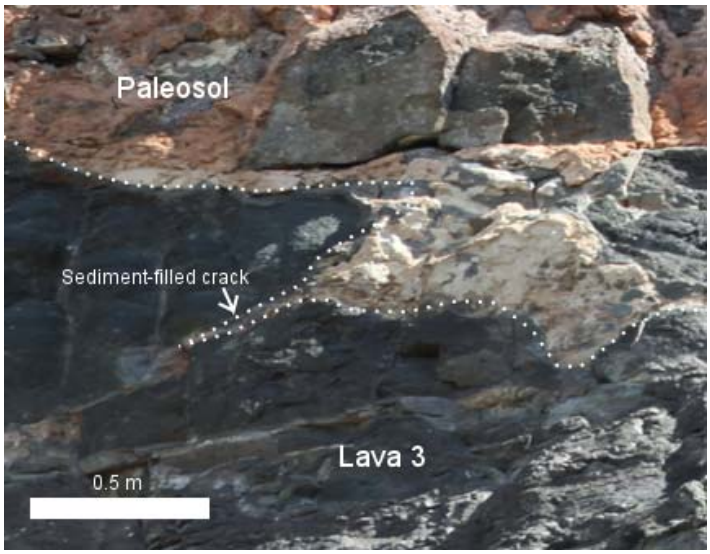

Figure 3-45. Image showing sediment filled crack in the upper boundary of Lava 3.

The paleosol overlying Lava 3 is orange to yellow in colour, is between 0-2 m thick, and contains blocks of (presumably) Lava 3 ranging in size from several centimeters to 0.5 m (Figure 3-44). It appears in photographs to be largely composed of unconsolidated, altered material, and shares a sharp, irregular contact with the overlying Lava 4.

In the Farrell et al. (2007) graphic log, Lava 4 exhibits an irregular thickness, such that in some cases it is not present. When observed, however, Lava 4 is amygdaloidal and vesicular (Figure 3-44). Much more variation was observed in the LI1 slope photography than is represented in the composite graphic log by Farrell et al. (2007). For example, pipe vesicles are observed in the flow bottom of Lava 4 up to approximately 6 cm long, and are filled with a white mineral, hence being so easily observed in photographs (Figure 3-46). Amygdales and vesicles are observed in large quantities (approximately 25-30%) immediately underlying an internal flow boundary, appearing as a band of highly vesicular and highly amygdaloidal lava in the middle of the Lava 4 unit (Figure 3-44, Figure 3-47). Above this internal flow boundary, the remainder of the Lava 4 flow is brownish-grey and approximately 4 m thick, which resulted in the underdevelopment of columnar jointing whereby columns are irregular in shape or non-uniform in size. The flow top of Lava 4 is also highly vesicular and amygdaloidal (30-40%), and shares a gradational and erosional boundary with the overlying paleosol (Figure 3-48).

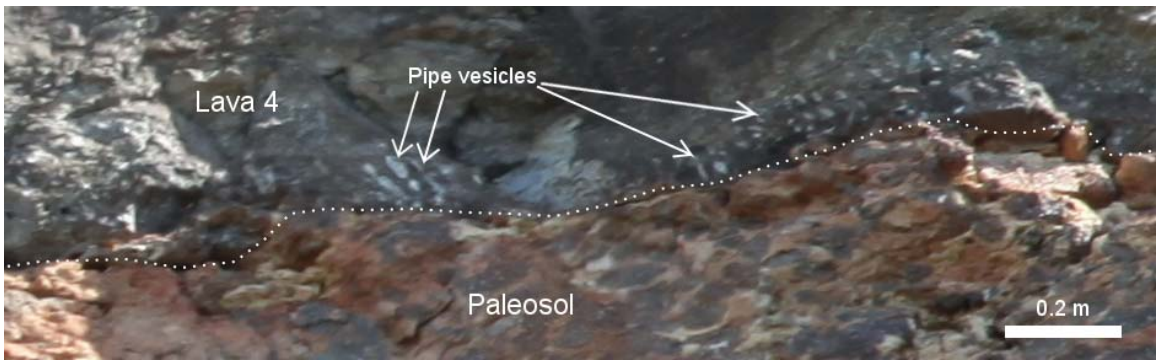

Figure 3-46. Pipe vesicles in the flow bottom of Lava 4, filled with a white mineral.

The second paleosol in the sequence exhibits more of a reddish-brown colour (in some places bright reddish orange), and varies in thickness from less than 0.1 m to ~0.2 m. It is comprised of unconsolidated soils which in some places have eroded away

leaving an overhang of Lava 5. Sediments infill cracks in the top of Lava 4 in some places.

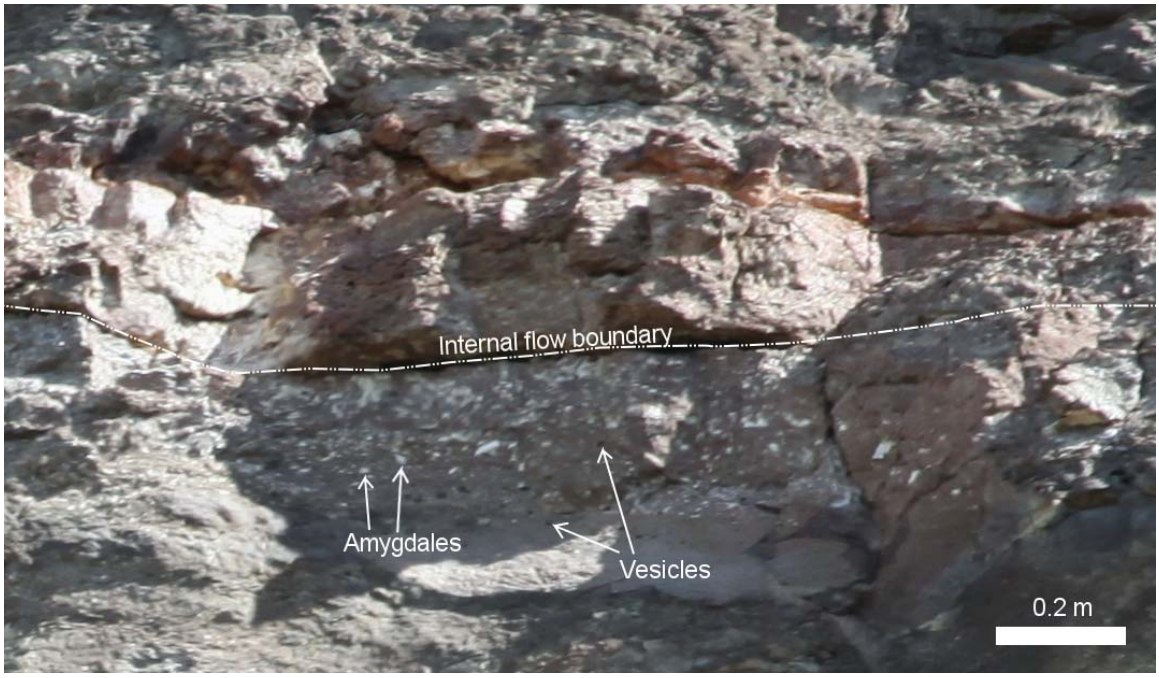

Figure 3-47. The internal flow boundary in Lava 4, with the underlying highly vesicular and amygdaloidal band.

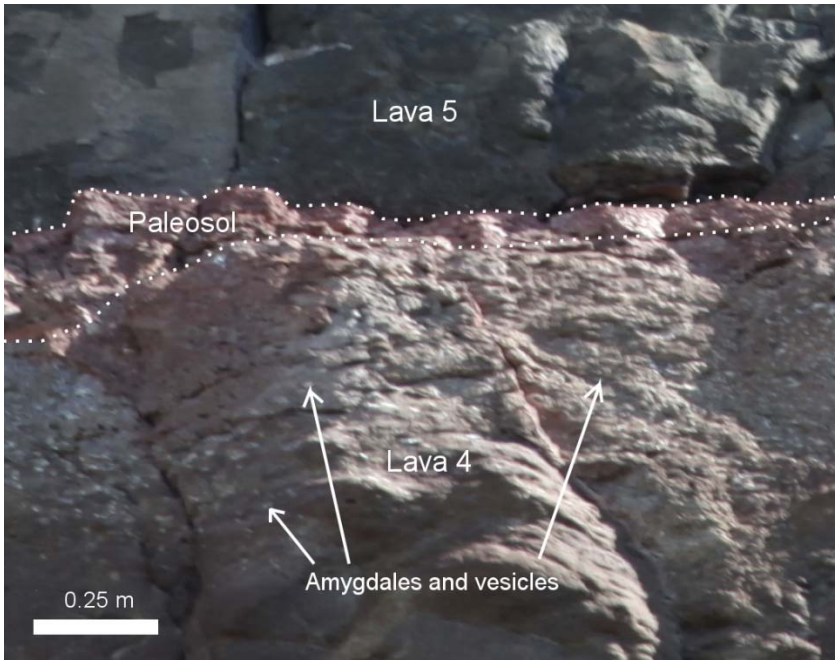

Figure 3-48. Amygdaloidal and vesicular flow top of Lava 4, also showing the gradational boundary between Lava 4 and the overlying paleosol.

Overlying a sharp and irregular upper boundary of the paleosol is Lava 5, the final unit observed in the LI1 outcrop. According to the graphic log by Farrell et al. (2007), Lava 5 is comprised of an amygdaloidal flow bottom with numerous pipe vesicles, the middle of the flow exhibits columnar jointing, and the unit is composed of lava lobes nearer to the flow top (Figure 3-44). All of these features are observed in the LI1 outcrop photography, as seen in the interpretive line drawing of the slope (Figure 3-44), with the exception of the flow top which was not within the window of observation. Amygdales and pipe vesicles in this section of the Lava 5 flow bottom are scarce (Figure 3-48), however columnar jointing is well developed as Lava 5 is quite thick (maximum observed thickness is approximately 12 m). The bottom and top thirds of the exposed Lava 5 in the LI1 outcrop have more regularly spaced and well-formed jointing, forming the colonnade portions of the flow, and the middle displays a more blocky and irregular texture as part of the entabulature zone (Figure 3-44). Lava 5 is also the most altered of the observed units in this slope, with large areas covered by white alteration (which is mainly reserved for the entabulature zone) and iron staining (generally observed in the upper colonnade). Chimney vesicles, however, are also found in the lower portions of Lava 5, ranging in size from 1-2 m. They are observed as tall and narrow, discoloured, vertical features in the slope (Figure 3-49).

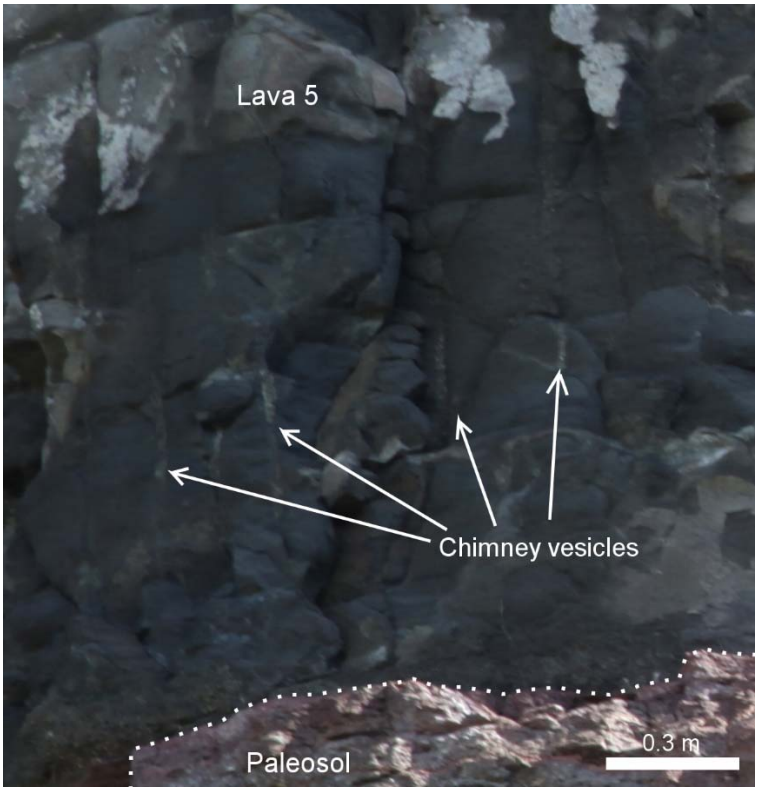

Figure 3-49. Chimney vesicles observed in the bottom portion of Lava 5 in the LI1 slope.

IRT

Unlike the windows on the LIP1 slope, the IRT survey on the LI1 slope revealed that most basic features of the outcrop (columnar and sub-horizontal jointing, unit boundaries, soil, vegetation, alteration) are visible in the thermal imagery at all times throughout the survey, with the exception of alteration (Figure 3-44). There are, however, observable differences between subsequent images which highlight various features at different times. For example, in the IRT image of LI1 at 20:45 on August 25, 2015 (Figure 3-50), the most distinguishable features in the slope are the cooler paleosols and amygdaloidal/vesicular portions of the slope, which exhibit a minimum difference in temperature from the non-vesicular lava of 1.2 °C. As unconsolidated sediments and porous rock have more surfaces exposed to air, it would follow the temperatures would appear cooler than surrounding solid rock.

Jointing in the 20:45 image is also observed, though does not have nearly the temperature difference as displayed in the 05:45 IRT image on August 26, 2015 (Figure 3-50). Columnar joints in the 05:45 image show temperatures at least 2.2 °C greater

than the surrounding lava blocks. This is likely because the exterior rock has cooled faster than the interior of the slope, which is radiating its heat out through the available flowpaths, the joints.

The resolution of the IRT imagery is much lower, as it was a 100 mm focal length lens from the same distance as the LiDAR and photography (400 mm lens) surveys, yielding approximately 2.5 cm/pixel resolution for the IRT imagery, and sub-centimeter resolution in the LiDAR and photography datasets. The fine details such as amygdales and the various forms of vesicles, therefore, are not observed in the IRT images of the LI1 slope. As noted with the two example thermal images, however, the effects of features such as amygdales and vesicles, which serve to increase the exposure of the slope to the air, are most certainly observed.

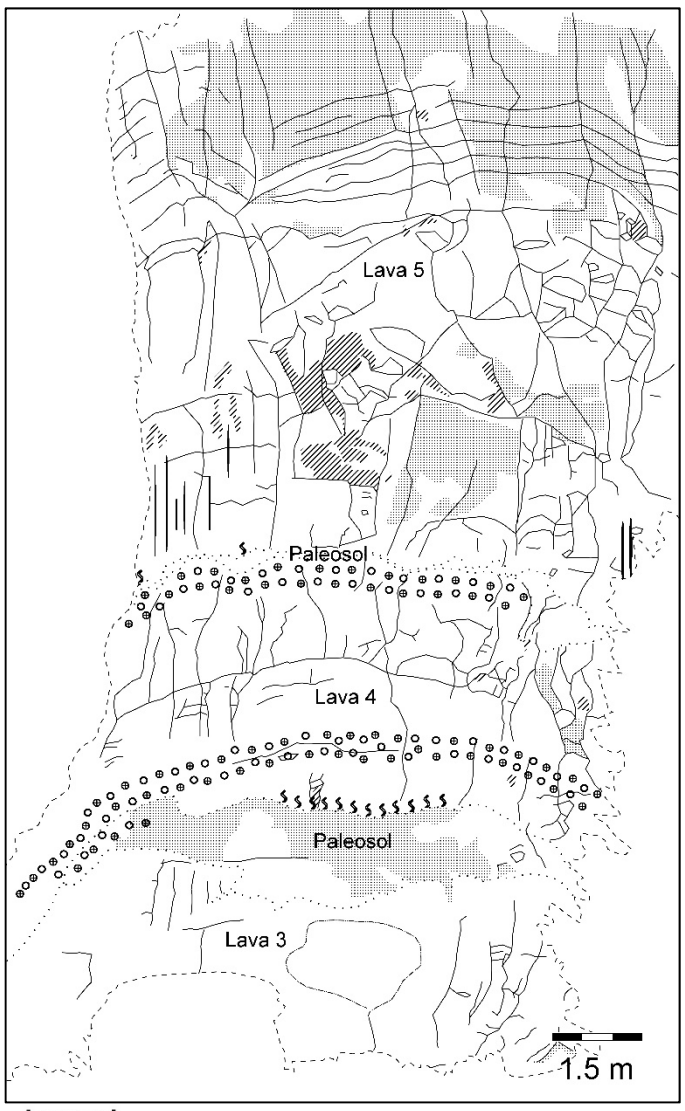

Legend

- Joint traces
- Unit boundary
- Limit of mapping
- Lava lobe
- White alteration
- Iron staining
- Pipe vesicles
- Amygdales
- Chimney vesicle
- Vesicles

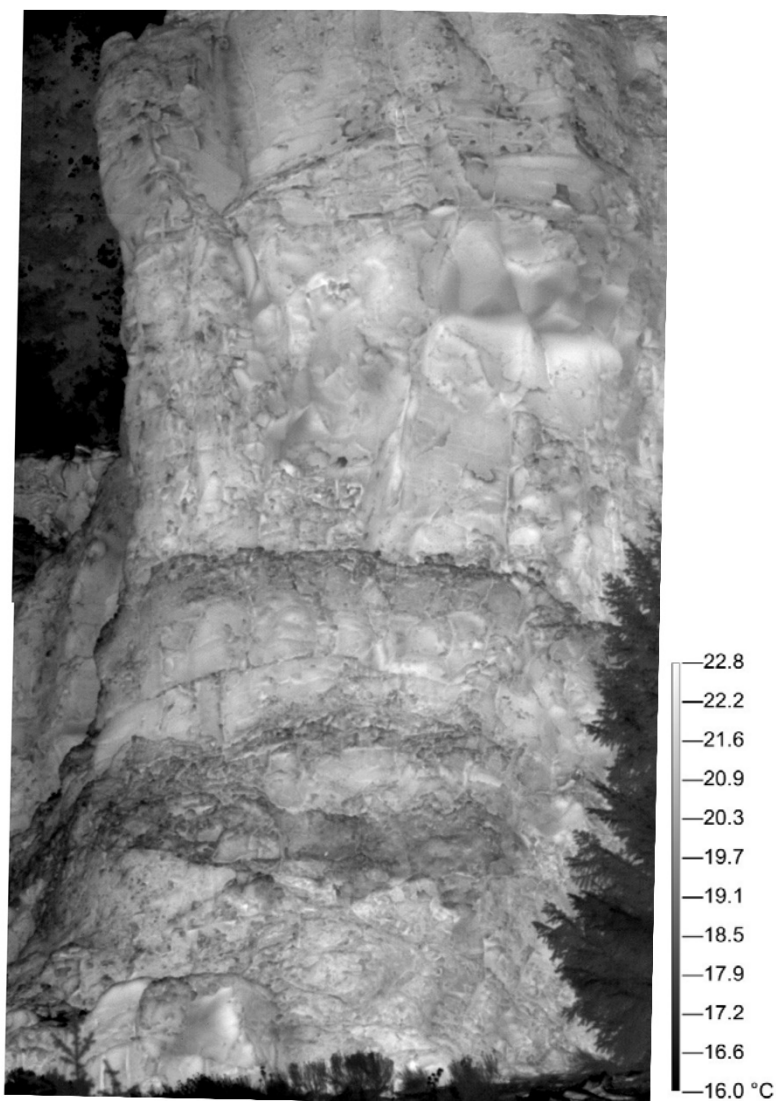

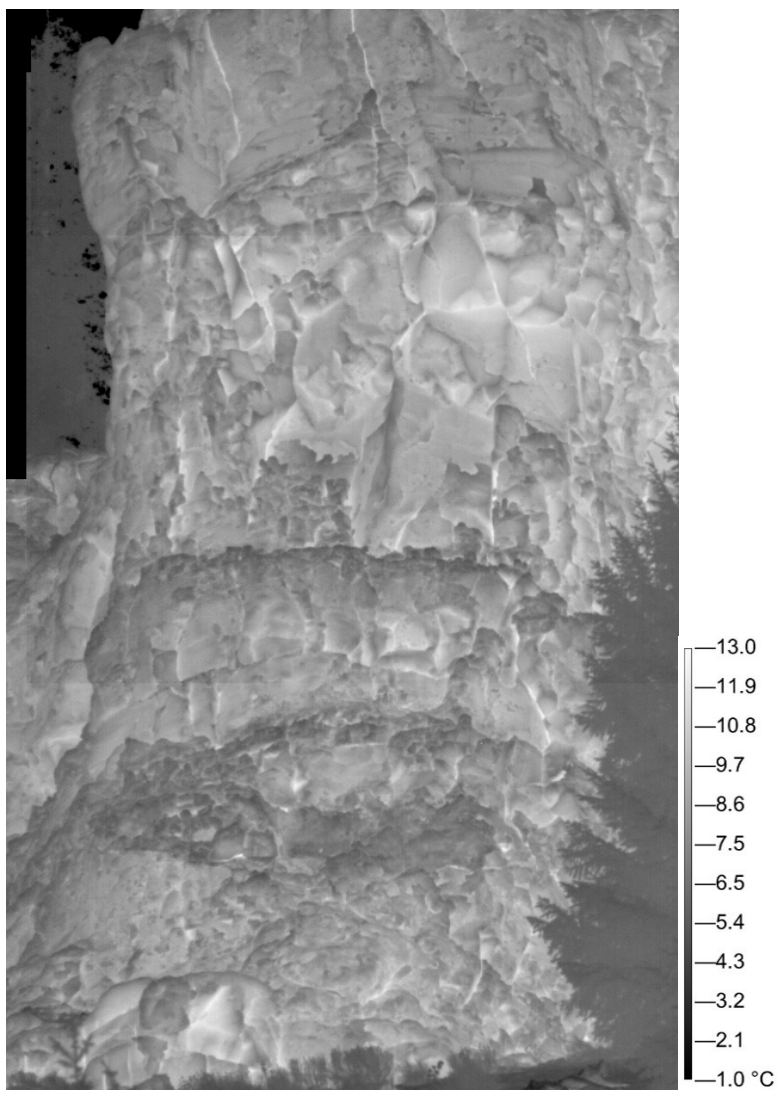

Figure 3-50. Photograph (top left), interpretive line drawing (top right), and IRT imagery of the LI1 slope. The bottom left image is that of 20:45 on August 25, 2015, and the bottom right image is at 05:45 on August 26, 2015.

LiDAR and Reflectivity

As LiDAR reflectivity is influenced by factors related to rock type, such as surface relief, texture, and colour, a LiDAR scan was completed for the LI1 slope to observe the patterns in reflectivity. The LiDAR points were divided into bins based on their value of reflectivity; the reflectivity values of points in the LI1 scan have a total range between -15 and 3 dB (Table 3-22), and have approximately a normal distribution (Figure 3-51).

Table 3-22. Point totals within each LiDAR reflectivity range. Points are selected as greater than or equal to the minimum reflectivity, and less than or equal to the reflectivity maximum. The total number of points in the type section point cloud is 8,535,165. The values in grey are the median range of the reflectivity values.

Reflectivity minimum (dB)	Reflectivity maximum (dB)	Points
3	---	0
2	2.99	1
1	1.99	1
0	0.99	2
-1	-0.01	44
-2	-1.01	5,926
-3	-2.01	98,821
-4	-3.01	259,948
-5	-4.01	650,344
-6	-5.01	1,651,980
-7	-6.01	2,358,514
-8	-7.01	1,798,095
-9	-8.01	1,162,327
-10	-9.01	381,614
-11	-10.01	88,081
-12	-11.01	25,134
-13	-12.01	18,542
-14	-13.01	16,893
-15	-14.01	8,898
---	-15.01	0

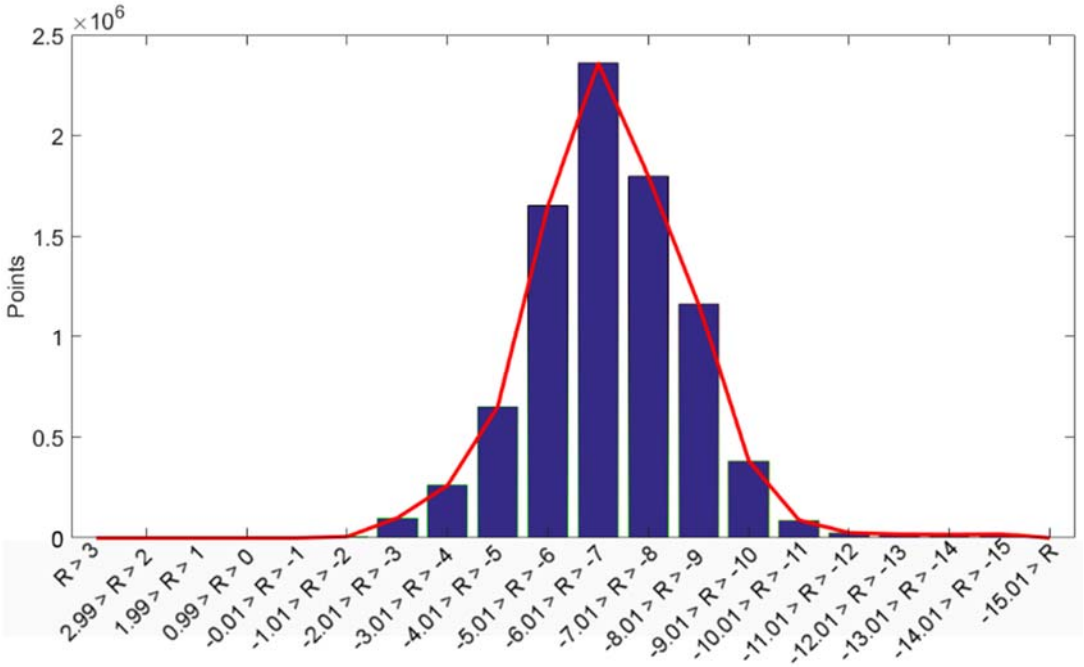

Figure 3-51. Histogram of reflectivity values. For exact point values see Table 3-22.

The reflectivity range which includes the greatest number of points can be considered as a 'critical divide', at which the trends of point reflectivity are reversed. The 'critical divide' for the Chasm type section point cloud is in the range -7 to -6 dB, where there is a shift from lighter coloured bands more prominent in the point clouds (Figure 3-52, A to E), to darker coloured bands in the lava slope becoming dominant (Figure 3-52, G to L). This is expected, as lighter colours are more reflective and darker colours absorptive, giving lighter colours higher values of reflectivity. Because of the influence colour has on reflectivity, it is observed that reflectivity between 0 and -4 dB is more representative of oxidized paleosol units (Paleosol 1=P1, Paleosol 2=P2), as well as the bands of amygdaloidal and vesicular lava within the lava units (Vesicular/Amygdaloidal Lava 4=VL4). Areas on the slope with alteration have reflectivity values more similar to the paleosols and amygdaloidal lava (White Altered Lava 5=WAL5, Iron Stained Lava 5=ISL5), between -3 and -5 dB. The unaltered, non-vesicular portions of the lava units (Unaltered Lava 3=UL3, Unaltered Lava 4=UL4, Unaltered Lava 5=UL5) are observed with reflectivity of -5 to -12 dB, and vegetation and slope edges (areas with large angles to the scanning instrument, i.e. slopes facing away) have the lowest reflectivity of -11 to -15 dB. There were either too few points (3 to -1 dB) or the point clouds looked similar to adjacent reflectivity ranges (-11 to -15 dB), so not all reflectivity point clouds of the LI1 slope are shown in Figure 3-52.

A reflectivity profile, RP7, was taken through the LI1 slope to further demonstrate the difference in reflectivity within and between units, based on unit characteristics (Figure 3-53, Table 3-23). The profile was taken between approximately 1016-1038 m a.s.l. elevation through the LiDAR scan of the slope, and at the lowest elevations features the lowest reflectivity values, which represent the vegetation at the base of the exposed rock face. The unaltered lava units exhibit the next lowest reflectivity, most commonly between approximately -9 and -7 dB. The altered portions of the slope (white altered and iron staining) have reflectivity values over a similar range to paleosol units and areas with high vesicularity, though they do have lower minimum reflectivity. Overall, the reflectivity response from units is: P or V units > ISL or WAL units > UL units > Vegetation.

Table 3-23. Reflectivity of units in the LI1 slope. Elevations and reflectivity values are rounded to the nearest half.

Unit	Elevation of Lower Boundary (m)	Elevation of Upper Boundary (m)	Reflectivity Minimum (dB)	Reflectivity Maximum (dB)
ISL5	1036.5	>1038	-6.5	-4
UL5	1033	1036.5	-10	-5
WAL5	1029.5	1033	-7.5	-3.5
UL5	1028	1029.5	-9	-6
P2	1028	1028	--	--
VL4	1027	1028	-5.5	-4.5
UL4	1024.5	1027	-8.5	-5.5
VL4	1023.5	1024.5	-6	-4
UL4	1022.5	1023.5	-9	-7
P1	1020.5	1022.5	-5.5	-3
UL3	1017.5	1020.5	-11	-4
Vegetation	1016	1017.5	-15	-8.5

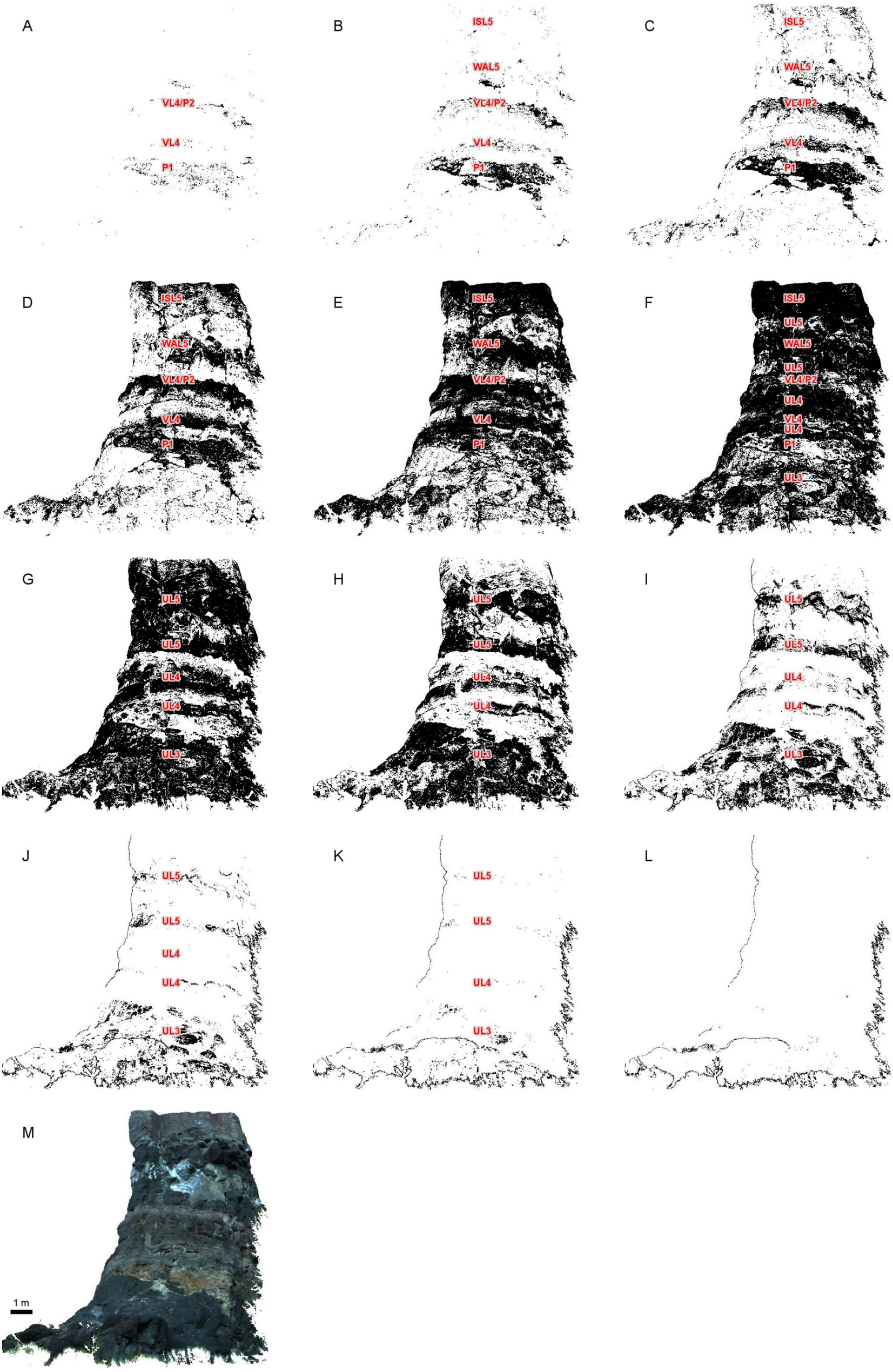

Figure 3-52. Point clouds of reflectivity values ranges in decibels; A: -1 to -2; B: -2 to -3; C: -3 to -4; D: -4 to -5; E: -5 to -6; F: -6 to -7; G: -7 to -8; H: -8 to -9; I: -9 to -10; J: -10 to -11; K: -11 to -12; L: -12 to -13; M: true colour LiDAR point cloud. Areas with points are annotated with numbers matching the Lava unit: UL = unaltered lava, P = paleosol, VL = vesicular/amygdaloidal lava, WAL = white altered lava, ISL = iron stained lava.

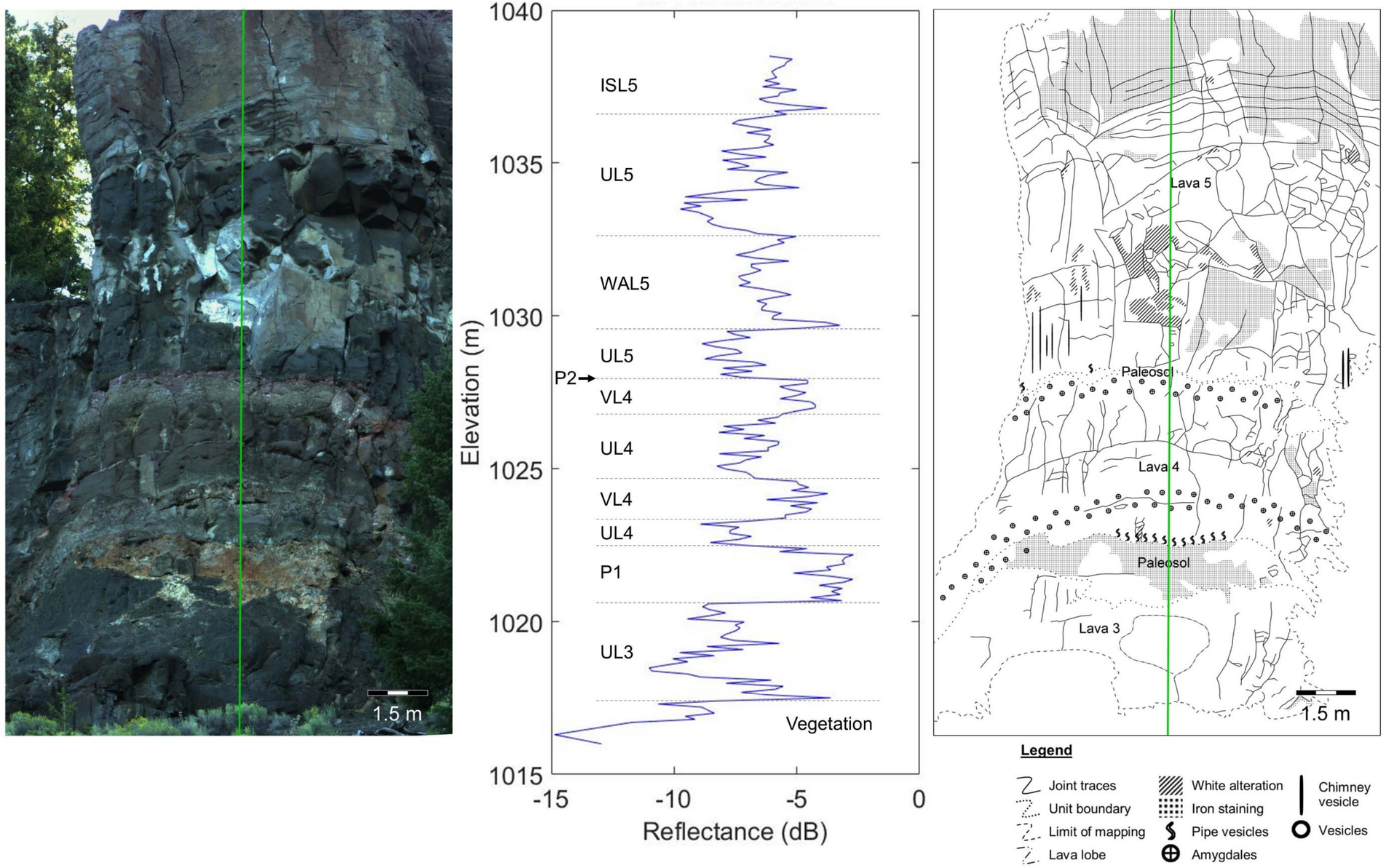

Figure 3-53. RP7 location on the LI1 slope is shown in the photograph (left) as well as the interpretive line drawing (right) as a vertical green line. Reflectivity along the profile is shown in the middle image, with changes in units and features annotated with numbers matching Lava units: UL = unaltered lava, P = paleosol, VL = vesicular/amygdaloidal lava, WAL = white altered lava, ISL = iron stained lava.

3.3. CVB

3.3.1. Field Description

A detailed field description was completed for CVB1 and CVB2 (Figure 3-54). Though both sites are Cheakamus basalts, the features visible in each of the rocks are slightly different, as the CVB2 samples are more weathered, making original texture and fabric more difficult to discern.

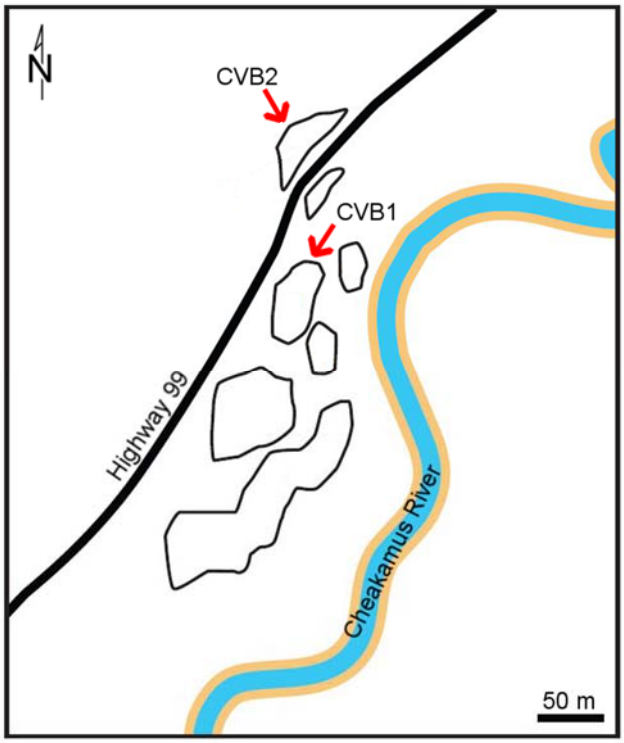

Figure 3-54. Zoomed-in map of outcrops in the CVB field area; outcrops used in this study are indicated with a red arrow (modified from Woodell, 2012).

Geology

The outcrop at CVB1 is about 21 m wide and 5-7 m high (Figure 3-55). The significant vegetation cover at this site did hinder the field surveys. There are two units at CVB1, solely divided according to the structures within the units, as their compositions are very similar if not identical. Unit 1, on the west side of the outcrop, is 5-7 m high and 9 m wide, and is composed of a dark grey aphanitic groundmass (~78%) with phenocrysts of feldspar (~20%) and olivine (~2%) between 1-2 mm in size (Figure 3-55).

Feldspar phenocrysts are elongate, but do not appear to have any preferred orientation. Several larger feldspar phenocrysts are visible, and range in size up to 6 mm; the edges of the crystals appear intact (there is no evidence to suggest resorption into the melt), however further petrographic studies are required to corroborate this. Olivine phenocrysts are less numerous than feldspar; no crystals larger than ~1.5 mm are visible. The weathered colour of the unit is light brown to rusty. The structures of Unit 1 consist of large, vertical to sub-vertical columns ~0.5 m in diameter. These columns also contain sub-horizontal, curved joints (concave-upwards) which approximately parallel chisel marks along the columns, and commonly have column corners that have fallen away. These types of horizontal joints on columns are generally referred to as ball-and-socket joints (Figure 3-56; Woodell, 2012).

A

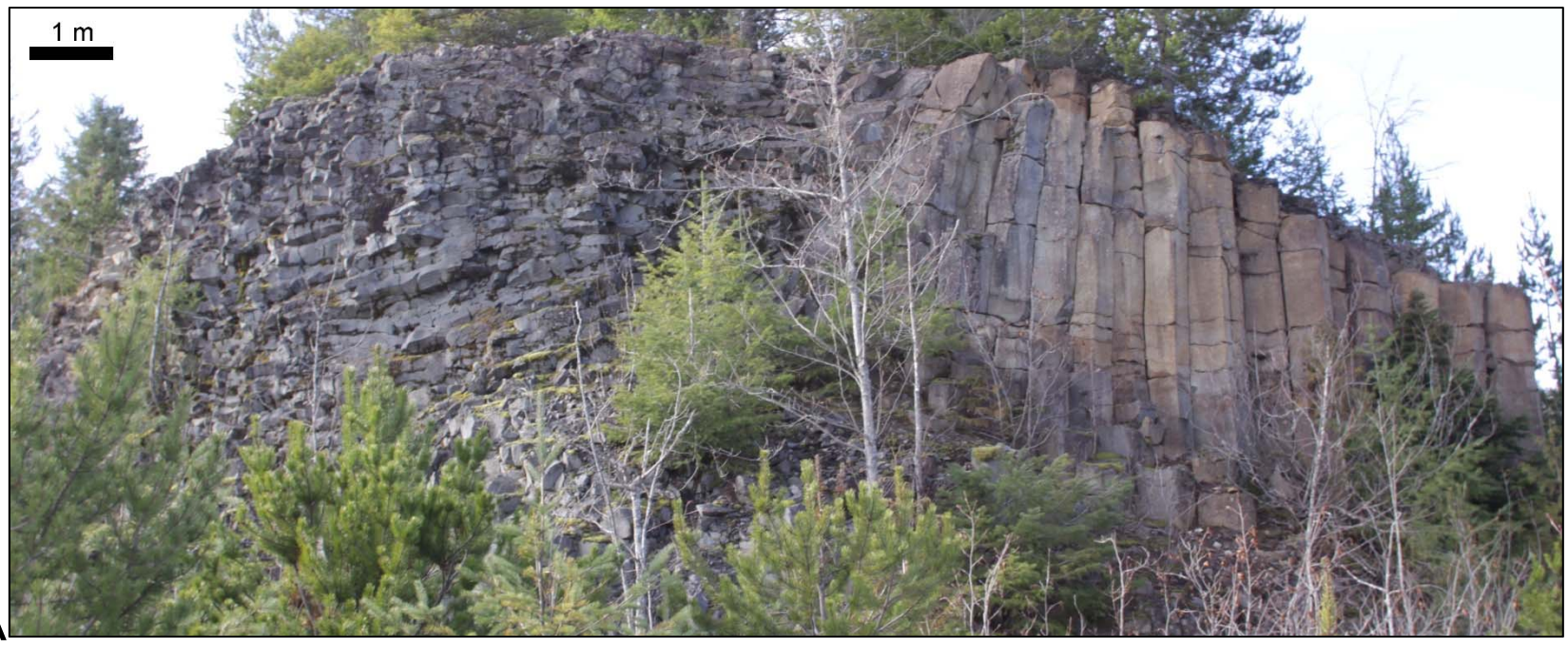

B

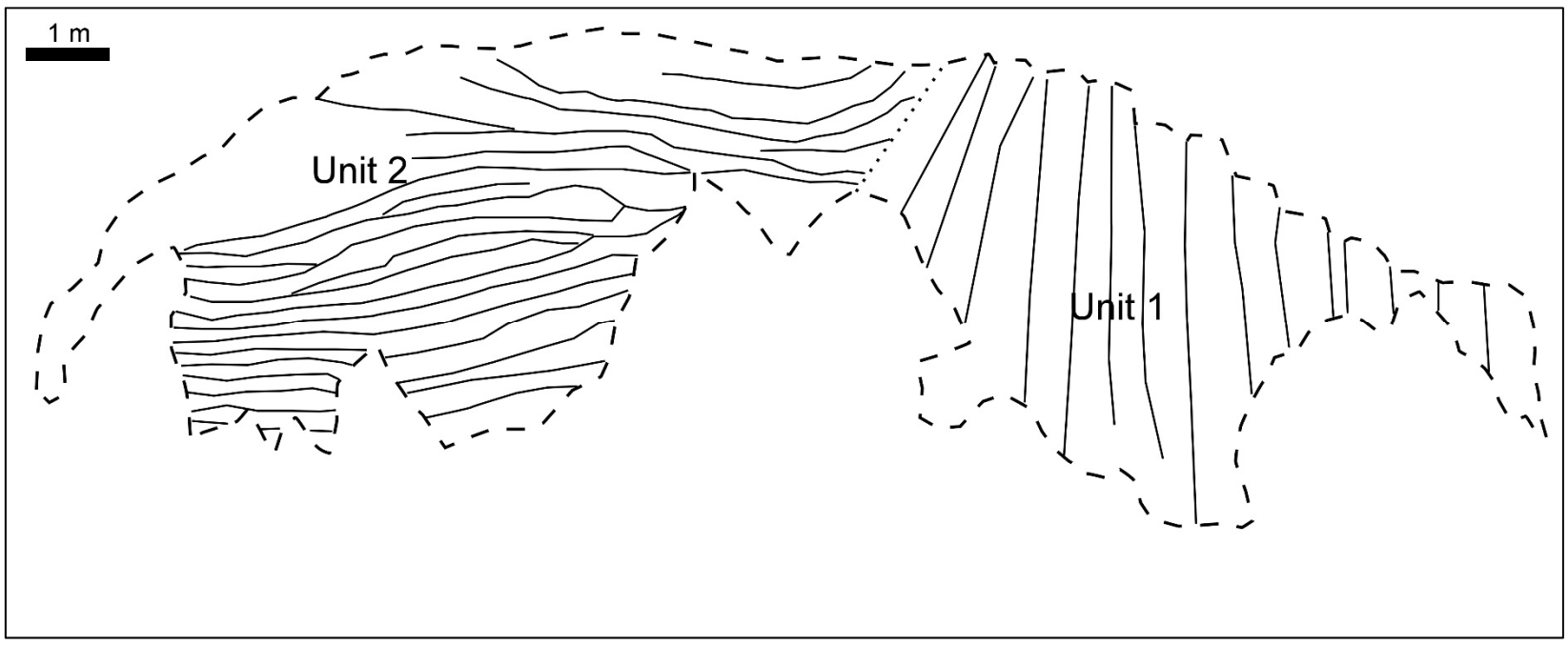

Legend

Column traces
Unit boundary
Limit of exposure

C

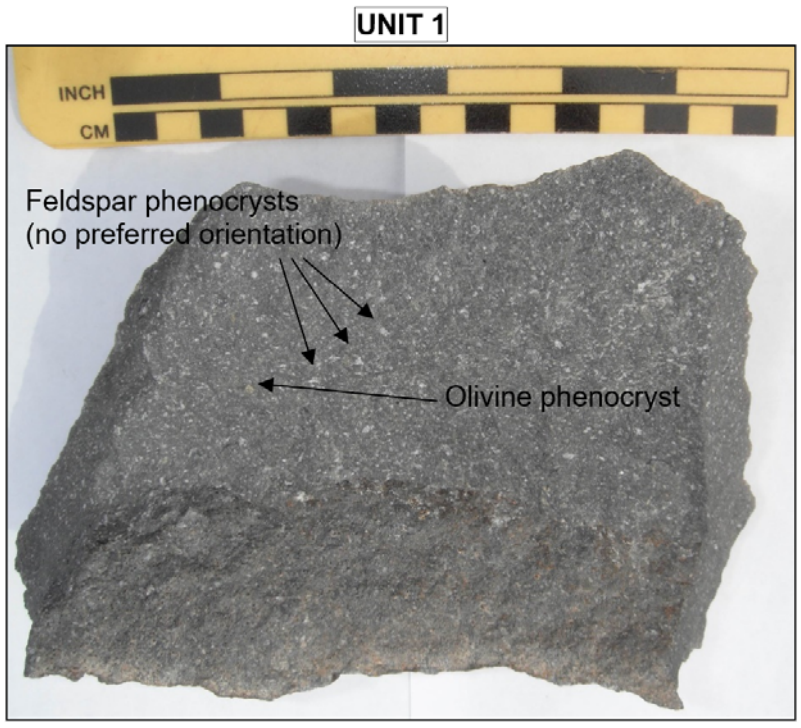

D

Figure 3-55. Outcrop at CVB1 (A), photograph taken facing ~210° (south-southwest). Due to vegetation and talus debris, the bottom of the flow is not visible. The interpretive line drawing of the photograph is shown in B, with full columns roughly delineated to give a representation of the relative column widths and orientations in the outcrop. Samples of the units at CVB1 are in C and D.

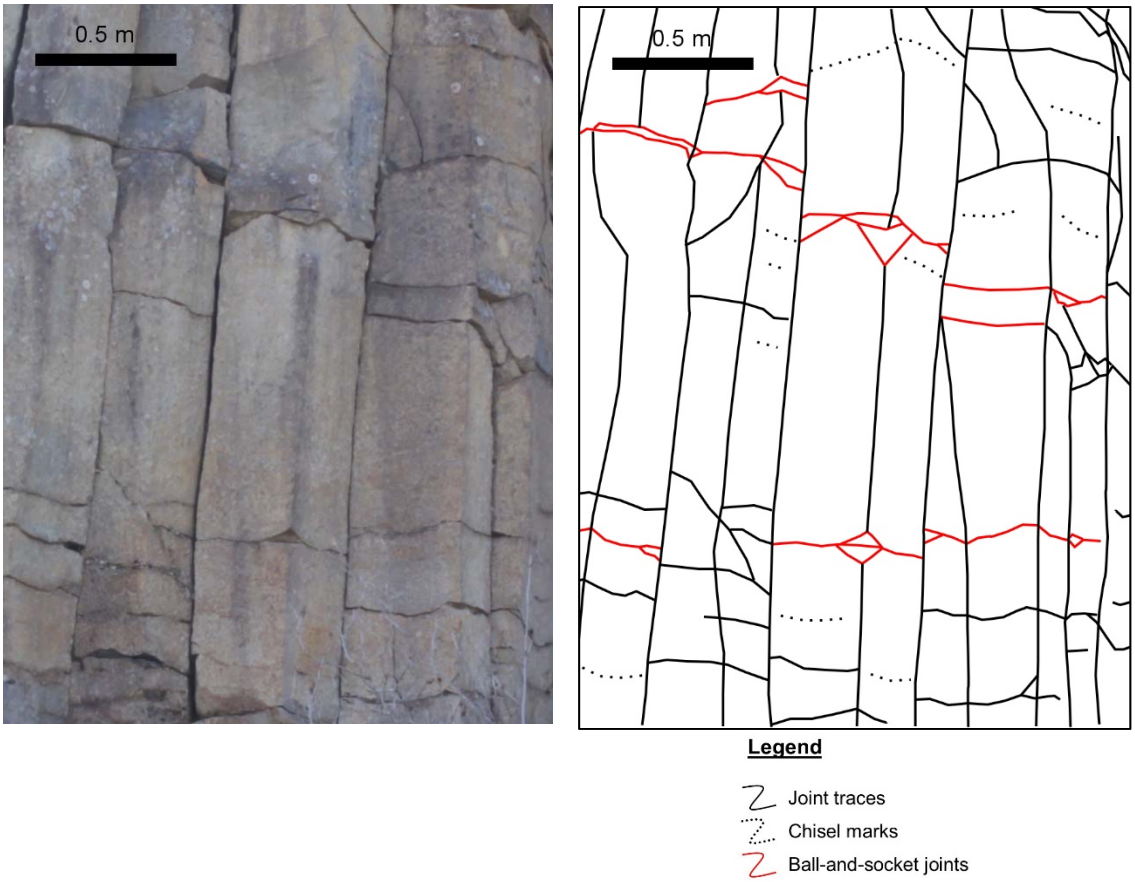

Figure 3-56. Close-up of the Unit 1 columns at CVB1, with ball-and-socket joints highlighted in red. Only ball-and-socket joints with typical morphology are highlighted.

Unit 2 at CVB1 is 5-7 m high, 12 m wide, and appears to be of the same or similar composition as Unit 1, however many of the elongate feldspar phenocrysts are aligned in a particular orientation (Figure 3-55). As the sample was found at the base of the outcrop in talus debris, this preferred orientation direction for the feldspar crystals could not be determined. The structures of Unit 2 consist of horizontal to sub-horizontal columns, approximately 0.1-0.2 m in diameter. Sub-vertical joints break down the columns into smaller blocks, just as the ball-and-socket joints do in Unit 1, however these joints do not appear to have a large curvature to them; those that are curved are concave to approximately the northwest.

The contact between Units 1 and 2 is a gradual change in orientation of the columnar jointing, as evidenced by the reclined column (column which at a 30-40° angle

from vertical) in the center of Figure 3-55, as well as a sharp change in column diameter. The rock composition does not appear to change across the contact.

The outcrop at CVB2 is approximately 28 m wide, and 12 m high (Figure 3-57). There are three units visible at CVB2: Unit 1, bedrock, is the lowermost visible layer, Unit 2 is the colonnade portion of the basalt lava flow (the lower portion); and Unit 3 is a massive, blocky upper colonnade portion of the basalt lava flow.

Unit 1 is approximately 2 m thick, and contains two sub-units (Figure 3-58). Leucocratic light grey crystalline rock containing quartz, biotite, plagioclase, potassium feldspar, and epidote veins characterizes Unit 1a, within which the crystals are between 1-3 mm in size. There are minor occurrences of pyrite in this unit, which results in a rusty weathered colour on several joint surfaces. Several large veins of microcrystalline pinkish-white material (mostly quartz) approximately 2-6 cm in width occur in Unit 1a, becoming very coarse-grained (approximately 0.5-1 cm crystals) further north in the outcrop, displaying quartz, potassium feldspar, and plagioclase crystals. Unit 1b is characterized by mesocratic, medium grey-green very fine-grained crystalline rock. Its colour possibly suggests chloritic alteration, or high pyroxene content. This unit weathers to a rusty colour, implying ferrous minerals are present; also within this unit are sub-millimeter sized pinkish-white veins. The contact between Units 1a and 1b is sharp, with Unit 1b occurring between two outcrops of Unit 1a, leading to the hypothesis that Unit 1b may be a dyke or other type of intrusion.

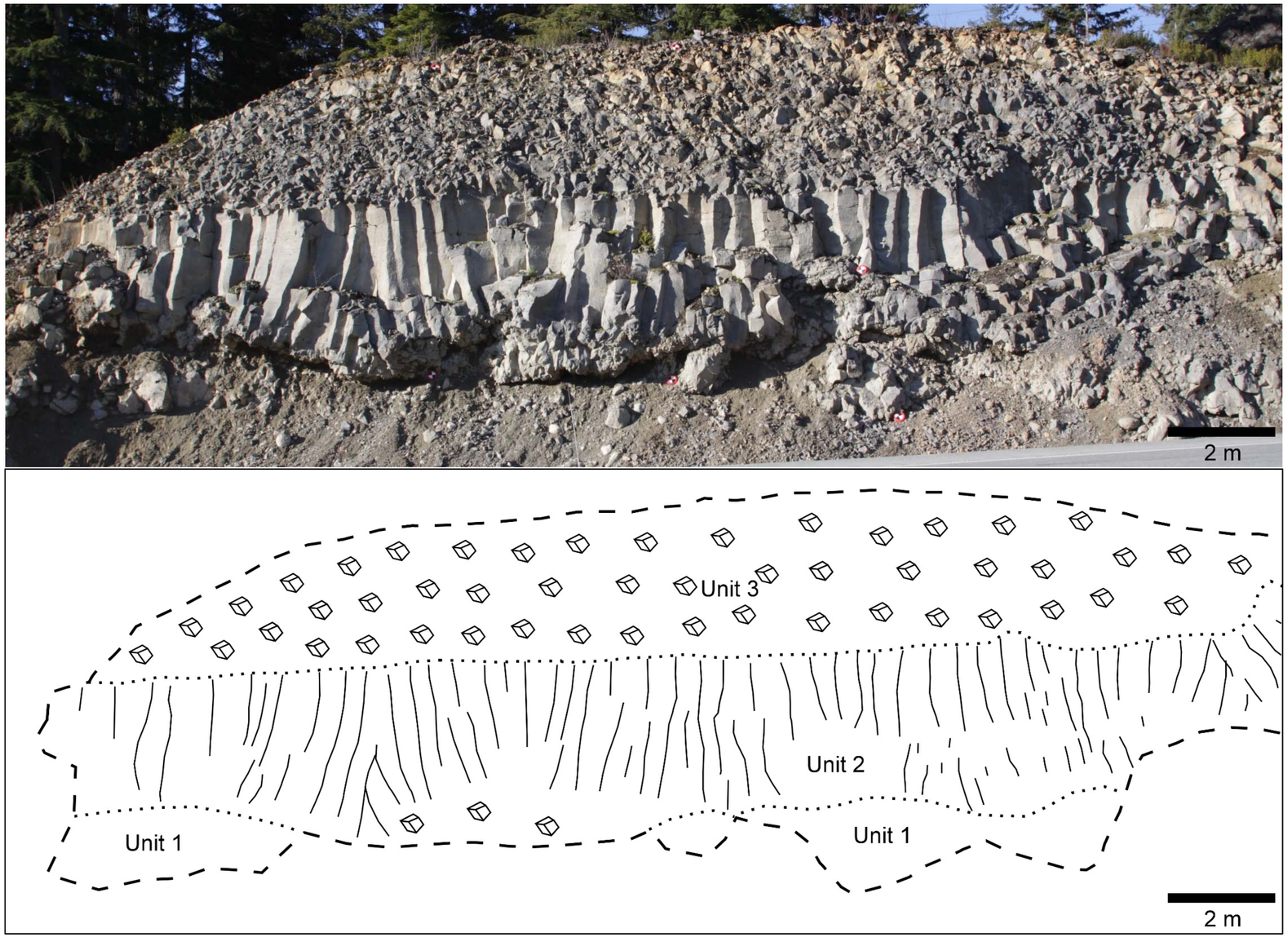

Figure 3-57. The three units of CVB2 (top) with interpretive line drawing (bottom); photograph was taken facing ~300° (west-northwest).

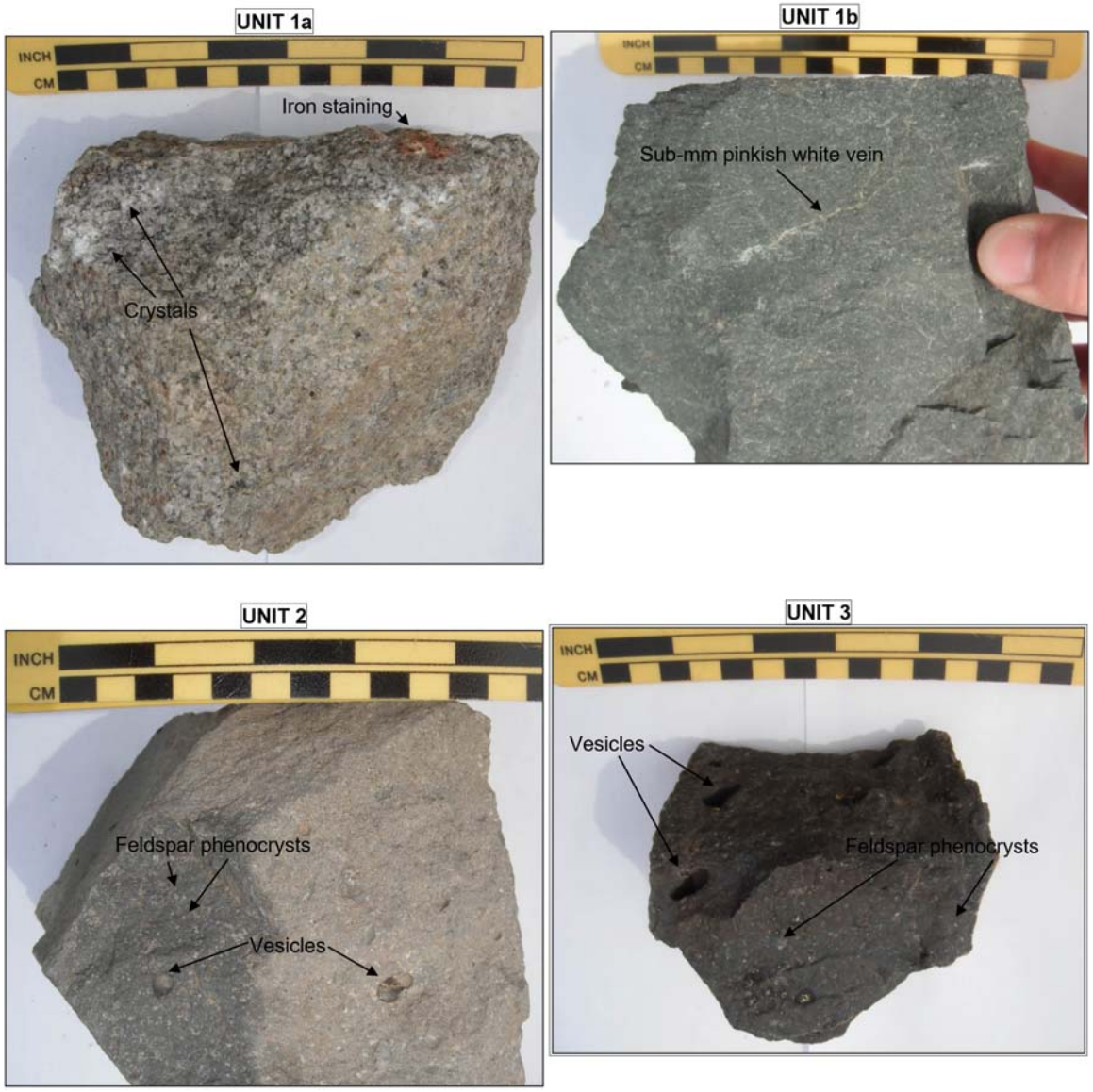

Figure 3-58. Samples of the units at CVB2. Top images are of the two subunits of Unit 1, showing crystals, iron staining, and a vein. Bottom left and bottom right images are of Unit 2 and Unit 3, respectively, and show feldspar phenocrysts and vesicles.

The contact between Unit 1 and Unit 2 is uneven and rubbly, as this is the bottom of the lava flow. Unit 2, which is 3-4 m thick, is basalt, dark grey when fresh, light brownish-grey to iron-stained when weathered (some of the surfaces have weathered to clays) (Figure 3-57). It has a very fine grained (aphanitic) groundmass, most likely because it consists largely of glass, and elongate feldspar phenocrysts (sub-millimeter to 3 mm in size). The feldspar phenocrysts do not appear to have any preferred orientation. The majority of this unit is columnar jointed; the columns are approximately

1-3 m tall and 30-50 cm wide, with an average width of about 35-40 cm. The faces of the columns are slightly irregular, and some have a curvature to them; chatter marks occur on most of the columns and are about 5-8 cm apart, aligning approximately perpendicular to the columnar jointing (Figure 3-59). The columns are vesicular, with irregularly shaped vesicles generally aligned with their direction of elongation approximately parallel to the basal contact of the flow. The lower ~30-40 cm of this unit is moderately vesicular (containing ~40-50 % vesicles), grading to ~5-10 % vesicles near the top of the unit. Vesicles near the bottom of the flow range in size from sub-millimeter to about 3 cm, whereas vesicles in the middle and upper parts of the unit have a much larger range in size, from about 1 mm to greater than 10 cm.

Figure 3-59. Chatter marks on columns in Unit 2 at CVB2.

Above a sharp contact with Unit 2 lies Unit 3, a 5-6 m thick blocky and irregular unit composed of material with a similar (if not identical) composition to Unit 2 (Figure 3-57). The blocks in this unit are approximately 10-20 cm in size and vesicles do occur, though very infrequently. There are several locations in Units 2 and 3 which show rusty-coloured weathering, which occur near the top of the lava flow in Unit 3, and on some column faces in Unit 2. Unit 3 is much more weathered and rusty-coloured than Unit 2, probably due to the greater number of fractures which create smaller blocks in this unit.

Structures

There are several joint sets visible at CVB1, all of which are sub-vertical columnar joints, excepting one joint set which is sub-horizontal. The columnar joints are generally planar, but some have a subtle curvature morphology, whereby either the base of the column curves outwards, giving a buttressed look, the entire column is curved (convex inwards to the flow), or one or two faces of the columns have a wavy appearance. The wavelengths of these curves, due to the range of lengths of the curving, range from ~0.5-3 m wavelengths, with an average of ~1 m. The only apertures which can be measured on the columnar joints are on the joints which extend into the outcrop, as these are the only joints with adjacent joint blocks. The apertures between these joints vary from less than a centimeter to 10 cm, with smaller apertures occurring on the eastern side of the outcrop (towards Unit 2). Overall, the small-scale joint roughness can be qualitatively characterized as smooth (ISRM, 1978).

The sub-horizontal joints at CVB1, interpreted to be ball-and-socket joints, are planar to curved (concave upwards), and have very small apparent apertures towards the centers of the columns (too small to measure), grading to larger apertures towards the column faces (sub-centimeter to 4 cm), with the largest apertures occurring at the corners of the column faces (4-10 cm). This gradational range of apertures is likely caused by the curved morphology of the planes, whereby the blocks of rock underneath the edges of the curves (at the edges and corners of the columns) fracture due to long-term point loading from the overlying column, combined with freeze-thaw cooling and heating. The wavelengths of the curved joints in this set are equal to the width of the columns (~0.5 m) as the joints extend the entire width of the column. Overall, the small-scale joint roughness can be qualitatively characterized as rough (ISRM, 1978).

There are also several joint sets visible at CVB2; all are sub-vertical columnar joints save for one sub-horizontal ball-and-socket joint set. The columnar joints are planar to curved, with most joints being at least slightly curved (convex inwards towards the flow). As most of the columnar joints have a single curve, the wavelength of the curvature of these joints is approximately equal to the heights of the columns, giving an average of ~1 m wavelength. Apertures could only be measured between columnar joints which extend into the outcrop, and were found to have a range of ~0-5 mm.

Again, measurements of joint roughness were not acquired, however the joint surfaces can be qualitatively described as smooth from field observations (ISRM, 1978).

The ball-and-socket joint surfaces can be described as rough (ISRM, 1978); these joints are planar to curved, with most joints having more of a planar morphology. These ball-and-socket joints are more planar in shape than the ones seen in CVB1, as such the aperture range is smaller (~0-20 mm). As with CVB1, the smaller apertures occur towards the centers of the columns, and larger apertures occur at the edges and corners of the column faces. The ball-and-socket joints generally extend through the entire width of the columns, making their wavelength (for those planes that are curved) approximately equal to the width of the columns (~0.5 m).

Neither outcrop shows obvious evidence of blasting as no star-shape radial fractures, drillholes for excavation blasts, or other blast features were observed. None of the joints on either outcrop appear to contain any infill or water seepage.

Weathering

The rocks at CVB1 are slightly weathered (ISRM, 1978), with minor occurrences of iron staining. Vegetation grows on top of the lava flow and on all sides, however only small occurrences of moss and lichen are visible on the outcrop itself. Several of the columns are much shorter than the others and appear to have had more of a column initially, but the toppling of the top of the columns occurred when possibly freeze-thaw action of water between columnar joints forced the column outwards, and it failed along a ball-and-socket joint. Pieces of former columns are visible at the base of the outcrop in a talus slope.

The outcrop at CVB2 shows slight weathering (ISRM, 1978), with more discolouration and decomposition than CVB1. Vegetation is minimal on the outcrop (spotty occurrences of moss and lichen). There is ubiquitous iron staining on block surfaces in Unit 3, whereas iron staining only occurs in several localities in Unit 2. Similar failure mechanisms are thought to have occurred at CVB2, whereby freeze-thaw action forces columns apart, and ball-and-socket joints allow for the top or bottom portion of the column to topple and fail. In CVB2, due to the flow being underlain by soil and talus along most of the slope, the flow slightly overhangs the underlying layers, thereby allowing ball-and-socket joints to also release the bottom portions of columns.

3.3.2. Field Survey Results

The photogrammetry, terrestrial LiDAR, and infrared data were analyzed, and several joint sets have been detected in each of the outcrops. The laser data were utilized in the determination of joint roughness, spacing, joint density, persistence, characterization of joint sets from dip and dip direction, and calculation of P_{21} values. Windows for P_{21} calculations were chosen as the most representative areas on the slope for joint density, based on where there was little to no distortion in the models, and where joints were observable and mappable. Photogrammetry data were used for observations of unit boundaries, compositions, and structural characteristics as well as joint persistence. The joint data are then assessed kinematically for potential failures.

CVB1

Photogrammetry

The completed photogrammetry model for CVB1 is shown below in Figure 3-60A. The edges of the model are highly distorted, however the ROI (the vertical columns on the right side of the outcrop) shows relatively little distortion, and so can be deemed reliable. Four joint sets were identified: a sub-horizontal set, which goes approximately parallel to chisel marks (Figure 3-60B), and three sub-vertical sets (Figure 3-60C-E). For the remainder of this section, when referring to specific joint sets, the abbreviation 'JS' will be utilized.

Due to the lack of targets on the outcrop, or control points with known GPS coordinates, it was impossible to register the photogrammetry model in the correct orientation. The resultant model, therefore, is not used in assessing joint orientations, however a summary of the basic properties of the joint sets is in Table 3-24.

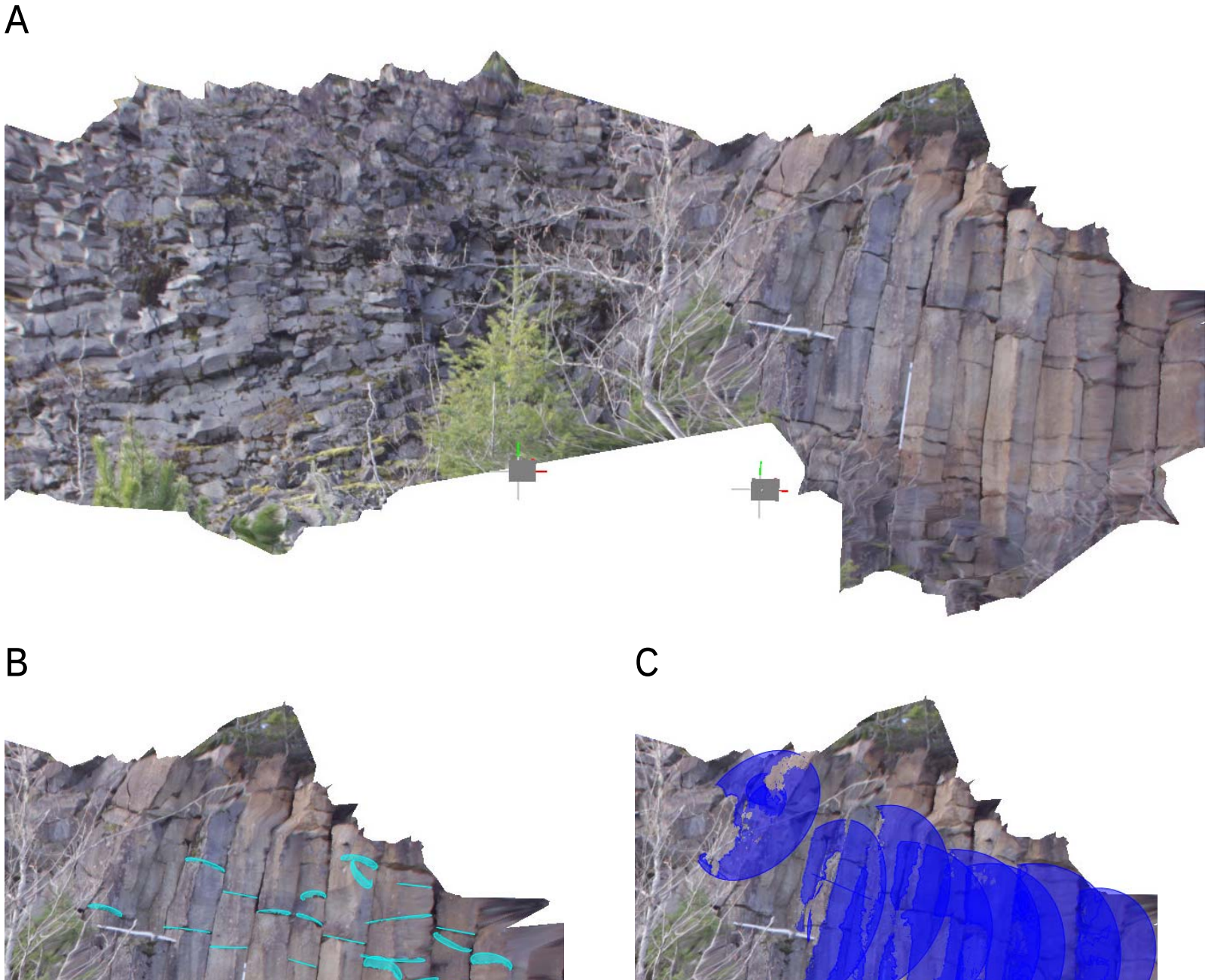

Figure 3-60. The photogrammetry model using a 20 mm focal length is shown in A for CVB1; B – JS 1 (aqua), C – JS 2 (blue), D – JS 3 (yellow), and E – JS 4 (red).

The average persistence of the joint sets was gained from averaging the diameters of the plane circles within each joint set. As expected, JS 1 has a significantly smaller persistence (by 0.5-0.6 m) than the other three sets, as these are the joints which cut across the columns. JS 2-4 have a larger persistence with quite similar values (largest difference is 0.1 m), as these are the long columnar joints which make up the faces of the columns.

Table 3-24. Joint sets obtained from the photogrammetry model of CVB1. Colours of joint sets correspond to those in Figure 3-60.

Joint Set (JS)	Description	Colour	Number of joints in set	Average persistence (m)
1	sub-horizontal, generally curved joints which follow chisel marks	aqua	36	0.2
2	sub-vertical, columnar joint; some are curved	blue	11	0.6
3	sub-vertical, columnar joint; some are curved	yellow	10	0.7
4	sub-vertical, columnar joint; some are curved	red	10	0.6

Terrestrial LiDAR

Four joint sets are visible in the laser scan of the outcrop at CVB1 (Figure 3-61); there are also twelve planes identified which do not fit into the joint sets (the full list of joints and their individual properties is shown in Appendix B; a summary is shown in Table 3-25). The greatest number of joints belongs to JS 1; these are the sub-horizontal joints (ball-and-socket joints) which follow chatter mark orientations. As these joints cut through the columns, it is logical that there would be more joints in this set than the columnar joint sets because there are multiple ball-and-socket joints per column. There are similar numbers of joints in each of the columnar joint sets (JS 2-4), indicating similar joint sets are visible in nearly all of the columns in the outcrop.

Table 3-25. Joint set data obtained using the point cloud of the terrestrial laser scan at CVB1.

Joint Set (JS)	Dip	Dip Direction	Description	Colour	Number of joints in set
1	<35°	any dip direction	sub-horizontal, generally curved joints which follow chisel marks	aqua	63
2	>35°	315°-335° or 135°-155°	sub-vertical, columnar joint; some are curved	blue	11
3	>35°	350°-020° or 170°-200°	sub-vertical, columnar joint; some are curved	yellow	17
4	>35°	240°-265° or 060°-085°	sub-vertical, columnar joint; some are curved	red	15

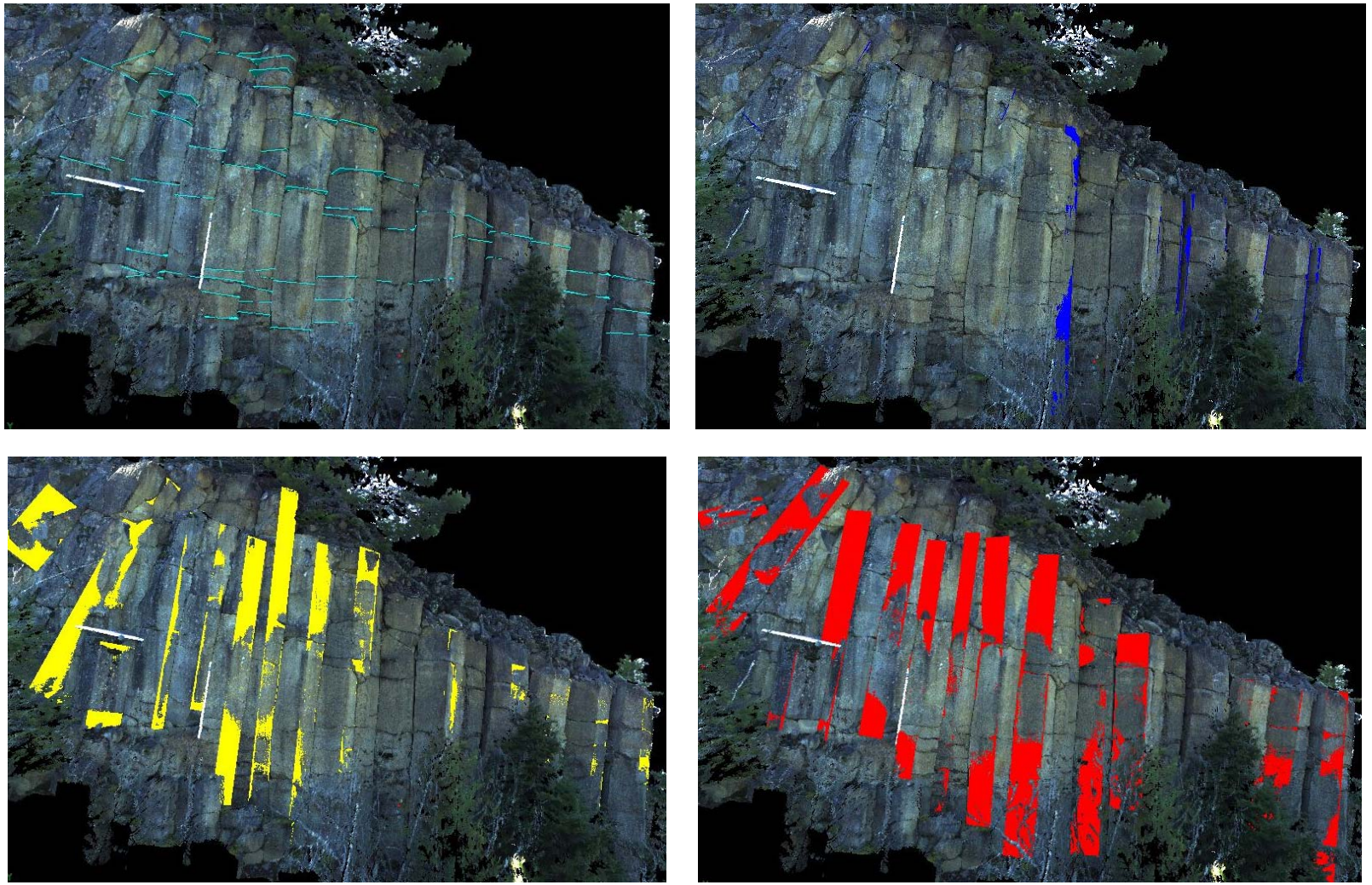

Figure 3-61. Laser point cloud model showing the joint sets at CVB1. A – JS 1 (aqua), B – JS 2 (blue), C – JS 3 (yellow), D – JS 4 (red).

The average heights and widths of each joint set are shown in Table 3-26; the longest length of the two values is used as the persistence of the joints. JS 4 is the longest joint set, however all of JS 2-4 have lengths greater than 1 m, which is consistent with the vertical columnar jointing seen in the outcrop. JS 1 has a much shorter persistence, which is expected, because these joints are the sub-horizontal ball-and-socket joints. The persistence length in the case of JS 1 is the width of the joint, and because these joints are generally extending across entire columns, this length can also be an approximate average diameter of the columns in the outcrop.

Table 3-26. Joint set lengths obtained from the laser point cloud at CVB1.

	JS 1	JS 2	JS 3	JS 4
Average Height (m)	0.2	2	2	3
Average Width (m)	0.5	0.3	0.3	0.4
Persistence (m)	0.5	2	2	3

A width to height ratio of the columns can give an estimate of the average size of the columns in the outcrop at CVB1. Distances were measured in the laser point cloud model, and width, height, and width to height ratio values are shown in Table 3-27. The average width to height ratio of the columns is 0.3, meaning the width of the columns is generally ~30% of the height. This suggests that the columns are much taller than they are wide, and so the center of gravity for the columns lies outside the base dimensions. If the width to height ratio were larger, the column would have a wider base, and its center of gravity would be within the base dimensions, making it inherently more stable than columns with lower width to height ratios (Figure 3-62).

The joint intensity value (P_{21}) was calculated for each joint set and for all joints within the window at CVB1; these values are in Table 3-28. JS 2 has the smallest P_{21} value (0.3 m/m^2), which could be explained by a smaller number of joints occurring in this joint set overall. JS 3 and JS 4 are the main columnar joints visible in the point cloud, and therefore have large P_{21} values (~2 m/m^2) because they extend for most, if not all, of the height of the window. Though the joints in JS 1 are generally not of large persistence, there is a large P_{21} value (2 m/m^2), due to the large quantity of these joints within the window.

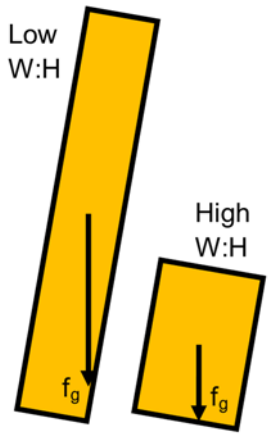

Figure 3-62. Schematic diagram showing the same 80° slope angle for both low (left) and high (right) width:height (W:H) ratio columns. The force of gravity vector (f_g) lies outside the base of the low W:H column (unstable), and inside the base of the high W:H column (stable).

Table 3-27. Width, height, and width to height ratio of the columns at CVB1.

Column	Width (m)	Height (m)	Width/Height
1	1.1	3.3	0.3
2	0.6	1.0	0.6
3	0.6	2.9	0.2
4	0.5	2.8	0.2
5	0.5	3.5	0.1
6	0.4	4.3	0.1
7	0.5	4.1	0.1
8	1.0	4.0	0.2
9	0.5	3.2	0.2
10	1.0	2.3	0.4
11	0.4	1.6	0.3
12	0.7	1.7	0.4
13	0.6	1.3	0.4
14	0.7	2.3	0.3
15	0.5	3.7	0.1
16	0.6	0.8	0.7

Table 3-28. P_{21} values for joint sets in CVB1.

	JS 1	JS 2	JS 3	JS 4	No Set	All Joints
P_{21} (m/m^2)	2	0.3	2	2	0.5	6

The spacing between joints within joint sets was obtained by measuring distances in the laser point cloud model; the average spacing values for each joint set are shown below in Table 3-29. The spacing between the columnar joint sets, JS 2-4, are generally in agreement with similar values. JS 2 has a smaller spacing, but this may be due to the greater number of exposed column faces in this orientation, and therefore there appears to be a smaller spacing. The average width of the columns at CVB1 is ~0.6 m, which is larger than the spacing between the columnar joint sets, though there is essentially one column in between each of the joints in a set. This discrepancy may be because of the averaging of the values, or possibly due to the visibility of the different joints in the outcrop as opposed to the entire column width.

Table 3-29. Average spacing between joints in the joint sets at CVB1, obtained from the laser point cloud model.

	JS 1	JS 2	JS 3	JS 4
Spacing (m)	0.5	0.5	0.6	0.6

Infrared Imagery

Columnar jointing (center) is very obvious in the infrared image of CVB1, and can be seen easily through differences in thermal signature due to their aspect with respect to the sunlight (Figure 3-63). Two major columnar joint sets are visible in the left side of the outcrop, with one more visible on the right side. The lighter coloured columnar joints are hotter than the darker vertical joint sets because they face the sun more directly. However, there is also temperature variation along a single joint, indicating a curvature of the joint, and therefore a variance in aspect over the joint surface. Sub-horizontal ball-and-socket jointing is also apparent, evidenced by the darker (cooler) lines across the columns. The vegetation in this image appears as very light grey to white, as vegetation more quickly absorbs radiant heat from sunlight. Moss cover can be seen on several of the columns as brighter (hotter) spots, generally of a very light grey. There are no bright streams or streaks down the columns, probably indicating a lack of water run-off over or out of the outcrop, which is consistent with field observations.

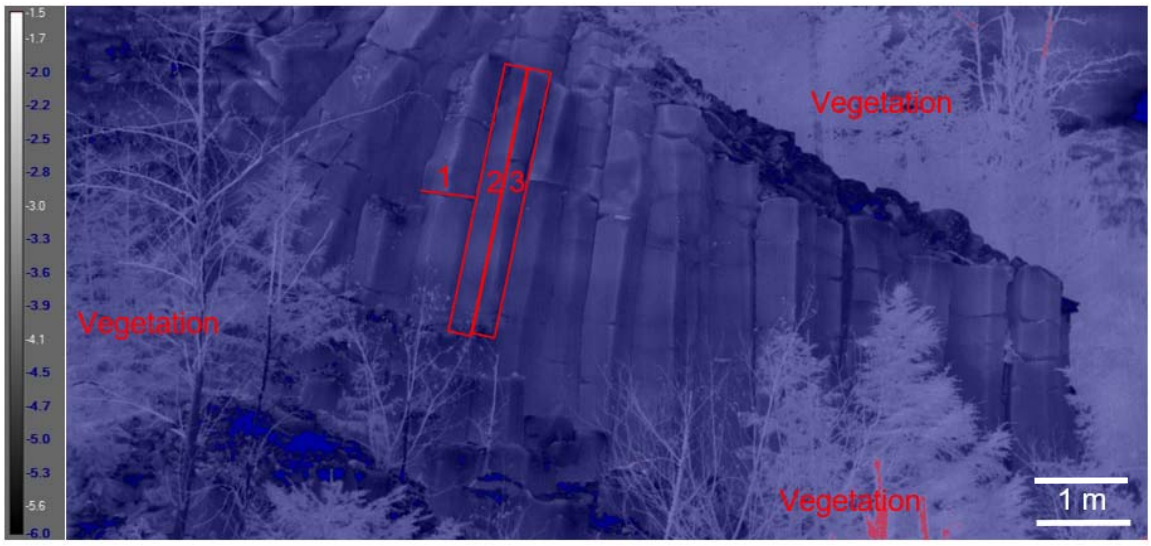

Figure 3-63. Annotated infrared image of CVB1. Numbers indicate joint sets. The colour scale to the left of the image is in degrees Celsius.

CVB2

Photogrammetry

Five joint sets were recognized in the photogrammetry model for CVB2: JS 1 (Figure 3-64A) is sub-horizontal, generally following the chatter marks on the columns, and JS 2-5 (Figure 3-64B-E) are sub-vertical columnar joints with four groupings of dip direction. A summary list of joint set properties is provided in Table 3-30.

The persistence of JS 1 is ~0.5 m, and because these are the joints which cut through the columns, this value can also be viewed as the average diameter of the columns. JS 2-5 have a persistence of approximately 1 m, which is to be expected, as these are the columnar joints, and generally all the joints around a single column will be of approximately the same length. The sub-vertical columnar joints at this outcrop vary in orientation more than at CVB1, therefore an extra columnar joint set was added. JS 4 has the least number of joints belonging to it, which suggests that this orientation is not as common as the other three sets.

A

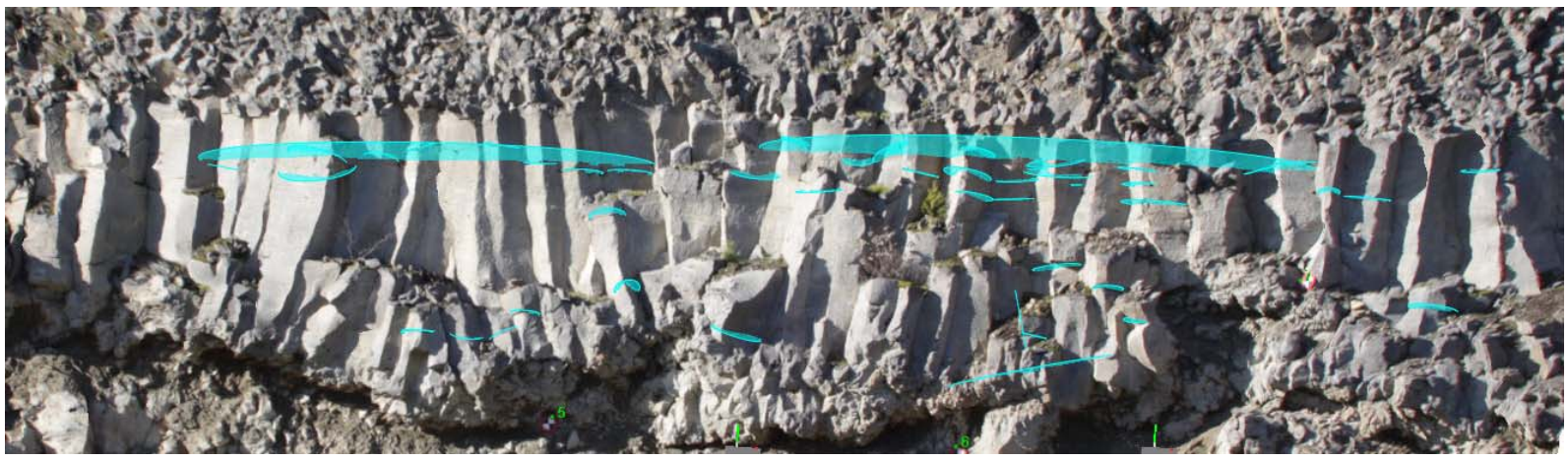

B

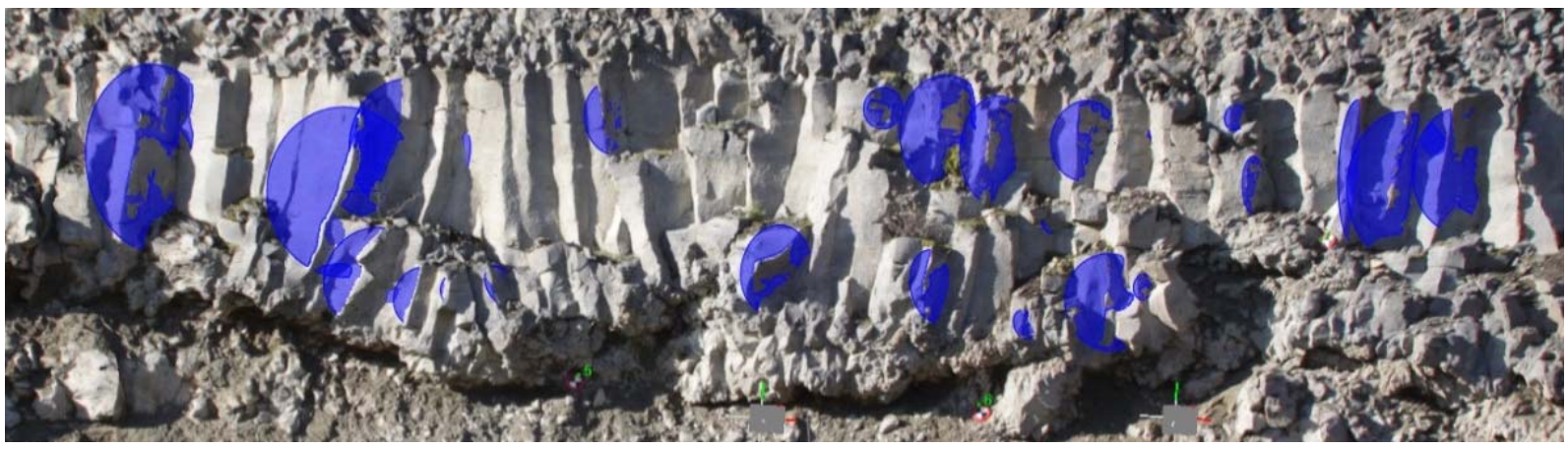

C

D

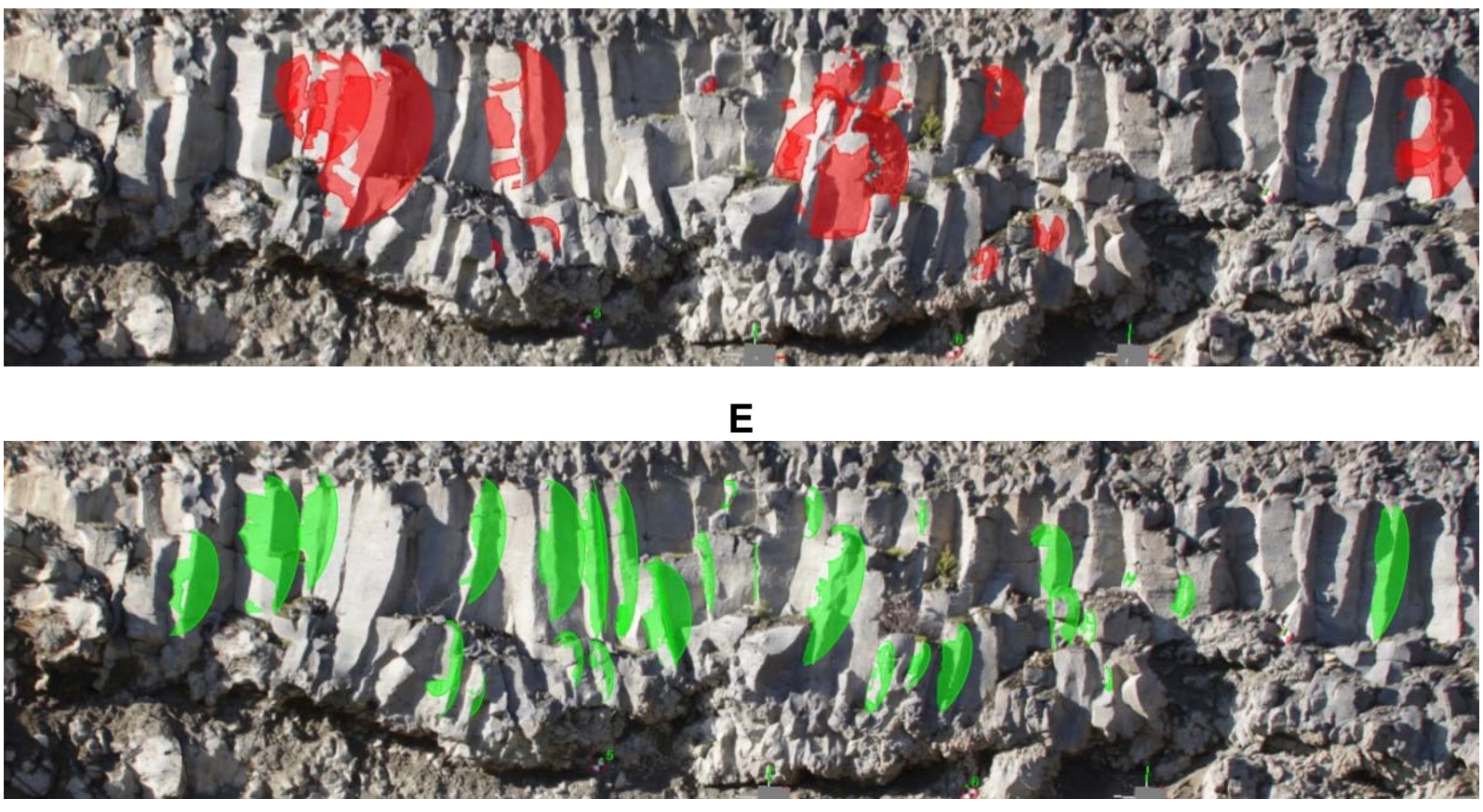

E

Figure 3-64. Photogrammetry model showing the joint sets of CVB2. A – JS 1 (aqua), B – JS 2 (blue), C – JS 3 (yellow), D – JS 4 (red), E – JS 5 (lime).

Table 3-30. Joint set properties from the CVB2 photogrammetry model. Colours correspond to those in Figure 3-64.

Joint Set	Dip	Dip Direction	Description	Colour	Number of joints in set	Average Persistence (m)
1	<35°	Any	Sub-horizontal, generally follow chisel marks	aqua	48	0.5
2	>35°	050°-080° or 220°-250°	Sub-vertical columnar joint, some are curved	blue	24	1.0
3	>35°	090°-110° or 255°-295°		yellow	35	1.0
4	>35°	130°-150° or 300°-325°		red	18	1.0
5	>35°	150°-200° or 330°-350°		lime	32	1.1

Terrestrial LiDAR

Five joint sets are present in the point cloud data obtained from the laser scan performed using the terrestrial LiDAR (Figure 3-65), and 16 more planes which do not fit into a set (Table 3-31; a full list of joints and their characteristics can be found in Appendix B). In this case, there are more columns than there are ball-and-socket joints, and therefore there are a greater number of joints in JS 2-5. Though JS 5 is a sub-vertical columnar joint, there are significantly less joints belonging to this set than the other columnar joints. This indicates an orientation bias, whereby the dip directions of JS 2-4 were preferred over the orientation of JS 5 for the formation of columnar joints as the lava flow was cooling.

A

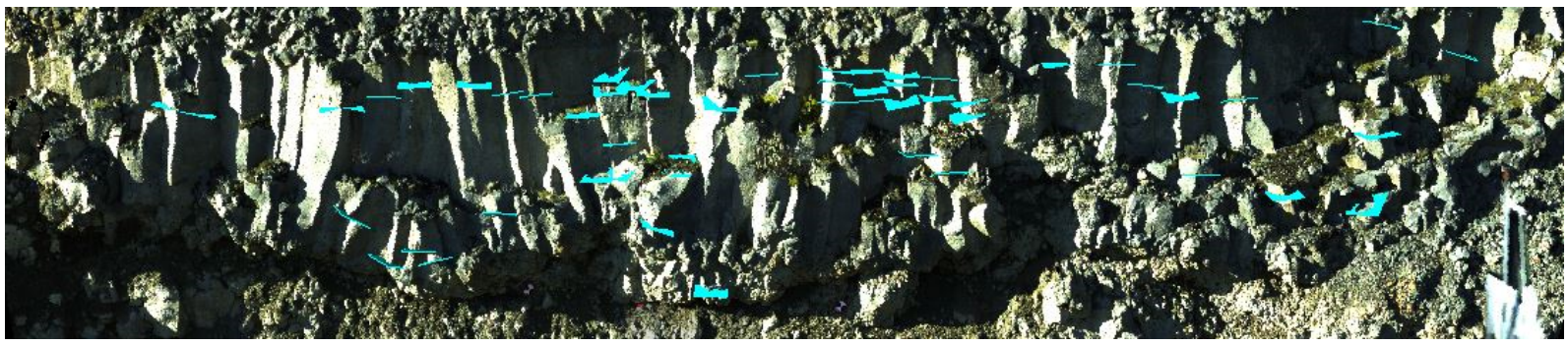

B

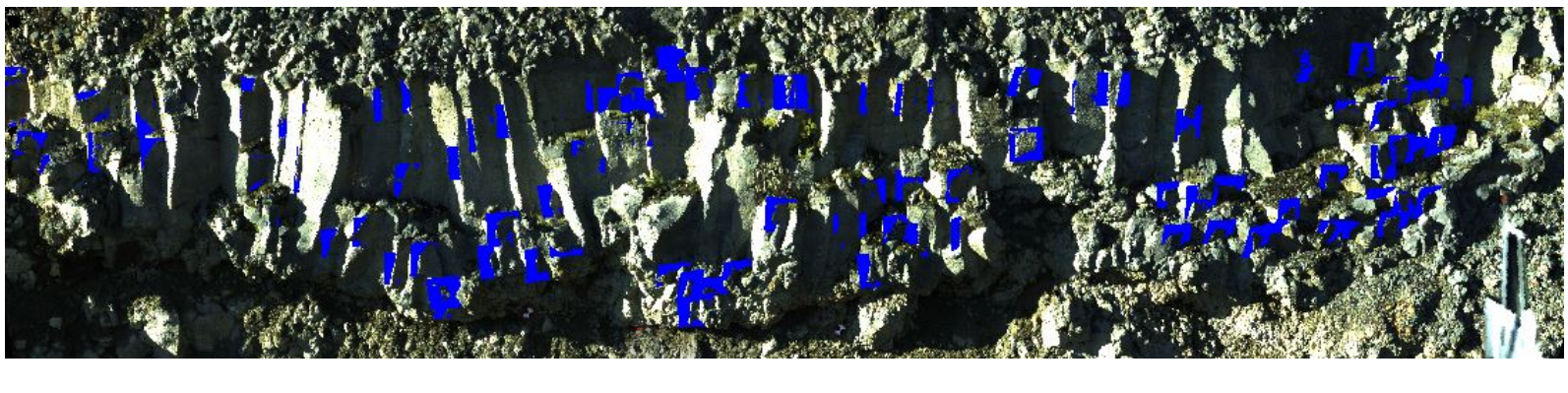

C

D

E

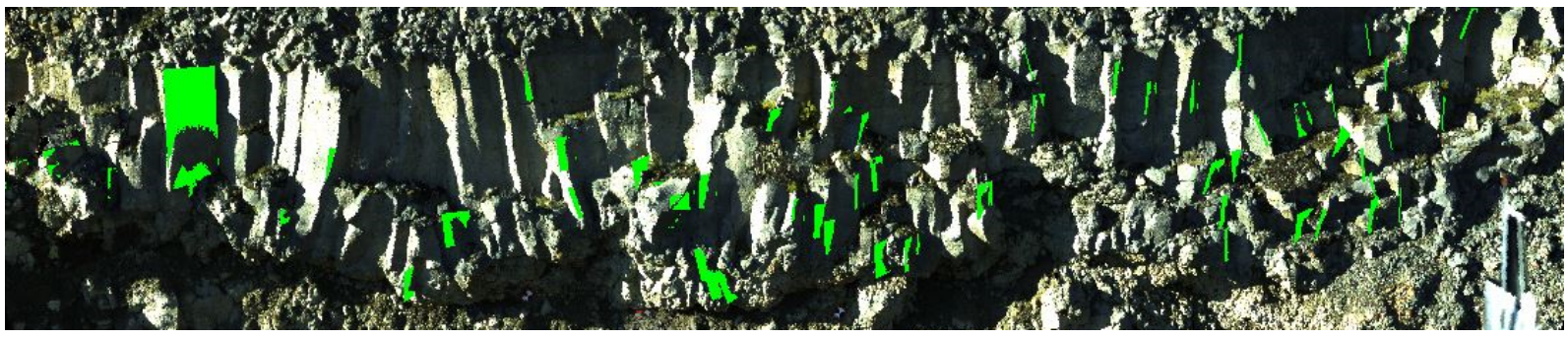

Figure 3-65. Laser point cloud model showing joint sets of CVB2. A – JS 1 (aqua), B – JS 2 (blue), C – JS 3 (yellow), D – JS 4 (red), E – JS 5 (lime).

The size of the columns in the CVB2 outcrop vary significantly, so in order to gain an estimate of the average size, widths and heights of each of the columns were measured within the laser point cloud model (see Appendix B). The average width to height ratio is 0.6, meaning the width of the columns is generally ~60% of the height. This ratio is significantly higher than the columns in CVB1, which means that the center of gravity for the columns at CVB2 is much lower than those of CVB1. Therefore, if stability of the columns was solely based on shape, CVB2 columns would be more stable.

Table 3-31. Joint set data obtained using the point cloud of the terrestrial laser scan at CVB2. Colours correspond to those in Figure 3-65.

Joint Set	Dip	Dip Direction	Description	Colour	Number of joints in set
1	<35°	any dip direction	sub-horizontal, generally curved joints which follow chisel marks	aqua	53
2	>35°	250°-275° or 070°-095°	sub-vertical, columnar joint; some are curved	blue	101
3	>35°	110°-135° or 290°-315°	sub-vertical, columnar joint; some are curved	yellow	88
4	>35°	325°-345° or 145°-165°	sub-vertical, columnar joint; some are curved	red	67
5	>35°	210°-230° or 030°-050°	sub-vertical, columnar joint; some are curved	lime	55

Spacing between joints within each of the joint sets was also determined using the laser point cloud model (the full table of values can be found in Appendix B). The average spacing of the joints is shown in Table 3-32. All of the columnar joint sets (JS 2-5) as would be expected have similar spacing, as each joint within the set is separated from a joint on either side by a single column. The average width for these columns is 0.5 m, which is generally consistent with the spacing values for the joints.

Table 3-32. Average values obtained for the spacing between each of the joint sets at CVB2 using the laser point cloud model.

	Joint Set 1	Joint Set 2	Joint Set 3	Joint Set 4	Joint Set 5
Spacing (m)	0.5	0.6	0.5	0.5	0.5

Infrared Imagery

It is easy to identify individual columns in the infrared imagery of CVB2 (Figure 3-66), though the contacts or divisions between them is not as clear as in the imagery of CVB1. The different joint sets are visible through differences in the thermal signature, or temperature, of the rock, which is related to the aspect with relation to the sun. The lighter colours (hotter temperatures) delineate joints which are facing the sunlight more directly, and darker colours on the columns indicate joints which are facing the sunlight at more of an angle or are in shadow. Many of the joints also have temperature variations on one face of the column, indicating a difference in aspect over a single joint surface (the joints are curved).

The very dark spots on the tops of some of the columns are soil, and some vegetation can be seen at these locations as well. The sub-horizontal joint set is very faint, and in many instances, not visible in the infrared imagery. Some minor temperature variations can be seen in a horizontal direction along the columns, however, with consistent spacing. These temperature variations may be attributed to the chatter marks along the columnar joint surfaces. As it is difficult to group colours within an infrared image, it is also difficult to determine how many joint sets may be visible in the image; the number of sub-vertical joint sets determined for this image is three, based upon a dark grey, medium grey, or light grey colouring.

Vegetation in this image is much darker than the outcrop and is mainly in the background. Tree trunks are visible in the top left of the image; the apparent darkness (or coolness) of the vegetation to the rocks in this image may be attributed to the difference in distance from the infrared camera itself—the trees above the outcrop were approximately 10-15 m further away from the camera than the outcrop face. As with CVB1, there are no bright streams or streaks down the columns or anywhere on the outcrop, probably indicating a lack of surface water run-off. This is consistent with the field observations.

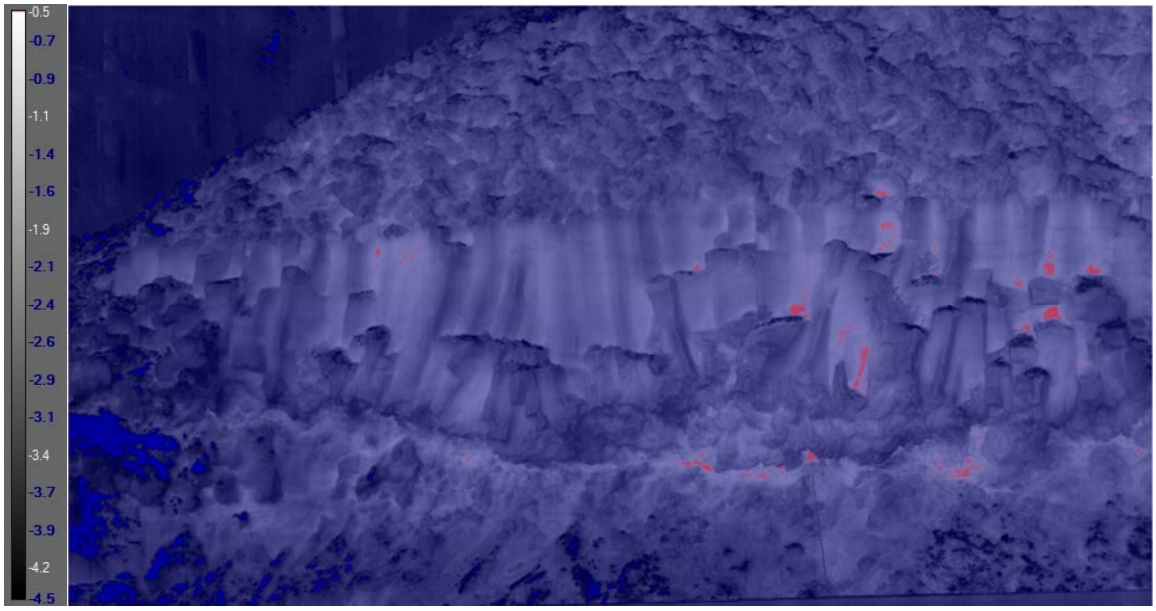

Figure 3-66. Infrared image of the outcrop at CVB2. The colour scale to the left of the image is in degrees Celsius.

Kinematic Analysis and Comparison of Models

In order to complete a kinematic analysis on the outcrops at the two sites, an angle of friction needed to be decided. Barton (1976) indicates internal angles of friction for dry basalt as 35-38° and wet basalt as 31-36°. As there are a range of possible friction angles for this material, an intermediate value of 34° was utilized for kinematic analyses. The remaining assumptions used in the kinematic analyses of the slopes at each outcrop are shown in Table 3-33.

Table 3-33. Parameters used for kinematic analysis. Lateral limit indicates the variation from slope dip direction allowed in the analysis for planar sliding and toppling failures.

	Slope Dip (°)	Slope Dip Direction (°)	Friction Angle (°)	Lateral Limit (°)
CVB1	90	030	34	20
CVB2	90	120	34	20

CVB1

Kinematic analysis for CVB1 was completed for the laser point cloud model joint data (Figure 3-67). The rosette diagram of the laser model joint data for CVB1 shows the frequency of apparent strikes of joints (Figure 3-67). Three directions are identified

as having the highest frequency: NNW-SSE, NE-SW, and ESE-WNW; these correspond to the strikes of the three columnar joint sets. The strike directions which have similar frequencies on the rosette diagram correspond to the ball-and-socket joint set (JS 1), as these joints have a wide range of orientations.

Table 3-34. Kinematic analysis results of the CVB1 laser point cloud joint data. Bolded joint sets indicate critical joints are above 50% for that joint set.

Type of failure	Critical Joints	Joint count	Critical %	Intersection count	Critical Intersections	Critical %	Critical Joint Sets
Planar	7	119	6%	-	-	-	1,3
Wedge	-	-	-	988	7020	14%	
Flexural Toppling	8	119	7%	-	-	-	3
Direct Toppling	-	-	-	486	7020	7%	-
Oblique Toppling	-	-	-	501	7020	7%	-
Base Plane	42	119	35%	-	-	-	1,3

Analysis of the various types of failure for the structures at CVB1 revealed that planar failures are geometrically feasible, however these are unlikely as the percentage of critical joints is 6%, and no possible planar failures were observed (Table 3-34). Wedge failures are indicated by the analysis as the most feasible type of failure, with many critical intersections which could potentially fail (14% of all intersections). All types of toppling failures have similar failure potential. Though by the joint set data wedge failures are the most likely type of failure, a large portion of the joints are vertical to sub-vertical, which means the intersection of two of these planes will be sub-vertical. Wedge failures are caused by the intersection of two daylighting joints, however because the slope angle is approximately 90°, all joints in this outcrop are daylighting. The apparent wedge failures in this analysis, therefore, are mostly the wedges created by the sub-vertical joint sets, and will thereby actually be involved in toppling failures. The joint sets attributed to the different failure types are mainly JS 1 and JS 3, due to their dip and dip directions with respect to the orientation of the slope face.

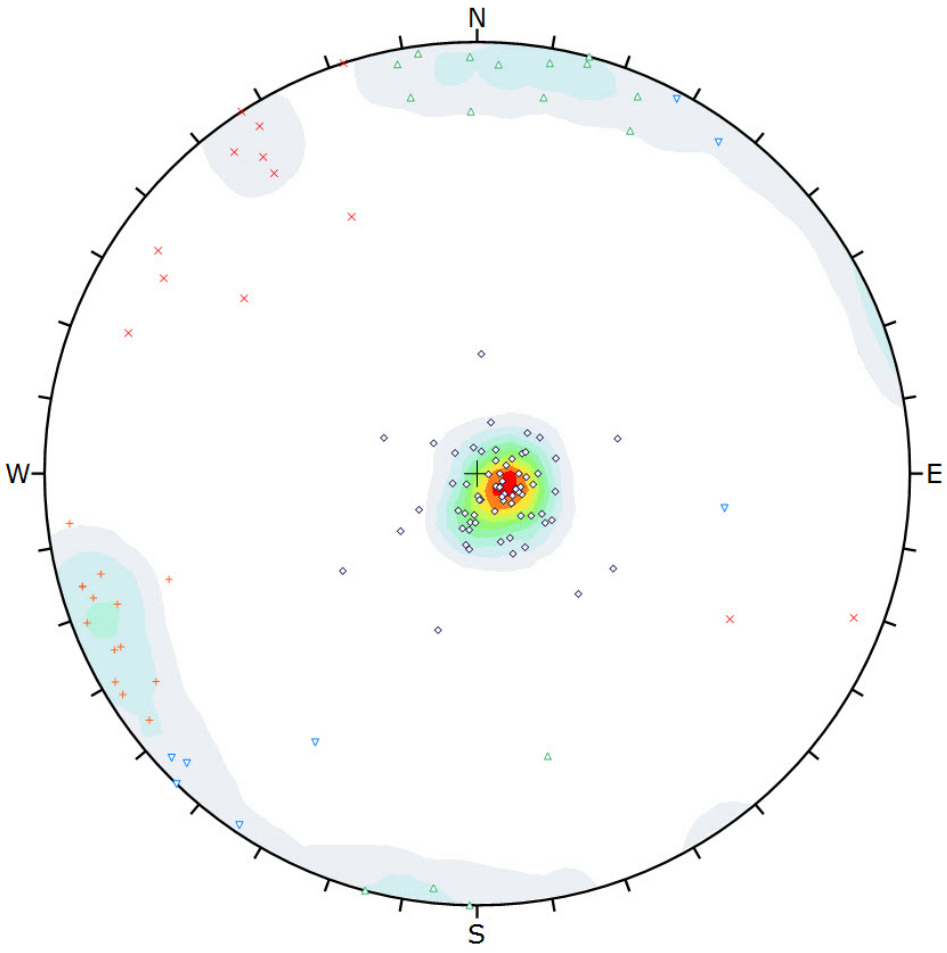

Symbol	Set	Quantity
◇	1	68
×	2	13
△	3	16
+	4	14
▽	[no data]	8

Plot Mode	Rosette
Plot Data	Apparent Strike
Face Normal Trend	0.0
Face Normal Plunge	90.0
Bin Size	10°
Outer Circle	10 planes per arc
Planes Plotted	51
Minimum Angle To Plot	45.0°
Maximum Angle To Plot	90.0°

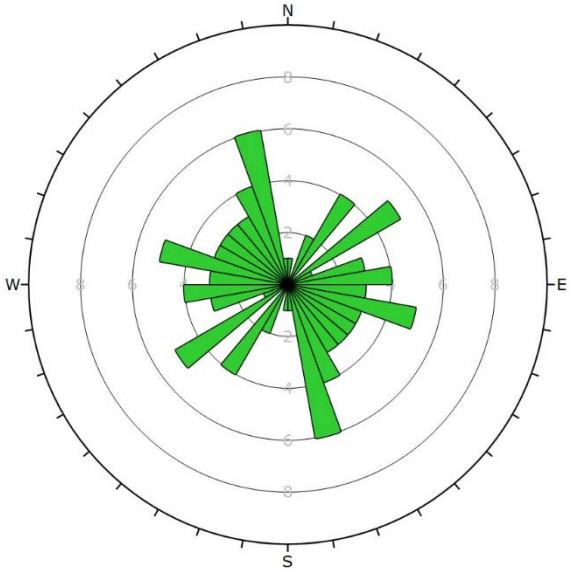

Figure 3-67. Contoured equal area lower hemisphere stereonet of the poles to joints and a rosette diagram of the CVB1 laser point cloud model.

CVB2

Plots of the poles to joints from the photogrammetry (Figure 3-68) and laser point cloud (Figure 3-69) datasets show similar trends for the joint sets, with one joint set plotting in the middle of the stereonet, and several others plotting around the edges. The sets around the edges of the stereonet in Figure 3-68, however, seem to have much more distinct groupings of joint orientations than the joints shown in Figure 3-69. This may just be due to the smaller number of joints in the photogrammetry data as compared to the LiDAR data. The orientations of the identified sub-vertical sets are also slightly different between datasets, varying by approximately 20° in some cases. Both datasets show a clear gap in joint dip direction approximately NNE-NE and SSW-SW, which indicates an orientation bias for the joints.

The rosette diagrams for the photogrammetry model and laser point cloud model at CVB2 (Figure 3-68 and Figure 3-69, respectively) have a slightly different appearance, however many trends in the data are similar. Both diagrams show a lack of joints having strikes oriented WNW-ESE, indicating that there is an orientation bias in the columns at CVB2, related to the strike of the slope. The highest frequencies of joint strikes occur in the WSW-ESE and ~N-S directions, however the N-S joint sets in the two datasets differ by ~10°-20°. Two more joint sets can be found in the LiDAR model rosette diagram, with strikes oriented NNE-SSW and NE-SW. The NE-SW joint set is also visible in the photogrammetry model rosette, however does not contain as many joints relative to other joint sets as in the LiDAR model data. The orientations of joint strikes in the photogrammetry data show clearer separation between different joint sets, whereas the laser model data shows joints oriented in many directions, none of which appears to have significantly more joints than the others. This discrepancy may be due to the greater number of joints mapped in the laser scan model data, or due to errors introduced into the photogrammetry model, which will be discussed in the following chapter.

Kinematic slope analysis using the joint data in DIPS showed that flexural and direct toppling are apparently the least feasible types of failure, where there are 11% or less critical planes and intersections (Table 3-35). As with CVB1, wedge failures are indicated in the analysis as the most feasible type of failure with supposedly over 30% of intersections critical in both datasets. The slope angle at CVB2 is also 90°, meaning all

joints daylight, and all the sub-vertical columnar joints which have sub-vertical intersections have been classed by DIPS as wedge failures, when in reality they may be related to toppling. It is interesting to note that in the photogrammetry data the critical joint sets are mostly JS 2 and JS 3, whereas the critical sets in the laser point cloud model are generally JS 3 and JS 4. This discrepancy may be caused by the difference in sample sizes, whereby the number of joints in the photogrammetry model is less than half of those which have been identified in the laser point cloud. In both cases, however, JS 3 generally contains greater than 50% critical planes, and therefore has the highest feasibility of the joint sets to fail. Field observations did not reveal any major planar or wedge failures; only potential toppling deformation was observed at both outcrops.

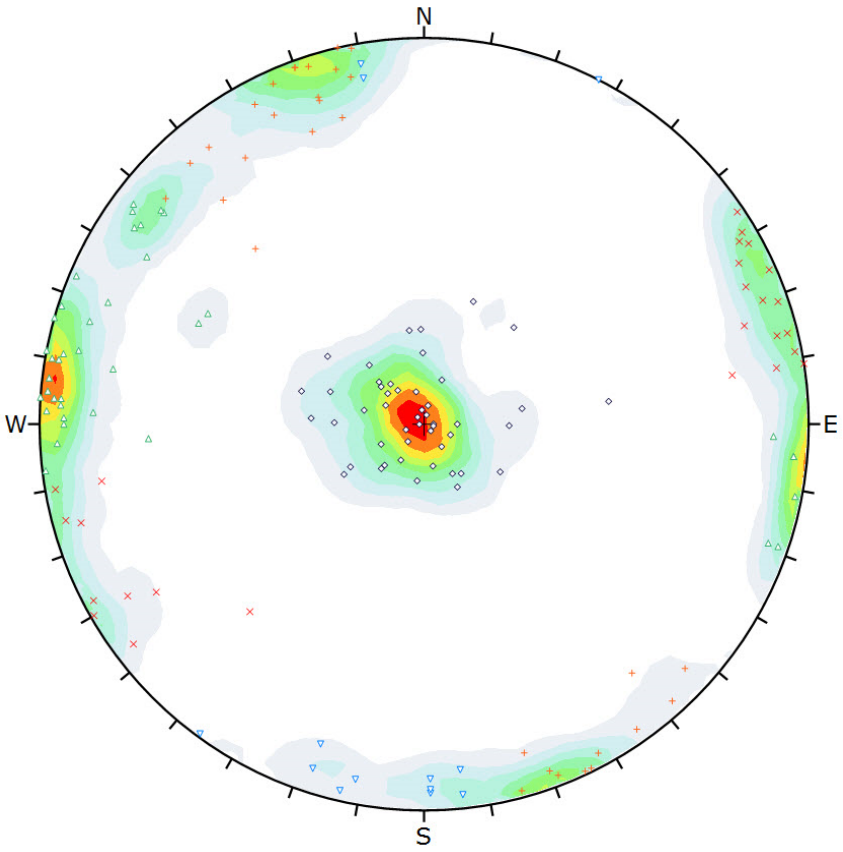

Symbol	Set	Quantity
◇	1	48
×	2	26
△	3	39
+	4	31
▽	5	13

Plot Mode	Rosette
Plot Data	Apparent Strike
Face Normal Trend	0.0
Face Normal Plunge	90.0
Bin Size	10°
Outer Circle	15 planes per arc
Planes Plotted	109
Minimum Angle To Plot	45.0°
Maximum Angle To Plot	90.0°

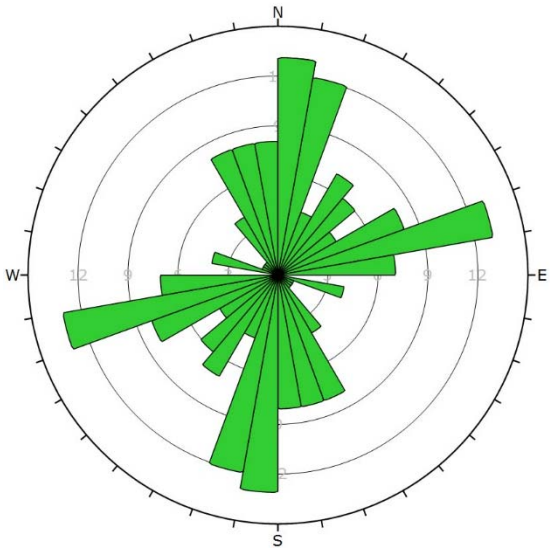

Figure 3-68. Equal area lower hemisphere stereonet of contoured joint set data and a rosette diagram for the CVB2 photogrammetry model.

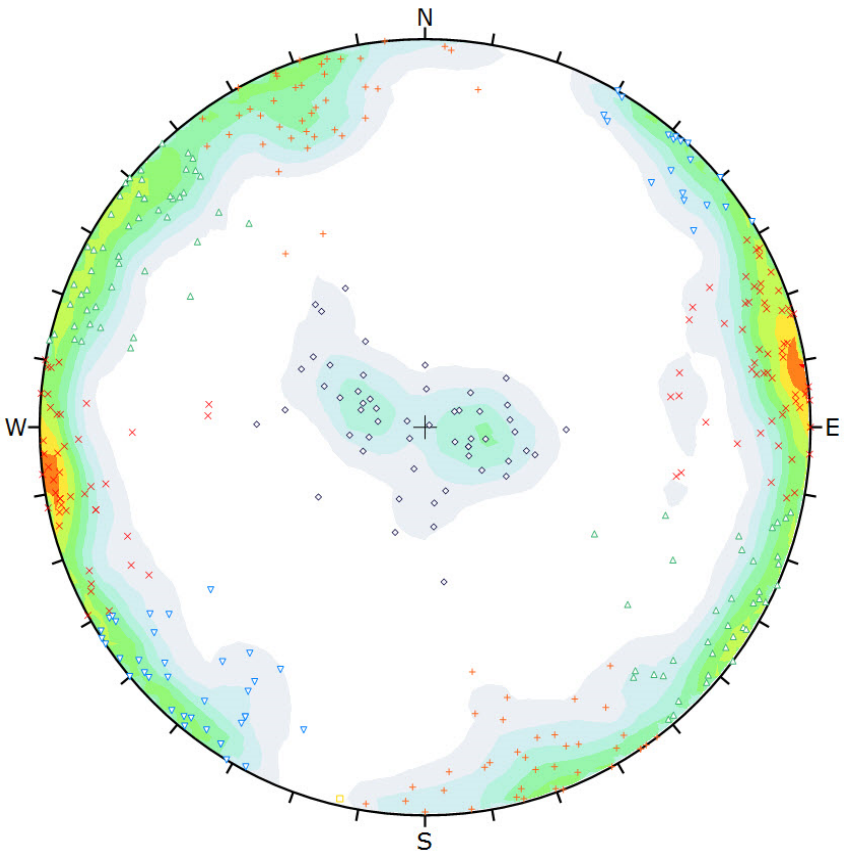

Symbol	Set	Quantity
◇	1	54
×	2	103
△	3	89
+	4	78
▽	5	55
□	[no data]	1

Plot Mode	Rosette
Plot Data	Apparent Strike
Face Normal Trend	0.0
Face Normal Plunge	90.0
Bin Size	10°
Outer Circle	35 planes per arc
Planes Plotted	325
Minimum Angle To Plot	45.0°
Maximum Angle To Plot	90.0°

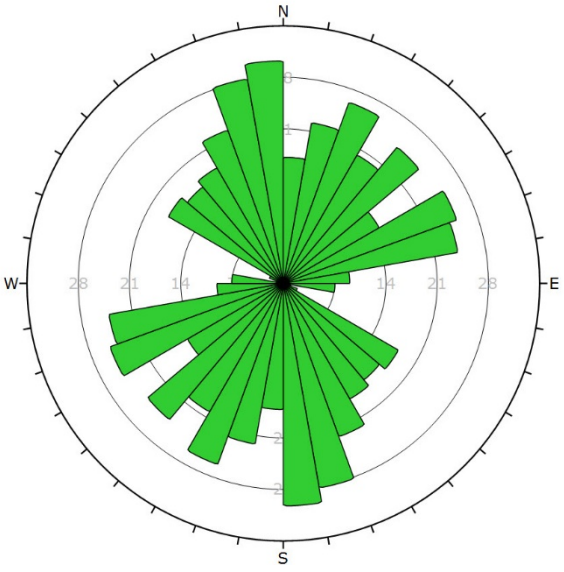

Figure 3-69. Equal area lower hemisphere stereonet of contoured joint set data and a rosette plot for the CVB2 laser point cloud model.

Table 3-35. Results of the kinematic analysis for photogrammetry and laser point cloud joint data at CVB2. Bolded joint sets indicate critical features are above 50% for that joint set.

	Photogrammetry Joint Data				Laser Point Cloud Joint Data			
Type of failure	Critical Features	Feature Count	Critical %	Critical Joint Sets	Critical Features	Feature Count	Critical %	Critical Joint Sets
Planar	24 planes	157 planes	15%	3,4	54 planes	380 planes	14%	1,2,3
Wedge	4053 intersections	12244 intersections	33%	-	27130 intersections	72001 intersections	38%	-
Flexural Toppling	6 planes	157 planes	4%	3,4	42 planes	380 planes	11%	2,3
Direct Toppling	519 intersections	12244 intersections	4%	-	5546 intersections	72001 intersections	7%	-
Oblique Toppling	1144 intersections	12244 intersections	9%	-	13929 intersections	72001 intersections	19%	-
Base Plane	56 planes	157 planes	36%	1,3,4	78 planes	380 planes	21%	1,2,3

Chapter 4. ‘Up Close with Virtual Outcrops’: A Virtual Field Site[1]

4.1. Abstract

Geologists require access to map the lithological, sedimentological, and structural characteristics of rock outcrops, and in many situations this may not be possible. Remote sensing methods have provided a means to map inaccessible outcrops. The interactivity between the geologist and the outcrop, however, has in most cases been limited due to the distance between the observer and the observed. In response to this problem, a geovisualization interface called ‘Up Close with Virtual Outcrops’ was created using a virtual reality game engine software to provide unrestricted access to a virtual field site at the Chasm Provincial Park, in central British Columbia, Canada. This interface includes high-resolution, multi-scale, multi-dimensional datasets acquired through remote sensing methods including terrestrial LiDAR, infrared thermography, and Structures-from-Motion photogrammetry. The developed interface allows the user to simulate virtual on-the-outcrop scenarios on steep, high, inaccessible rock slopes. Intended for professional geoscientists, engineers, and students alike, ‘Up Close with Virtual Outcrops’ provides a tool with major potential for improved research, analysis, and learning, and allowsmd a virtual interaction between the geologist and inaccessible rock slope outcrops.

Keywords: remote sensing, terrestrial LiDAR, thermal imaging, photogrammetry, virtual environment, lava, geology

4.2. Introduction

Remote sensing data can be represented in a multitude of formats and in various degrees of dimensionality. Visual representations of geographical and geological data have been termed ‘visualizations’, or ‘geovisualizations’ for geographical data (MacEachren and Kraak, 1997). Each of the visualizations represents a method of

[1] This chapter is written as a manuscript to be submitted to the journal “Computers and Geosciences”.

presentation of the data, chosen specifically to highlight certain aspects or results of the dataset. Two-dimensional visualizations include graphs, images, and figures; three-dimensional visualizations include 3D meshes or surfaces, point clouds, and 3D plots; and four-dimensional forms generally display three dimensions of data through a fourth dimension, time.

The concepts of virtual reality and virtual environments for visualization of geographical and geological data have become increasingly prevalent in recent years (Saini-Eidukat et al., 2002; Thurmond et al., 2005; Jones et al., 2009, De Paor and Whitmeyer, 2011; De Paor et al., 2016). Virtual environments, whereby real or abstract datasets are simulated in an interactive setting between human and computer, provide a medium for exploration and learning to scientists, students, and the general public (Hedley, 2015).

Several previous studies have demonstrated the visualization of geological datasets, including the use of the KML language by De Paor and Whitmeyer (2011) and De Paor et al. (2016) for the display of geological and geophysical data on a virtual globe in Google Earth (Google, 2020). Using a combination of 3D datasets and interactive user interface elements such as sliders, De Paor and Whitmeyer (2011) have developed a means for viewing structural data such as strike and dip, fault plane solutions, and cross-sections, and De Paor et al. (2016) extended the virtual globe to several different planets with three-dimensional models, draped maps, and movies included. Blenkinsop (2012) took this idea further by creating three-dimensional symbols for planes (e.g., bedding) and lineations (e.g., fold hinge), and adapted these into Google Earth so as to more easily visualize the relationship between structural geology and the land surface. A geovisualization at multiple scales was completed using Virtual Reality Modeling Language (VRML) by Thurmond et al. (2005), whereby the user can view point data such as facies boundaries and sample transects collected at various locations, and through clicking on a point with an embedded link, can view an image of the outcrop and a thin section of the rock.

In order to improve the user-understanding of concepts, scientists have attempted to increase the interactivity between the user and geovisualization. González-Delgado et al. (2015), for example, developed a virtual tour within Google Earth of paleontological sites in Spain, providing a virtual route to follow, several types of map

with photographs, and interpretations for each site. A game-like web browser interface is described by Saini-Eidukat et al. (2002) called 'Geology Explorer', which allows students to roam through a virtual world of outcrops, and use several different testing techniques to determine the lithology. Through exploring this virtual region, the students learn not only field and laboratory geological techniques, but a modality to observe geological features in a landscape. Jones et al. (2009) used more traditional geospatial analysis software packages such as ArcGIS Desktop (Esri, 2016) and GOCAD (Mira Geoscience Ltd., 2019) to create multi-scale visualizations of a wide range of 3D geological data, upon which analyses can be made within the software. Lin et al. (2013) propose that 'general understanding can be acquired more easily by viewing and experiencing such a digital geographic world than by viewing various figures and tables', implying these types of interactive geovisualizations are extremely powerful for geological and geographical data visualization and analysis.

The present research clearly demonstrates the potential advantages in using a virtual reality approach to visualize state-of-the-art remote sensing data. A variety of multi-scale, multi-dimensional, high-resolution data provide the detail and complexity of a real outcrop in a virtual, accessible setting. This comprehensive tour of an outcrop, called 'Up Close with Virtual Outcrops', presents an innovative method of delivering a field site to the user through a computer screen. With this research, resource and time limitations which may impede visiting a field site are made irrelevant, as the resolution of the remote sensing data in the geovisualization provide a virtual alternative which closely resembles reality. 'Up Close with Virtual Outcrops' is therefore an application which benefits both research and teaching endeavours alike, allowing multi-disciplinary users to efficiently interrogate a field site in a virtual environment.

4.3. Study Area

The Chasm field site in the Chasm Provincial Park (hereafter referred to as the Chasm), is located approximately 20 km northeast of the town of Clinton in British Columbia, Canada (Figure 4-1), and is a ~300 m deep canyon with slope angles of outcropping rocks nearly vertical, between 70°-90°. The Chasm exposes a nearly continuous outcrop of ten basalt flows in the canyon walls for approximately 7 km on either side (Andrews and Russell, 2007; Farrell et al., 2007). Ten lava flows are visible

over the length of the Chasm, slightly tilted from horizontal. Successive lava flows are typically intercalated with a red-brown paleosol and erosion surface with monolithic regolith basalt breccia; these paleosols are interpreted by Andrews and Russell (2007) to indicate many thousands of years between successive flows. The lavas were dated by Farrell (2010) at between 8.72 ± 0.37 Ma and 10.00 ± 0.48 Ma, with the estimated duration of volcanism in the Chasm area as 1.28 ± 0.61 Ma.

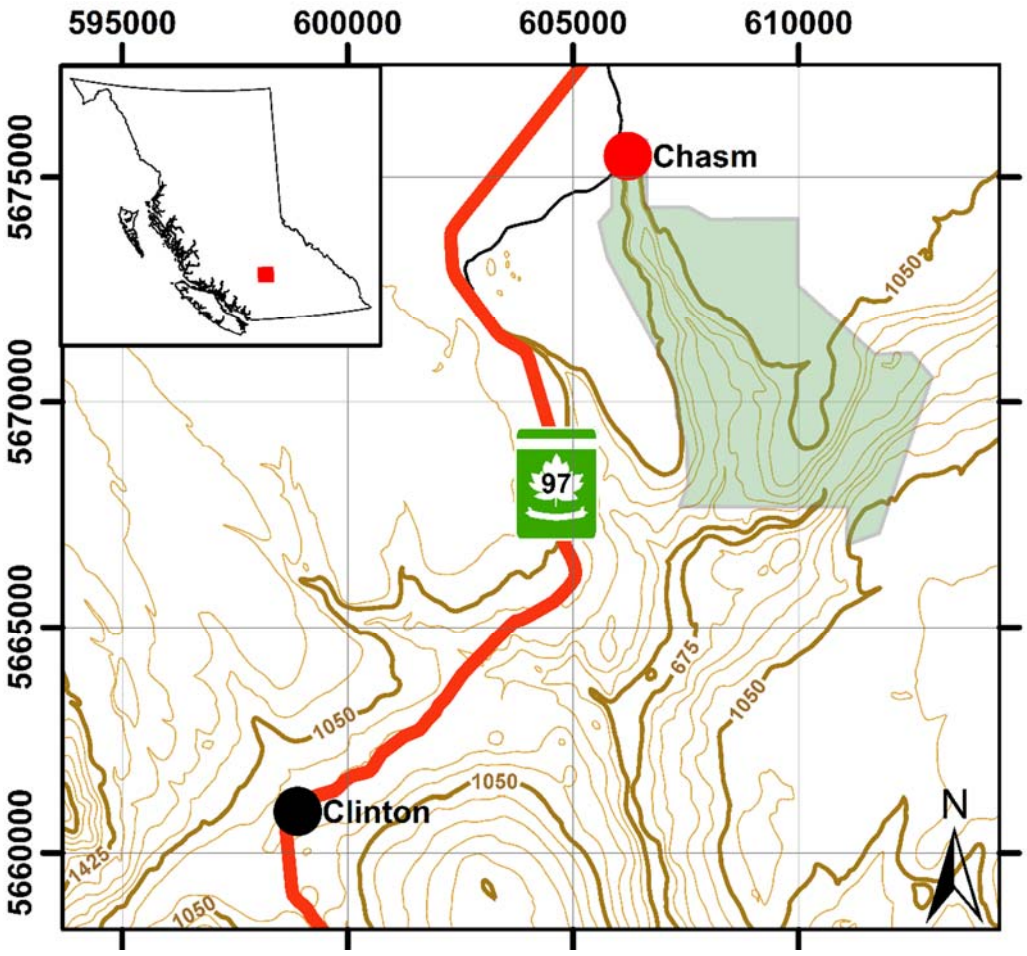

Figure 4-1. Map of location of Chasm Provincial Park (shaded in green). Topographic contour interval is 75 m. Inset map shows location in British Columbia province, Canada.

4.4. Methodology

'Up Close with Virtual Outcrops' was set up to be a virtual environment, within which the user can visualize several types of data. An empty 3D space, infinite in size, was used as the medium for starting the environment; this 3D space is a 'scene'. All

data visualizations and corresponding objects were put into the scene, including cameras for viewing, Graphic User Interface (GUI) objects for interaction and movement through the space and data, and the data models and images.

4.4.1. Data Visualizations

'Up Close with Virtual Outcrops' contains both two-dimensional and three-dimensional datasets. Two-dimensional datasets in the geovisualization include temperature decay curves, LiDAR reflectivity profiles, infrared imagery, and thin section images. A photorealistic model, which is a three-dimensional model with real colours created from the matching of photographs (Thurmond et al., 2005), forming a 3D mesh, was created for a portion of the Chasm slopes. Models of two detailed windows and each of five hand samples taken from the slope were added with the locations of samples and windows indicated on the slope model within the geovisualization.

To obtain the data required for the visualizations, remote sensing surveys at the Chasm were conducted in August 2015, including terrestrial LiDAR, both conventional and Structures-from-Motion (SfM) photogrammetry, and terrestrial infrared thermography (IRT). Laboratory testing included SfM imaging and experiments with IRT on hand samples.

All remote sensing data for the slope face was gathered from a distance of approximately 300 m from the slope at the Chasm (Figure 4-2). A Riegl VZ-4000 full waveform terrestrial laser scanner (TLS) system captured the LiDAR scans at a resolution on the slope of ~1 cm; the scans were then processed using the RIEGL proprietary laser scanning software package, RiSCAN PRO v.2.1 (Riegl Laser Measurement Systems, 2018). Post-processing, the laser scans were used to create reflectivity profiles, where reflectivity is a scalar value describing the brightness of a target on a -25 (low, e.g. black tar paper) to 25 dB (high, e.g. limestone) range (Riegl Laser Measurement Systems, 2015). The reflectivity profiles were generated by extracting a subset of the point cloud in the shape of a column (Step 1, Figure 4-3), and exporting the column of points from RiSCAN PRO into a text file. A data processing and coding software, MATLAB v.2018b (The MathWorks, Inc., 2019), was used to create the script *ReflProf.m* (Appendix A) which reads the point cloud text file, averages the elevations of the points (Step 2, Figure 4-3), averages the reflectivity values which occur

at the same elevation (Step 3, Figure 4-3), and finally graphs the reflectivity values with the elevation, resulting in a reflectivity profile (Step 4, Figure 4-3). The final profiles, as well as an interpretation of the geology based on reflectivity values, are visualized in the virtual environment as 2D images, which are georeferenced to their position on the slope face through lines placed in front of the cliff.

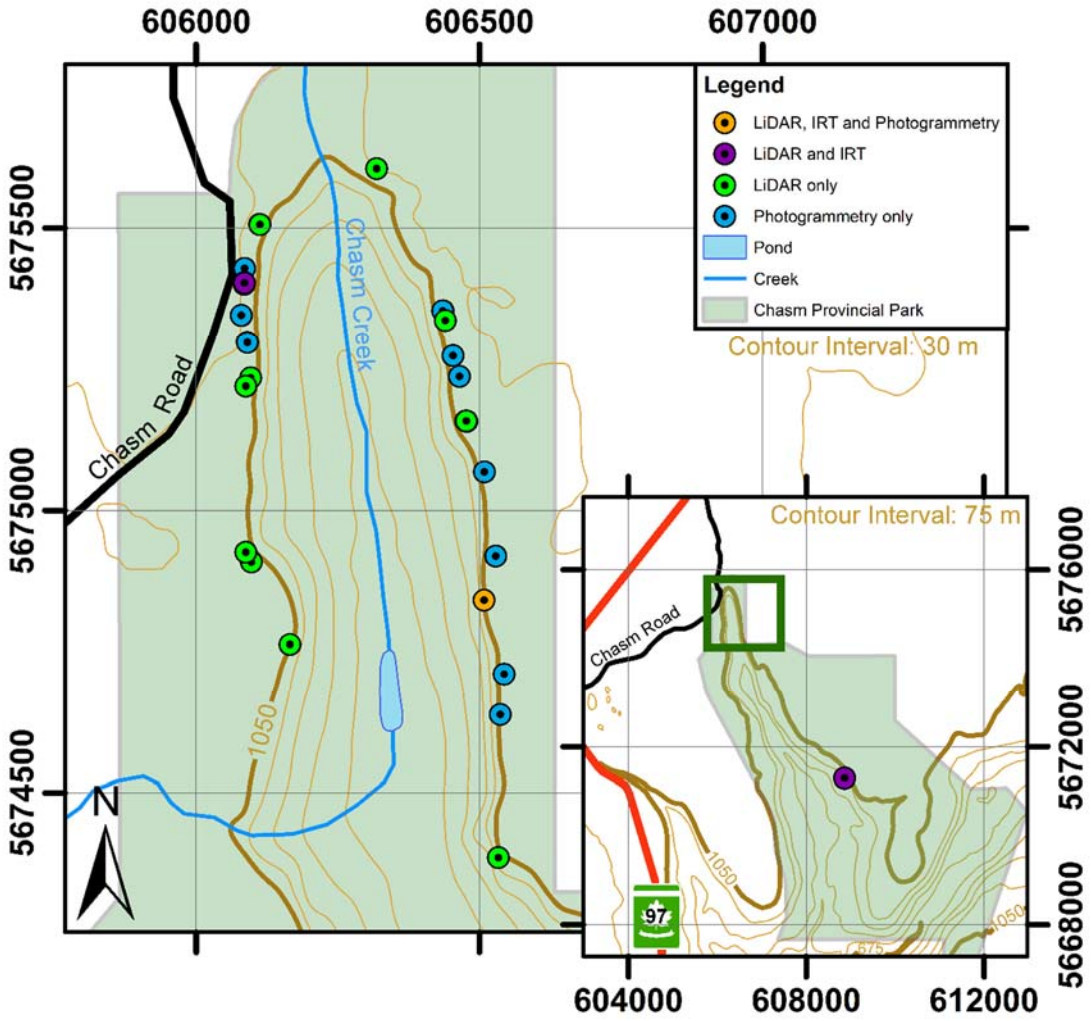

Figure 4-2. Stations for field surveys at the Chasm field site. Stations on the west side were for surveys of the east side slope, and vice versa. Inset shows location of type section from Andrews and Russell (2007) and Farrell et al. (2007), at which surveys in this study were undertaken; green box shows extent of smaller scale map near apex of canyon. UTM coordinates are in the WGS 84, Zone 10 datum.

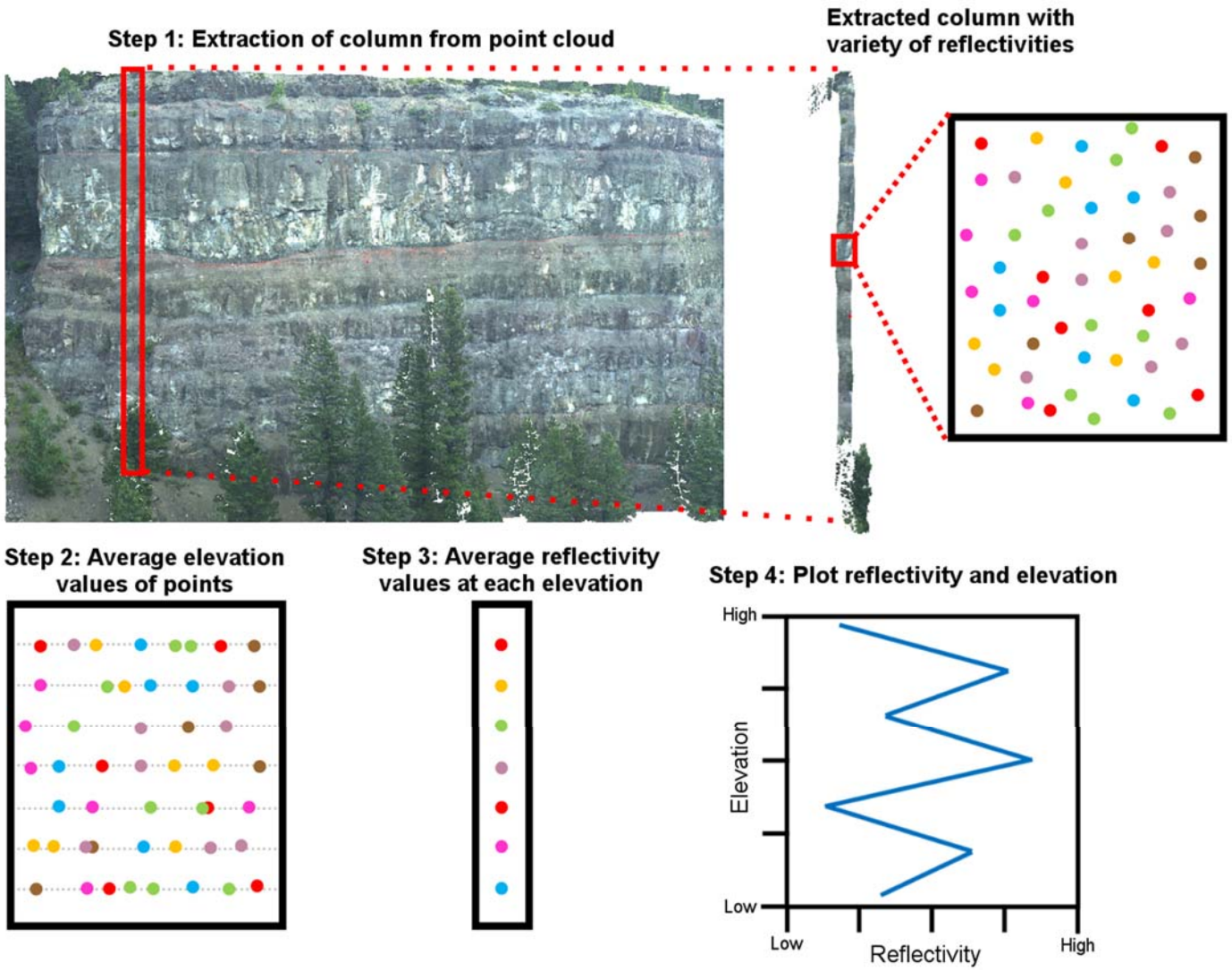

Figure 4-3. Schematic of workflow for creation of reflectivity profiles from a LiDAR point cloud.

To examine fractures, joints, and geological characteristics of slopes at the Chasm, a FLIR SC-7650 infrared camera with a focal length, *f = 100 mm* lens was employed for a rock slope IRT survey, which was carried out at a single station (purple station on the canyon apex map, Figure 4-2) over a cooling cycle of the rock slope, with images taken every 60 minutes between 20:05 and 05:05 the next day. As the rock slope in this study is too large to be contained in one frame of a lens with this focal length, multiple images were taken at each time interval, with approximately 40-50% overlap, to capture the entire slope. The thermal images were processed using the FLIR proprietary infrared camera software, ResearchIR MAX (FLIR Systems, Inc., 2015), exported individually as *.tif files from the program, and subsequently imported into a public domain panorama-stitching software, Hugin (d'Angelo et al., 2019) to create a single thermal image which included the complete rock face. The resulting stitched panoramic images are included in the virtual field site as 2D images, and coarsely georeferenced through positioning in front of the slope.

The laboratory IRT surveys were completed with a focal length, *f = 50 mm* lens with the infrared camera kept stationary, and samples were heated in an oven at 93 °C (200 °F) for approximately 48 hours. The samples were then placed into a white paper-lined box, which provided a high contrast background. The box was placed approximately 3 m from the camera lens, and temperature values were recorded through the capturing of images every ten minutes for seven hours. The images were processed in ResearchIR MAX, whereby Points of Interest (POI) were marked, and statistics on the temperature of each POI within the image were generated. As the camera was kept stationary, the POI has the same location in every image, and the change in temperature of a point over time can be found through the POI statistics from each individual image. The temperature statistics for every image, therefore, were exported individually from ResearchIR MAX as text files, and subsequently imported into MATLAB, where through running of the *LabIRT_timeseries.m* script (Appendix A), the statistics were extracted for each individual POI, copied and graphed as temperature decay curves.

SfM images were gathered using a Canon EOS 50D digital camera. Capture of images was completed at the Chasm from five stations (Figure 4-2) using a focal length, *f = 200 mm* lens for the entire slope model and a *f = 400 mm* lens for the detailed windows, with a distance between stations of ~30-60 m. The hand sample SfM was completed in the laboratory with a focal length, *f = 35 mm* lens. The hand sample was

placed on a white sheet of paper, which acted as a high contrast and visible target, allowing for an easily removable background. The set-up also gave easy access to all sides of the sample, allowing for a 360° model of each hand sample. The images were loaded into an SfM photogrammetry software program, Agisoft Metashape (Agisoft LLC, 2020), which matches features between images and analyzes the perspective on the target object within each of the individual images; from this information, the software creates a photorealistic, three-dimensional model of the target object. Once within Metashape, the images were organized into the stations they were captured from, to assist the program with determining the camera perspectives, and the software automatically aligned the images to create three-dimensional point clouds. After removing all background points (e.g., points from the white paper underneath the sample) from the clouds, meshes were made from the remaining points in the form of *.obj files, and textured with colours from the images. The textures include one or more *.tif files, which are the actual colours for the mesh, and a *.mat file, which acts as a map for the *.tif file(s), indicating to the program which sections of the *.tif file(s) correspond to which sections of the *.obj file.

A complete review of the workflows for the various datasets described is presented in Figure 4-4, including data formats for interoperability between software packages, and scripts created for data analysis.

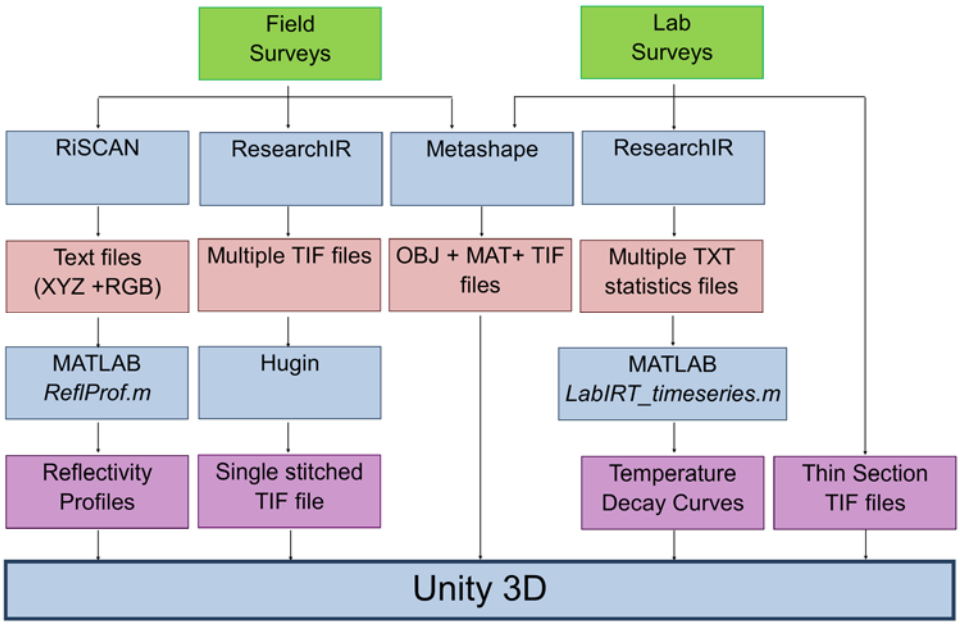

Figure 4-4. Geovisualization design and workflows. Green boxes indicate surveys for data collection, blue boxes represent software packages used for processing, pink boxes show file formats for interoperability, and purple boxes show processed data products which were input into Unity 3D. Italicized text indicates the scripts written for data processing.

4.4.2. User Interface

The user interface for 'Up Close with Virtual Outcrops' has been designed as a self-guided experience, where the user can be involved in a virtual field site which simulates organic methods of field surveying. This is especially important at a site like the Chasm, as the near-vertical slopes severely impede traditional investigation of the slope. In contrast, a virtual Chasm model can be viewed from any angle, distance or scale.

'Up Close with Virtual Outcrops' was created in Unity 5.3.4f1 (Unity Technologies, 2016), a game engine software within which the user can create a three-dimensional interactive virtual environment. The virtual space, or scene, is built using 3D and 2D objects, as well as Graphical User Interface (GUI) elements; scripts created with C# or Javascript codes are used to carry out actions and functions within the environment. A separate scene was used for each 3D model, to facilitate faster loading capabilities and prevent lagging of the virtual environment with large datasets. Two-dimensional (planar) objects in the Unity software are termed 'sprites' (Unity

Technologies, 2016), and are normally used in game engines as boundaries (e.g., walls) or background imagery. In the developed interface, however, sprites display datasets which have only two dimensions, such as graphs and images.

Virtual camera objects are included in the environment to control the user's viewpoints and perspectives; the user can only view where the camera object is pointing. Movement of the user through the scene, therefore, is allowed through the use of a C# script attached to the main camera object, *ExtendedFlyCam.cs* (Lochhead, 2016), which gives the user the ability to move through the environment with the computer mouse and keyboard keys (arrow keys and WASD).

GUI elements are those with which the user interacts, such as a button, and change the conditions of the virtual environment. This is possible through attaching one or more scripts to the GUI object, and through an action by the user on the object such as a click, functions within the attached script(s) are carried out. Two basic GUI elements were utilized to facilitate user interaction in the 'Up Close with Virtual Outcrops' scenes, buttons and toggles. Toggles, which are essentially logical (true/false) indicators, were used to display datasets. When the toggle box is checked, the function is called in which the 'active' attribute of the element is turned on, and a data visualization appears on the screen. Buttons were used in this interface to both switch scenes through the *ButtonNextLevel.cs* script (Appendix A), and facilitate tours in which certain characteristics of the three-dimensional models are pointed out. For all toggles and buttons which switch between datasets, the *CameraPos.cs* script (Appendix A) is also attached to the main camera, and adjusts the position and lighting to optimal settings for viewing the different types of data. The complete design and flow of the geovisualization interface is shown in Figure 4-5.

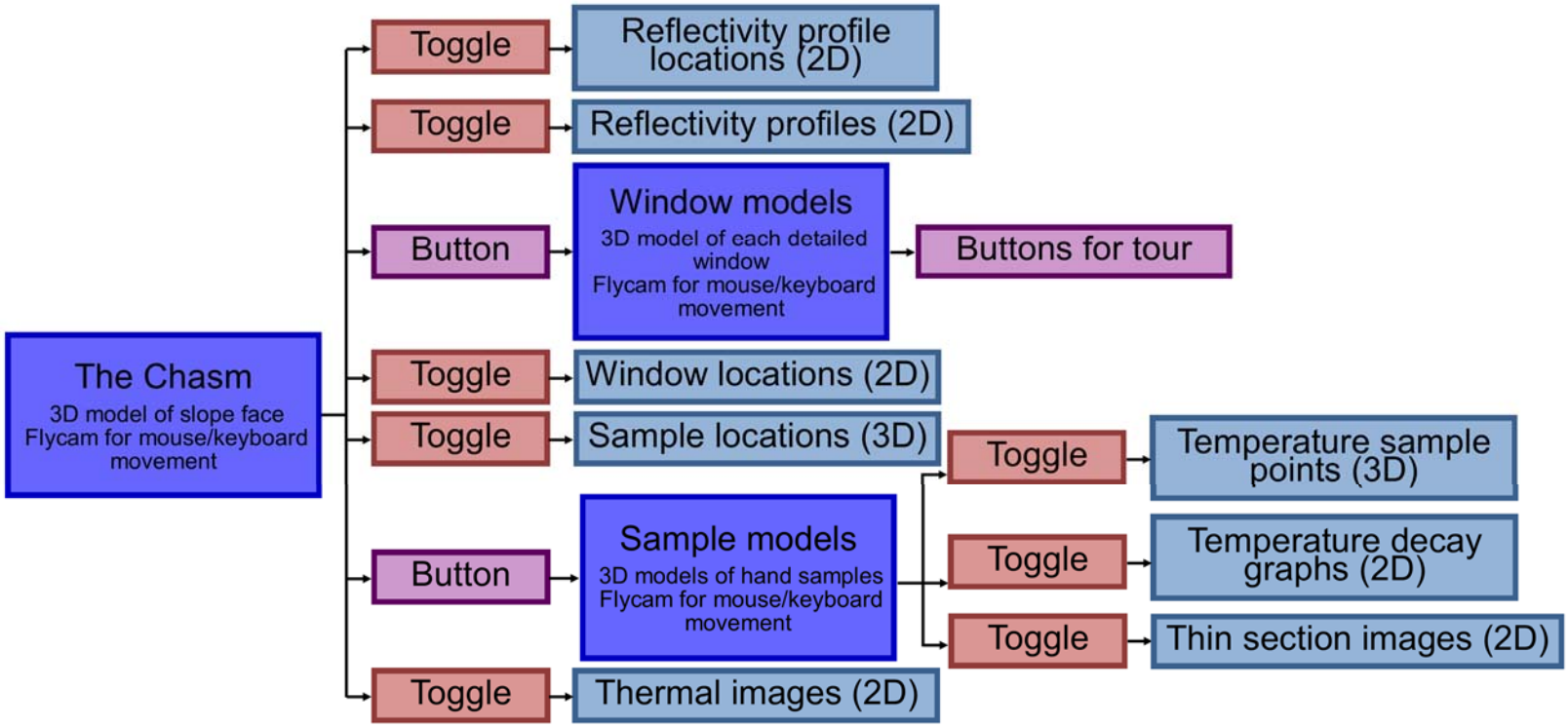

Figure 4-5. Geovisualization interface design. Dark blue boxes indicate scenes, pink boxes denote toggles, purple boxes buttons; light blue boxes show data visualizations with dimensionality indicated.

4.5. Results

The virtual experience commences with a scene displaying one of the slopes at the Chasm (Figure 4-6). Within this initial scene are several toggles and buttons which allow the user to switch easily between various datasets and viewpoints. The reflectivity profiles are viewed through clicking the toggles which show the profile locations (lines on the slope face) (Figure 4-7), as well as the raw and mapped graphs of reflectivity with elevation. IRT images are available through several toggles each accessing a thermal image from a different time stamp. A toggle exists to show the locations on the slope face from which hand samples were taken through colour-coded spheres (Figure 4-8), which correspond to coloured buttons. Sample buttons bring the user to separate scenes, with one sample in each scene. These sample scenes offer 3D SfM models (Figure 4-8) of the samples, temperature decay curves (Figure 4-8) obtained from laboratory thermal experiments through toggles which appear on the side, as well as images of thin sections (Figure 4-8). Temperature sampling points used to create the graphs can also be viewed with colour-coded spheres through a toggle (Figure 4-8). Windows where detailed SfM models were created on the slope (Figure 4-8) are accessible through colour-coded buttons in the main Chasm scene; these correspond to the windows shown on the slope when the toggle for window locations is activated (Figure 4-8). Within these detailed window scenes are guided tours, whereby the user's attention is drawn to specific features visible on the window models when they click on the buttons of the tour in sequence.

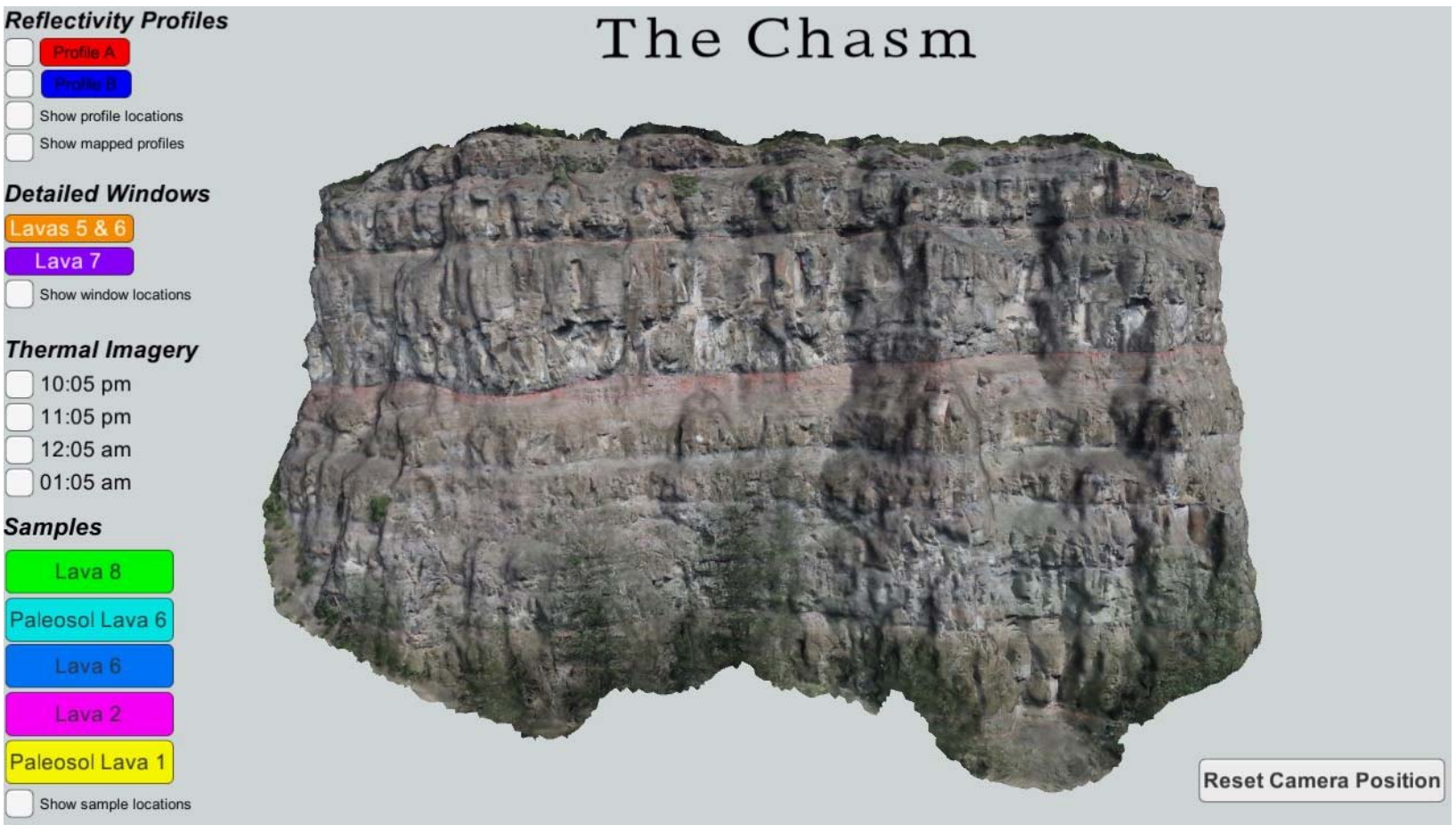

Figure 4-6. Main page of 'Up Close with Virtual Outcrops' interface.

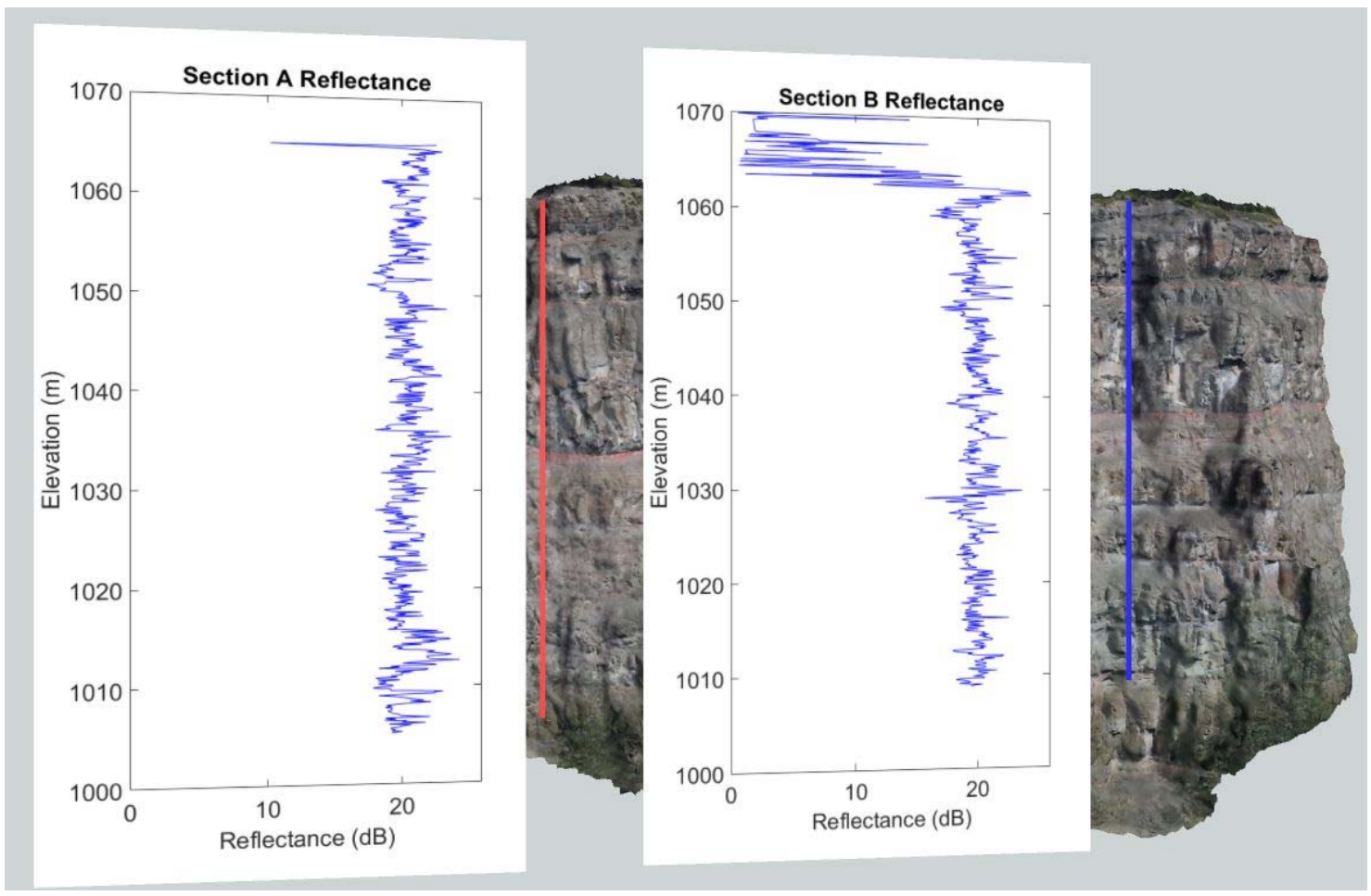

Figure 4-7. LiDAR reflectivity profiles, shown as they appear in the 'Up Close with Virtual Outcrops' interface. Red and blue lines on the slope indicate where the profiles are located on the slope face.

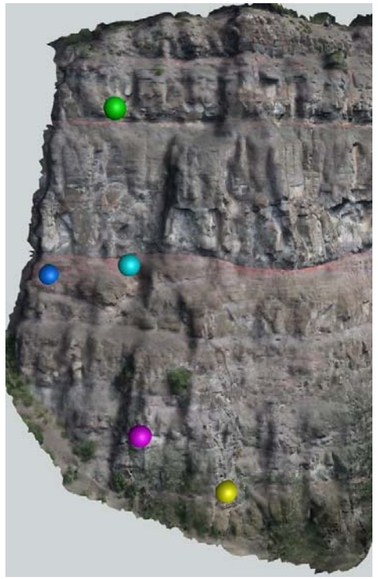

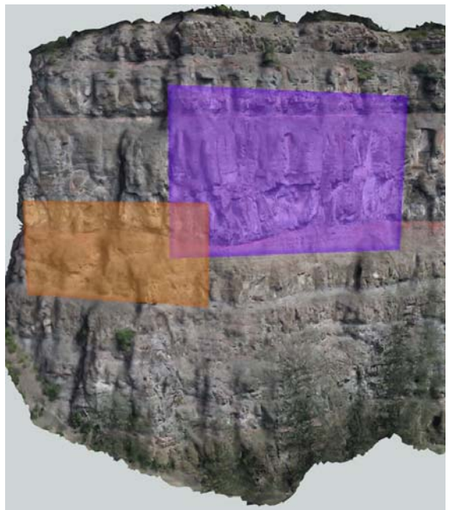

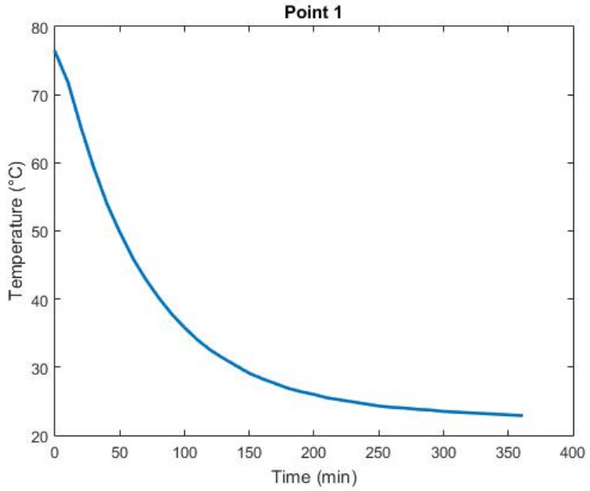

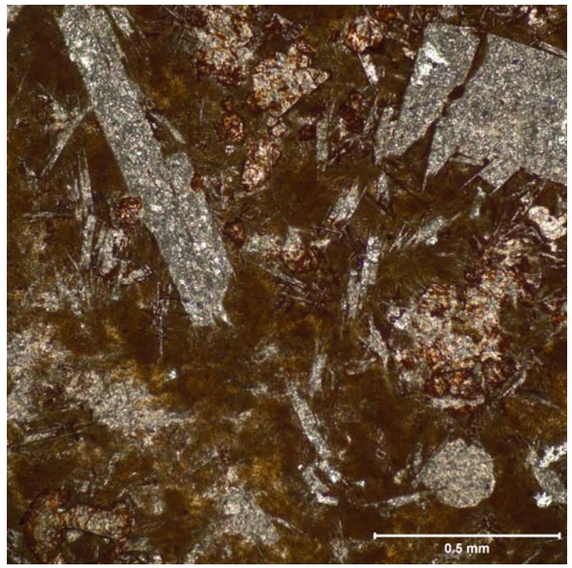

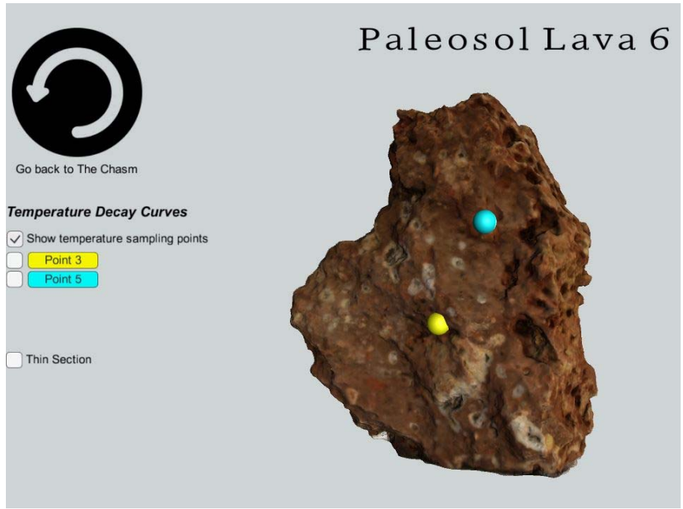

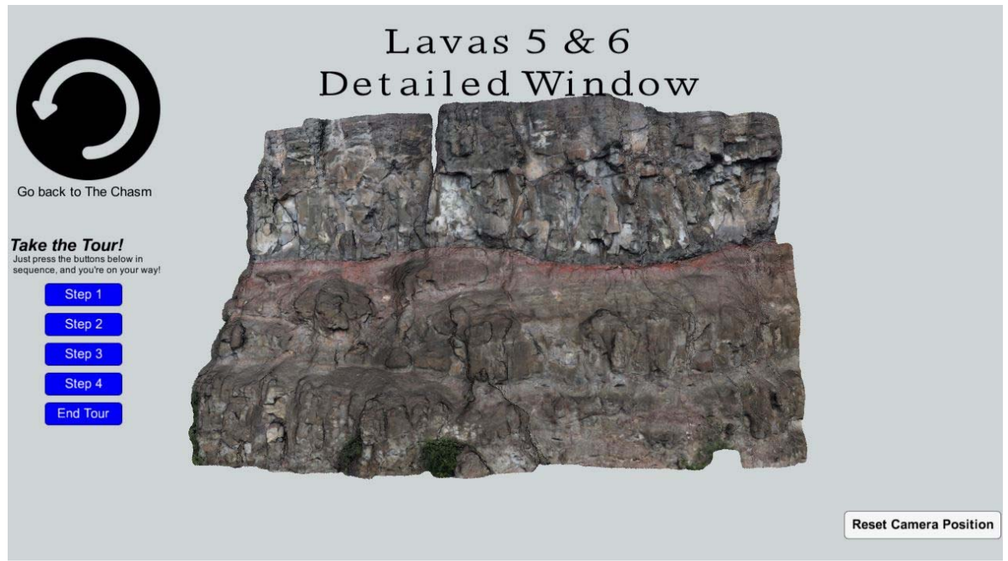

Figure 4-8. Coloured spheres showing locations of hand samples on the Chasm slope (top left), temperature decay curve for one of the lava hand samples (top middle), main screen showing one of the scenes for hand samples, as a 3D SfM photogrammetry model (coloured spheres denote locations of temperature sampling points for laboratory IRT experiments, top right), main Chasm rock slope model with the SfM photogrammetry window locations shown (bottom left), thin section image of one of the lava hand samples (bottom middle), and the main screen of one of the detailed slope window scenes, showing a 3D SfM photogrammetry model of the Chasm slope window (bottom right). All views are as shown in the 'Up Close with Virtual Outcrops' interface.

Through a visual interface such as that described above researchers and students can obtain maximum benefit from both the raw remote sensing data and the interpreted field and laboratory data. The 'Up Close with Virtual Outcrops' interface allows the user to fully explore the multiple datasets collected for the virtual Chasm field site in a similar manner to how they would have done at a real-world field site. In a learning environment, the guided tours in the detailed window scenes are analogous to a lecture on the features to look for in the outcrop, while providing a narrative of the geological history of the region inferred by these attributes. The storyline provided by this interface is non-linear, providing a logical flow of information with the differences between dataset characteristics.

Within Unity, several modules allow for the geovisualization interface to be viewed through different platforms. The current compatible platform for 'Up Close with Virtual Outcrops' is a desktop interface, whereby the user uses a desktop computer, tablet, or laptop to launch the application; this was exported from Unity as a PC executable. This platform was chosen for its ubiquitous compatibility with readily available machinery, however a more immersive virtual reality/mixed reality (VR/MR) technology such as Microsoft HoloLens 2 or Oculus Rift may be available in future applications.

4.6. Discussion

The geovisualizations created for 'Up Close with Virtual Outcrops' are a combination of photo-realistic three-dimensional models, images, and graphs, and are all representations of the data gathered in field and laboratory environments. Several of the geovisualization methods of the data can be improved for future versions, as they do not fully represent the quality of the gathered data.

SfM photogrammetry and terrestrial LiDAR models present high-resolution geometries of the Chasm samples and slope. As geological phenomena are inherently three-dimensional in nature, SfM and LiDAR models are excellent tools for accurate representation. The combination of RGB (natural) colour with high-resolution three-dimensional data presents a powerful medium for viewing and analysis of data in a virtual environment.

Thermal images, though a form of 2D data, are actually 3D data in the real world. This discrepancy in dimensionality occurs due to the camera only viewing a single perspective, and consequently not being able to record depth of pixels into the image. Thermal imagery, therefore, is not a pure representation of the temperature data, but rather implies that certain parameters (such as depth, angle, distance, height, etc.) remain constant for all pixels in the image. In the current version, when the user activates one of the toggles to show a thermal image, the camera view is changed to a location where the image is shown in front of the 3D model. If the user changes the viewpoint or zooms in or out, the thermal image is no longer in the correct position with respect to the slope model. This can lead to misinterpretation of temperatures on the slope face, as the user is forced to estimate where on the slope a certain point matches up. With this in mind, future versions of the application will include thermal imagery which has been draped over a three-dimensional mesh, so as to better embody the nature of the real-world temperatures, and allow for easier interpretation and visualization.

The thermal graphs depicted within the Chasm sample geovisualizations are viewed as 2D sprites, which fully describe the characteristics of the data they signify. The objective of these data is to demonstrate the variability of the temperature of one point through time, and therefore a simple graphical representation such as that in ‘Up Close with Virtual Outcrops’ is adequate. An improvement in future versions would be to have a ‘virtual cooling’ (Figure 4-9), whereby the points (the symbols on the 3D mesh) change colour when a slider with time values is changed (and therefore changes the temperature). This slider could be attached to all temperature sampling points within the scene, and therefore the change in temperature for several points could be displayed at once, and with direct user interaction with the time scale. A visualization such as this for temperature decay could greatly improve understanding of the rate of cooling for points on a hand sample relative to neighbouring points.

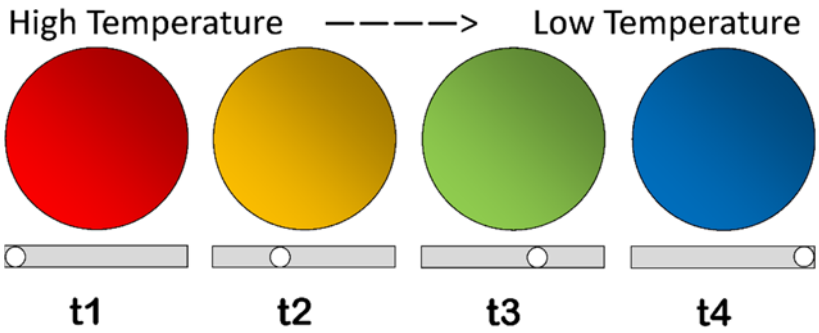

Figure 4-9. Example of virtual cooling, whereby spheres on the three-dimensional model of the hand sample could depict the temperature of that point over time (from t1 to t4) through a change in colour corresponding to change in temperature.

The reflectivity profiles were taken from 3D point clouds and simplified into a 2D diagram. This simplification allows for easier understanding of the phenomenon, and facilitates comprehension on the topic as a whole by exemplifying the change of reflectivity with differing lithologies. On the other hand, these data are similar to the thermal imagery in that in reality they exist in three dimensions, and therefore a more authentic representation would display the data in 3D. This may be accomplished using a separate 3D mesh or set of points with reflectivity values for the column of data represented by different colours along a colour scale.

As many of the geovisualizations are three-dimensional, an interface which can fully immerse the user into the experience, such as Microsoft HoloLens 2, Oculus Rift or Samsung Gear VR, would allow improved understanding of the features being demonstrated, as the dimensionality of these geovisualizations are the most influential factor for overall comprehension. The interaction design for 'Up Close with Virtual Outcrops' is currently a simplified preliminary version, and is considered suitable for a first-order interpretation of a field site. The interactions and visualization capabilities mentioned for future versions, however, would significantly improve the user experience through a more direct visual interaction in an immersive environment allowing a deeper understanding of the geological environment.

In order to ascertain whether 'Up Close with Virtual Outcrops' enhances overall data visualization and analysis, a test group of students and scientists who are allowed to explore the application individually and are subsequently surveyed about their user experience, would likely yield a better understanding of the effectiveness of the

geovisualization and interface methods chosen. In future versions, the entire section of the Chasm which has been imaged (approximately 3 km from the apex of the canyon, on both sides), could be visualized with zoom-in options for the three main study areas. Currently, only one part of the slope in the study area is shown. The addition of these extra sections would not only improve the perception of where the current slope model fits into the lava sequence as a whole, but also allow for comparison between sections with detailed data collection and observe the similarities and differences therein.

4.7. Conclusions and Future Work

'Up Close with Virtual Outcrops' provides an interactive virtual field site experience and a medium for virtual interaction between the geologist and the outcrop. Through several different geovisualization methods, this interface allows for learning and analysis of multiple detailed field and laboratory datasets. Several previous studies have created visualizations of geological data, however the direct intractability with high-quality and multi-dimensional data within 'Up Close with Virtual Outcrops' makes it a more cooperative effort between human and machine, and allows for a viable alternative for research and learning in a virtual setting.

The developed geovisualization interface combines the use of existing functionality of the Unity game engine with scripts specifically designed for the 'Up Close with Virtual Outcrops' environment. Unity is an ideal workspace, as it provides modes for displaying, viewing, moving, and interacting with many types of data, and is a relatively easy software to learn and use. The ability to change the functions of Unity objects with personalized scripts makes it extremely versatile, and consequently an invaluable tool for design and execution of data visualizations.

The variety of data within the developed geovisualization interface highlights the versatility of a visualization method such as this, as well as allows the user to view the field site from different perspectives, scales, and compare different remote sensing and traditional mapping methods. The high resolution of the included remote sensing datasets enhances the capability of the user to examine every aspect of the field site at multiple scales, thereby increasing overall effectivity in demonstrating a real-world outcrop in a virtual space. An interface like 'Up Close with Virtual Outcrops' can host

virtually any type of data, and therefore could be adapted to suit any surveyed field site. This flexibility and adaptability makes virtual reality an extremely powerful tool for the future of geoscience and geoscience education, as inaccessible areas around the world are brought within reach of geoscientists in a virtual world of outcrops. Tools such as this are becoming increasingly relevant, especially during the COVID-19 global pandemic in 2020, whereby the majority of learning has been taken online, and students must learn field techniques virtually. A series of outcrops in a virtual “field trip” format could significantly increase the teaching potential in an increasingly online world. Future versions of ‘Up Close with Virtual Outcrops’ will have several updated features, however the current simplified version demonstrates the great potential of a virtual field site in user interaction, education, and analysis of rock outcrops and slopes.

Chapter 5. Discussion

This chapter provides a critical assessment with a focus on the survey data collection, data processing, analysis, and results, as well as possible improvements for the future. Details of each area of the project will be considered, such as survey parameters, set up and execution of data collection, the effectiveness of the methods used in the evolution of data from raw to results, the quality of those results, as well as how they compare to other methods and studies.

5.1. Assessment of Field Sites

Both field sites chosen, the CVB outcrops and the CG basalts at the Chasm, were composed mainly of basalt lava. This relatively uniform composition allowed for a close comparison of the two field sites, the different methods used at each, and the comparison of approaches using remote sensing on such outcrops. These outcrops have also been studied before, providing a base of knowledge upon which to build, and a unit of reference to frame the objectives of this research.

The field sites chosen for this research were optimal for determination of the quality of data, as there were locations for ground-truthing the validity of the results, as there were areas with uniformity as well as variation in the outcrops, and the comparison of field methods, as there were a variety of survey techniques and instruments employed. The CVB outcrops were easily accessible and offered an opportunity for contact mapping as a reference for the remote sensing field work. Access to the outcrop at the Chasm site was limited due to the steepness and height of the slopes. The interstratified paleosols, as well as the changes in colour, structure, and textures in the lavas at the Chasm provided enough variability in the data for marker horizons to be captured by the remote sensing techniques used. As the basalts at the Chasm did not show significant variation in the overall composition however, the results could also be critically assessed for quality, as the working theory for mapping with remote sensing is that similar rock types would yield similar responses.

5.2. Alteration Mapping

LiDAR reflectivity and RGB values were used to map alteration on the LIP1 slope, with different levels of success. LiDAR reflectivity is dependent upon colour, texture, lithology, and slope aspect, and therefore was tested for differentiating alteration from other characteristics on the slope. As noted in subsection “Alteration Mapping Using LiDAR and Photographs” of Section 3.2.1, the values of reflectivity found from the representative altered areas on the slope (e.g. white alteration was -8.65 to -4.29 dB) yielded ranges too broad to map alteration conclusively.

It was then hypothesized that patterns may be more visible if using specific and narrow ranges of reflectivity, such as were used in Section 3.2.2, subsection “LiDAR and Reflectivity”. Through viewing a 1 dB change in reflectivity at a time, it became evident that a large range in reflectivity (e.g. -8.65 to -4.29 dB) leads to a large area of slope represented. Smaller ranges of reflectivity offer more specific views of the slope, and -3 to -5 dB was found to be the optimal range for capturing white alteration and iron staining on the slope via observations of the smaller ranges. This means that a single value of reflectivity is not exclusive to a single slope feature, and patterns in the reflectivity values provide more meaningful information.

Red, green and blue (RGB) colour values from photograph pixels were tested as an alternative method for mapping alteration on the Chasm slope, with photographs from two sources (“Alteration Mapping Using LiDAR and Photographs” in Section 3.2.1). LiDAR photographs were taken during the LiDAR scan of the slope, and automatically georeferenced to the point cloud in the RiSCAN software, such that each point possessed its own set of RGB values from the photographs. Photographs from the photogrammetry surveys were also used, and pixel values were assessed in GIMP.

Generally, the RGB method of mapping alteration was successful in identifying main areas on the slope with white alteration or iron staining. It tended, however, to include extra regions in the maps which either did not have any alteration (a negative result), or the altered area was too small or spotty to map in the manual delineation (a positive result). As this discrepancy exists in the validity of results, it is thought that the RGB method would be best used in conjunction with another method to yield the optimal results.

RGB values depend upon the light and shadow within the photograph, the instrument sensor, settings on the instrument, and processing of the photographs after being taken (e.g. using filters). These values, therefore, are highly dependent upon the survey parameters, especially the time of day. This is seen in the differences between photographs for RGB values used in the same representative areas for mapping (Table 3-2), where values sometimes varied by up to 75 (on a 0-255 scale). To circumvent this problem, each dataset (LiDAR photographs and photogrammetry photographs) was treated individually, thereby proving that a photograph taken with any instrument can be useful in the employment of this technique. To obtain the best results, the time of day and lighting issues need to be considered, and a time with daylight but no shadows (i.e. an overcast day, or dusk) is best to obtain images with useful RGB values.

LiDAR reflectivity does not depend on the position of the sun or lighting with respect to the slope, so is a useful tool regardless of when the survey took place. As patterns rather than specific values must be used, however, this method is a less exact technique for mapping alteration than the RGB method, and so is thought to be optimal for outcrop-scale observations.

5.3. Discontinuity Characterisation

The joint data obtained for CVB1 could not be compared between terrestrial laser scanning and photogrammetry methods, as the orientations of the joints in the photogrammetry model were not available. The laser point cloud model and the infrared imagery, however, were compared, and it was found that both show similar numbers of joint sets in the western portion of the outcrop, however the joint sets visible in the eastern section differ. As only one station was used in the infrared survey, the benefit of another point of view of the outcrop was not available; this may account for the discrepancy between datasets (i.e. occlusion).

The CVB2 datasets differ slightly in their joint set orientations. The photogrammetry joint data show distinct groupings of joint orientations, whereas the laser model joint data has a more dispersed pattern for their orientations. This apparent dispersion may be caused by either a larger amount of joint data available from the laser model, the variability in joint identification was introduced while measuring orientations in AdamTech, or the joints in the outcrop do actually have a large range in orientations.

The photogrammetry data may also be less reliable, in that the model created by stereopairs of images at CVB2 was found to have large data ‘holes’. Where a columnar shape is expected by looking at the laser point cloud model and real-colour photographs of the outcrop, an indentation into the model, rather than an extrusion, is observed (Figure 5-1). These holes may be caused by the nature of columnar jointing itself, in that if the station spacing was too large, certain faces of the columns may be visible in images taken from one station and not the other. This leads to a lack of control points for these particular areas of the slopes, and therefore points in the point cloud have a large margin of error, leading to large holes in the model.

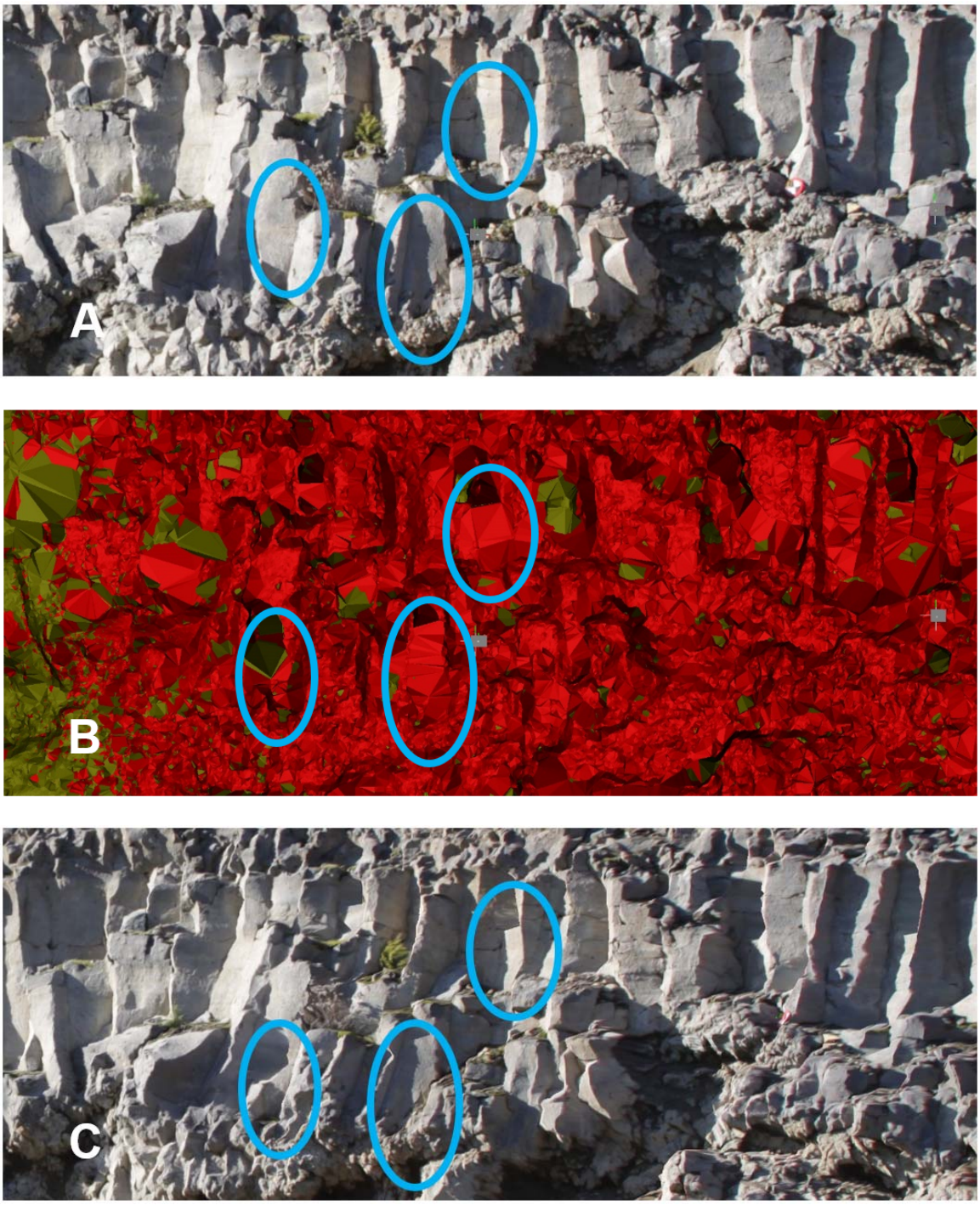

Figure 5-1. Close-up of the CVB2 photogrammetry model showing the 'holes' in the model; three of these holes are indicated in the figures by blue circles. A: real-colour photogrammetry model image taken facing outcrop, B: triangles of model from point cloud, C: real-colour image of photogrammetry model taken looking at the outcrop from the right side.

In future studies, to prevent a loss of orientation data of joints and the presence of holes in the photogrammetry model, it would likely be beneficial to use the SfM approach for obtaining photogrammetric images, as well as using georeferenced targets on the outcrop. A greater number of stations, more closely spaced, may be advantageous when assessing slopes with columnar jointing, so as to maximize the control points visible on columns between sets of images. CVB1 was also surrounded, and in some cases obscured, by a significant amount of vegetation, which may have caused some error in the data collected. For future surveys, therefore, outcrops with less vegetative cover would most likely yield more reliable results for both photogrammetry and laser surveys.

Columns are present at both CVB1 and CVB2, however the shape and size of these columns differ between the outcrops. The columns in the outcrop at CVB2 are much shorter than those at CVB1, though both sets of columns have similar widths. At CVB2, a defined boundary between the upper and lower colonnades of the lava flow is visible, but only the lower colonnade is observed at CVB1. This difference in structure may be attributed to the thicknesses of the lava flows, whereby the flow at CVB1 is several meters thinner than that at CVB2, possibly inhibiting the formation of an upper colonnade. The columns at CVB1 are also much more regular in orientation and size than those at CVB2, as can be observed in the distribution of the joints within joint sets (a more regular distribution suggests more regular orientations of joints). This variance between the columns at both sites cannot be attributed solely to compositional differences, as the composition of the basalts at CVB1 is similar to that at CVB2 with only minor variations in geochemistry (Woodell, 2012). A difference in effusion rate, thickness, relative locations of glacial margins, and many other factors may have contributed to the differences in column morphology at the Cheakamus basalt sites.

Discontinuities were mapped for all four windows at the Chasm on SfM models created in Metashape. The resultant point clouds and mesh were high quality, as field surveys included four stations, relatively evenly spaced along the opposite Chasm cliff edge, all providing photographs of the LIP1 slope. The access to viewpoints of the slope from multiple directions, in this case, was extremely beneficial to data collection, and as a result, data from the processed models could be relied upon for quality. Orientations were planned to be made for photogrammetric models through locations on the slope obtained with the Total Station, however since the windows for detailed analysis had not

yet been decided, many of the points chosen to aid in model georeferencing were outside the areas of the windows. The orientations were therefore carried out with the use of points in the LiDAR scan, where the resolution of the scan (approximately 1 cm distance between points on slope) and photographs (1 pixel is approximately 1 cm) were the same. This match in resolution rendered the search for common points simple and accurate, resulting in well-oriented window models.

The process of mapping joints in CloudCompare with the Compass plugin was straightforward, but the main area in which error could be introduced is the segmentation step. As the specific area of the point cloud selected is that which the plane representing the joint is fit, this region of interest must be selected very carefully, and attention must be paid to ensure only the joint surface is selected. Error was reduced in this step, however, by leaving a margin equivalent to 2 centimeters unselected at the approximate edges of the joint surface.

Columnar jointing usually consists of three joint sets, since columns are hexagonal. The observations of the four Chasm windows on the LIP1 slope and at CVB1 are consistent with this, and have three sub-vertical joint sets representing columnar jointing, with also a sub-horizontal joint set following chatter marks and ball-and-socket joints on the columns. CVB2 is the one exception and has four columnar joint sets with a sub-horizontal fifth joint set. CVB2 therefore has more variability in column orientations, indicating there was a more irregular development of columnar joints in this lava flow.

The average dip of all columnar jointing mapped at the Chasm is 82°, with a range between 77-86°. Columnar jointing forms perpendicular to cooling margins of the flow (i.e. the ground, the air, a glacier), indicating successive flows at the Chasm were emplaced with cooling margins at approximately the same orientation with every flow. Based upon the current orientation of the unit boundaries, the flows were emplaced sub-horizontally, and the lava was in contact with the cooler paleo-topography and atmosphere, yielding sub-vertical columns during cooling.

As each unit at the Chasm is a separate lava flow, it is not expected that the orientations of joint sets (i.e. dip directions) would be the same between units. It is important to note, however, that JS1 in Units 1 and 3 (Window 1) is mapped with dip

directions about NE-SW, and rotates clockwise with decreased elevation in the slope to approximately ENE-WSW in the lower units (Windows 2-4). JS2 in Unit 1 is comprised of W-E dip directions, and rotates slightly clockwise to alternate between units (Unit 3 and below) between WNW-ESE and NW-SE. Dip directions in JS3 also rotate further down in the sequence, from NNW-SSE in Window 1 to NNE-SSW in Windows 2-4. All joint sets, therefore, have rotated in dip direction by 45-70° with respect to the difference in dip direction between Unit 1 and Unit 15. This indicates the cooling surface was not identical between successive flows, which is to be expected due to each flow being emplaced on top of the former.

JS4 varies greatly in orientation between windows, as the characteristics used to map joints as JS4 are inherently variable. JS4 is the sub-vertical joint set in all windows, and a threshold of approximately 30° from horizontal was used. As such, all dip directions can be included in this joint set, and no pattern between units for orientation of this set was observed.

In Windows 1, 2, and 4, the joint sets are distinctive, and a dispersed array of orientations is generally not observed. Window 3, however, exhibits significant scatter of joint orientations in the stereonet. The joints in Window 3 were not mapped into separate units, and this window was not comprised of regularly spaced columnar jointing, resulting in a more chaotic distribution of joint poles than other windows.

The highest joint persistence observed throughout all windows was in the sub-horizontal joints in Unit 1 (13 m), where ball-and-socket joints were propagated across several columns. The columnar joints in Unit 15 have the highest persistence of all mapped columns in the LIP1 outcrop, and is also comprised of the widest columns observed at the Chasm (up to 3 m). This indicates Unit 15 likely cooled the slowest of the visible Chasm units, as the larger the column diameter, the slower the cooling rate of the flow (Hetényi et al., 2012). Interestingly, though, Unit 15 is not the thickest unit (up to 10 m); rather Unit 5 is the thickest of the LIP1 slope flows at 16 m. This is indicative of a faster cooling rate in Unit 5 compared to Unit 15, and resultant columns are approximately 2 m in diameter. It is expected that a thicker flow would take longer to cool, so possibly the climate may have been cooler (than that of the climate during emplacement of Unit 15) or the underlying Units 6 and 7 may have cooled completely before Unit 5 was emplaced (as opposed to Units 16 and 17 under Unit 15, which may

have not been cooled to regular ground temperature yet). Unit 7 is a thin, discontinuous lava flow, so the theory of it having completely cooled before Unit 5 flowed over it is possible.

Kinematic slope analysis using the DIPS software was only completed on the CVB1 and CVB2 discontinuity data and slope geometry. DIPS solely uses joint orientations to make its determinations for the kinematic model, and does not consider any field observations other than slope dip, slope dip direction, and friction angle of the slope material. This means that the DIPS analysis if efficient for a first approximation of potential slope failure mechanism, but as the persistence and spacing of the joints are not considered, care needs to be taken in interpreting the results. For example, as the columnar jointing at both CVB1 and CVB2 inherently is composed of intersecting joints, wedge failures were deemed by DIPS as the most feasible type of failure. No large wedges, however, were observed in the field, and the previous failures observed on the slope consisted of portions of columns (between ball-and-socket joints) rotating forward off the slope as toppling failures.

5.4. Thermal Imagery

The thermal imagery for CVB2 displayed several different joint sets, however the sunlight was more direct onto this outcrop than the outcrop at CVB1, and so significant variations in temperature between joint sets are much less visible (Section 3.3.2). It is therefore difficult to determine how many joint sets are visible in the thermal imagery, however a minimum estimate of three vertical joint sets based on the thermal variations in the slope from joint surface aspect with respect to the Sun. This number is different from the laser and photogrammetry values, probably due to the direct sunlight reducing the temperature variability, or the coarser resolution of the thermal imagery as compared to LiDAR and photogrammetry.

At the Chasm, thermal images were taken in two cooling cycle surveys, one at the LIP1 outcrop, and one at the LI1 outcrop (Sections 3.2.1, “Infrared Thermography” and 3.2.2, “IRT”, respectively). Both of the outcrops were larger than the field of view of the infrared camera lens, requiring stitching of panoramas and alignment of successive images before analysis.

The LIP1 outcrop region of interest is large (approximately 67 m high and 118 m wide), which meant that on average 124 images were captured for each time stamp. The moving of the camera in a snake/switchback pattern over the outcrop for each time in the survey took about 4-5 minutes, resulting in a slightly different time stamp for each image. This is thought to have introduced minimal error in the survey results, as the temperatures over the entire survey decreased by an average of 15.3 °C over 9 hours, which means a possible change in temperature of 0.1 °C over 4-5 minutes. Temperatures are analyzed in the range of 0.2 °C to several degrees of difference, so this possible difference in temperature is considered insignificant to the overall findings, but should be kept in mind for detailed temperature analyses.

Greyscale images were exported from ResearchIR MAX, using the same scale for images within the same time frame of the survey. Though the same scale was used, there was the possibility of slight temperature variations in the same feature of the slope in different images of the same survey time, due to the switchback pattern error mentioned above. For example, this slight variation is noticeable in the stitched imagery for Window 3 (Figure 5-2), where a vertical line appears in the righthand side of the image. This is not an error that can be corrected and should be considered in the analysis of results. Future surveys of smaller areas which do not require a 4-5 minute delay to capture the whole outcrop would remove this error.

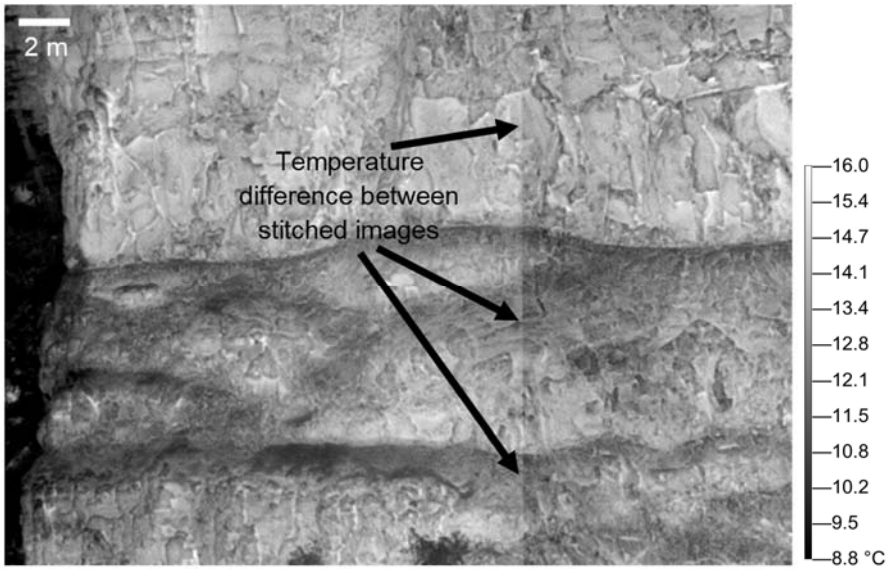

Figure 5-2. IRT image of Window 3 at 04:05 am, August 3, 2015, showing a slight temperature difference between stitched images (vertical line).

The panoramas for the LIP1 outcrop were stitched together using the Hugin software, which uses common points in each of the images to create matches. RGB photographs have over 16 million possibilities of colour combinations as each R, G, and B value has 255 numbers (on the 0-255 scale used). Greyscale images, conversely, have 255 possible values of colour and consequently have much less variation in the images than in RGB images. As a result of the reduced variation, it was sometimes difficult to find suitable matches for common points between images, and the resultant stitched image was warped and incorrect. The thermal images for Windows 1-4 were stitched manually in GIMP for this reason, to ensure accuracy and quality of the images for subsequent processing in MATLAB.

Temperature scales were kept consistent for each set of images taken at the same time in the survey, but were different for each time, each contrast image, and each thermal profile. The choice was made to optimize the scale for the images, rather than keep the scale constant, as details are lost in the imagery otherwise. The maximum is 30.5 °C and minimum 6 °C over the entire survey, and over a greyscale value range of 255, each increase by 1 along the 0-255 scale equals a 0.1 °C change in temperature. Realistically, changes in greyscale value less than 10-15 are not distinguishable to the naked eye, meaning a change of less than 1-1.5 °C is not visualized. The variations of temperature analyzed in Chapter 3 are in the range of 0.2 ° to several degrees difference, therefore a consistent scale across all images does not provide the necessary detail for the analyses.

5.4.1. Hourly Imagery

Hourly thermal images were useful in this study for identifying the thermal response of certain features within the outcrop, including jointing, unit boundaries, as well as weathering and alteration. Jointing generally was observed as 0.2-2 °C cooler than the surrounding rock face, but was obscured in most images after the first few hours of the surveys (20:05-22:05, August 2, 2015). Contacts between units were visible in the imagery due to the interstratified paleosols exhibiting temperatures approximately 1-2 °C cooler than the lava units. In most cases, alteration was difficult to identify, but in some images it was observed as an area 0.2-2 °C warmer than surrounding unaltered rock.

The observations of jointing and alteration are likely largely based upon the aspect of facets in the slope. Joints give shape to the slope, meaning that some joint surfaces will face towards the sunlight, and some will not. The differences in temperature observed in thermal imagery for joints were the result of the variation in solar radiation available to joint surfaces in the slope. This is why joints were mostly observed in the first two to three hours of the survey, which were the two to three hours after sunset. A time bias was therefore observed, whereby a variable number, persistence, orientation and spacing of joints is found in thermal imagery from different times, which will yield different P_{21} values for the same area on the slope.

Beyond the first few hours of the thermal survey, the immediate effects of the daily solar radiation had dissipated, and the temperatures of the slope were more dependent upon slope composition characteristics, such as vesicularity, mineralogy, and textures. Therefore, unit boundaries were more readily observed in the middle to latter portions of the surveys, as the vesicular and oxidized paleosols exhibited lower temperatures than the lava units. Alteration was observed to be warmer than the surrounding unaltered rock in two images of the thermal surveys. As there were only two images, alteration is not thought to significantly influence the thermal response of the slope, but can have enough of an effect to be observed in rare circumstances.

5.4.2. Contrast Imagery

Temperature contrast images were created by subtracting an image of a particular area of the slope from the previous survey image. As the conversion of the raw greyscale thermal images was done using the maximum and minimum temperatures on a 0-255 greyscale, no error was introduced in this step of the process. In the subtraction of the converted temperatures, there was no rounding of temperature values, simply a direct subtraction of one temperature from another, resulting in reliable data.

The only part of the process of contrast imagery creation inducing error was in the alignment of the images before processing. As stated before, the images were aligned for each window manually in GIMP. While manual alignment was used to reduce errors in the alignment, the elimination of errors in aligning thermal imagery is not possible. Temperatures in thermal imagery are dependent upon the features in the slope, but sometimes slope features are indistinguishable on this basis. Control points

used to align the images, therefore, may not appear in all images of the same window as temperatures change over the length of the survey. This led to several contrast images in the windows appearing to have radial patterns (Figure 5-3). It is unlikely the slope will exhibit such a pattern of thermal contrast, and is thought to be produced by a slight rotation of one image with respect to the other, centered in the radial pattern on the contrast image. The majority of images, however, did not exhibit this pattern and were used in analysis.

Hourly temperature contrast allowed for the distinction of units, joints, alteration, soil and vegetation based on their respective thermal responses. Jointing was generally observed through an approximately 0.2-0.5 °C difference in thermal contrast, as compared to surrounding rock. Joints are areas of the slope that are shaded, provide openings into the rock face, and are most commonly altered due to water moving through them, which is why joints would have a different thermal response.

Units were observed to not always have different contrasts in temperature, and were generally more distinctive in the earlier to middle times of the survey contrast images between 21:05 and 01:05. At the beginning of the surveys, as mentioned in the previous section, most of the thermal responses are from the residual effects of the daily solar radiation. Beyond this time, temperatures are governed predominantly by the lithological and structural characteristics of the rock. These characteristics typically differ between units, hence units have contrasting thermal changes towards the middle of the surveys.

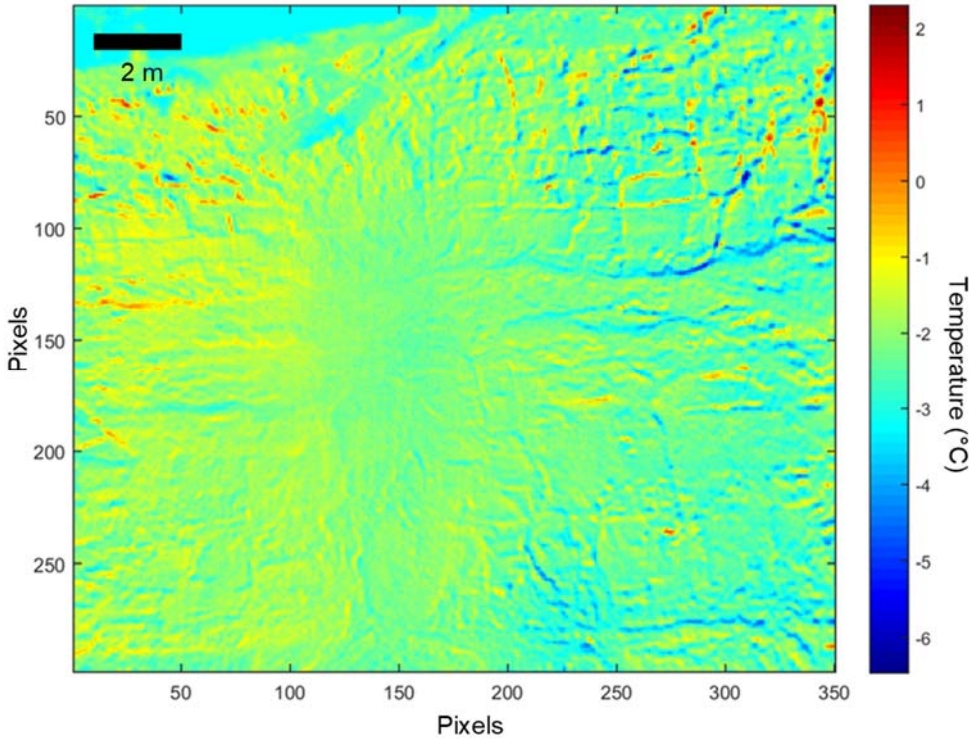

Figure 5-3. Contrast image of Window 1 from 04:05-05:05 on August 3, 2015. Pixels are shown along the x and y axes.

Soils, as unconsolidated small particles, and vegetation, as moist, living entities, have significantly different properties from rock. As expected, therefore, the thermal responses of soil and vegetation contrast with the rock face temperatures. These differences were primarily observed in the 20:05-00:05 contrast images, as later in the survey, all elements in the image were closer to equilibrium with the air temperature.

Alteration was found in temperature contrasts more often than in the hourly thermal images (seven images as opposed to two), likely because the static temperatures of altered areas on the slope did not differ significantly enough to be detected. When the hourly difference in temperature was studied, however, the altered thermal response could be distinguished from the unaltered. This means that alteration is distinct from unaltered rock in the way that its temperature changes over time, rather than in static temperature images. Alteration changes the surface of the rock such that the porosity, colour, texture, and composition are possibly different. A difference in thermal response is thereby expected in altered areas, and as with other features on the slope, it was not observable in all temperature contrast images throughout the survey.

5.4.3. Laboratory Results vs. Field Surveys

Laboratory surveys were completed by inserting all samples into a 93 °C (200 °F) oven, removing them from the oven to be placed on a uniform background of white paper, and taking thermal images every 10 minutes until the samples reached room temperature (approximately 22 °C). The oven temperature was chosen so as to illustrate the temperature decay curves of each sample when a large difference between sample and air temperatures existed. For the purposes of this study, the survey parameters chosen were optimal, in that the result of the surveys were data without gaps, sufficient spacing, and well suited for finding best-fit equations for analysis.

The only step of the process which may have induced errors is when the samples were taken out of the oven and placed into the survey apparatus. The time required to place the samples in the box, upright and in an optimal position, and begin the survey differed for each sample and survey. The temperatures observed at the start of the surveys would be the same as the oven temperature, 93 °C, if there was no hiatus in time between the oven and first image. This was not observed, and temperatures of approximately 74-76 °C were the first to be recorded in the samples, indicating a large enough time lag for the samples to drop 7-9 °C. As the temperature decay patterns as a whole are used for analysis, however, the errors introduced by oven transfer are not significant to overall results.

For window POI graphs, the temperature data was gathered through following the same process as the hourly images, then extracting the correct pixel temperatures from the converted greyscale images and graphing the data. The only error-inducing step, as stated in Section 5.4, was the alignment of the thermal images in each window. The temperature patterns are what are being analyzed, however, so any error from misalignment is thought to be insignificant to the overall process.

Laboratory surveys were conducted in a room with the thermostat air temperature set to 22 °C, but for the field IRT surveys, the air temperature was decreasing throughout the entire survey. The base condition for temperature change in the samples and on the slope is a temperature differential between the rock and the air temperature. As the two types of surveys have different parameters for this condition, results are compared and discussed qualitatively. Three units contained POIs in both

the laboratory and field work, Unit 3, a porphyritic lava, Unit 6, an oxidized and amygdaloidal paleosol, and Unit 13, an aphanitic and vesicular lava (Table 5-1).

Table 5-1. POI descriptions for points used in comparisons between laboratory and field IRT data.

Unit	Sample/Window	POI	Description
3	MD-CH08-01	1	Phenocryst
		4	Fresh
	Window 1	4	White alteration
		5	Fresh
6	MDCH-P67-02	2	Fresh
		3	Fracture trace
		5	White alteration
	MDCH-P67-01	1	Fresh
		4	White alteration
	Window 3	1	Fresh
13	MD-CH03-01	2	Vesicle
	MD-CH03-02	3	Fresh
		5	Fresh
	Window 4	1	White alteration

In all units, laboratory sample temperature curves fit best with power equations, whereas field thermal data fit best with linear equations (Figure 5-4). In the laboratory data, samples were heated to nearly five times room temperature, yielding a larger temperature gradient between sample and air temperatures. These conditions are expected to generate an exponential decay curve, as temperatures rapidly adjust to find equilibrium. As the survey progresses, equilibrium becomes closer, and therefore the temperature adjustment becomes slower. In the field data, however, the temperature gradient between slope and air temperatures was constantly changing, as both the slope temperatures and air temperatures were changing. The difference between the two at the beginning of the field IRT surveys was between 4-5 °C, or approximately 14-18% of the POI temperatures. As this temperature difference is not nearly as marked, and the air temperature is also constantly decreasing (the equilibrium temperature value is constantly changing), the temperature decay curves are expected to have a more linear decrease with time.

In Unit 3, POI 4 from the MD-CH08-01 lab sample (blue line in B, Figure 5-4) and POI 5 from Window 1 (yellow line in A, Figure 5-4) are fresh surfaces. Both curves are consistently lower in temperature than their graphed pair (POI 1 from MD-CH08-01 and POI 4 from Window 1), which are points exhibiting lighter coloured aspects of Unit 3 (a phenocryst and white alteration, respectively). In both survey types, the fresh surface of Unit 3 exhibits a steeper slope in the temperature curves, indicating a more drastic reduction in temperature than altered or porphyritic portions of the slope.

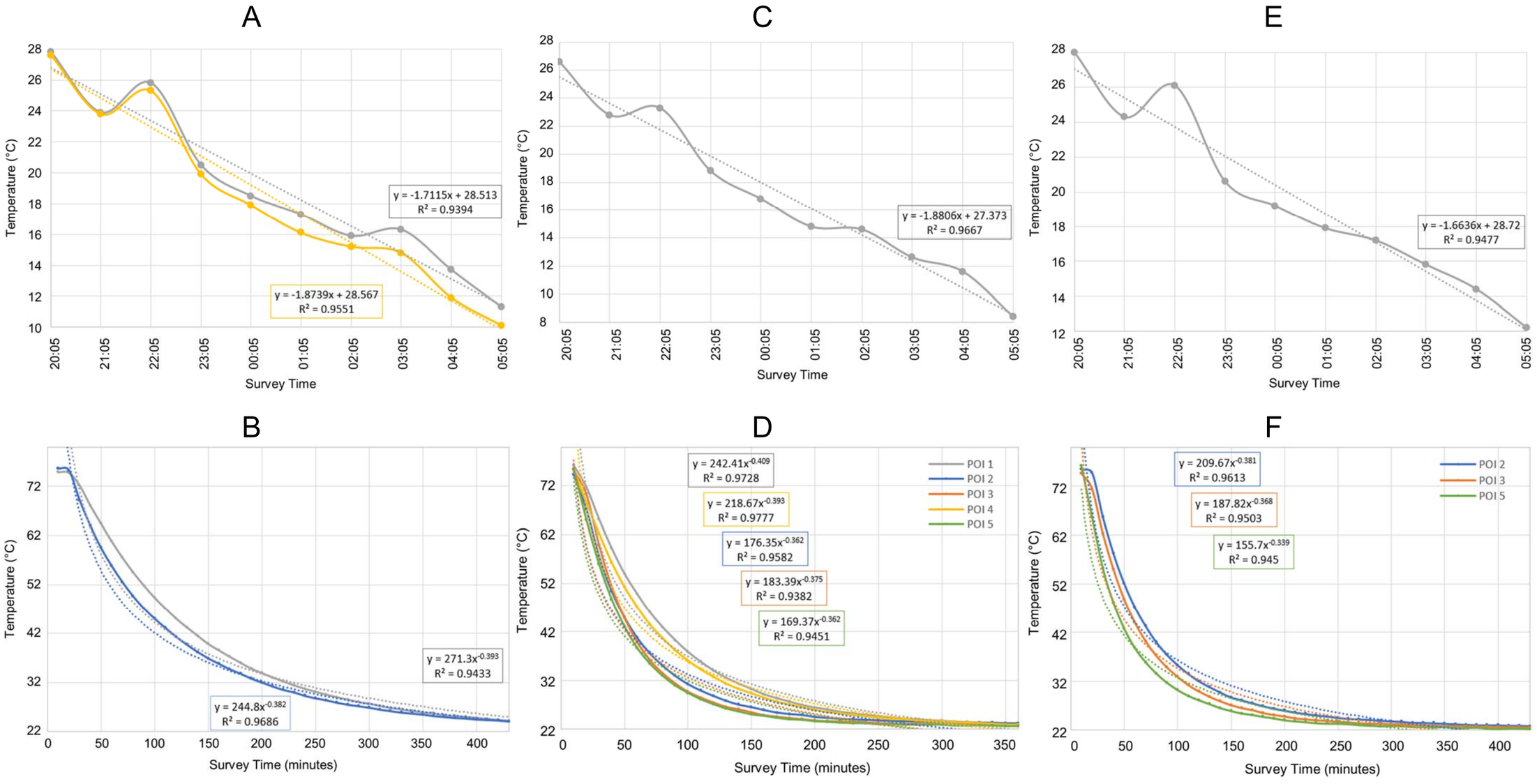

Figure 5-4. A: Field survey data for Unit 3; Window 1, POI 4 (grey) and POI 5 (yellow), with best-fit linear equations shown (dotted lines). B: Lab survey data for Unit 3; MDCH-08-01, POI 1 (grey) and POI 4 (blue). C: Field survey data for Unit 6; Window 3, POI 1 (top image), with best-fit linear equation shown (dotted line). D: Lab survey data for Unit 6; MDCH-P67-01 and MDCH-P67-02, POI 1-5. E: Field survey data for Unit 13; Window 4, POI 1 (top image), with best-fit linear equation shown (dotted line). F: Lab survey data for Unit 13; MDCH-03-01 and MDCH-03-02, POI 2, POI 3, and POI 5.

Laboratory IRT surveys showed that Unit 3 exhibited higher temperatures than paleosols, and a shallower exponential decay (higher constant and higher exponent; Table 5-2). Unit 3 in this sample in non-vesicular, and therefore retained more heat in the survey than other samples. In the field POI data, however, points within Unit 3 do not exhibit the shallowest temperature decay as would be expected from the laboratory data (Table 5-3). Unit 3 slopes are closer to average slope values of all points studied on the slope.

The discrepancy observed may be a result of the slope sampling technique, such that the majority of samples were taken from the base or top of the units, as these were areas where samples could be broken off with a rock hammer. The center of units were too competent and stable for samples to be collected, but many of the POI used in the field thermal characterization were from the center of the unit, so as to obtain the best measure of thermal properties of the majority of the unit. The base and top of the lava units were, in most cases, comprised of vesicular lava characteristics of flow bottoms and flow tops. The vesicularity of the lab samples therefore yielded different results from the field data. The size of the sample taken should also be considered, as larger samples will require more time to cool.

Patterns within the laboratory data equations are difficult to discern, but clear relationships between POI location and thermal decay slope are observed in the field thermal data. Oxidized paleosols and iron stained surfaces exhibit the steepest slopes (-1.9261 to -1.8752 °C/hour), indicating the temperatures decrease more quickly through the survey. The unconsolidated and/or vesicular nature of the paleosols allow for more air flow and greater surface area on which contact with the cool air temperature can occur. The steeper slopes of the temperature decay curves are therefore expected for paleosols, though Unit 7 is a clear outlier, as it exhibits the steepest slope of the window POI data, but is not a paleosol. Unit 7 is at this location, however, a thin unit between two paleosols. Its temperature is likely affected by this, as Unit 7 was in contact with cooler units above and below, as well as with the cooler air temperature.

Table 5-2. Power functions fit to the POI temperature decay curves (ordered by decreasing slope), and their associated R^2 values. Red text is paleosols.

Sample	Unit	POI	Description	Equation	R^2
MD-CH06-03 (Sample 1)	7	3	Baseline/fresh	$y = 117.6x^{-0.285}$	0.8542
MD-CH06-03 (Sample 2)		2	White alteration	$y = 131.65x^{-0.302}$	0.8823
		5	Baseline/fresh	$y = 134.03x^{-0.306}$	0.8740
MD-CH03-02	13	5	Baseline/fresh	$y = 153.49x^{-0.336}$	0.9423
MD-CH-P67-01 (Sample 2)	6	5	White alteration	$y = 166.31x^{-0.358}$	0.9416
MD-CH-P67-01 (Sample 1)		2	Baseline/fresh	$y = 173.68x^{-0.359}$	0.9559
MD-CH-P67-01 (Sample 2)		3	Fracture trace	$y = 180.02x^{-0.371}$	0.9351
MD-CH03-02	13	3	Baseline/fresh	$y = 185.1x^{-0.364}$	0.9480
MD-CH-P23-01	14	1	Amygdale	$y = 194.45x^{-0.361}$	0.9552
		4	Amygdale	$y = 202.5x^{-0.369}$	0.9483
MD-CH03-01	13	2	Vesicle	$y = 207.12x^{-0.378}$	0.9599
MD-CH-P67-02	6	4	White alteration	$y = 216.79x^{-0.391}$	0.9774
		1	Baseline/fresh	$y = 240.37x^{-0.407}$	0.9727
MD-CH08-01	3	4	Baseline/fresh	$y = 244.65x^{-0.382}$	0.9694
		1	Phenocryst	$y = 272.03x^{-0.394}$	0.9448

Table 5-3. POI chosen for the study of temperature decay in each window, ordered by decreasing slope. Red text is paleosols.

Window	Unit	POI	Equation	R^2	Description
3	7	3	$y = -1.937x + 29.053$	0.9603	Baseline/fresh
1	2	3	$y = -1.9261x + 28.933$	0.9482	Oxidized paleosol
3	6	1	$y = -1.8806x + 27.373$	0.9667	Oxidized paleosol
1	1	2	$y = -1.8752x + 29.913$	0.9376	Iron staining
1	3	5	$y = -1.8739x + 28.567$	0.9551	Baseline/fresh
2	5	1	$y = -1.86x + 28.96$	0.9521	Baseline/fresh
1	1	1	$y = -1.803x + 29.847$	0.9363	Baseline/fresh
4	15	2	$y = -1.7897x + 29.893$	0.9429	Baseline/fresh
1	3	4	$y = -1.7115x + 28.513$	0.9394	White alteration
2	5	2	$y = -1.6848x + 28.367$	0.9397	White alteration
4	13	1	$y = -1.6636x + 28.72$	0.9477	White alteration
3	5	2	$y = -1.557x + 26.353$	0.9598	Columnar joint
2	5	3	$y = -1.4055x + 25.52$	0.9642	Columnar joint
4	15	3	$y = -1.2491x + 25.18$	0.9406	Corner of two joints

The second steepest thermal decay slopes belong to the fresh lava units (-1.8739 to -1.7897), then areas on the slope with white alteration (-1.7115 to -1.6636). As white alteration has slopes that are 0.0782-0.2103 different, it is evident that white alteration has an effect on the thermal response of the slope by decreasing the temperature change over time. White alteration changes the colour, texture, and composition of the slope, so it would follow that the thermal response is different as well.

Joints are areas on the slope which are inherently have more exposure to air, as most visible joints at this scale have at least a small aperture. This is why the least change in temperature (shallowest slopes of -1.557 to -1.2491) is recorded in the joints.

The laboratory IRT data proved useful in determining relationships between and within specific samples from the slope, and similar to Mineo and Pappalardo (2016), differences in vesicularity were observed. General patterns within the data, however, could not be distinguished, likely caused the sampling technique or a problem with using samples of different sizes and shapes. Thermal conductivity depends largely on surface area available, composition, and size of the item being surveyed, and therefore a systemic problem with correlating lab and field thermal data is the difference in sample size. Also problematic is that the laboratory surveys were conducted in a room with controlled and constant air temperature, whereas the field thermal data was gathered in conditions where air temperature was constantly changing. Future improvements in the laboratory methodology would therefore include: uniformity in size and shape of samples, unbiased sampling techniques, and a way to mimic the decrease in air temperature over time in the survey room.

5.5. Reflectivity and Thermal Profile Logging

5.5.1. Reflectivity Profiles

Burton et al. (2011) created LiDAR intensity profiles, compared them to core which had been logged by lithology, and found there was some merit in determining rock properties by the LiDAR intensity values and patterns. Similarly, in this study, LiDAR reflectivity profiles were generated in the analysis of the Chasm slopes, and created manually through several steps.

The first step, the extraction of the point cloud which is to be used as the reflectivity profile, requires judicious selection of which points to extract from the full scan of the slope based on the objective of the analysis. As the most accurate profile is required for an accurate comparison, the points chosen must reside in a very narrow area relative to the entire scan swath. This method of choosing an area for extraction can induce errors in the resultant profile if the area chosen is too wide, as in later steps all points of the same elevation are averaged with respect to the reflectivity values. A wider area, therefore, will produce a reflectivity profile with more averaged values of reflectivity over a larger area, rather than the desired profile depicting reflectivity values of a specific column of points on the slope. This versatility, however, allows for many types of analysis, such as averaging reflectivity over an entire unit, on certain structures, vegetation, or areas of alteration, and can thereby have many applications.

The second step in the process is completed using an original MATLAB script, *ReflProf.m* (Appendix A), which organizes the point cloud by rounding the elevation value of each point to the nearest tenth of a meter. Elevation values are recorded from the laser scanner to the nearest thousandth of a meter, however the scale at which the profiles were analyzed in this study did not require more than one point every ten centimeters. The heights of the areas of interest are in the 15 m range which equates to 150 points in the profile at this scale, which was determined to be adequate and permitted detailed analysis of each window.

The points which were at the same elevation values then had their reflectivity values averaged in the third and final step in the process. This averaging of reflectivity values at each elevation served to create the best estimate of the representative reflectivity at that location. Reflectivity will inherently have variation, even in areas with similar lithology, colour, and alteration, so the variability is smoothed over the profile through this averaging process. Averaging will not always create representative values due to possible outliers in the area, however for the purposes of this study, it was thought to provide the most simple, consistent, and accurate comparison.

5.5.2. Thermal Profiles

Profiles within each window were made from the infrared thermography imagery using an original MATLAB script, *IRT_IMPROC2.m* (Appendix A). The script processes

the images by converting the grayscale images to temperature matrices, then extracts rows and columns from the temperature matrices. The extracted rows and columns are graphed and labelled, then analyzed.

In the first step of the script, the grayscale images are directly converted to temperature values, and no averaging is required. This provides the most accurate values, as there is only conversion of units from a grayscale value between 0 and 255, to a temperature value for that specific image. The exact maximum and minimum temperatures are used in the conversion, and the images were exported from ResearchIR MAX with a linear grayscale, so the integrity and accuracy of the data is maintained throughout the processing. As the subsequent steps of the thermal profile generation are simply extracting data from the matrix and graphing the data, the entire process of creating thermal profiles uses the raw data obtained, without averaging or modifying the data in any way other than to visualize differently.

5.5.3. Logging Reflectivity and Thermal Profiles

Reflectivity and observed temperatures of an area are dependent upon different factors. Reflectivity, as mentioned before, depends upon the colour of the material, angle of the surface with respect to the laser pulse, and surface roughness. The thermal response of a material is dependent upon the ambient air temperature, external heat sources (such as the Sun), surface area or size of blocks, and the thermal conductivity of the material. These differences in determining factors, however, can be reconciled by analyzing the results in profiles, as the changes in value of reflectivity and temperature can sometimes be attributed to changes in lithology. As seen in Section 3.2.1, “Combining LiDAR and IRT Techniques”, peaks and troughs in these two types of profiles can be indicative of variations in colour, structures, textures, and composition, all of which are the basis for the differentiation of units.

The most significant relationships observed in the reflectivity and thermal profiles were generated by correlation or inverse correlation between the two sets of values in their patterns, rather than the individual values themselves (Table 5-4). Peaks or troughs in the reflectivity profiles did not always match with peaks or troughs in temperature, but a significant change in the temperature patterns generally had corresponding changes in the reflectivity patterns. For example, in Unit 2 in Window 1, RP1 shows that reflectivity

increases with descending elevation, and Column 54 thermal profiles show increasing temperature as elevation decreases (Figure 3-37). The correlation of reflectivity and temperature in this unit is indicative of the soil grading from unconsolidated material with minor cobbles and gravel, to minor unconsolidated soil between larger blocks of the underlying Unit 1. Soil scatters light and therefore does not reflect as well as rock, and soil contains many air pockets resulting in cooler temperatures than rock. Relationships such as these are described in detail in Section 3.2.1, “Combining LiDAR and IRT Techniques”; important observations are shown in Table 5-4.

The correlations between reflectivity and temperature are not always positive, indicating an inverse relationship between the two for certain units. Soil and vegetation are most distinctive from soil and rock units by their discrete temperatures and reflectivities (lower temperatures and reflectivities are exhibited by both), and their changes in profile patterns are less distinctive. White alteration does not show a significant difference in reflectivity from unaltered rock, and temperatures are slightly higher, so no correlation between the two types of profiles is indicative of this type of alteration. In all sections, joints in the rock mass exhibit a positive correlation between reflectivity and thermal responses, and in both types of profiles are observed distinctively as large troughs.

Paleosols in the LIP1 slope are generally found to have both increases of reflectivity and temperature with depth, forming a positive correlation between the two. Most paleosols at the Chasm exhibited a gradational boundary between the underlying lava unit, whereby they infilled cracks of the lava, contained lava blocks, and at their tops were unconsolidated soils. Soils scatter light and have increased exposure to the air, decreasing reflectivity and temperatures. As the paleosol grades into the lava unit below, however, the rock to soil ratio increases, and therefore the reflectivity and temperature increase with depth in the unit.

Lava units were not observed to have any set pattern or correlation between reflectivity and thermal responses. In some cases, the correlation between reflectivity and temperature was positive, in some cases, negative, and in some units no correlation was perceived at all. On a basic level, the units are the same composition, but it is apparent that small variations in mineralogy and texture can illicit a detectable change in

remote sensing response. A change in vesicularity, for example, increased the reflectivity and decreased the temperature in the flow top and bottom of Unit 7.

The relationship between reflectivity and temperature can also be quantified in reflectivity point clouds and thermal imagery, as described in Sections 3.2.2, “IRT” and “LiDAR and Reflectivity”. In these sections, higher reflectivities (between -7.5 and -3 dB) were characteristic of paleosols and altered (white alteration and iron staining) areas of the slope. These same areas were also of lower temperatures than unaltered rock (2-3 °C). Reflectivity and temperature are thereby shown in this study to be closely related, and respond differently to variations in texture, composition, and structure.

Table 5-4. Relationships between reflectivity (RP) and thermal (IRT) responses in the LIP1 slope, with magnitudes, if applicable. Correlations between the two profiles are described as positive (i.e. reflectivity increases, temperature increases) or negative (i.e. reflectivity increases, temperature decreases).

Unit/Feature	Response in RP (magnitude)	Response in IRT (magnitude)	Correlation between RP/IRT
Jointing	Trough (1-2 dB)	Trough (1-2 °C)	Positive
White alteration	Similar reflectivities to unaltered rock	Higher temperatures than unaltered rock (0.5-1 °C)	-
Soil	Increases with depth; lower reflectivites than rock (1-3 dB)	Decreases with depth; lower temperatures than rock (1-4 °C)	Negative
Vegetation	Extreme variability (15-20 dB); lower reflectivities than rock and soil (5-10 dB)	Lower temperatures than rock and soil (2-3 °C)	Positive
Unit 1	Decreases with depth	Decreases with depth	Positive
Unit 2	Increases with depth	Increases with depth	Positive
Unit 3	Relatively consistent	Relatively consistent	-
Unit 4	Increases with depth*	Increases with depth*	Positive*
Unit 5	Lower at top and within entabulature (1-3 dB)	Less at top and within entabulature (2-3 °C)	Positive
Unit 6	Increases with depth	Relatively consistent	-
Unit 7	Higher at top and bottom of unit (2-4 dB)	Lower at top and bottom of unit (2-3 °C)	Negative
Unit 8	Increases with depth*	Decreases with depth*	Negative*
Unit 9	Increases with depth	Increases with depth	Positive
Unit 13	Decreases with depth	Relatively consistent	-
Unit 14	Increases with depth	Increases with depth	Positive
Unit 15	Higher at top and bottom of unit (2-3 dB)	Lower at top and bottom of unit (2-3 °C)	Negative
Unit 16	Increases with depth	Increases with depth	Positive
Unit 17	Relatively consistent	Decreases with depth	-

*Insufficient depth of data to fully corroborate

5.6. Erosional Profiles

In the creation of erosional profiles along the LIP1 slope, just as with reflectivity profiles, a column point cloud is extracted from the slope point cloud. The elevation

values of all points in the extracted point cloud are rounded to the nearest tenth of a meter. Consequently, there are multiple points at each elevation value, so the average location of these points at a certain elevation needs to be determined. This is done through averaging the Northing and Easting values at each unique elevation, and as the Chasm slope is not parallel with the UTM grid (N-S or W-E), trigonometry ($a^2 + b^2 = c^2$) was used to find the oblique distance from the UTM grid reference point. This minimum oblique distance is subtracted from all values, resulting in the normalized distance of each point at each elevation. As all points are normalized using the same distance value, no errors are introduced during this part of the process. The distance and elevation values are then plotted.

All five erosional profiles along the LIP1 slope show differential erosion between the lava and paleosol units. Generally, the paleosols are areas in the slope profile which are concave towards the slope, due to the paleosols primarily being composed of unconsolidated material which can be mobilized more easily by water and wind. In the upper portions of the north (EP1) and lower portions of the south (EP5) side of the LIP1 slope, the paleosol concavities are more pronounced, indicating thicker, and more developed paleosol units. These units are zones of weakness in the rock mass, and as they are eroded, the overlying lava units are undercut, reducing their stability, and allowing for blocks to fall. There are places in the profiles where these concavities in the profiles are not significant in size, and sometimes not observed even though a paleosol unit occurs there. This is where paleosol units are thin, and therefore do not affect the erosional response of the units above or below. The lava units in comparison are convex in the profiles, as they are coherent and competent rock, not as easily eroded away.

Erosional profiles, as shown in this study, can be used for gaining insights into the overall slope stability and the stability of specific units. They can also provide a basis on which to complete kinematic analysis, measurements for differential erosion, and numerical modelling.

5.7. Contact vs. Remote Sensing Mapping

Detailed mapping of the Chasm-type lithofacies by Farrell et al. (2007) and Farrell et al. (2008) provides a geological type section from which to base a comparison

between data obtained through traditional contact field mapping methods, and remotely sensed data. Hand sample data obtained through slope sampling, petrography and IRT laboratory tests described in Section 3.2.1 provided base-level data for comparison with remote sensing methods, and was used to evaluate the difference between the varied techniques for data collection. The data collected via the TLS and FLIR camera were used to create remote sensing composite logs (Figure 5-5), respectively allowing a characterization of the sequence solely through data obtained from a distance. These logs are directly evaluated for differences with the geological type section by Farrell et al. (2007) and hand sample data from this study, allowing for an assessment of the accuracy of terrestrial LiDAR and infrared thermography for the prediction of geological parameters, and the value of the remote sensing methods for mapping volcanic lava flow characteristics.

The composite remote sensing logs were generated using RP1, RP2, RP3 and RP4 for the reflectivity log, and temperatures from 05:05 on August 3, 2015 from Column 54, Column 155, Column 256, and Column 89 (for the temperature log) from Windows 1, 2, 3, and 4, respectively (Figure 5-5). As no detailed window was completed to include Units 10-12, these units are omitted from the interpreted geological log. The geological log in Figure 5-5 is based on a combination of data from photogrammetry, hand samples, petrography, LiDAR reflectivity and IRT, and therefore is a result of the combined effort from multiple remote sensing methods, supplemented by sample data.

The logs, created from detailed work described in Section 3.2.1, “Combining LiDAR and IRT Techniques” and discussed in Section 5.5, show clear relationships between temperatures and reflectivity. These correlations and inverse correlations are successfully used, along with photogrammetry, to find variations in composition, texture, and structure in the LIP1 outcrop.

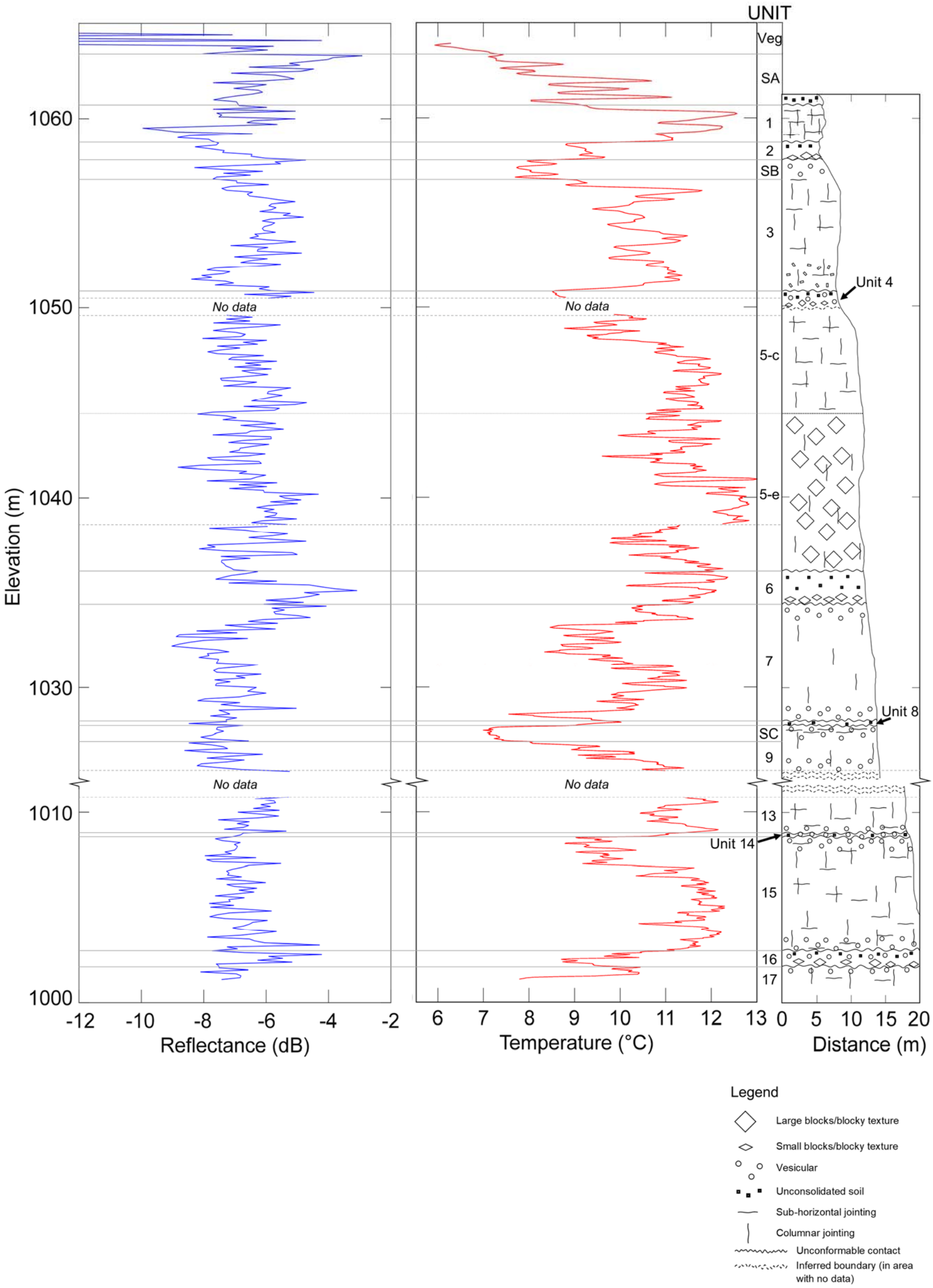

Figure 5-5. Remote sensing composite logs for the LIP1 slope. RP1, RP2, RP3, and RP4 for Windows 1, 2, 3, and 4 (respectively) are shown in the first graph (blue). Thermal column profiles composed of temperatures at 05:05 on August 3, 2015 of Column 54, Column 155, Column 256, and Column 89 for Window 1, Window 2, Window 3, and Window 4, respectively are shown in the second graph (red). The graphic log, generated with information from hand samples, photographs, reflectivity and IRT is shown on the EP1 erosional profile (black, third graph). Units: Veg = Vegetation, SA = Soil A, SB = Soil B, 5-c = Unit 5 (colonnade), 5-e = Unit 5 (entabulature), SC = Soil C. Soils A, B, and C are eroded materials on the slope, and thereby affect the remote sensing profiles, but are not geological units in the sequence.

The site at which a direct comparison between remote sensing and contact mapping can be made is the Chasm-lithofacies type section by Farrell et al. (2007), the LI1 slope. The difference between methods is shown in Table 5-5, wherein the crucial slope features observed with each technique are presented. It is evident from countless previous studies that traditional methods provide a myriad of valuable information, but this study has shown that remote sensing methods are viable alternatives when contact with the slope is not possible. In some cases, more information can be learned of the slope characteristics from remote sensing, such as reflectivity and thermal response.

Table 5-5. Mappable features observed in each data-gathering method.

Feature	IRT	LiDAR	Photogrammetry	Contact Mapping
Columnar Jointing	✓	✓	✓	✓
Horizontal Jointing	✓	✓	✓	✓
Joint Persistence		✓	✓	✓
Joint Spacing		✓	✓	✓
Joint Roughness		✓*	✓*	✓
Units	✓	✓	✓	✓
Soil	✓	✓	✓	✓
Vegetation	✓	✓	✓	✓
Alteration		✓	✓	✓
Lava lobes	✓	✓	✓	✓
Amygdales		✓	✓	✓
Vesicles		✓	✓	✓
Pipe Vesicles		✓	✓	✓
Chimney Vesicles		✓	✓	✓
Reflectivity		✓		
Thermal response	✓			

*Sometimes applicable

Not all these features were visible in the LIP1 slope data, however, as the slope was further from the survey location. The increased distance did not make a difference in the LiDAR data, as the maximum distance to achieve the maximum resolution available from the TLS was still not reached. Resolution of the IRT and photography methods depend on the lenses available, and therefore with the same lenses (100 mm and 400 mm for IRT and photography, respectively), a larger distance consequently means a lower resolution. Characteristics such as amygdales and various types of

vesicles were missed in the LIP1 slope IRT and photogrammetry imagery, and resulted in the discovery of a limitation to using these methods of remote sensing. A limitation such as this, though, can be resolved by obtaining higher focal length lenses for the different types of cameras, if the intention is to image longer distances. As contact mapping by definition is completed through gaining access to the slope, distances for photographs and imagery are not an issue, and the same information that can be mapped at one outcrop can be mapped at another, providing they have the same level of access available.

5.8. Comparison of Remote Sensing Methods

As seen in Table 5-5 in the previous section, the three remote sensing methods used were not able to glean all information available from slope through one individual technique. Also factoring in the survey and processing, there are advantages and disadvantages to using each type of instrumentation. A summary comparison of methods used to acquire and process data in the photogrammetry, IRT and TLS software is shown in Table 5-6.

TLS, IRT and digital photogrammetry acquire high resolution datasets, and have the ability to obtain data from large distances (in some cases, up to a few kilometers), but as was seen in the previous section, the resolution of IRT and photogrammetry depends largely on the distance to the slope and focal length of the available lenses. To obtain the various results in this study, a multitude of programs were learned and used, and several scripts were written to process the data in a novel way. This rendered some of the processing tedious and time-consuming, but many of the capabilities of the data collected through remote sensing were used to the best advantage in this way.

The differences between the remote sensing methods result in each being favourable or unfavourable for certain purposes and budgetary restrictions for surveys. TLS instruments and FLIR cameras are expensive pieces of equipment, as are the software licenses required to process the data in the proprietary software post-survey. Digital cameras are relatively inexpensive and readily available, and photogrammetry can be done even from photographs taken on a smartphone camera (Micheletti et al., 2015). The resolution of a camera such as this, of course, is not ideal for long-range studies, but much of the data required to simply map the geology of an outcrop from a

distance can be found in photographs. The addition of the higher-caliber equipment, however, provides a much wider range of possible studies with the resultant data.

Table 5-6. Advantages and disadvantages of the remote sensing techniques used for the purposes of this study.

Subject/Purpose	Photogrammetry	LiDAR	IRT
Survey	• long range, high resolution (depends on available lenses) • easy setup and survey • requires GPS or Total Station coordinates for stations and targets on outcrops to register its orientation and create the model	• long range, very high resolution • easy setup and survey • contains internal GPS, so no need to register the data in order to create the model	• long range, high resolution (depends on available lenses) • easy setup and survey • requires post-survey processing with control points on the slope to georeferenced
General data processing	• Most processing has preset functions • Several different programs are required to take full advantage of the data: AdamTech, Metashape, DIPS, CloudCompare, GIMP, Publisher • Numerous commercial and public domain codes are available for specialized processing of the data	• Most processing has preset functions • Easy to extract different types of information in RiSCAN program • To take full advantage of data, RiSCAN PRO, CloudCompare, DIPS and MATLAB were used • Numerous commercial and some public domain codes are available for specialized processing	• Most of processing was done outside of ResearchIR software • Several different programs were used to take advantage of all forms of data: ResearchIR, MATLAB, GIMP, Publisher • Commercial and public domain codes available to process data
General rock descriptions/logging	• Easy to overlay and create line drawing	• Easy to view features in the point cloud or by creating a mesh	• Optimal temperature scale must be determined before exporting from software for viewing features, but subsequently easy to overlay and create line drawing
Discontinuity characterization	• can be done in AdamTech software, or in CloudCompare with ease	• can be done manually in RiSCAN software, or more easily in CloudCompare	• images need to be overlain on 3D model of the slope before discontinuity mapping can be done (not done in this study)
Alteration mapping	• Easy to find pixel RGB values	• Easy to find point RGB values	• Must be done by looking at thermal patterns in hourly and contrast imagery
Laboratory tests	• Correct lighting and focus were the only obstacles in SfM models of samples	• Attempted, but Riegl VZ-4000 TLS instrument is meant for longer range, so lab surveys did not result in usable data. Would require hand-held laser scanner	• The ideal environment would include a way of decreasing air temperature with time • surveys are easy to complete with an oven
Profile mapping	• Could be used for erosional profiles	• Must use two different programs (RiSCAN and MATLAB) • Script was written to graph profile	• Must use two different programs (ResearchIR and MATLAB) • Script written to convert the images, extract the necessary information, and graph profile
Virtual outcrop compatibility	• Easy to export as correct 3D model format and import into Unity	• Easy to export as correct 3D model format and import into Unity	• Images are easily imported into Unity as flat images • Images must first be draped on a 3D model to get 3D thermal outcrops in Unity
Overall number of features observed	• High number of features observed	• High number of features observed	• Moderate number of features observed

5.9. Virtual Outcrops

The question of slope access and the improvement of technology has sparked a comparison between mapping with traditionally used methods in close contact with the slope, and remote sensing. The data gathered in this research was collected through remote sensing methods in the field, and subsequently brought into a virtual environment to take advantage of the key benefits of both types of mapping: the ability to get into close contact with an outcrop, and the ability to gather data from a distance. 'Up Close with Virtual Outcrops' is a geovisualization tool created with multiple datasets, and shows the potential of using virtual reality as a research and teaching tool. As this is a preliminary version of the virtual field site, several improvements are planned for future versions, including the addition of new data, the modification of 2D data into 3D, the addition of more opportunities of interaction with the data by the user, and a release version which is compatible with virtual reality/mixed reality hardware, such as Microsoft Hololens 2.

'Up Close with Virtual Outcrops' clearly demonstrates the potential advantages in using a virtual reality approach to visualize state-of-the-art remote sensing data. Multiple scales and dimensions of high-resolution data provide the detail of a real outcrop in a virtual setting. Regardless of the accessibility of the outcrop in the real world, a virtual environment offers an opportunity to study outcrops in close detail, delivering the field site to the user on a computer screen, or in later versions, in virtual reality headsets. Remote sensing data combined with virtual reality provides an alternative to contact mapping which can closely simulate real-word field mapping, and allow for all types of users to explore any outcrop on which there is data available. A tool such as this significantly increases the potential of mapping with remote sensing, and aids in meeting research objectives by providing another means for mapping and visualizing data. A more detailed discussion of the virtual outcrop created in this study is in Section 4.6.

Chapter 6. Conclusions and Future Work

Remote sensing and traditional mapping data were gathered at two field sites in British Columbia in the pursuit of fulfilling the research objectives. The majority of field work and data processing was completed for the Chasm, a sequence of lava flows interstratified with oxidized paleosols, and exposed in 300 m-high steep slopes for several kilometers. Two outcrops were studied at the Chasm: LIP1, at which data in the form of terrestrial LiDAR scans, IRT time-series imagery, and photogrammetry were analyzed in four detailed windows on the slope, and LI1, at which the same three remote sensing techniques were used in comparison with previous field studies. Two outcrops of the CVB, isolated lava flows with distinct patterns of columnar jointing, were also part of the study, at which remote sensing was carried out in conjunction with field observations.

The first and third objectives of this research were the development of techniques for mapping inaccessible volcanic rocks, and mapping the two field sites using a combination of remote sensing and traditional contact mapping, respectively. These were achieved through the processing of remote sensing data in both established and novel ways at the Chasm and CVB sites, in combination with field observations.

Profiles down the slope of LiDAR reflectivity, similar to those which were done on sedimentary rocks previous studies, were created for the Chasm basalts in each of the four detailed windows on the LIP1 outcrop. The profiles show that reflectivity is distinctive between paleosol and lava units, and can also be used to identify features within the lava flows, such as jointing and vesicularity. Point clouds of specific 1 dB ranges of reflectivity proved that a single value of reflectivity is not unique to a unit, type of unit, or feature on the slope. A specific range of reflectivity, however, is more prevalent in certain units or areas of alteration on the slope, and was thereby used to map units on the LI1 slope.

Three-dimensional models generated from LiDAR scans were the source data for discontinuity characterization at the LIP1 slope at the Chasm, and both of the CVB outcrops. Joints identified at the Chasm and CVB sites were found to belong to 4-5 joint sets, including 3-4 sub-vertical columnar joint sets, and one sub-horizontal joint set composed primarily of ball-and-socket joints and joints parallel to chatter marks.

Alteration was mapped in the LIP1 windows using two techniques, LiDAR reflectivity values and RGB colour values, the latter of which was tested on both coloured LiDAR point clouds and photographs of the windows. As it was found in the LiDAR reflectivity portion of this study that specific values of LiDAR are not exclusive to certain features (including alteration), the limitations of this approach were highlighted. The representative area chosen to find the reflectivity specific to iron staining and white alteration encompassed too broad a range of reflectivity, and was found to represent the majority of the slope instead. Similar representative areas were chosen using RGB colour values to select points on the slope for iron staining and white alteration. The resultant selected areas closely resembled those mapped manually on photographs, and many areas which were too small or too spottily altered to delineate in manual mapping, were able to be mapped in this way.

IRT images were taken at the two CVB outcrops, and the single images of the slopes exhibited distinctive differences between the vegetation, soil, jointing, and various units of the two outcrops. More detailed time-series IRT imagery was completed at the Chasm, with images taken hourly through a cooling cycle of sunset to sunrise at the LIP1 and LI1 slopes. Hourly imagery, similar to the CVB IRT images, revealed that features on the slope can be distinguished by contrasts in temperatures, however the time-series images also exhibited a change in observations over time. Not all characteristics of the slope are visible throughout the whole survey, leading to the conclusion that the optimal time for mapping joints in IRT imagery is between sunset and a few hours later, and the optimal time for mapping units is between a few hours after sunset and sunrise.

Temperature contrast images, which were created by subtracting one time-series IRT image from the previous, showed that because various materials will react differently to changing temperatures, temperature changes of geological units will change over time. It was discovered that jointing, similar to the hourly imagery, was most visible in temperature contrasts for the first few hours of the survey, and units were best observed in the middle of the night.

Profiles form the IRT time-series imagery were constructed from temperatures along a single column in each of the Chasm LIP1 slope windows, and were comparable to the profiles of LiDAR reflectivity, such that correlations and inverse correlations

between reflectivity and temperature were observed. Paleosols had consistently lower temperatures than lava units, and exhibited both increasing temperatures and reflectivity with depth in the units. Joints presented as troughs in both types of profiles, as compared to the reflectivity and temperature values of the lava units. The lava units were comprised of variable temperatures and reflectivity, but changes in vesicularity in the flow tops and bottoms were detected through and increase in reflectivity and corresponding decrease in temperature in the profiles.

Laboratory IRT time-series imagery, completed after heating samples taken from the LIP1 Chasm slope in an oven, showed that a better analog for the field IRT survey, in which the room temperature decreased over the test, was necessary to make direct comparisons. The laboratory study did show, however, that vesicular and amygdaloidal paleosol samples cooled significantly faster than non-vesicular lava samples, given the same conditions.

Petrography of the samples collected at the Chasm, as well as photography and field observations, augmented the remote sensing work and solidified the information compiled from all sources in creating a composite geological and remote sensing log of the Chasm. In this research, lithology, texture, structural, and alteration data from petrography and hand samples calibrated the remote sensing results, and allowed for detailed interpretations.

The second research objective, the evaluation of the advantages and limitations of remote sensing for inaccessible outcrops, was addressed through the comparison of data collected through remote sensing methods, and the visualization of this data in an interactive interface with a virtual Chasm outcrop.

Much of the data obtained and processed in the study were used as input for a virtual outcrop created in a game engine software, which was called ‘Up Close with Virtual Outcrops’. The interface acts as a virtual field site, in which users can take tours of the site, view multiple scales of multi-dimensional data, and make detailed observations on the slopes within. The geovisualization methods used allow for a simulated experience of traditional contact mapping, through the visualization of and interaction with, remotely sensed data.

The remote sensing methods and techniques used in the pursuits of this research were directly compared to information collected through traditional field mapping, and were found to provide most of the same data, and in some cases, more than field observations alone. Remote sensing also offers a multitude of possible ways of studying data from the same survey, whereas the survey methods for contact mapping need to be determined beforehand, in order to plan what features will be looked for and recorded. The data from remote sensing in this study was used in conjunction with field mapping and samples, demonstrating the collaboration of traditional contact techniques with remote sensing, and how a harmonized synthesis of the two methods is recommended for best results for mapping inaccessible outcrops.

Future work for this research should include improvements to laboratory data surveys, the furthering of the slope and unit characterization with regards to reflectivity and temperature, increasing the amount and quality of data in the geovisualization interface, and applications of this research to more types of volcanic outcrops. Laboratory surveys with decreasing air temperature, similarly sized and shaped samples, and more types of samples, would improve the comparison between laboratory and field IRT surveys. Patterns and ranges of reflectivity and temperatures were observed using profiles along the slope, but a detailed study into the patterns and specific values across the slope (i.e. within units) would add significant information to the characterization of slopes using remote sensing. The characterization of 'domains', such as reflectivity domains or thermal domains, whereby portions of the slope which behave similarly (with regards to reflectivity values and thermal response, respectively) could be grouped, and would provide the means for further assessments of the Chasm and other slopes based on defined remote sensing domains. To augment and further the remote sensing work done at the Chasm and CVB outcrops, further surveys with hyperspectral imagery, hand-held laser scanning (on laboratory samples), as well as the use of higher focal length lenses for more detailed thermal imagery could be completed, and would significantly elevate the remote sensing mapping done in this study. The 'Up Close with Virtual Outcrops' geovisualization is a preliminary version, and would be updated to be compatible with virtual and augmented reality hardware, as well as contain additions of more interactivity between the user and the data. As more data becomes available, it would also be interesting to input this data into 'Up Close with

Virtual Outcrops', to continually upgrade the quality and quantity of data within the interface.

Both the CVB and Chasm outcrops are composed of basalts, and significant useful data has been gleaned for how to map these sites from a distance. As many volcanoes, their deposits, and their history cannot be mapped due to steep slopes, volcanic activity, and instability, it would be beneficial to address this problem by using the techniques in this research on felsic and intermediate composition volcanic rocks. A field site such as Mount Meager volcano, which hosts a myriad of deposit types, would expose the possibility of expanding the capabilities of remote sensing in mapping remote outcrops.

The research completed in this study fulfilled the outlined objectives, and through mapping of two CVB and two Chasm outcrops, demonstrated the significant potential for mapping volcanic rocks using multi-sensor remote sensing techniques.

References

Adam Technology (2014). 3DM Analyst and CalibCam [Computer software]. Available from http://www.adamtech.com.au

Agisoft LLC (2020). Metashape (Version 1.6.3)[Computer software]. St. Petersburg, Russia.

Anderson, R.G., Resnick, J., Russell, J.K., Woodsworth, G.J., Villeneuve, M.E., and Grainger, N.C. (2001). The Cheslatta Lake suite: Miocene mafic, alkaline magmatism in central British Columbia. *Canadian Journal of Earth Sciences, 38*, 697-717. doi: 10.1139/cjes-38-4-697

Andrews, G.D.M. and Russell, J.K. (2007). Mineral exploration potential beneath the Chilcotin Group (NTS 092O, P; 093A, B, C, F, G, J, K), South-Central British Columbia: Preliminary insights from volcanic facies analysis. *Geoscience BC, Report 2007-1*, 229-238.

Barton, N. (1976). The shear strength of rock and rock joints. *International Journal of Rock Mechanics, Mining Sciences and Geomechanics Abstracts, 13*, 255-279.

Bellian, J.A., Kerans, C., and Jennette, D.C. (2005). Digital Outcrop Models: applications of terrestrial scanning LiDAR technology in stratigraphic modeling. *Journal of Sedimentary Research, 75(2)*, 166-176. doi: 10.2110/jsr.2005.013

Bevier, M.L. (1982). Geology and petrology of Mio-Pliocene Chilcotin Group basalts, British Columbia. Ph.D. Thesis, University of California, Santa Barbara, USA. 110p.

Bevier, M.L. (1983*a*). Implications of chemical and isotopic composition for petrogenesis of Chilcotin Group Basalts, British Columbia. *Journal of Petrology, 24(2)*, 207-226.

Bevier, M.L. (1983*b*). Regional stratigraphy and age of Chilcotin Group basalts, south-central British Columbia. *Canadian Journal of Earth Sciences, 20*, 515-524.

Blenkinsop, T.G. (2012). Visualizing structural geology: From Excel to Google Earth. *Computers and Geosciences, 45*, 52-56. doi: 10.1016/j.cageo.2012.03.007

Buckley, S.J., Enge, H.D., Carlsson, C., and Howell, J.A. (2010). Terrestrial laser scanning for use in virtual outcrop geology. *The Photogrammetric Record, 25(131)*, 225-239.

Buckley, S.J., Howell, J.A., Enge, H.D., and Kurz, T.H. (2008). Terrestrial laser scanning in geology: data acquisition, processing and accuracy considerations. *Journal of the Geology Society London*, *165*, 625-638.

Burton, D., Dunlap, D.B., Wood, L.J., and Flaig, P.P. (2011). Lidar intensity as a remote sensor of rock properties. *Journal of Sedimentary Research*, *81*, 339-347.

Campbell, J.B. (2007). Lidar. In *Introduction to remote sensing, 4th ed.* (pp. 239-251). New York, NY: The Guildford Press.

Chang, K.-T., Yu, F.-C., Chang, Y., Hwang, J.-T., Liu, J.-K., Hsu, W.-C., and Shih, P.T.-Y. (2015). Land cover classification accuracy assessment using full-waveform LiDAR data. *Terr. Atmos. Ocean. Sci.*, *26(2)*, 169-181. doi: 10.3319/TAO.2014.12.02.02(EOSI)

CloudCompare (2020). (Version 2.11.0) [Computer software]. Open source. Retrieved from http://cloudcompare.org/

D'Angelo, P., Achleitner, F., van Andrel, B., Ballo, G., Bay, H., Behrmann, K., …Yaniv, Z. (2019). Hugin (Version 2019.2.0) [Computer software]. Retrieved from http://hugin.sourceforge.net/

De Paor, D., Coba, F. and Burgin, S. (2016). A Google Earth grand tour of the terrestrial planets. *Journal of Geoscience Education, 64*, 292-302.

De Paor, D.G., and Whitmeyer, S.J. (2011). Geological and geophysical modeling on virtual globes using KML, COLLADA, and Javascript. *Computers and Geosciences, 37*, 100-110. doi: 10.1016/j.cageo.2010.05.003

Dohaney, J.A.M. (2009). Distribution of the Chilcotin Group basalts, British Columbia. M.Sc. Thesis, University of British Columbia, Vancouver, Canada. 125p.

Dostal, J., Hamilton, T.S., and Church, B.N. (1996). The Chilcotin basalts, British Columbia (Canada): Geochemistry, petrogenesis and tectonic significance. *Neues Jahrbuch Für Mineralogie Abhandlungen, 170(2)*, 207-229.

Esri (2016). ArcGIS Desktop (Version 10.3) [Computer software]. Redlands, California, USA.

ESRI (2015). World topographic basemap. Retrieved on October 3, 2015 from http://www.arcgis.com/home/item.html?id=30e5fe3149c34df1ba922e6f5bbf808f

Farquharson, R.B. and Stipp, J.J. (1969). Potassium-argon ages of dolerite plugs in the South Cariboo region, British Columbia. *Canadian Journal of Earth Sciences, 6*, 1468-1470.

Farrell, R.E. (2010). Volcanic facies architecture of the Chilcotin Group basalts at Chasm Provincial Park, British Columbia. M.Sc. Thesis, University of British Columbia, Vancouver, Canada. 164p.

Farrell, R.E., Andrews, G.D.M., Russell, J.K., and Anderson, R.G. (2007). Chasm and Dog Creek lithofacies, Chilcotin Group basalt, Bonaparte Lake map area, British Columbia. *Geological Survey of Canada, Current Research 2007-A5*, 11p.

Farrell, R.E., Simpson, K.A., Andrews, G.D.M., Russell, J.K., and Anderson, R.G. (2008). Preliminary interpretations of detailed mapping in the Chilcotin Group, Chasm Provincial Park, British Columbia. *Geological Survey of Canada, Current Research 2008-13*, 11p.

FLIR Systems, Inc. (2015). FLIR SC7000 Series Datasheet. Retrieved from https://www.flir.ca/support/products/sc7650#Overview

FLIR Systems, Inc. (2018). ResearchIR MAX (Version 4.20.2.74)[Computer software]. Portland, USA.

Franceschi, M., Teza, G., Preto, N., Pesci, A., Galgaro, A., Girardi, S. (2009). Discrimination between marls and limestones using intensity data from terrestrial laser scanner. *ISPRS Journal of Photogrammetry and Remote Sensing, 64*, 522-528.

Google (2020). Google Earth [Computer software]. Mountain View, CA, U.S.A.

González-Delgado, J.A., Martínez-Graña, A.M., Civis, J., Sierro, F.J., Goy, J.L., Dabrio, C.J., Ruiz, F., González-Regalado, M.L., and Abad, M. (2015). Virtual 3D tour of the Neogene palaeontological heritage of Huelva (Guadalquivir Basin, Spain). *Environmental Earth Sciences, 73*, 4609-4618. doi: 10.1007/s12665-014-3747-y

Green, N.L., Armstrong, R.L., Harakal, J.E., Souther, J.G., and Read, P.B. (1988). Eruptive history and K-Ar geochronology of the late Cenozoic Garibaldi volcanic belt, southwestern British Columbia. *Geological Society of America Bulletin*, *100*, 563-579.

Green, N.L. (1981). Geology and petrology of Quaternary volcanic rocks, Garibaldi Lake area, southwestern British Columbia: Summary. *Geological Society of America Bulletin*, *Part 2*, *92(10)*, 1359-1470.

Hedley, N. (2015). Cartography and Virtual Reality in the 20th Century. In *The History of Cartography Volume 6: Cartography in the Twentieth Century*. Chicago, USA: University of Chicago Press. Monmonier, M.S. (Ed.) 1960 pp. ISBN: 9780226534695

Hetényi, G., Taisne, B., Garel, F., Médard, É., Bosshard, S., and Mattsson, H. (2012). Scales of columnar jointing in igneous rocks: field measurements and controlling factors. *Bulletin of Volcanology, 74(2)*, 457-482.

International Society for Rock Mechanics (ISRM)(1978). Suggested methods for the quantitative description of discontinuities in rock masses. *International Journal of Rock Mechanics, Mining Sciences and Geomechanics Abstracts, 15*, 319-368.

Jensen, J.R. (2006a). LiDAR remote sensing. In *Remote sensing of the environment: An Earth resource perspective, 2nd ed.* (pp. 335-354). Pearson Prentice Hall.

Jensen, J.R. (2006b). Thermal infrared remote sensing. In *Remote sensing of the environment: An Earth resource perspective, 2nd ed.* (pp. 249-290). Pearson Prentice Hall.

Jones, L.D. (2006). Monitoring landslides in hazardous terrain using terrestrial LiDAR: an example from Montserrat. *Quarterly Journal of Engineering Geology and Hydrogeology, 39*, 371-373.

Jones, R.R., McCaffrey, K.J.W., Clegg, P., Wilson, R.W., Holliman, N.S., Holdsworth, R.E., Imber, J., and Waggott, S. (2009). Integration of regional to outcrop digital data: 3D visualisation of multi-scale geological models. *Computers and Geosciences, 35*, 4-18. doi: 10.1016/j.cageo.2007.09.007

Kromer, R.A., Abellán, A., Hutchinson, D.J., Lato, M., Chanut, M-A., Dubois, L., and Jaboyedoff, M. (2017). Automated terrestrial laser scanning with near-real-time change detection – monitoring of the Séchilienne landslide. *Earth Surface Dynamics, 5,* 293-310. doi: 10.5194/esurf-5-293-2017

Lin, H., Chen, M., Lu, G., Zhu, Q., Gong, J., You, X., Wen, Y., Xu, B., and Hu, M. (2013). Virtual Geographic Environments (VGEs): A New Generation of Geographic Analysis Tool. *Earth-Science Reviews, 126*, 74-84. doi: 10.1016/j.earscirev.2013.08.001

Linder, W. (2009). *Digital photogrammetry: a practical course.* Berlin, Germany: Springer-Verlag.

Lochhead, I. (2016). ExtendedFlyCam (Version 1) [C# script]. Personal communication, received March 20, 2016.

MacEachren, A.M. and Kraak, M.J. (1997). Exploratory cartographic visualization: advancing the agenda. *Computers & Geosciences, 23(4)*, pp. 335-343.

Mathews, W.H. (1958). Geology of the Mount Garibaldi map area, southwestern British Columbia—II. Geomorphology and Quaternary volcanic rocks. *Geological Society of America Bulletin*, *69*, 179-198.

Mathews, W.H. (1989). Neogene Chilcotin basalts in south-central British Columbia: geology, ages and geomorphic history. *Canadian Journal of Earth Sciences, 26*, 969-982.

Mauldon, M. and Dershowitz, W. (2000). A Multi-Dimensional System of Fracture Abundance Measures. Paper presented at Geological Society of America Annual Meeting, Reno, Nevada, USA.

Mazzarini, F., Pareschi, M.T., Favalli, M., Isola, I., Tarquini, S., and Boschi, E. (2007). Lava flow identification and aging by means of LiDAR intensity: Mount Etna case. *Journal of Geophysical Research, 112*, B02201. doi: 10.1029/2005JB004166

Micheletti, N., Chandler, J.H. and Lane, S.N. (2015). Investigating the geomorphological potential of freely available and accessible structure-from-motion photogrammetry using a smartphone. *Earth Surface Processes and Landforms, 40*, 473-486. doi: 10.1002/esp.3648

Microsoft (2016). Excel (Version 2016) [Computer software]. Redmond, WA, U.S.A.

Mineo, S. and Pappalardo, G. (2016). The use of infrared thermography for porosity assessment of intact rock. *Rock Mechanics and Rock Engineering, 49*, 3027-3039. doi: 10.1007/s00603-016-0992-2

Mira Geoscience Ltd. (2019). GOCAD [Computer software]. Vancouver, Canada.

National Geographic (2016). Retrieved from http://science.nationalgeographic.com/science/earth/inside-the-earth/rocks-article/

Pesci, A., Loddo, F., and Conforti, D. (2007). The first terrestrial laser scanner application over Vesuvius: High resolution model of a volcano crater. *International Journal of Remote Sensing, 28(1)*, 203-219. doi: 10.1080/01431160500534473

Pesci, A., Teza, G., Casula, G., Loddo, F., De Martino, P., Dolce, M., Obrizzo, F., and Pingue, F. (2011). Multi-temporal laser scanner-based observation of the Mt. Vesuvius crater: Characterization of overall geometry and recognition of landslide events. *ISPRS Journal of Photogrammetry and Remote Sensing, 66(3)*, 327-336. doi: 10.1016/j.isprsjprs.2010.12.002

Pesci, A., Teza, G., and Ventura, G. (2008). Remote sensing of volcanic terrains by terrestrial laser scanner: preliminary reflectance and RGB implications for studying Vesuvius crater (Italy). *Annals of Geophysics, 51(4)*, 633-653.

Riegl Laser Measurement Systems GmbH. (2015). Riegl VZ-4000 Data Sheet. Horn, Austria.

Riegl Laser Measurement Systems GmbH. (2018). RiSCAN PRO (Version 2.1) [Computer software]. Horn, Austria.

Rocscience, Inc. (2020). DIPS (Version 6.0) [Computer software]. Retrieved from https://www.rocscience.com/software/dips

Saini-Eidukat, B., Schwert, D.P., and Slator, B.M. (2002). Geology explorer: virtual geologic mapping and interpretation. *Computers and Geosciences, 28*, 1167-1176.

Shevchenko, A.V., Dvigalo, V.N., and Svirid, I.Y. (2015). Airborne photogrammetry and geomorphological analysis of the 2001-2012 exogenous dome growth at Molodoy Shiveluch Volcano, Kamchatka. *Journal of Volcanology and Geothermal Research, 304*, 94-107.

Spampinato, L., Calvari, S., Oppenheimer, C., and Boschi, E. (2011). Volcano surveillance using infrared cameras. *Earth Science Reviews, 106*, 63-91. doi: 10.1016/j.earscirev.2011.01.003

Sturzenegger, M. (2010). Multi-scale characterization of rock mass discontinuities and rock slope geometry using terrestrial remote sensing techniques. Ph.D. Thesis, Simon Fraser University, Burnaby, Canada. 371p.

Sturzenegger, M. and Stead, D. (2009). Close-range terrestrial digital photogrammetry and terrestrial laser scanning for discontinuity characterization on rock cuts. *Engineering Geology, 106*, 163-182.

Teza, G., Marcato, G., Castelli, E., and Galgaro, A. (2012). IRTROCK: A MATLAB toolbox for contactless recognition of surface and shallow weakness of a rock cliff by infrared thermography. *Computers and Geosciences, 45*, 109-118. doi: 10.1016/j.cageo.2011.10.022

Teza, G., Marcato, G., Pasuto, A., and Galgaro, A. (2015). Integration of laser scanning and thermal imaging in monitoring optimization and assessment of rockfall hazard: a case history in the Carnic Alps (Northeastern Italy). *Natural Hazards, 76*, 1535-1549.

The Gimp Team (2018). GIMP (Version 2.10.8) [Computer Software]. Retrieved from http://www.gimp.org

The MathWorks, Inc. (2019). MATLAB (Version 2018b) [Computer Software]. Natick, Massachusetts, U.S.A.

Thurmond, J.B., Drzewiecki, P.A., and Xu, X. (2005). Building simple multiscale visualizations of outcrop geology using virtual reality modeling language (VRML). *Computers and Geosciences, 31*, 913-919. doi: 10.1016/j.cageo.2005.03.007

Tipper, H.W. (1971). Glacial geomorphology and Pleistocene history of central British Columbia. Geological Survey of Canada, Bulletin 196, 89p.

Unity Technologies (2016). Unity3D (Version 5.3.4f1) [Computer software]. Retrieved from https://unity3d.com/get-unity

Westoby, M.J., Brasington, J., Glasser, N.F., Hambrey, M.J., and Reynolds, J.M. (2012). 'Structure-from-Motion' photogrammetry: A low-cost, effective tool for geoscience applications. *Geomorphology, 179*, 300-314. doi: 10.1016/j.geomorph.2012.08.021

Woodell, D.R. (2012). Constraint on formation of columnar joints in basaltic lava. M.Sc. Thesis, University of British Columbia, Vancouver, Canada. 147p.

Appendix A. Data Analysis Scripts and Code

Description:

All scripts and code created and used for data analysis, written in MATLAB, Javascript, and C#. Scripts are available from the author upon request.

Filename:

Appendix A_Data Analysis Scripts and Code.pdf

Appendix B. Joint Properties

Description:

Data tables of joint properties for joints described in this research.

Filename:

Appendix B_Joint Properties.pdf

Appendix C. Temperature Data

Description:

Weather station, point of interest, and window temperature data as described in this research.

Filename:

Appendix C_Temperature Data.pdf

Appendix D. Thermal Imagery

Description:

Hourly and contrast thermal imagery for windows, and laboratory survey thermal imagery for samples used in this research.

Filename:

Appendix D_Thermal Imagery.pdf

Appendix E. Photographs of Hand Samples and Thin Sections

Description:

Hand sample and thin section imagery for samples used in this research.

Filename:

Appendix E_Photographs of Hand Samples and Thin Sections.pdf

Appendix F. LiDAR Data

Description:

Point data for reflectivity profiles created in this research.

Filename:

Appendix F_LiDAR Data.pdf